

Copyright
by
Kathryn O'Rourke Fry
2015

**The Thesis Committee for Kathryn O'Rourke Fry
Certifies that this is the approved version of the following thesis:**

**Lithofacies, Biostratigraphy, Chemostratigraphy, and Stratal
Architecture of the Boquillas Formation and Eagle Ford Group: A
Comparison of Outcrop and Core Data from Big Bend National Park to
Maverick Basin, Southwest Texas, USA**

**APPROVED BY
SUPERVISING COMMITTEE:**

Supervisor:

Robert Loucks

Co-Supervisor:

Gregory Frébourg

William Fisher

Charlie Kerans

**Lithofacies, Biostratigraphy, Chemostratigraphy, and Stratal
Architecture of the Boquillas Formation and Eagle Ford Group: A
Comparison of Outcrop and Core Data from Big Bend National Park to
Maverick Basin, Southwest Texas, USA**

by

Kathryn O'Rourke Fry B.S.

Thesis

Presented to the Faculty of the Graduate School of
The University of Texas at Austin
in Partial Fulfillment
of the Requirements
for the Degree of

Master of Science in Geological Sciences

The University of Texas at Austin

May 2015

Acknowledgements

I would like to thank the MSRL consortium members and sponsors for supporting current and ongoing research. MSRL consortium members include Anadarko, Apache, BHP, BP, Cenovus, Centrica, Chesapeake, Chevron, Cima, Cimarex, Concho, ConocoPhillips, Cypress, Devon, Encana, ENI, EOG, EXCO, ExxonMobil, Hess, Husky, IMP, Kerogen, Marathon, Murphy, Newfield, Oxy, Penn West, Penn Virginia Pioneer, QEP, Samson, Shell, StatOil, Talisman, Texas American Resources, The Unconventionals, US EnerCorp, Valence, and YPF. I would also like to thank Strata-X for allowing me to study a beautiful, continuous section of Eagle Ford from the Maverick Basin.

Thank you to my co-advisors, Bob Loucks and Greg Frébourg, for providing me with a truly irreplaceable and memorable experience through graduate school. It would not have been the same with any other team. Thank you also for the guidance during my research. I would also like to thank my committee members, Bill Fisher and Charlie Kerans for their support and encouragement.

I'd also like to thank Dr. Stephen C. Ruppel for allowing me to participate in and granting me funding through MSRL. Additionally, thank you for the masterful editing and review of my thesis.

I'd like to express my extreme gratitude to Richard Denne for taking the time to coach me about planktonic foraminifera identification, classification, and biostratigraphic application. I'd also like to thank Harry Rowe. Without his guidance, support, encouragement, and mentoring I would not have made it to where I am today. Another

thank you to all those who have worked in Harry's geochemical laboratory: Evan Sivil, Michael Nieto, Rob Nikirk, and Krystal Heibel.

I'd like to extend a huge thank you to all of my colleagues at the Core Research Center and Bureau of Economic Geology for making my experience enjoyable. These individuals include: James Donnelly, Nate Ivicic, Joseph Smitherman, Brandon Williamson, Bill Moulden, and Donnie Brooks.

And lastly, I'd like to thank my friends and family for their constant love, support, and encouragement.

Abstract

Lithofacies, Biostratigraphy, Chemostratigraphy, and Stratal Architecture of the Boquillas Formation and Eagle Ford Group: A Comparison of Outcrop and Core Data from Big Bend National Park to Maverick Basin, Southwest Texas, USA

Kathryn O'Rourke Fry, M.S.Geo.Sci.

The University of Texas at Austin, 2015

Supervisor: Robert Loucks

Co-Supervisor: Gregory Frébourg

The late Cretaceous-aged Eagle Ford and Boquillas Formations were deposited on the Texas paleoshelf during a major transgressive sequence wherein organic-rich mudrocks accumulated across the paleoshelf. This study investigates lithofacies; biostratigraphy, chemostratigraphy, and stratal architecture of the Eagle Ford and Boquillas Formations to characterize the depositional environment present during deposition, as well as define and describe the Cenomanian-Turonian (C-T) stage boundary and the Oceanic Anoxic Event II (OAE2). Comprehensive, high-resolution data sets compare geologic and geochemical interpretations of subsurface Eagle Ford Group conventional core from the Maverick Basin and chrono-synchronous Boquillas Formation outcrop strata from Big Bend National Park.

Results from core and outcrop show a dynamic depositional environment regularly influenced by bottom-currents, debris-flows, and deposition during anoxic bottom-water conditions. Elemental and biostratigraphic data show that the water-column was stratified – surface-waters experienced high levels of primary productivity while deeper waters were anoxic to euxinic. The Eagle Ford strata are divided into a lower and upper group defined geochemically by the appearance of a titanium-rich chemofacies correlative to massive argillaceous claystone. This change in deposition has been defined to occur concurrently with the C-T boundary (identified biostratigraphically) and OAE2 (identified chemostratigraphically and isotopically). The OAE2 as documented within both cores shows an ‘oxygenated’ anoxic event, wherein burrowing and low molybdenum are documented during the positive $\delta^{13}\text{C}$ isotope excursion. Outcrop and core data comparison demonstrate a similar depositional system between Big Bend National Park and Maverick Basin; bottom-currents, debris-flows, and periodic anoxia are all documented within both sections, however, further investigations are needed to correlate the sections.

Table of Contents

List of Tables	xii
List of Figures	xiii
INTRODUCTION.....	1
Problem and Objectives	2
Geographic Setting.....	5
Previous Studies.....	7
Trans-Pecos Texas	7
Maverick Basin and East Texas Studies	12
GEOLOGIC SETTING	17
Tectonics	17
South Texas Shelf	18
Comanchean Series	19
Gulfian Series.....	20
Structures	22
Oceanic Anoxic Events.....	25
METHODS.....	28
Core and Outcrop Data Summary	28
Facies Definition and Stratigraphy	29
Outcrop	29
Conventional Core Data.....	30
Petrography	31
Portable Gamma-Spectrometer	33
Energy Dispersive X-Ray Fluorescence (XRF).....	35
Methods for XRF Data Calibration.....	36

Methods for XRF Application	37
X-Ray Diffraction (XRD)	38
Carbon and Isotope Data.....	38
RESULTS	40
Facies, Facies Successions, and Chemostratigraphy	40
Mineralogy	40
Hot Springs Outcrop	42
Interpretation.....	45
Core-X Conventional Core	47
Interpretation.....	51
Winterbotham J.M. Jr. #1 Conventional Core	54
Interpretation.....	58
Paleoceanography	60
Hot Springs Outcrop	61
Interpretation.....	61
Core-X Conventional Core	62
Interpretation.....	63
Winterbotham J.M. Jr. #1 Conventional Core	65
Interpretation.....	66
Total Organic Carbon	68
Hot Springs Outcrop	68
Interpretation.....	69
Core-X Conventional Core	71
Interpretation.....	72
Winterbotham J.M. Jr. #1 Conventional Core	73
Interpretation.....	74
Lithofacies.....	75
Burrowed Skeletal Wackestone	79
Laminated argillaceous planktonic foraminifera wackestone.....	81

Laminated argillaceous inoceramid wackestone	82
Weakly laminated wackestone.....	85
Massive argillaceous claystone.....	87
Laminated calcisphere grainstone.....	89
Laminated skeletal grain-dominated packstone.....	92
Burrowed foraminifera wackestone	94
Laminated skeletal packstone-grainstone	97
Volcanic ash.....	99
Massive limestone.....	102
Recessive argillaceous mudrock	104
Peloidal crystalline mudrock.....	105
Facies Successions	108
Hot Springs Outcrop	111
Interpretation.....	115
Core-X Conventional Core	120
Interpretation.....	127
Winterbotham J.M. Jr. #1 Conventional Core	133
Interpretation.....	137
Fauna and Biostratigraphy	139
Faunal Descriptions	140
Planktonic Foraminifera.....	140
Radiolarians	146
Calcispheres	147
Inoceramids and Filaments	147
Biostratigraphy.....	148
Hot Springs Outcrop	148
Interpretation.....	151
Core-X Conventional Core	153
Interpretation.....	156
Winterbotham J.M. Jr. #1 Conventional Core	159

Interpretation.....	161
Isotope Data	163
Hot Springs Outcrop	163
Interpretation.....	165
Core-X Conventional Core	167
Interpretation.....	169
Winterbotham J.M. Jr. #1 Conventional Core	171
Interpretation.....	173
Carbon Isotope Regional Comparison	174
INTEGRATION OF MULTIDISCIPLINARY DATA SETS	178
Hot Springs Outcrop	178
Core-X Conventional Core	181
Winterbotham J.M. Jr. #1 Conventional Core	186
REGIONAL STRATIGRAPHY AND CORRELATION	190
Outcrop versus Subsurface Data	192
Comparison between Core-X and Winterbotham J.M. Jr. #1 Cores	194
CONCLUSIONS.....	199
Appendices.....	202
Appendix A: Description of Core and Outcrop Sections.....	202
Hot Springs Outcrop Section, Big Bend National Park Description	202
Core-X Conventional Core	206
Winterbotham J.M. Jr. #1 Conventional Core Description	211
REFERENCES.....	213
VITA	225

List of Tables

Table 1: Summary of core and outcrop data. Latitude, longitude, and API of Core-X are proprietary and have been removed.	28
Table 2: Thin-section sampling frequency.	32
Table 3: Portable gamma-spectrometer-data summary.	34
Table 4: XRF-scan type and energy summary.....	36
Table 5: XRD color key. Each mineral is assigned a specific color on XRD weight percent graphs.	42
Table 6: Summary of lithofacies. The table contains lithofacies name, in which locations it occurs, what formations it occurs in, the weathering character if applicable, dominant fauna per lithofacies, sedimentary structures, and a brief summary of the lithofacies. Mineralogy and TOC values included for each facies represent an average of values.	78
Table 7: Description of debris-flow at the top of the Buda Limestone. The Buda Limestone is composed of burrowed skeletal wackestone; the debris flow described above is composed of brecciated clasts of the same facies.	123

List of Figures

Figure 1: Paleogeography of the southern Western Interior Seaway and Texas paleoshelf in the Late Cretaceous. Color shading shows different geologic systems present. The light blue “Drowned Carbonate Shelf” contains the study area. Illustrations after Goldhammer, 1999; map from Blakey, 2011.	3
Figure 2: General Eagle Ford Group stratigraphy with accepted OAE2 and C-T boundary as defined only from the specific localities discussed within this study. The wavy line represents a major unconformity and separates the Buda Limestone from overlying formations. Data considered: Schlanger et al. (1976), Jenkyns (1980), Cooper et al. (2005), Lock et al. (2010), Donovan et al. (2012), Cooper (2014)	4
Figure 3: Map of study locations. Red stars on the right show locations of core from Maverick Basin. Green star represents location of outcrop section in Big Bend National Park. Names of each section are within the grey boxes.	6
Figure 4: Stratigraphic break out of south Texas and proto-Gulf series. Paleotopography present during the Coahuilan and Comanchean influenced Gulfian series deposition. The red box highlights stratigraphy documented in cores used for this study. WB stands for Winterbotham J.M. Jr. #1, CX stands for Core-X, HS stands for Hot Springs outcrop s. After Wilson and Ward (1993) and Gray (2008), Tiedemann (2010), Cooper (2014).	19

Figure 5: Paleogeography and structures of the Cenomanian-Turonian on the South Texas Shelf and in the Western Interior Seaway in Texas. The red stars show the core locations from Maverick Basin. The green star shows the location of the outcrop section. Structures after Adkins (1932), Shepard and Walper (1982), Wilson et al. (1984), Rose (1986), Goldhammer (1999, 2001), Driskill et al. (2012), Ruppel (2012), Denne (2014)..22

Figure 6: Map of Hot Springs outcrop locality in Big Bend National Park, Trans-Pecos, Texas. The red trail shows the path traversed to collect samples and data for a measured section. The base of the section is picked where the Buda Limestone is identified in the river bed; the top of the section is identified by a large fold visible on the south bank, wherein Ernst and San Vicente Member strata begin to repeat.30

Figure 7: XRD for outcrop samples from the Hot Springs outcrop section. Nine minerals are presented in weight percent. CGR and SGR are provided in the center. An interpreted mineralogy/lithology is provided on the right.43

Figure 8: XRF data showing proxies for mineralogy for Hot Springs outcrop samples. Gamma ray response and interpreted mineralogy/lithology is included on the right.44

Figure 9: XRD for conventional core samples from Core-X. Nine minerals are presented in weight percent. CGR and SGR are provided in the center. Interpreted mineralogy/lithology is shown on the right.....49

Figure 10: XRF data showing proxies for mineralogy for Core-X conventional core samples. Samples are plotted as either ppm or weight percent. Gamma ray response and interpreted mineralogy/lithology is included on the right.	50
Figure 11: XRD for conventional core samples from Winterbotham J.M. Jr. #1 Nine minerals are presented in weight percent. SGR are provided in the center. The SGR curves have been created using XRF elemental data – not downhole instruments or handheld gamma-spectrometer. An interpreted mineralogy/lithology is provided on the right.	56
Figure 12: XRF data showing proxies for mineralogy for Winterbotham J.M. Jr. #1 conventional core samples. Data are plotted in either ppm or weight percent. SGR and interpreted mineralogy/lithology has been provided on the right.	57
Figure 13: XRF data showing trace elements and proxies for paleoceanographic conditions for Hot Springs outcrop samples. Gamma ray response and interpreted mineralogy are included on the right.	61
Figure 14: XRF data showing trace elements and proxies for paleoceanographic conditions for Core-X. Redox sensitive elements are plotted as enrichment factors to show increase of element in terms of elemental concentration in the rest of the section. Gamma ray response and interpreted mineralogy are included on the right.	63

Figure 15: XRF data showing trace elements and proxies for paleoceanographic conditions for Winterbotham J.M. Jr. #1. Redox sensitive elements are plotted as enrichment factors to show increase of element in terms of elemental concentration in the rest of the section. Gamma ray response and interpreted mineralogy are included on the right.	66
Figure 16: C/N atomic ratio, TOC, molybdenum ppm, uranium ppm, and gamma ray data for outcrop samples from the Hot Springs outcrop. Exposure to weathering can decrease the amount of preserved organic matter. ..	69
Figure 17: C/N atomic ratio, TOC, molybdenum ppm, uranium ppm, and gamma ray for Core-X conventional core samples.	71
Figure 18: C/N atomic ratio, TOC, molybdenum ppm, uranium ppm, and gamma ray for Winterbotham J.M. Jr. #1 conventional core samples. Gamma ray values have been computed using XRF data.	74
Figure 19: Burrowed skeletal wackestone: A) Burrowed skeletal wackestone in core slab in Buda Limestone. B) Horsetail stylolites are dark grey in burrowed skeletal wackestones in Buda Limestone. C) Photomicrograph of burrowed skeletal wackestone with abundant calcispheres, echinoid fragment (C1), and planktonic foraminifera (C2) in Buda Limestone. D) Stylolite with dolomitization along seam in Buda Limestone.	80
Figure 20: Laminated argillaceous planktonic foraminifera wackestone: A) Core slab Laminated argillaceous planktonic foraminifera wackestone with interval of diagenetic calcite and volcanic ash in lower Eagle Ford strata. B) Photomicrograph with planktonic foraminifera laminations (outline by dashed red lines) in lower Eagle Ford strata.	82

Figure 21: Laminated argillaceous inoceramid wackestone: A) Core slab showing dominant inoceramid along bedding planes in lower Eagle Ford strata. B) Accumulation of inoceramid prisms in lower Eagle Ford strata. C) inoceramid filament in lower Eagle Ford strata. D) Cone-in-cone cement in lower Eagle Ford strata.84

Figure 22: Weakly laminated wackestone: A) Weakly laminated wackestone core slab in lower Eagle Ford strata. B) Photomicrograph of horizontal mud laminations outlined in white in lower Eagle Ford strata. C) Photomicrograph of *Heterohelix* sp. foraminifera in lower Eagle Ford strata. D) UV + yellow filter photomicrograph of weakly laminated wackestone with clay matrix and peloids (D1) in lower Eagle Ford strata.86

Figure 23: Massive argillaceous claystone: A) Core slab shows massive argillaceous claystone (red boxes) interfingering with laminated argillaceous planktonic foraminifera wackestones in upper Eagle Ford strata. B) Photomicrograph of argillaceous mud lamination with planktonic foraminifera below massive argillaceous claystone in upper Eagle Ford strata. C) Photomicrograph of abundant, calcified radiolarians (C1) and calcispheres (C2) within mud matrix in upper Eagle Ford strata. D) Photomicrograph in XPL of recrystallized planktonic foraminifera within extinct, argillaceous matrix in upper Eagle Ford strata.88

Figure 24: Laminated calcisphere grainstone: A) Core slab with calcisphere bed forms outlined in orange in upper Eagle Ford strata. B) Photomicrograph of inclined calcisphere lamina (yellow) with differential compaction in upper Eagle Ford strata. C) Photomicrograph of semi-coherent ductile fold, bedding outlined in yellow in in upper Eagle Ford strata. D) Photomicrograph of inoceramid (D1) in calcisphere grain lamination in upper Eagle Ford strata. E) Heterohelcidae planktonic foraminifera (E1) within possibly argillaceous muddy lamination in upper Eagle Ford strata.91

Figure 25: Laminated skeletal grain-dominated packstone: A) Core slab with flame structure in carbonate mud lamination in upper Eagle Ford strata. B) Photomicrograph of grain laminations outlined in red in upper Eagle Ford strata. C) inoceramid (C1), oyster (C2), and fish bones (C3) in grain lamination in upper Eagle Ford strata. D) Saccocomid echinoid fragments (D1) have a fuzzy, angular appearance compared to white, globular planktonic foraminifera (D2) in upper Eagle Ford strata. E) Core slab with angular intraclasts in in upper Eagle Ford strata.93

Figure 26: Burrowed foraminifera wackestone: A) Core slab with red line dividing burrowed zone and laminated zone in Austin Chalk. B) Burrow in unlaminated interval in Austin Chalk. C) Keeled (C1 *Marginotruncana* (poss.) sp.) and globular (C2 *Whiteinella* (poss.) sp.) planktonic foraminifera in burrowed interval in Austin Chalk. D) Imbricated keeled planktonic foraminifera *Marginotruncana* (poss.) sp. (D1), oyster fragment (D2), and globular foraminifera (D3) in grain lamination in Austin Chalk. E) Abundant dolomitization and unaltered peloids (E1) in Austin Chalk.96

Figure 27: Laminated skeletal packstone-grainstone: A) Outcrop photo of laminated skeletal packstone-grainstone with white grain laminations and brown carbonate mud laminations in lower Boquillas strata. B) Photomicrograph of laminated skeletal packstone-grainstone in lower Boquillas strata. C) Photomicrograph of grain lamination with relic fish bones (C1), calcispheres (C2), globular planktonic foraminifera (C3), and an echinoderm with calcite overgrowth (C4) in lower Boquillas strata. D) Photomicrograph of carbonate mud lamination with matrix-supported radiolarians (D1) in lower Boquillas strata. E) Photomicrograph of deformed grain and mud laminations from water escape in lower Boquillas strata.....98

Figure 28: Volcanic ash: A) Outcrop slab of volcanic ash is grey-yellow and fissile in Eagle Ford strata. B) Photomicrograph has pale yellow clay matrix with various phenocrysts in Eagle Ford strata. C) Photomicrograph with beta quartz (C1), globular planktonic foraminifera (C2), and inoceramid prisms (C3) in ash in Eagle Ford strata. D) Phyllosilicate grain within calcitized ash matrix in Eagle Ford strata. E) UV + yellow filter photomicrograph of globular planktonic foraminifera (E1) and peloids (E2) in fluorescing ash matrix in Eagle Ford strata.101

Figure 29: Massive limestone pseudolithofacies: Black arrows show massive limestone beds. A) Outcrop photo in the upper Ernst Member of plane-bedded indurated limestone outlined in red, color alternations on staff equal 1 ft. B) Outcrop photo in the lower Ernst Member of planar and lenticular laminated limestone interbedded with recessive argillaceous mudrock.103

Figure 30: Recessive argillaceous mudrock pseudolithofacies: Black arrow highlights recessive argillaceous mudrock beds. A) Outcrop photo of alternating recessive marl and massive limestone in upper Boquillas Member, staff equals 6ft. B) Outcrop photo of recessive argillaceous mudrock with small thrust fault in lower Boquillas Member.105

Figure 31: Peloidal crystalline mudrock: A and B) Peloidal crystalline mudrock in lower Boquillas strata as it appears in discrete beds at outcrop. Beds can have different outward appearance but look comparable when observed in thin-section. C) Small interlocking calcite crystals within the matrix with recrystallized radiolarians, planktonic foraminifera, and unaltered peloids in lower Boquillas strata. D) Hedgergellid planktonic foraminifera within secondary calcite crystals in lower Boquillas strata.106

Figure 32: Peloidal crystalline mudrock in core: A) Core slab in lower Eagle Ford strata of diagenetic calcite has sharp base and gradational top. Laminations in peloidal crystalline mudrock (A1) are less compacted than compacted lamina (A2). B) Pervasive crystallization of matrix and radiolarians (B1) in lower Eagle Ford strata. C) Pyritized radiolarians (C1) and peloids (C2) within diagenetic calcite crystals in lower Eagle Ford strata.108

Figure 33: Legend for stratigraphic sections included within this chapter and within the appendix.110

Figure 34: Outcrop photos from the Hot Springs locality in Big Bend National Park.

A) Base of measured section with the Buda Limestone (burrowed skeletal wackestone, 0 ft) outcropping in the Rio Grande river bed. B) Boquillas Formation as it appears in outcrop (13 ft). Contact between the Buda (lower bed, burrowed skeletal wackestone) and Ernst Member of the Boquillas Formation (upper bed, laminated skeletal packstone-grainstone). C) Contact between the Ernst and San Vicente Members of the Boquillas Formation (275 ft) marked by the *Allocrioceras hazzardi* zone outlined in red (note cyclicity of massive limestone and recessive argillaceous mudrock). D) Large in situ inoceramid in the Ernst Member of the Boquillas Formation on the bedding plane of laminated skeletal packstone-grainstone (24 ft).112

Figure 35: Hot Springs outcrops, Big Bend National Park lithostratigraphy. Color blocks refer to facies defined in Fig. 33.....113

Figure 36: Core-X lithostratigraphy. A key to lithologies can be found in Fig. 33. Ash abundance histogram (center) represents number of ashes present per 10 ft bin. Gamma (right) is from downhole logs.121

Figure 37: Contact between Buda Limestone and Eagle Ford Group at 4,032.5 ft. A) Core slab showing the stark color contrast between the Buda Limestone (burrowed skeletal wackestone) and Eagle Ford Group (laminated argillaceous planktonic foraminifera wackestone). B) Photomicrograph showing Buda Limestone lithoclasts within the Eagle Ford Group. The contact is outlined in red.124

Figure 38: Winterbotham J.M. Jr. #1 lithostratigraphy. Ash abundance is displayed as a histogram showing ash beds per nine foot interval. Gamma ray values have been computed using XRF data. Key is contained in Fig. 33.134

Figure 39: Winterbotham J.M. Jr. #1 photographs and photomicrographs. A) Thickest volcanic ash bed in the core at 6,332 ft I the upper Eagle Ford strata. The small dark patches are authigenic pyrite. B) Brittle lithified intraclasts in a debris-flow deposit in the upper Eagle Ford Group at 6,293 ft (overlain by laminated skeletal grain-dominated packstone).....136

Figure 40: Generalized distribution of Cretaceous planktonic foraminifera within the water-column. This image is a visual model and should not be read to scale. Modified from Boudagher-Fadel (2013) and Denne et al. (2014). Hedbergellidae represents surface-dwelling planktonic foraminifera and are eutrophic (1: *Hedbergella* sp. in Core-X lower Eagle Ford strata in laminated argillaceous planktonic foraminifera wackestone at 4,008 ft and 2: *Whiteinella* in Hot Springs upper Ernst Member strata in laminated skeletal grain-dominated packstone at 168 ft). Heterohelicidae represents intermediate water-depth planktonic foraminifera and generally exist in eutrophic to mesotrophic water conditions (3: *Heterohelix* sp. in Core-X in lower Eagle Ford strata laminated argillaceous planktonic foraminifera wackestone at 3,955 ft and 4: *Heterohelix* sp. in Core-X upper Eagle Ford strata at 3,720 ft). Keeled planktonic foraminifera represent deep-dwelling planktonic foraminifera that can live in more specialized conditions (5: *Rotalipora cushmani* in Core-X lower Eagle Ford strata in laminated argillaceous planktonic foraminifera wackestone at 3,851 ft and 6 *Globotruncana* sp. in the Core-x Austin Chalk strata in burrowed foraminifera wackestone at 3,550 ft).....142

Figure 41: Hot Springs outcrop section biostratigraphy. Bubble size denotes general abundance, smaller bubbles correlate to rare or lesser abundance, larger bubbles correlate to commonly abundant to dominant. FAD = first appearance datum; LAD – last appearance datum.....149

Figure 42: Photo plate of Hot Springs outcrop section biostratigraphy microfossils. A) Buda Limestone (burrowed skeletal wackestone) with large hedbergellid planktonic foraminifera and small calcispheres. B) Lower Ernst Member (laminated argillaceous planktonic foraminifera wackestone) with small *Heterohelix* sp. (B1) and possible *R. greenhornensis* (B2). C) *Heterohelix globulosa* in the upper Ernst Member (laminated skeletal grain-dominated packstone). (D) Undifferentiated hedbergellid and heterohelcid foraminifera in the San Vicente Member (burrowed foraminifera wackestone).....150

Figure 43: Core-X biostratigraphy. Bubble size denotes general abundance, smaller bubbles correlate to rare or lesser abundance, larger bubbles correlate to common or extremely abundant. FAD = first appearance datum, LAD = last appearance datum. The red box shows the position of the OAE2.153

Figure 44: Photo plate of Core-X biostratigraphy microfossils. A) Planktonic foraminifera (hedbergellids) and calcispheres in Buda Limestone (burrowed skeletal wackestone). B) Two red arrows show inoceramid filaments in lower Eagle Ford. C) *Rotalipora* (poss.) *greenhornensis* in the lower Eagle Ford (laminated argillaceous planktonic foraminifera wackestone). D) *Rotalipora cushmani* in the lower Eagle Ford (laminated argillaceous planktonic foraminifera wackestone). E) *Heterohelix globulosa* (red arrow) in upper Eagle Ford (laminated argillaceous planktonic foraminifera wackestone). F) Inoceramid fragment (red arrow) in calcispheres in the upper Eagle Ford (laminated calcisphere grainstone). G) *Heterohelix globulosa* (bottom left) and unidentified keeled planktonic foraminifera (possibly a globotruncanid, top middle) in burrowed foraminifera wackestone in the Austin Chalk. H) Unidentified keeled planktonic foraminifera (left, globotruncanid) and hedbergellid foraminifera (right) in Austin Chalk (burrowed foraminifera wackestone).....154

Figure 45: Winterbotham J.M. Jr. #1 core biostratigraphy. Bubble size denotes general abundance, smaller bubbles correlate to rare or lesser abundance, larger bubbles correlate to common or extremely abundant. FAD = first appearance datum, LAD = last appearance datum. The red box shows the position of the OAE2.159

Figure 46: Photo plate of Winterbotham J.M. Jr. #1 core biostratigraphy microfossils.

A) Calcite recrystallization within the remnant of a radiolarian in the lower Eagle Ford (laminated argillaceous planktonic foraminifera wackestone). B) Possible *Rotalipora* sp. in the lower Eagle Ford. C) *Heterohelix globulosa* ? (red arrow) in the upper Eagle Ford (laminated argillaceous planktonic foraminifera wackestone). D) Calcite-cemented, undifferentiated *Hebergella* sp. and calcispheres in the upper Eagle Ford (in mass transport unit similar to laminated skeletal grain-dominated packstone). E) Unidentified keeled planktonic foraminifera (E1) and *Heterohelix globulosa* ? (E2) in the Austin Chalk (burrowed foraminifera wackestone).....160

Figure 47: Hot Springs outcrops isotope stratigraphy. Data points are plotted individually without a trend line because of poor data resolution.

Gamma ray is included for correlation.164

Figure 48: Hot Springs outcrops organic carbon crossplots. A) Annotations after Meyers (1997) help delineate organic matter variety. B) Annotations after Algeo and Lyons (2006) and Rowe et al. (2008) showing basin restriction.165

Figure 49: Core-X conventional core isotope stratigraphy. Two red boxes outline areas of positive excursions of $\delta^{13}\text{C}$. The OAE2 encompasses the lower positive isotope excursion. Gamma ray is included for correlation.168

Figure 50: Core-X conventional core organic carbon crossplots. A) Annotations after Meyers (1997) help to delineate organic matter variety. B) Annotations after Algeo and Lyons (2006) and Rowe et al. (2008) show basin restriction.169

Figure 51: Winterbotham J.M. Jr. #1 conventional core isotope stratigraphy. The red box outlines a zone of positive excursions of $\delta^{13}\text{C}$. The OAE2 occurs during the boxed positive isotope excursion. Gamma ray is included for correlation.	172
Figure 52: Winterbotham J.M. Jr. #1 conventional core organic carbon crossplots. A) Annotations after Meyers (1997) help to delineate organic matter variety. B) Annotations after Algeo and Lyons (2006) and Rowe et al. (2008) show basin restriction.	173
Figure 53: Comparison of $\delta^{13}\text{C}$ Data. Carbon isotope data is provided from Phelps (2011) and Donovan (2012) for comparison of the interpreted OAE2 shown in this study.	177
Figure 54: Hot Springs outcrop composite stratigraphy. Graphic integrates data from individual data sets to show correlation. Color keys for lithofacies and biostratigraphy are included in Fig. 35 and Fig. 41.	179
Figure 55: Core-X composite stratigraphy. Graphic integrates data from individual data sets to show correlation. Color keys for lithofacies and biostratigraphy are included in Fig. 36 and Fig. 43.	182
Figure 56: Winterbotham J.M. Jr. #1 composite stratigraphy. Graphic integrates data from individual data sets to show correlation. Color keys for lithofacies and biostratigraphy are included in Fig. 38 and Fig. 45.	187
Figure 57: Regional cross section comparing all three data sets. CGR, SGR, calcium, silica, titanium, molybdenum (ppm), and $\delta^{13}\text{C}$ have been included for comparison. Cross section is not to scale and represents suggested correlations.	191

INTRODUCTION

The Eagle Ford Group (South Texas) and Boquillas Formation (Trans-Pecos Texas) represent chronosynchronous deposition on the South Texas Shelf (Fig. 1) during the Late Cretaceous (Barnes, 1977). The Eagle Ford Group and Boquillas Formation contain unburrowed skeletal wackestones and argillaceous to calcareous laminated mudrocks and wackestones. Lack of burrowing and benthic fauna, as well as preservation of original sedimentary features demonstrates deposition in a potentially anoxic environment. After the discovery of the Eagle Ford Group as an unconventional resource play in 2008 (Railroad Commission of Texas), both academia and industry have focused studies on better understanding the play in order to efficiently utilize the system for economic development.

Both the Eagle Ford Group and Boquillas Formation were deposited during a widespread marine transgression (Barnes, 1977), creating a major unconformity between the Eagle Ford Group (Boquillas Formation) and the underlying Buda Formation. The Buda Formation was deposited during a time of healthy carbonate production on the South Texas Shelf (Fig. 2). The shift in deposition style from healthy marine to anoxic demonstrates a major change in sediment deposition and water habitability. The Eagle Ford Group is overlain by the Austin Chalk, demonstrating a depositional change to a more habitable, carbonate shelfal environment as documented by a change in sedimentary features, preserved fauna, and burrowing. The Boquillas Formation of Trans-Pecos Texas displays this same depositional regime shift: the lower Ernst Member represents 'Eagle-Ford-style deposition,' whereas the overlying San Vicente Member represents a healthier, carbonate shelf system. Deposition of the Ernst Member of the Boquillas Formation and the Eagle Ford Group occurs across the Cenomanian-Turonian stage boundary (Fig. 2).

This boundary is defined by the occurrence of the Oceanic Anoxic Event II (Schlanger, 1987; Jenkyns, 2013; Phelps et al., 2013).

Increasing industry interest in resource play utilization has created a need to properly characterize and understand the geology and depositional environment of the Eagle Ford Group. This study integrates petrography, stratigraphy, biostratigraphy, and chemostratigraphy to characterize the subsurface resource play using core (Eagle Ford Group) and outcrop (Boquillas Formation). Objectives include (1) defining and describing lithofacies within the Eagle Ford Group, (2) documenting fauna and biostratigraphic markers throughout the Cenomanian-Turonian-age succession, (3) characterizing the geochemistry and chemostratigraphy of the Eagle Ford Group and Boquillas Formation (4) defining and describing the Oceanic Anoxic Event II (5) integrating subsurface (Eagle Ford Group) and outcrop (Boquillas Formation) data for correlativity.

Problem and Objectives

The Late Cretaceous (Cenomanian-Turonian) Eagle Ford and Boquillas Formations were deposited on a drowned carbonate shelf as the result of a major transgression (Galloway, 2008) on the South Texas Shelf (Fig. 1). The Boquillas and Eagle Ford have been defined as age-equivalent units deposited during the same transgression (Barnes, 1977). Strata deposited west of the Devils River are described as the Boquillas Formation, while those east of the Devils River are named Eagle Ford Group. Deposition on the drowned shelf was laterally expansive, however, local structures such as the San Marcos Arch, Maverick Basin, Coahuila Platform, and Chihuahua Trough created different types of deposition and variation in unit thickness within time-equivalent strata (Hentz and Ruppel, 2011). Heterogeneities within

lithofacies, sedimentary features, geochemical data, and lateral connectivity have caused inconsistent conclusions defining the paleodepositional environment and paleoceanographic conditions at the time Eagle Ford deposition.

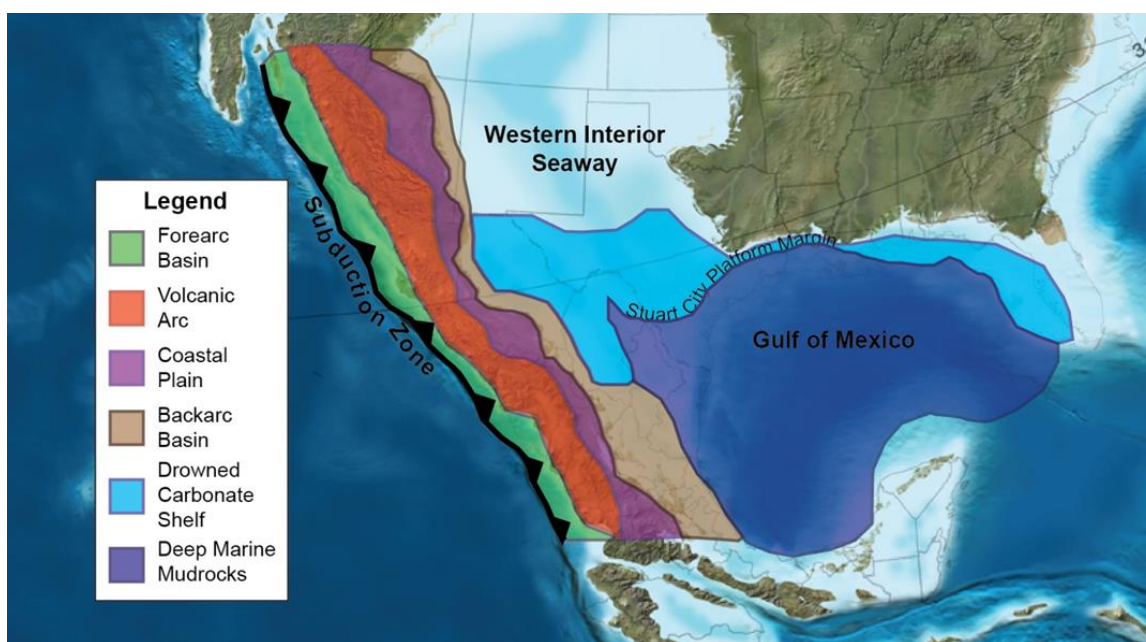


Figure 1: Paleogeography of the southern Western Interior Seaway and Texas paleoshelf in the Late Cretaceous. Color shading shows different geologic systems present. The light blue “Drowned Carbonate Shelf” contains the study area. Illustrations after Goldhammer, 1999; map from Blakey, 2011.

During the Cretaceous time, the world oceans experienced several major disturbances that impacted the global carbon cycle (Jenkyns, 2010). One of the most significant events occurred at the Cenomanian-Turonian (C-T) stage boundary, documented as the Oceanic Anoxic Event 2 (OAE2) (Jenkyns, 1980; Fig. 2). The OAE2 is defined and identified within the rock record by a positive excursion of $\delta^{13}\text{C}$ (Schlanger, 1987; Phelps et al., 2013). The occurrence of the OAE2 coincides with Eagle Ford and Boquillas deposition on the Texas paleoshelf (Fig. 2). While anoxic events are

generally documented as condensed, black shales deposited under anoxic conditions resulting in organic matter accumulation (Schlanger and Jenkyns, 1976), documentation of the OAE2 within the Eagle Ford Group has shown a range of lithofacies and mineralogies. OAE2 strata documented within the Eagle Ford within the Maverick Basin deviate from the condensed black shales defined within the classic definition.

Period	Epoch	Stage	Big Bend National Park		Maverick Basin	
Cretaceous	Upper	Coniacian	Boquillas	San Vicente	Austin	
		Turonian		Ernst	Eagle Ford	Upper
		Cenomanian				OAE2
			Buda		Buda	

Figure 2: General Eagle Ford Group stratigraphy with accepted OAE2 and C-T boundary as defined only from the specific localities discussed within this study. The wavy line represents a major unconformity and separates the Buda Limestone from overlying formations. Data considered: Schlanger et al. (1976), Jenkyns (1980), Cooper et al. (2005), Lock et al. (2010), Donovan et al. (2012), Cooper (2014)

This study incorporates visual geologic, geochemical, and chemostratigraphic data from both outcrop and core to define the paleodepositional and paleoceanographic

conditions present during Eagle Ford deposition on the South Texas Shelf. Locations have been selected within the Maverick Basin, as well as near the Chihuahua Trough – data from different localities are compared to understand changes in deposition across the South Texas Shelf. Lithofacies and chemofacies are used to describe conditions of Eagle Ford deposition at each locality. The Eagle Ford Group is divided into an upper and lower member using gamma ray, elemental, facies, and fauna data. Using isotopic and biostratigraphic data, the C-T boundary and OAE2 are identified in the Eagle Ford Group. Identification of both C-T boundary and OAE2 produce a paleoceanographic and lithofacies description of the OAE2 as it appears in the Eagle Ford Group deposited within the Maverick Basin. Lithofacies, chemofacies, and chemostratigraphy are used in tandem to describe and define the paleoceanic conditions impacting deposition of the Eagle Ford Group during the OAE2.

Geographic Setting

Three individual Eagle Ford and Boquillas sections are used for this study, one outcrop (Boquillas) and two cores (Eagle Ford) (Fig. 3). All locations are located on the Cretaceous-age South Texas Shelf.

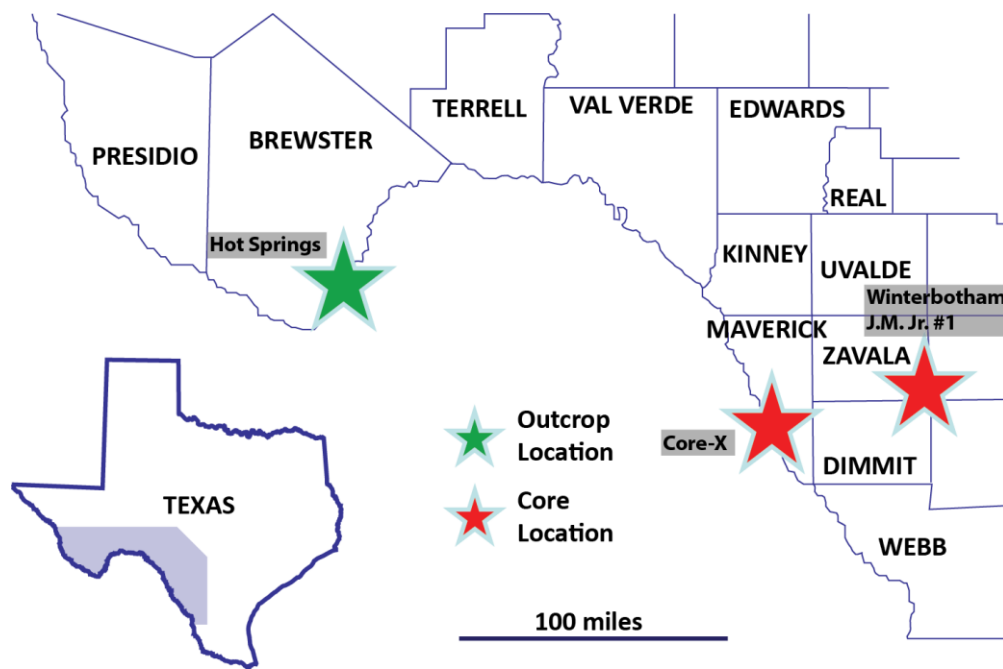


Figure 3: Map of study locations. Red stars on the right show locations of core from Maverick Basin. Green star represents location of outcrop section in Big Bend National Park. Names of each section are within the grey boxes.

The Boquillas outcrop section, located in Brewster County, Trans-Pecos Texas, represents Cenomanian-Santonian aged strata. The observed section at the Hot Springs outcrop locality within Big Bend National Park contains the Buda Limestone and the overlying Boquillas Formation (Fig. 2). The Boquillas Formation is divided into two units: the Ernst Member (Cenomanian-Turonian) and the San Vicente Member (Turonian-Santonian). The Ernst Member is the age-equivalent, Eagle Ford Group strata in south and East Texas (Barnes, 1977). This study will focus on observations of the Ernst Member. Paleogeographically, this area is located along the Coahuila Platform east of the Chihuahua Trough.

The two cores used in this study are located within the Maverick Basin (Fig. 3). The Maverick Basin in south Texas represents the thickest succession of Eagle Ford Group deposits on the drowned Late Cretaceous shelf (Hentz and Ruppel, 2011). The Winterbotham J.M. Jr. #1, operated by Prairie Producing Co., is located in the southeast corner of Zavala County. The Core-X (actual well name has been withheld for privacy), operated by Strata-X, is located in southwestern Maverick County along the Texas-Mexico border. Both cores will be referred to within the text using only well name. These two cores create an approximate dip-profile, where the Winterbotham J.M. Jr. #1 is proximal and the Core-X is distal to the basin edge.

Previous Studies

Interpretation of the depositional regime present during accumulation of the Boquillas Formation and the Eagle Ford Group has been a topic of debate for the past century. While there is no argument that there are carbonate and clastic influences, almost every other aspect, such as depth of deposition, depositional environment, ocean chemistry, and lithofacies, has been discussed in opposing directions. Most common topics of debate include but are not limited to: water depth at time of deposition, depth to storm -wave base, the occurrence of and subsequent levels of anoxia, the potential for an unconformity between Eagle Ford or Boquillas Formations and the Buda Limestone below, and interpretation of fauna presence and abundance. The following section aims to give a fair representation of influential works from the past century, paying attention to different hypotheses.

TRANS-PECOS TEXAS

The Boquillas Formation within Big Bend National Park has been the subject of several prior investigations. The Boquillas Formation first appeared in literature in 1907

when Udden compiled documentation regarding the geologic units present within the “Chisos Country.” The Boquillas Formation was originally named the Boquillas Flags by Udden for the old Boquillas post office in Tornillo Creek. Udden noted that the Boquillas Formation section marks a stark contrast to the underlying "heavy-bedded limestones" and that the unit is rich in organic matter. Udden also described the presence of foraminifera and *Inoceramus*, and correlated the Boquillas Formation to the Eagle Ford Group in the east. The Boquillas Formation was later divided into two distinct units, the lower Ernst Member and upper San Vicente Member, by Maxwell in 1965 and 1967. Maxwell created a geologic map of units within Big Bend National Park and Brewster County, compiling stratigraphic descriptions of each unit from several localities within the area. Maxwell (1965, 1967) described the Ernst Member of the Boquillas Formation as an alternating flagstone and clay succession with an abrupt, unconformable contact with the underlying Buda Formation. Maxwell defined the contact between the Ernst Member and overlying San Vicente Member by the appearance of the ammonite *Allocrioceras hazzardi*.

Fossil identification by W. A. Cobban from outcrop studies was summarized by Freeman in 1961. Classification of fossils placed the Boquillas Formation within the Cenomanian to Turonian ages. Freeman summarized the lithologies within the outcrops of Boquillas strata in Val Verde, Terrell and Brewster Counties, and divided the Boquillas strata into four units based on rock components and weathering character. Powell (1965) compared the Boquillas Formation to two other neighboring, laterally equivalent units (Ojinaga and Chispa Summit). He characterized those facies within the Boquillas as being shelfal, rather than basinal as are the Ojinaga and Chispa Summit Formations. Powell pushed his shelfal interpretation even further, making the hypothesis that the Boquillas strata may even represent a tidal flat. Work by Pessagno (1969) divided

the Late Cretaceous into six different zones based on planktonic foraminifera assemblages and zonation. He divided the Boquillas strata into two distinct members: the Rock Pens Member and the Austin Chalk. Pessagno also divided eastern Eagle Ford deposits into three substages: the Lozerian (lowest Eagle Ford and upper Cenomanian), the Bocian (middle Eagle Ford – commonly absent in Texas, early Turonian), and the Sycamorian (uppermost Eagle Ford, late Turonian). The comparison of planktonic foraminifera assemblages and ammonite assemblages (Adkins, 1951) show that the Lozerian and Sycamorian stages are unconformable in most areas of central and East Texas; the middle Bocian (early Turonian) stage is absent (Pessagno, 1969).

The investigation of the Boquillas strata had a renaissance in the late eighties to early nineties, with several Master's theses covering topics such as sedimentology and isotope geology (Sanders, 1988) and facies and depositional environments (Trevino, 1988) of Boquillas Formation outcrops in West Texas. Sanders (1988) illustrated a deepening paleoenvironment with normally anoxic bottom-waters at the Hot Springs outcrop location in Big Bend National Park using light microscopy, outcrop lithostratigraphy, and geochemical methods (x-ray diffraction, total organic carbon, stable isotopes). Sanders concluded that the Ernst Member of the Boquillas Formation is composed of open-marine carbonates, deposited disconformably below storm-wave base onto the Buda Limestone. Trevino (1988) concluded that the Buda-Boquillas contact is conformable and represents no significant lapse of time based on the study of several outcrop locations in southwest Texas near the Rio Grande River (Note: this conclusion has since been retracted by Trevino through verbal communication). Trevino explained that the outcrops appear to illustrate that the Boquillas was deposited in moderately deep shelfal conditions with anoxic ocean bottom sediments. Hummocky cross-stratification is described in specific intervals within the Boquillas Formation; such intervals are

described as deposited at approximately 50 meters water depth under anoxic conditions. (Note: the identification of hummocky cross stratification within the Boquillas has also been retracted by Trevino). Miller (1990) compared strata deposited at the Hot Springs outcrop location within Big Bend National Park and strata within the Maverick Basin, concluding that deposition in the Chihuahua Trough and within Maverick Basin may have been similar. Deposits at both localities are defined as being deposited in density stratified anoxic basins. Miller also compared the Hot Springs outcrops in Big Bend and Maverick Basin deposits to Lozier Canyon outcrops. Miller concluded that Lozier Canyon outcrops exhibit a completely different depositional environment that was interpreted to have been located on a topographic high. The deposits in Lozier Canyon may have been deposited in a much shallower environment between 100-200 feet.

Utilization of unconventional plays initiated a new wave of geologic research in the Boquillas Formation. Barnes (1977) concluded that the Boquillas Formation west of the Devils River is time-equivalent to the hydrocarbon producing Eagle Ford Group to the east. A geochemical investigation of central Texas outcrops by Liro (1994) revisited the idea that the Eagle Ford near the San Marcos Arch is possibly interdeltic or lagoonal and was deposited in 60-100 feet water depth. Lock and Peschier (2006) and Lock et al. (2010) redefined the interpretation of the Boquillas section in Val Verde and Terrell counties as slope deposits, rather than shallow-shelf or tidal-flat deposits. Lock et al. divided the Boquillas section into three distinct units (a lower, middle, and upper member) that represent a transgressive-regressive sequence. Donovan and Staerker (2010) concluded that the Boquillas and Langtry Formations in the nearby subsurface can be correlated to local outcrops. Donovan and Staerker proposed that the contact between the Rock Pens and overlying Langtry actually represents the unconformable contact between the Eagle Ford and Austin Chalk units as documented in East Texas. Donovan

and Staerker (2010) did not discuss the relationship between the Rock Pens and Langtry as compared to the Ernst and San Vicente Members of the Boquillas Formation. Donovan et al. (2012) used outcrops near Del Rio, Texas to overturn the conventional mindset that Eagle Ford style reservoirs are homogenous. The Eagle Ford is separated into five distinct units that create the lower Eagle Ford upper Eagle Ford, and Austin Chalk. Donovan et al. (2012) placed the OAE2 in the middle of the lower, upper Eagle Ford. Forkner (2014) correlated outcrop and core near Del Rio, Texas. He compared weathered outcrop and unweathered core facies to define “cycle motifs.” Forkner’s study has potential to connect studies in the Big Bend region to those in the Maverick Basin region.

In recent years, Cooper and Cooper (2007, 2008, 2014) published field guides dealing with the *Allocrioceras hazzardi* zone (AHZ) within the Boquillas Formation in and around Big Bend National Park. They proposed and defined the type section of the Ernst Member of the Boquillas Formation at the Hot Springs Trail (2007). Cooper and Cooper (2008) created a composite section of the AHZ, linking several measured *Allocrioceras hazzardi* zones throughout Big Bend National Park. *Allocrioceras hazzardi* is used as an index fossil representing the early Coniacian. The AHZ marks the boundary between the Ernst and San Vicente Members of the Boquillas Formation, as well as the Turonian-Coniacian boundary. The field guide by Cooper and Cooper (2014) is the culmination of approximately two decades work mapping Turonian-Coniacian contact between the Ernst and San Vicente Members, defining the type Ernst Member section, creating a composite-section of the AHZ zone throughout the park, biostratigraphy of the Boquillas Formation, and mapping structures within the formations. The field guide proposes the Cenomanian-Turonian Stage boundary and OAE2 as being located 23 meters above the Buda-Ernst contact. Cooper and Cooper (2014) used chronocorrelation of the AHZ zone and biostratigraphy of ammonites and cephalopods to define a shallow

depositional environment (the lowest Ernst being supratidal, the upper Ernst being below storm-wave base), periodically influenced by strong currents, on an isolated bathymetric high.

MAVERICK BASIN AND EAST TEXAS STUDIES

The Eagle Ford Group has been a topic of many geologic studies in this area for over a century, with recent research expanding and increasing exponentially following the unconventional energy boom. Most studies focus on Eagle Ford deposits within the East Texas Basin and near the San Marcos Arch, or Eagle Ford Group outcrops in Dallas and Austin area. Very few published studies have focused on subsurface Eagle Ford Group within Maverick Basin; hence, the following section will summarize significant findings from East Texas.

Eagle Ford strata were first mentioned by Roemer in 1852, but the formation was not labeled the Eagle Ford until 1887 by Hill when he established the type locality within the Eagle Ford village in Dallas County, Texas. Regional observations by Stephenson (1929) concluded that the unconformity between Eagle Ford and Austin Chalk that appears near the San Marcos Arch and East Texas Basin is substantial and marks a significant event. Early work in the Eagle Ford by Adkins (in Sellards, 1933) discussed the stratigraphic and formation changes throughout the succession ranging from deposits near the San Marcos Arch to Austin to Dallas and into Trans-Pecos Texas. Adkins (1933) summarized that the Eagle Ford strata in East Texas is far thinner and contains a much different biota than the substantially thicker deposits in West Texas. Adkins and Lozo (1951) divided the Eagle Ford Group into several divisions based on ammonite assemblages. McNulty (1964) used foraminifera assemblages to hypothesize that the depositional system of the Eagle Ford Group was toxic (anoxic) and occurred in a deeper

water setting, as compared to the shallower water deposited and oxygenated Austin Chalk. The author inferred that there is stratigraphic importance of the lag deposits that contain abundant phosphate and other biogenic debris at the Eagle Ford-Austin Chalk contact in East Texas. A complete analysis of regional East Texas Basin lithology and stratigraphy was conducted by Surles (1987). Surles concluded that the Eagle Ford Group in East Texas is composed of mostly shale and is correlative to other time-equivalent units on the South Texas Shelf.

Many studies of the Eagle Ford Group in central and East Texas have attempted to break the Eagle Ford section into several subdivisions based on locality, potential age, and lithologic variation. Several studies (Adkins, 1951; Brown and Pierce, 1963; Pessagno, 1969; Surles, 1987; Jiang, 1989; Dawson, 2010) concluded that the Eagle Ford is both laterally and vertically heterogeneous because of depositional variability of the mudrock systems. Adkins (1951) divided the Eagle Ford Group into numerous subdivisions based on ammonite assemblages, giving defined ages to the group biostratigraphically. Brown and Pierce (1963) considered the possibility of correlating the Eagle Ford Group on the basis of palynology, or pollen, in the area near Dallas, Waco, and the East Texas Basin. Wireline logs and ammonite biostratigraphy were used in tandem with palynology to conclude that there is one perfectly correlative interval near one large bentonite, and that the ages of the Eagle Ford is late Cenomanian to middle Turonian. Pessagno (1969) created a three stage division of the Eagle Ford Group in central and East Texas based on planktonic foraminifera assemblages. Surles (1987) studied Eagle Ford deposits in East Texas, attempting to interpret depositional changes between four accepted subdivisions (subdivisions are as follows: Tarrant, Woodbine, Britton, Arcadia Park). Jiang (1989) compiled several of the numerous different divisions, including his own Eagle Ford Group subdivisions for the purposes of his study.

Dawson (2010) conducted a study defining micro-scale variability in Eagle Ford facies, noting that the Eagle Ford strata is composed of high-frequency alternations of both high- and low-energy deposits (e.g., pelagic mud versus turbidity flow deposits). Unfortunately, there have been few efforts to consolidate or agree upon formation divisions.

Denne et al. (2014) conducted a paleontological study on subsurface Eagle Ford deposits from the East Texas Basin. Denne et al. (2014) demonstrated that thin-section based foraminifera identification is a better method for foraminifera documentation as compared to the standard use of residue samples. The paper disagrees with the conclusion made by Fairbanks (2012) that the dominant limestone facies are related to planktonic foraminifera test accumulation. The dominant foraminifera accumulations are in the muddier; marl layers and the limestone layers are composed of diagenetic calcite and calcified radiolarians. Denne et al. (2014) divides the Eagle Ford Group into thirteen distinct groups that are defined by planktonic foraminifera, benthic foraminifera, and *Inoceramus* filaments (filaments refer to the planktonic *Inoceramus* larvae stage). The study concluded that the majority of the Eagle Ford was deposited under anoxic to euxinic conditions, and that production of the limestone-marl interval of the Eagle Ford is dominantly because of ocean mixing.

Only recently have studies begun focusing on the Maverick Basin. Hentz and Ruppel (2011) presented stratigraphic interpretations from gamma ray correlations throughout East and south Texas that defined the occurrence and thickness of the Eagle Ford Group, as well as laterally equivalent units east of the San Marcos Arch. The Eagle Ford section in East Texas (as divided by Hentz and Ruppel, 2011) is composed of a consistent, thin deposit of the lower Eagle Ford and varied intervals of the upper Eagle Ford. The upper Eagle Ford in East Texas pinches out to the west, and is not present in

some areas. The Austin Chalk unconformably overlies the Eagle Ford in this region. This is in contrast with Eagle Ford Group deposition in west/southwest Texas where the Maverick Basin is located. In this area, the lower Eagle Ford section creates a relatively consistent blanket, followed by a greatly thickened and continuous upper Eagle Ford section. Hentz and Ruppel (2011) concluded that the Eagle Ford in this region forms a gradational contact with the overlying Austin Chalk (so much so that a transitional or pseudo-Austin Chalk unit could be added). Driskill et al. (2012) used a suite of both geological and geochemical data to define the depositional systems in the Maverick Basin area. His work concluded that the Eagle Ford strata were deposited in deepwater (300-600 feet) under low-energy conditions with periods of anoxia. The author proposed an upward shallowing depositional cycle, wherein marl grades to limestone, TOC decreases, and lamination turns to bioturbation.

Increased economic interest in the Eagle Ford Group in recent years has provided topics for several Master's theses. Harbor (2011) identified nine facies from cores between the San Marcos Arch and Maverick Basin. Harbor separated the facies into an upper and lower Eagle Ford; facies within the upper Eagle Ford section displays increased facies variability, more energetic, and proximal deposits as compared to the facies within the lower Eagle Ford section. Fairbanks (2012) investigated facies variability across the San Marcos Arch. He used closely spaced cores to show that facies variability impacts lithologic and regional correlation – even on a lateral scale of a few hundred feet. Additionally, Fairbanks used x-ray fluorescence (XRF) data to conclude that the Bouldin Member of the Eagle Ford represents maximum basinal restriction. McGarity (2013) used lithofacies descriptions of several cores from East and south Texas in tandem with wireline logs to conclude that the Eagle Ford strata were deposited in very shallow water. McGarity included and interpreted geochemical data from Liro (1994),

concluding that the Eagle Ford Group could not have been deposited within an anoxic environment.

Many recent Master's theses have focused on the geochemistry of the Eagle Ford Group. Moran (2010) concludes that TOC is highest in areas associated with basin restriction and inhospitable conditions. Kearns (2011) used enrichment of phosphorous and manganese to determine that upwelling was prevalent during Eagle Ford deposition. Kearns also established that the Eagle Ford strata are geochemically heterogeneous, and therefore difficult to correlate laterally. Wokasch (2014) used chemostratigraphy (XRF) coupled with core description from two wells in south Texas to conclude that Eagle Ford depositional conditions were probably suboxic to anoxic, and in some areas, euxinic. Wokasch also used trace metal abundance to define depositional conditions; however, he did not consider circulation patterns or restriction as potential influences on sedimentation and oxygen levels. Boling (2014) investigated accumulation of organic matter in the Pepper Shale, Eagle Ford Group, and South Bosque Member of the Eagle Ford Group using outcrop and geochemical data. According to Boling, the Pepper Shale is clay-rich, has low TOC, and low redox metals. The Eagle Ford Group is calcareous, has high TOC, enriched redox metals, and high carbon over nitrogen (C/N) ratios; the paleoenvironment was anoxic and allowed for accumulation of organic matter. Lastly, the South Bosque is distinguished by a positive carbon isotope excursion; this is interpreted to be the Cenomanian-Turonian boundary.

GEOLOGIC SETTING

The following section will introduce the regional depositional environment and local and regional stratigraphy that preceded and occurred during Boquillas and Eagle Ford Group deposition.

Tectonics

The Mesozoic Era constituted a time of major tectonic change for North America. Two significant events began in the Early Jurassic which impacted the South Texas Shelf: 1. Rifting of the Laurentia craton initiated the opening of the proto-Gulf of Mexico (Pearson, 2010) and 2. Subduction of the Farallon plate below the continental craton west of present day California created thrusting, folding, volcanism, and crustal flexure (Fig. 1).

At the start of the Cretaceous 144 million years ago, the super continent Pangaea had already rifted into two smaller sub-supercontinents: Laurasia in the northern hemisphere and Gondwana in the southern hemisphere (Encyclopedia Britannica online, 2014). By the mid-Cretaceous, Laurasia and Gondwana had also begun to separate into smaller continents; the North American craton was named Laurentia. Entering the upper Cretaceous, high sea level inundated Laurasia drowning the South Texas Shelf and creating the Western Interior Seaway. Subsequent transgression and regression sequences on the flooded South Texas Shelf are divided into three distinct groups: the Coahuilan Series, Comanchean Series, and Gulfian Series (Murray, 1961; McFarlan, 1991).

South Texas Shelf

The Western Interior of North America during the Early Cretaceous was dominated by healthy, carbonate shelf systems and reef trends. Within Texas, two dominant reef trends have helped to physically shape the proto- and present-day Gulf of Mexico, as well as impacted later sedimentation and deposition. The Coahuilan series represents Neocomian to Aptian time and the Comanchean series represents late Aptian through Cenomanian time (Murray, 1961; McFarlan, 1991) (Fig. 4). A major transgression in the Cenomanian drowned the Stuart City carbonate reef system, caused for transitional deposition of non-reef formations (Del Rio Clay and Buda Limestone), and then allowed for deposition of organic-rich mudrocks to be deposited onto the pre-existing Coahuilan and Comanchean shelves.

The regional stratigraphy (Fig. 4) highlights the interval of Eagle Ford within the Maverick Basin used for this study. The Eagle Ford is divided into a lower and upper member based on chemostratigraphy, bioturbation, lithofacies, depositional environment, and age. The initiation of the upper Eagle Ford strata is defined elementally by a major increase in titanium and manganese. The resultant massive argillaceous mudrock shows a lack of fauna, sedimentary features, and weathering character (extremely friable). In some cases, the highest lower Eagle Ford strata show a thin interval of fabric-destructive bioturbation; this interval is missing in the Winterbotham J.M. Jr. #1. The lower Eagle Ford strata are dominantly composed of carbonate-dominated mudrocks and wackestones with thin, starved ripples and few fauna. The upper Eagle Ford strata are dominantly composed of packstones and grainstones and displays well developed sedimentary features and much higher faunal abundances.

Period	Epoch	STAGE	TRANS-PECOS TEXAS	MAVERICK BASIN (This Study)	EAST TEXAS	SERIES	WB	CX	HS
Cretaceous	Upper	Maastrichtian	Black Peaks	Not Observed	Navarro	Gulfian			
			Javelina		Taylor				
		Campanian	Aguja						
			Pen		Austin				
		Santonian	Bosquillas	Austin					
		Coniacian			Eagle Ford				
		Turonian	Ernst	Upper					
	Lower	Cenomanian			Woodbine	Comanchean			
			Buda	Not Observed	Buda				
		Albian	Del Rio		Del Rio				
			Santa Elena		Georgetown				
			Sue Peaks		Edwards				
			Del Carmen		Walnut				
			Telephone Canyon		Glen Rose				
		Aptian	Glen Rose		Pearsall	Coahuilan			
			Late Paleozoic Undifferentiated		Cupido-Sligo				
		Barremian			Hosston				
		Neocomian							

Figure 4: Stratigraphic break out of south Texas and proto-Gulf series. Paleotopography present during the Coahuilan and Comanchean influenced Gulfian series deposition. The red box highlights stratigraphy documented in cores used for this study. WB stands for Winterbotham J.M. Jr. #1, CX stands for Core-X, HS stands for Hot Springs outcrop s. After Wilson and Ward (1993) and Gray (2008), Tiedemann (2010), Cooper (2014).

COMANCHEAN SERIES

The Comanchean series is composed of a thick package of progradational carbonates deposited during the latest Aptian, Albian, and early Cenomanian. The shelf was composed of several different profiles of carbonate platforms: raised rim, ramp and flat-top (Harbor, 2011). Each carbonate package is composed of deposition during several transgressive-regressive sequences. In Trans-Pecos Texas, the start of the Comanchean series is marked by a lower conglomerate. The Comanchean series in East Texas is identified by the Pearsall Formation. The Pearsall Formation is a transgressing organic-rich mudrock deposited onto the Coahuilan series carbonate reefs. Backstepping of the Pearsall Formation caused the following progradational reef sequences to be slightly landward of the older Coahuilan series platform margin (Salvador, 1989). This

younger, landward margin is called the Stuart City shelf margin. The dominant reef facies in Trans-Pecos Texas is the Del Carmen Limestone and the equivalent dominant reef facies in East Texas is the Edwards Limestone (McCormick, 1996). In some areas of south Texas, the combination of the Coahuilan and Comanchean margins created a “two-step” continental margin (Donovan, 2010); in some cases the Coahuilan and Comanchean reef systems are stacked. In other areas on the shelf, progradation of the Comanchean series continued moving basinward creating a “physiographic break” between the shelf and continental slope (Fairbanks, 2012). The rudist reefs of the Stuart City shelf margin created a carbonate rim around the Gulf of Mexico and helped to protect the inner shelf from wave action (Scott, 2010).

GULFIAN SERIES

The Gulfian series comprises the middle and late Cenomanian, Coniacian, Santonian, Campanian, and Maastrichtian stages. The Gulfian Series began with a major transgression that caused carbonate mudrock deposition on the Comanchean series shelf. This caused for a shift in dominant deposition from the shelf margin to the intrashelf (Winker and Buffler, 1988; Wu et al., 1990; Sohl et al., 1991; Mancini and Puckett, 1995; Goldhammer and Johnson, 2000; Liu, 2004; Galloway, 2008). The Coahuilan and Comanchean series reef trends influenced deposition on the drowned shelf where the Eagle Ford Group was deposited. The reef trends created a silled basin, producing basinal restriction and decreased water mass renewal (Algeo and Rowe, 2012). Organic-rich mudrocks were deposited onto the drowned carbonate shelf until a regression in the Coniacian brought back healthy, shelfal limestones (Austin Chalk in East Texas and San Vicente Member of the Boquillas Formation in Trans-Pecos). Following deposition of the

Boquillas Formation and Austin Chalk, nonmarine sediments become dominant in Trans-Pecos Texas while marine sediments remained dominant in central Texas.

STRUCTURES

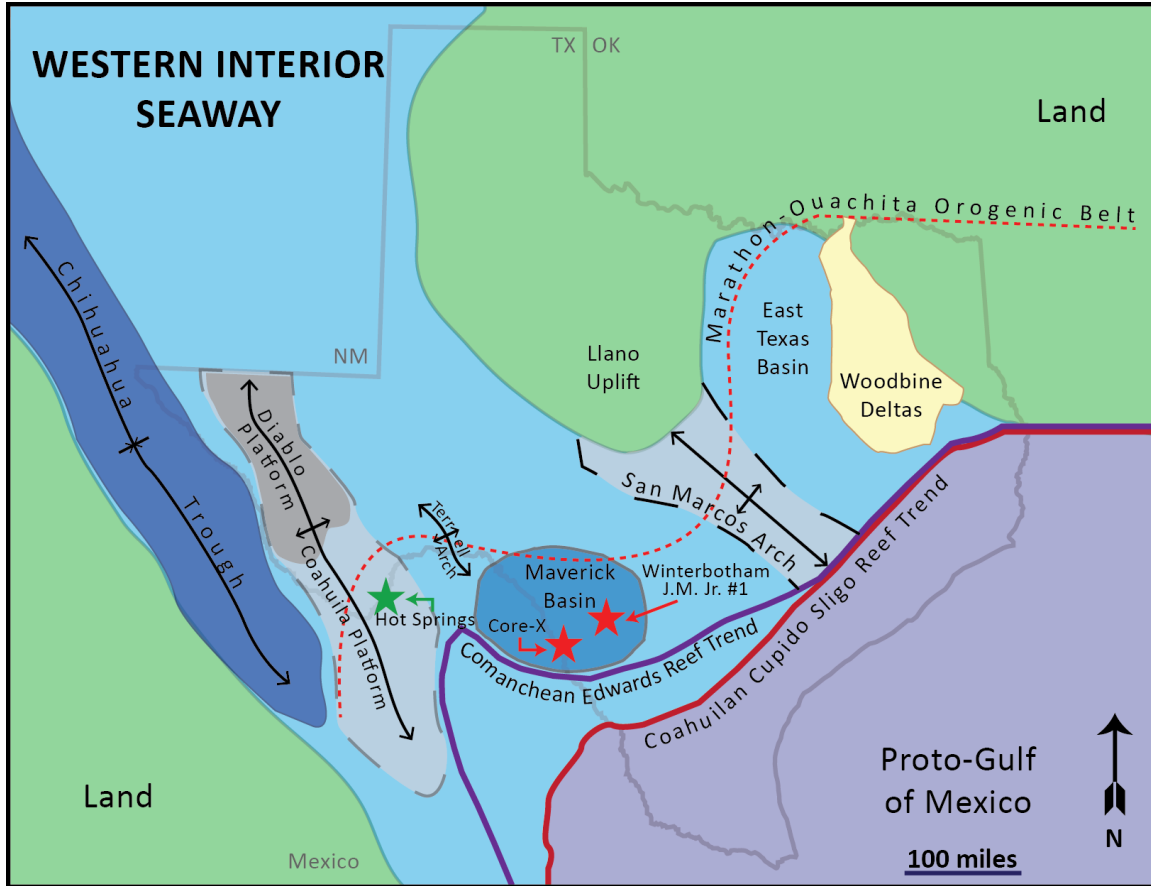


Figure 5: Paleogeography and structures of the Cenomanian-Turonian on the South Texas Shelf and in the Western Interior Seaway in Texas. The red stars show the core locations from Maverick Basin. The green star shows the location of the outcrop section. Structures after Adkins (1932), Shepard and Walper (1982), Wilson et al. (1984), Rose (1986), Goldhammer (1999, 2001), Driskill et al. (2012), Ruppel (2012), Denne (2014)

Several local structures and paleotopographic features within Texas have impacted Eagle Ford and Boquillas deposition (Fig. 5). The proto-Gulf of Mexico margin in Texas, as well as present day Gulf of Mexico, is bound by the Late Paleozoic Ouachita structural front (Driskill et al., 2012). The Ouachita structural front trends southward

through east-central Texas, turning abruptly westward just below the Llano Uplift and San Marcos Arch, and takes an abrupt turn southward through the Big Bend region. The propagation of the Ouachita structural front was impeded and essentially stopped because of the intersection with Grenville-age Van Horn mobile belt (Shepard and Walper, 1982). The Llano Uplift is the result of the 1.0 Ga Grenville orogeny during the assemblage of the supercontinent Rodinia (Dalziel, 1991; Moores, 1991; Borg, 1994). The orogeny uplifted and exposed deformed core and metavolcanics (Culotta, 1992). The uplift extends further into Texas as a northwest-southeast trending arch separating the East Texas and Maverick Basins; this arch has been dubbed the San Marcos Arch (Dravis, 1980; Young, 1986). The San Marcos Arch remained a topographic high during deposition of Coahuilan, Comanchean, and Gulfian series.

The Maverick Basin has been a persistent topographic low since at least the Aptian evidenced by thickening of Pearsall Formation deposits (Loucks, 1978; Driskill et al., 2012). The basin has been poorly resolved because of its location along the Texas-Mexico border and may have changed shape over time. Subsurface studies in Texas suggest that the basin is ovate and has developed as the result of crustal thinning from the rifting of the Gulf of Mexico margin. Intrabasinal and shelfal deposition are the dominant forms of sedimentation within the Maverick Basin; siliciclastic influx from the Woodbine Delta to the east was blocked by the San Marcos Arch.

The Chittum Arch (also spelled Chittim) trends northwest-southeast through the Maverick Basin and was a product of the Laramide Orogeny that occurred between 70-40 Ma (Rose, 1986). This structure occurred after the deposition of the Eagle Ford and Boquillas and is not relevant to interpretation of depositional environment at the time of Eagle Ford deposition.

Both reef margins developed within the Coahuilan and Comanchean series have created a barrier and topographic high (Driskill et al., 2012). These have allowed for the Boquillas and Eagle Ford to be deposited on a shallow shelf and separated from deeper Gulf of Mexico deposits (Driskill et al., 2012).

The Terrell Arch is a north-northwest trending arch located in Terrell and Val Verde Counties (Adkins, 1932). Deposition over the arch thickens towards the flanks and pinches out towards the arch axis. Strata of the Del Rio Formation (unit stratigraphically below the Buda Limestone, Fig. 4) are eroded across the arch (Freeman, 1968). The processes that created the paleogeographic positive feature that formed the Terrell Arch are poorly understood, but are believed to have solely impacted deposition of Cretaceous strata (Freeman, 1986).

The Late Proterozoic Van Horn mobile thrust belt created a topographic high trending approximately south-southeast through Trans-Pecos Texas (Shepard and Walper, 1982). This ancient thrust belt is the base of a positive topographic area termed the Diablo Platform (King, 1942). The Diablo Platform serves as the southwestern margin of the Late Paleozoic Delaware (Permian) Basins (Galley, 1958; Adams, 1965). The southern-most extension of the Van Horn mobile belt and Diablo Platform provide the foundation for the Coahuila Platform (Shepard and Walper, 1982).

The Coahuila Block is a positive topographic feature located approximately south-southeast of the tip of the Coahuila Platform. This feature represents the roots of an Ouachita-Marathon orogeny island arc system that is supported by Permo-Triassic age granite and granodiorite intrusions (Wilson et al., 1984). The topographic high persisted through upper Jurassic through Cretaceous, strongly influencing deposition, facies, and stratigraphy within the Trans-Pecos area of the South Texas Shelf (Goldhammer, 2001).

Early Mesozoic subduction of the Farallon plate beneath the North American craton caused the development of a volcanic arc and subsequent backarc basin (Fig. 2) (Coney, 1978; Shepard and Walper, 1982; Goldhammer, 1999). Two main volcanic arcs influenced basin development: the Jurassic to Late Cretaceous Sinaloa Arc and the latest Cretaceous Alisitos Arc (Goldhammer, 2001). The backarc basin, or Chihuahua Trough, trended approximately northwest-southeast, bordered by the Diablo and Coahuila Platforms on the east and a narrow coastal plain to the west. The location of the Chihuahua Trough plays an integral role in deposition on the South Texas Shelf. Clastic sediments from the volcanic arc and coastal plain are deposited within the trough; the topographic low collects clastic sediments inhibiting them from deposition on the Diablo or Coahuila Platforms. This features kept clastic, coastal sediments from reaching Boquillas depocenters.

OCEANIC ANOXIC EVENTS

Schlanger and Jenkyns (1976) coined the term Oceanic Anoxic Event to refer to any period of wide-spread, low-oxygen events that in some situations result in source rock generation. The Cretaceous period represented a time of major disturbance in the global oceans, containing at least nine individual oceanic anoxic events (Jenkyns, 1980; Jenkyns, 2010). Low-oxygen and anoxic to euxinic conditions within the ocean allow for organic matter accumulation and slow to no degradation of organic matter before burial. Identification of the OAE2 is important for geologic interpretation, mapping, age dating, as well as identifying potential intervals of viable TOC-rich sections for industrial utilization.

The Cenomanian-Turonian boundary is associated with a major anoxic event: the Oceanic Anoxic Event 2 (OAE2) (Jenkyns, 1980; Schlanger et al., 1987). Additionally,

the Cenomanian-Turonian boundary represents one of the more prominent extinction events since the Permian-Triassic extinction event 250 m.y. (Raup and Sepkoski, 1984). The OAE2 is documented to have lasted approximately 500 kyr (Sageman et al. 2006; Voigt et al., 2008). The OAE2 that occurs in the Cretaceous near the Cenomanian-Turonian stage boundary (Jenkyns, 1980) is defined by a positive excursion of $\delta^{13}\text{C}$. The global ocean became enriched in $\delta^{13}\text{C}$ because of lack of recycling of ^{12}C trapped within organic material accumulating on the sea floor (Schlanger et al., 1987). An oxygenated system would have allowed for ^{12}C within marine plankton and organic material to be recycled back into the global ocean by bacteria and degradation, keeping the $\delta^{13}\text{C}/^{12}\text{C}$ ratio near -27 (accepted value of $\delta^{13}\text{C}/^{12}\text{C}$ isotopic data in an oxygenated system).

Documentation of the OAE2 in recent years has focused on defining features and potential causes of the event in order to better understand the OAE2 as it impacted the global ocean. Lithofacies attributed to the OAE2 consist of widespread black shale deposition (Schlanger and Jenkyns, 1976; Arthur et al., 1987; Jarvis et al. 2011). While the single defining feature of the OAE2 is a positive excursion of $\delta^{13}\text{C}$, new, high-resolution studies have documented three individual peak events that make up the positive excursion event (Jarvis et al. 2011). Causes for the OAE2 are widely debated with hypotheses ranging from upwelling, increased nutrient availability, increased volcanism, increase in world temperature, basin restriction, poor water oxygenation, poor water circulation, and density stratification of the water-column (Jarvis et al., 2011; Jenkyns, 2010).

Anoxic events allow for an enrichment of redox sensitive trace metals such as molybdenum, vanadium, and uranium (Rowe et al., 2008; Algeo and Rowe, 2012). Redox sensitive trace metals are forced to precipitate out of the water-column if no

oxygen is present to form bonds; enrichment in such elements effectively demonstrates oceanic anoxia sediment (Algeo and Lyons, 2006; Algeo et al., 2007; Algeo et al., 2008).

Recent studies (Negra et al., 2011; Denne et al., 2014) have identified a filament event related to the Cenomanian-Turonian boundary and associated OAE2 (Jenkyns, 1980). Filaments (the planktonic larvae stage of *Inoceramus* bivalves) appear draping sediments in an apparent death assemblage. The submillimeter calcareous shells cannot be identified in core slab and require petrographic identification. Positive identification of this filament event can help with correlation between data sets, as well as help to locate the OAE2 and possibly the C-T boundary.

METHODS

The following section details descriptive, sampling, preparatory, and analytical methodologies used within this study.

Core and Outcrop Data Summary

Three locations were used for this study, one outcrop and two cores. Table 1 graphically summarizes location information and analysis types, as well as quantities of each analysis. X-ray fluorescence (XRF), x-ray diffraction (XRD), total organic carbon (TOC), and stable carbon and nitrogen isotopes analyses were conducted under the direction of Dr. Harry Rowe at the Core Research Center. Gamma ray scans were collected at the field site in Big Bend National Park. All methods listed within Table 1 will be described individually within the following sections.

Name	Type	County	Latitude Longitude	API	Section Length	XRF Scans	XRD Scans	TOC and Isotopes	Thin Sections	Gamma Ray Scans
Winterbotham J. M. Jr. #1	Slabbed Core	Zavala	28.7684 -99.4617	425073053700	192 feet	1,762	91	91	34	N/A
Core-X	Slabbed Core	Maverick	Restricted	Restricted	602 feet	7,248	365	365	93	N/A
Hot Springs, Big Bend National Park	Outcrop	Brewster	29.1777 -102.9990	N/A	+/- 255 feet	82	41	41	50	348

Table 1: Summary of core and outcrop data. Latitude, longitude, and API of Core-X are proprietary and have been removed.

Facies Definition and Stratigraphy

OUTCROP

Samples for thin-sectioning and geochemical testing were collected at a minimum one per six foot interval. Samples were collected using guidelines outlined in a Scientific Research and Collecting Permit issued by the National Parks Service. Gamma ray scans were collected one per foot within the Ernst Member and one per three feet in the lower San Vicente Member.

Outcrops at the Hot Springs outcrop locality range in age from late Cenomanian-Santonian and contain the Buda Limestone and the Boquillas Formation (Maxwell et al., 1932; Turner et al., 2011; Cooper, 2014; Figs. 2, 4). The full section of the Ernst Member was logged at a scale of one inch equals ten feet along the Hot Springs Trail from the upper 15 feet of the underlying Buda Limestone through the Ernst-San Vicente contact (the *Allocrioceras hazzardi* zone), and into the lowest San Vicente Member (Fig. 6). For the purposes of logging, individual units and facies divisions in the field were separated largely by the physical character of each individual bed, whether fissile/recessive or indurated. Additionally, attention was paid to bed continuity, faunal assemblage, sedimentary structures, mineralogy, and diagenetic features. Stratigraphic units were divided using overall appearance of sections, similar to the division method used by Sanders (1988). Individual facies names have been delineated using petrographic description and mineralogy. Each lithofacies is named using Dunham's (1964) carbonate classification or Folk's (1980) classification as a general guide. Local structures, such as small thrust faults and folds, were accounted for during logging.

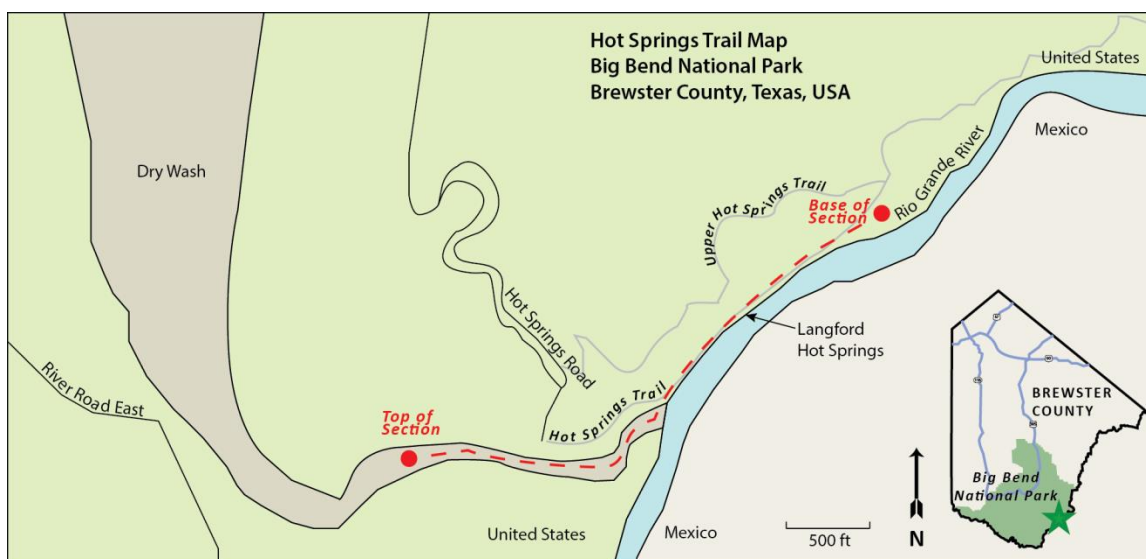


Figure 6: Map of Hot Springs outcrop locality in Big Bend National Park, Trans-Pecos, Texas. The red trail shows the path traversed to collect samples and data for a measured section. The base of the section is picked where the Buda Limestone is identified in the river bed; the top of the section is identified by a large fold visible on the south bank, wherein Ernst and San Vicente Member strata begin to repeat.

CONVENTIONAL CORE DATA

Cores were described at the Bureau of Economic Geology's Austin Core Research Center at the J. J. Pickle Research Facility. Cores were logged at a one inch equals ten foot scale. Cores are described at higher resolution than outcrop data because detail was lacking in weathered outcrops.

Mudrock variability on a lamination (millimeter) scale causes obstacles when delineating precise facies names and groupings. Contacts between facies are gradational below the resolution of logging. Facies have been defined by describing features visible in the core: appearance of fauna, type of fauna, laminations (or lack thereof), lamination constituents, lamination frequency, lamination thickness, color, sedimentary features, deformation structures, authigenic minerals and cements, differential compaction, small-scale facies alternations, and ratio of alternating facies. Each facies has been named using

Dunham (1964) as a general guide; most samples contain varied amounts of muddy matrix and grains or fauna. Dunham's (1964) classification scheme was used for naming samples based on the matrix to allochem ratio. Individual lithofacies defined in this study are similar to 'motifs' defined in other studies (Forkner, 2014) to illustrate small-scale lamination heterogeneity. Individually defined lithofacies have been compiled to create the stratigraphic column. X-ray fluorescence and x-ray diffraction data were used while logging the core to help separate distinct chemical and mineralogical boundaries where appropriate.

Volcanic ash is a dominant component within the Eagle Ford and Boquillas Formation depositional systems. Ashes are present as either discrete beds or mixed with fauna and carbonate matrix. To accurately document individual ash occurrences, ultraviolet light was used to identify deposits. Volcanic ash fluoresces a bright yellow-green when viewed under ultraviolet light. Ash beds greater than two millimeters have been documented individually within the stratigraphic description. Submillimeter, individual ash beds are incorporated into the volcanic ash stratigraphy. Ash stratigraphy is documented using a histogram displaying ash occurrence (both greater than and less than 2 mm) versus depth per bin interval (with bin sizes of 9 or 10 feet per bin) through the length of each core.

Petrography

Thin-section rock stubs were prepared at the Core Research Center. Grinding, mounting, and polishing of thin-sections were outsourced.

Name	Sample Frequency	Total Thin-sections	Thin-section Preparation
Winterbotham J.M. Jr. #1	1 per 9 feet, inconsistent	34	National Petrographic Service, Inc.
Core-X	Minimum 1 per 10 feet	93	Spectrum Petrographics, Inc.
Hot Springs outcrop	Minimum 1 per Outcrop Sample	50	National Petrographic Service, Inc.

Table 2: Thin-section sampling frequency.

Thin-section stubs were cut perpendicular to bedding from core or outcrop sample using a water lubricated rock saw. Stubs were cut to approximately 1 inch by 2¾ inch. Winterbotham J.M. Jr. #1 and Hot Springs outcrop stubs were sent to National Petrographic Service, Inc. Core-X stubs were sent to Spectrum Petrographics, Inc. All stubs were ground to 30µm, polished, and impregnated with blue fluorescent epoxy.

Light microscopy was conducted using a petrographic microscope. Thin-sections were described using plane-polarized light, cross-polarized light, ultra-violet light with a yellow filter, and reflected light. All thin-sections were analyzed for allochem variety and abundance, ratio of matrix to grains, presence of ash, presence of phosphate, sedimentary features, compactional features, diagenetic alterations, and authigenic mineral growth. Qualitative amounts were assigned to each present allochem variety on a scale of zero to five, zero being non-existent in the slide and five being highly abundant. Special attention is given to divisions of planktonic foraminifera. Qualitative abundance data has been used to create a visual representation of biostratigraphy (nontraditional biostratigraphy).

Portable Gamma-Spectrometer

A Radiation Solution Incorporated RS-230 BGO Super-SPEC portable gamma-spectrometer was used to collect percent potassium, uranium parts per million, and thorium parts per million at the Hot Springs outcrops in Big Bend National Park. Each sixty second scan was collected with the detector held flush against a flat surface and orthogonal to bedding (commonly along a joint surface). Portable gamma ray data was collected in the park by Joseph Smitherman (Bureau of Economic Geology, Core Research Center). Table 3 shows frequency of scans through differing formations, as well as the formula used to convert raw data to API units.

Lithologic Unit	Scan Duration	Scan Frequency	Total Scans
Buda Limestone	60 seconds	1 scan per foot	12
Ernst Member, Boquillas Formation	60 seconds	1 scan per foot	216
San Vicente Member, Boquillas Formation	60 seconds	1 scan per 3 feet	21
API CONVERSION FORMULA			
$\text{API} = 18 * \text{K}\% + 10 * \text{U (ppm)} + 5 * \text{Th (ppm)}$			

Table 3: Portable gamma-spectrometer-data summary.

The Radiation Solution Incorporated RS-230 BGO Super-SPEC is documented by the manufacturer to function in temperatures between -4°F to 120°F. Unfortunately, field use has demonstrated that using the instrument is inconsistent in the sun or in ‘hot’ locations causes the instrument to not calibrate (Robert Loucks, personal communication). At the time of collection, temperatures at the Hot Springs outcrop locality were in the area of 100°F to 115°F. Lack of proper calibration to natural gamma ray background noise can negatively impact collected outcrop data. Additionally, outcrop specimens have much higher potential for contamination. Volcanic ash beds within the Big Bend area, hydrothermal alteration while subsurface, close locality of the Rio Grande River and other such factors may impact the accuracy of collected data. While the collected data and converted API data show changes in measured quantities, it is advised that the data be considered qualitative and should not be directly related to downhole gamma ray data. There is no current calibration of this instrument or other gamma ray data for the Big Bend area available to potentially check or compare collected results.

Further calibration and control group studies must be conducted to develop a better understanding of the relationship between the two data types.

Energy Dispersive X-Ray Fluorescence (XRF)

XRF data was collected using a Bruker TRACER-III-V AXS Handheld XRF Analyzer. Instrument settings must be adjusted for either trace or major elemental data (Table 4), and are scanned once in the same location marked by a numbered sticker for each energy level. Both cores were scanned at 2 inch intervals through the length of the core. Each outcrop sample was scanned a minimum of one time, with additional scans representing lamination, lithology, or weathering heterogeneities. Scanning involves placing each sample directly on the detector, flush with the 3 x 4 mm screen. Samples are prepared by insuring that the area to be scanned is flat, clean, and devoid of chlorides (salts), drill mud, or dust. XRF data collected from weathered outcrop samples will not be perfectly correlative to freshly cut, unweathered core samples. This is because calcium is leached from exhumed outcrops related to rain water, ground water, or other chemical weathering processes present at the surface. This occurs because rainwater, groundwater, and hydrothermal fluids are mildly acidic. Leached calcite components are commonly reprecipitated elsewhere within the system.

Data Type	Elements	Scan Time	Voltage	Amps	Vacuum	Filter
Major	Mg, Al, Si, P, S, K, Ca, Ba, Ti, V, Cr, Mn, Fe	60 seconds	15.00 kV	20.70 μ A	Yes	None
Trace	Ni, Cu, Zn, Th, Rb, U, Sr, Y, Zr, Nb, Mo	90 seconds	40.00 kV	14.00 μ A	No	Al-Ti- Cu

Table 4: XRF-scan type and energy summary.

METHODS FOR XRF DATA CALIBRATION

Raw XRF data are calibrated using ninety shale and limestone standards (Rowe et al., 2012). The sample population consists of international standards, Devonian-Mississippian Ohio Shale, Pennsylvanian Smithwick Formation, Devonian-Mississippian Woodford Formation, late Cretaceous Eagle Ford Shale, and Mississippian Barnett Formation. A full list of standards can be found in Rowe (2012). Standardized reference material is pulverized using a TM Engineering pulverizer using stainless steel cups and pucks. Eight grams of 200 mesh powders are pressed to forty tons on a Carver press using a 40mm die and boric acid backing. Each reference standard was scanned three times for major elements and three times for trace elements. The cumulative 270 x-ray spectrum analyses were compared to accepted elemental concentration data for each sample using Bruker CalProcess software. A 95% confidence interval was implemented to eradicate outlier data that did not correlate with the slope or background inter-element

correction of accepted elemental concentration data. This standardized calibration technique is applied to all scans included within this study.

Pressed and measured standard pucks are scanned twice daily during the collection of new XRF data. Ideally, two standards will be scanned 4-8 times each for a duration of 180 seconds. The two standards will represent opposite ends of the compositional mudrock spectrum – one representing a clay-rich, siliceous mudrock and one representing a calcite-rich mudrock. (Note: The term mudrock used here refers to artificially pressed peloids composed of clay-sized particles. Clay-sized particles that compose each mudrock calibration pellet are composed of a distinct mineralogic composition and elemental spectra.) Spectra from these standards are compared to known and accepted measurements for each standard in order to observe potential inconsistencies in daily collected data. Any inconsistency between accepted and measured values is used to calibrate and correct raw data collected that day.

METHODS FOR XRF APPLICATION

Elemental data can be used as a proxy for paleoceanographic settings and depositional environment. For the purpose of this study, XRF data is considered in several ways. After calibration, elemental data can be plotted by depth to create a chemostratigraphic model of elemental abundance in ppm, percent, or enrichment factor throughout the length of the core. An elemental enrichment factor defines a sample's abundance relative to the average abundance for the data set. Enrichment factor values greater than one show enrichment of the measured element relative to the average, whereas values less than one demonstrate element depletion relative to the measured average.

X-Ray Diffraction (XRD)

Powder samples were drilled using a drill press loaded with either a one-fourth-inch or tile drill bit. XRD powder samples are analyzed using an InXitu BTX 308 Portable XRD Analyzer. The inner chamber of the instrument is maintained at a temperature of -10°C to -35°C and operates at 30kV and 10W. Approximately 15 milligrams of <150µm powder are analyzed 30 times to constitute one complete XRD data spectrum. Raw XRD spectra analyses are interpreted using X Powder mineral identification software (Martin, 2008). Mineral spectra have been selected and matched under the guidance of Dr. Harry Rowe (Bureau of Economic Geology). Each sample's spectrum is compared to accepted mineral spectra within the database. Spectra peaks are matched to the accepted mineral information with the best-fit spectra to identify minerals present within the sample. Individually matched minerals are combined to create a total mineral composition for each sample. Total matched mineralogy has an error of <10% amorphous (unidentifiable) material.

Carbon and Isotope Data

Total organic carbon (TOC), total nitrogen (TN), and stable isotopic total organic carbon ($\delta^{13}\text{C}$) and nitrogen ($\delta^{15}\text{N}$) were analyzed at the University of Texas at Austin in Dr. Harry Rowe's Geochemistry Laboratory located at the Bureau of Economic Geology's Core Research Center on the J. J. Pickle Research Campus. All $\delta^{13}\text{C}$ referred to after this point refers to the organic carbon isotopic fraction.

Total inorganic carbon (TIC) was determined using a UIC, Inc. CM5015 Coulometer and a UIC, Inc. CM5230 Acidification Unit. Four to six milligrams of sample powder were loaded into a flat-bottom glass vial and acidified using 8%

phosphoric acid solution. TIC for each sample is used to determine the quantity of sample required for TOC.

TOC powder samples $<150\mu\text{m}$ were measured using a Sartorius Cubis series scale and loaded into Costech 5 x 9mm pressed silver capsules; darker colored samples require 12-15mg, lighter samples require 40-50 mg. Samples were acidified using 37% fuming hydrochloric acid in a closed chamber. Acid vapor was allowed to dissolve inorganic carbon within each cup for up to two weeks. To ensure all inorganic carbon has been dissolved, samples were doused with 6% sulfurous acid (Verardo, 1990). After acidification, silver capsules were transferred into Costech 5 x 9mm pressed tin capsules. Tin-wrapped samples were pressed into small cubes using metal tweezers. Samples were analyzed using a Costech 4010 Elemental Analyzer coupled with a Thermo Finnigan Conflo IV device and Thermo Finnigan Delta-V Isotopic Ratio Mass Spectrometer (IRMS). Output data from the instrument were reported in per mille (‰) relative to air for $\delta^{15}\text{N}$ and the Vienna Pee Dee Belemnite standard (V-PDB) for $\delta^{13}\text{C}$.

RESULTS

The following section describes data collected and presents interpretation for each data set. Data sets will be discussed individually for each locality.

Facies, Facies Successions, and Chemostratigraphy

The below section presents data and discusses interpretations for each data set per locality. Chemostratigraphy and elemental data is presented in the *Mineralogy* and *Paleoceanography* sections. Mineralogy as defined by x-ray diffraction and x-ray fluorescence will be introduced to understand the variety of rocks present in each system. Next, the oceanographic conditions will be discussed using x-ray fluorescence elemental data. After discussing mineralogy and ocean conditions, lithofacies will be defined and described using visual and petrographic attributes. The aforementioned attributes are then discussed in regards to 2D architecture.

MINERALOGY

Graphs showing XRD and XRF mineralogy are presented below to identify the mineralogy of each section. Table 5 shows mineral and correlative line color on each XRD weight percent graph. Minerals are also labeled within the individual graphs. Gamma ray logs have been included with each XRD and XRF plot for reference. Provenance defined geochemically refers to whether discussed elements or minerals are intrabasinal or extrabasinal (terrestrial/detrital). Similarities within individual locality data sets may be compared and used to distinguish commonalities and differences between depositional environments (Manning et al., 2008). Because of general sea water chemistry similarities, these individually processed data sets can be compared. Chemostratigraphy is used to show dominant environmental factors at the time of

deposition such as dominant mineralogy, level of oxygenation, nutrient flux, and intrabasinal or extrabasinal origin.

Chemofacies herein are defined using XRF elemental data. Several studies have defined depositional interpretations for individual elements or element groups (Calvert and Pedersen, 1993; Van Cappellen and Ingall, 1994; Ingall and Jahnke, 1997; Tribovillard et al., 2006; Rowe et al., 2008; Algeo and Tribovillard, 2009; Boling, 2014). Many different elements can originate within the detrital fraction of the rock. Major elements such as calcium and silicon are generally detrital as either extra-basinal grains or intra-basinal biogenic tests or skeletal debris (Rowe et al., 2008). Trace elements such as titanium, aluminum, and zirconium are generally associated with the detrital fraction and are rarely mobile during diagenesis (Calvert and Pedersen, 1993). These trace elements are generally found within clay minerals or feldspars in volcanic ash. Silicon over aluminum is plotted against depth to investigate silica enrichment (Algeo and Tribovillard, 2009). Elemental quantities of silicon and aluminum will have a one to one ratio (or a slope of one if plotted against each other) if both exist within clays. Deviation from the one to one slope in the positive direction (an increase in Si/Al ratio) represents silicon enrichment is not related to increase in clay mineral content or enrichment, rather it is related to quartz enrichment. This increased silicon may be related to terrestrial detrital material or biogenic debris, the origin of the silicon must be investigated using visual (petrographic) analytical methods.

Mineral	XRD Line Color
Calcite	Maroon
Quartz	Red
Dolomite	Orange
Albite	Yellow
Pyrite	Light green
Fluorapatite	Dark green
Illite	Light blue
Kaolinite	Navy
Montmorillinite	Purple

Table 5: XRD color key. Each mineral is assigned a specific color on XRD weight percent graphs.

Hot Springs Outcrop

Figure 7 contains XRD-based mineralogy for the Hot Springs outcrop section in Big Bend National Park. Calcite is the dominant mineral within the samples with lesser amounts of quartz, dolomite, and clay (Fig. 7). Dolomite is highest within the Buda Limestone section and the basal Ernst Member (Fig.7). Quartz content varies relative to different quantities of radiolarians and terrestrial silica content (Fig. 7, petrographic description). The two dominant quartz peaks at 200 ft represent a very small amount of chert within concretions (this phenomenon is an outlier and has not been further investigated in this study, except for testing mineralogy). The anomalous sample with abundant albite at 302 ft represents an igneous intrusion.

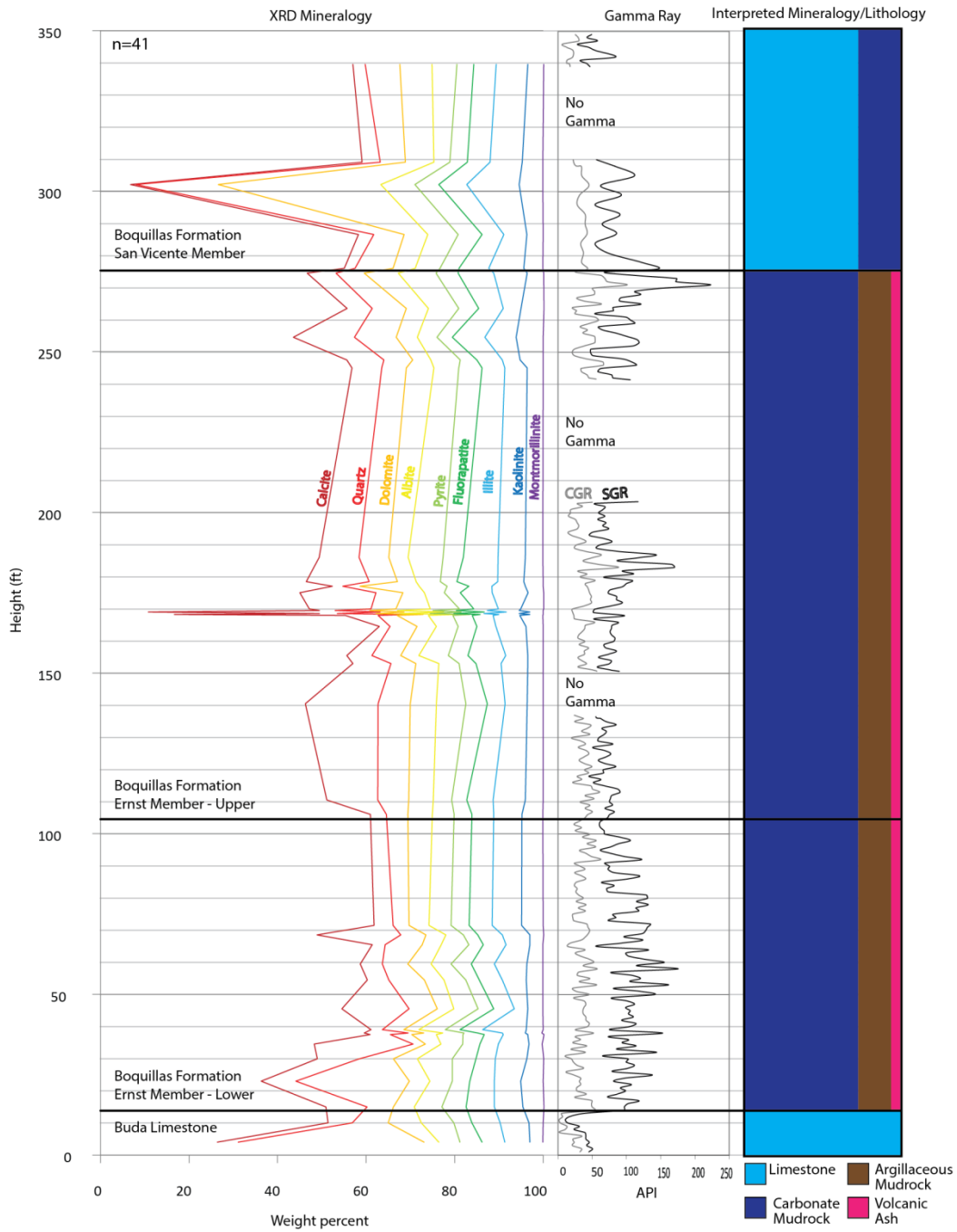


Figure 7: XRD for outcrop samples from the Hot Springs outcrop section. Nine minerals are presented in weight percent. CGR and SGR are provided in the center. An interpreted mineralogy/lithology is provided on the right.

Figure 8 contains predominantly major elemental data representing sediment provenance. Calcium is associated with biogenic intrabasinal sediments (Rowe et al., 2008). Aluminum, potassium, and titanium are associated with detrital clay minerals that come from exposed terrain (Calvert and Pedersen, 1993). Silicon and zirconium are associated with detrital clay or other grains. Silicon to aluminum ratio shows silicon enrichment outside of clay minerals, indicating potential increase in silica minerals (biogenic, detrital, or authigenic; Algeo and Tribovillard, 2009). Molybdenum is plotted on the far right as a proxy for redox sensitive trace elements (discussed in *Paleoceanography*).

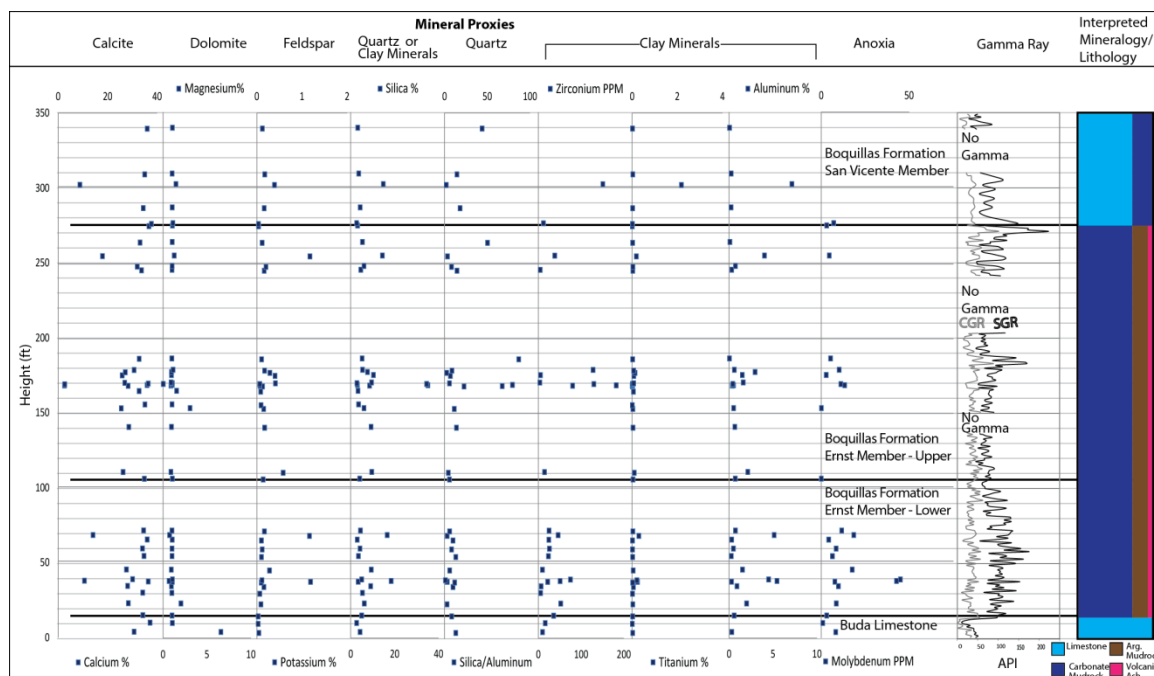


Figure 8: XRF data showing proxies for mineralogy for Hot Springs outcrop samples. Gamma ray response and interpreted mineralogy/lithology is included on the right.

Interpretation

Buda Limestone

The Buda Limestone from 0-13 ft (Fig. 7) is pervasively dolomitized documented in both thin-section and confirmed by XRD. Thin-section documentation will be shown in lithofacies and facies successions. Stacking patterns in the Buda Limestone defined mineralogically and elementally demonstrates little heterogeneity. The section described at the Hot Springs outcrops in Big Bend National Park is composed of limestone with diagenetic dolomite.

Boquillas Formation

Mineral composition defined by XRD (Fig. 7) shows that the Boquillas Formation is composed dominantly of calcite with varying amounts of quartz, feldspar, dolomite and clay. Calcite is most dominant in massive limestone beds and peloidal crystalline mudrock (discussed in *Lithofacies*). Calcic tests of foraminifera and inoceramid also add to the high calcite content. Because calcite is dominant in muddier or peloidal facies, it is interpreted that matrix material may be composed largely of nanometer-sized calcite material (potentially coccoliths; Pommer, 2014) making these facies dominated by carbonate mud.

Increased quartz (Fig. 7) is concluded to be the result of diagenesis representing a discrete, discontinuous interval of microcrystalline quartz (confirmed through field description and petrography). This sample is not representative of surrounding lithology because of small size, discontinuity, and amygdaloidal shape (supported by field descriptions).

Major elemental data with stratigraphic breakouts (Fig. 8) shows poorly defined chemostratigraphic trends. This is largely related to a less populous sample set compared to the size of the measured section.

Calcium values throughout the section are high (Fig. 8), aside from five individual data points with less than 20% calcium content. These individual data points each correspond with increased aluminum, potassium, titanium, and silicon. All three of these elements are interpreted as increases in detrital clay minerals. These observations show that the Boquillas Formation strata are calcite-dominated rocks with irregular and uncommon punctuated intervals of detrital, clay mineral input. This trend infers calcite content dilution occurs when clay minerals or detrital sediments are introduced into the system. The Si/Al curve should follow a 1:1 trend unless there is enrichment in silicon outside of clay minerals. The upper Ernst and San Vicente Members (as defined by Cooper, 2014) shows terrestrial silica enrichment (Figs. 7, 8). This observation shows that while clay minerals may not be largely impacting the depositional environment, increased quartz content is causing a dilution of calcite content.

Ernst Member of the Boquillas Formation

The Ernst Member shows two main trends. Cenomanian-age, lower Ernst Member is influenced by detrital clay input that dilutes intrabasinal calcium accumulation. This is shown using the Si/Al plot (Fig. 8). The aluminum to silicon ratio remains 1:1, indicating no substantial enrichment of silicon from quartz. High silicon values in the lower Ernst Member are solely related to clay mineral enrichment. Zirconium values in the lower Ernst Member vary. Enrichment may be related to volcanic ash.

The upper Ernst Member has less aluminum, potassium, and titanium when compared to the lower Ernst Member (Fig. 8). Slight enrichment in those three elements imply clay mineral or detrital input to the system, however, it is on a lesser scale than that

of the lower Ernst Member. Additionally, the upper Ernst Member contains silicon enrichment not documented in the lower Ernst Member.

Stacking patterns defined mineralogically and elementally in the Ernst Member show a calcite and calcium dominated system with minor increases in phyllosilicate amount (Figs. 7, 8). The upper Ernst Member maintains a similar pattern of calcite and calcium dominated intervals with thin, punctuated phyllosilicate-rich intervals (Figs. 7, 8). The upper Ernst differs from the lower Ernst Member because the more dominant calcite and calcium dominated intervals contain more phyllosilicate minerals than in the lower Ernst Member.

San Vicente Member of the Boquillas Formation

The San Vicente Member contains the highest amount of calcite within the Boquillas Formation (Fig. 7). This implies that there has been either a decrease in phyllosilicate input or that calcite production has increased and is effectively diluting any phyllosilicates entering the system. Poor sampling resolution for mineralogic and elemental data cannot be used to define stacking patterns in this interval.

Core-X Conventional Core

Figure 9 contains XRD mineralogy for the Core-X core from Maverick County (Fig. 3). Calcite is the most abundant mineral in the system based on weight percent. Volcanic ash beds are defined by increases in clay mineral weight percent (illite, kaolinite, montmorillinite) and significant decrease in calcite content. The Buda Limestone, below 4,032.5 ft, contains the most consistently abundant dolomite. Argillaceous solution seams within the Buda Limestone are enriched in clay minerals, especially kaolinite.

The interval from 3,843-4,032 ft in the lower Eagle Ford strata has the most frequent and high enrichments of quartz within the section. Quartz within this interval can be up to 23%. At 3,833 ft and 3,843 ft dolomite is highly enriched with 34% and 45%, respectively. These samples contain decreased calcite content, and minor enrichment is quartz and albite. Above 3,833ft in the upper Eagle Ford Group, overall weight percent of quartz decreases.

The Austin Chalk section demonstrates higher calcite weight percent than in the underlying Eagle Ford Group. Quartz abundance is minimal.

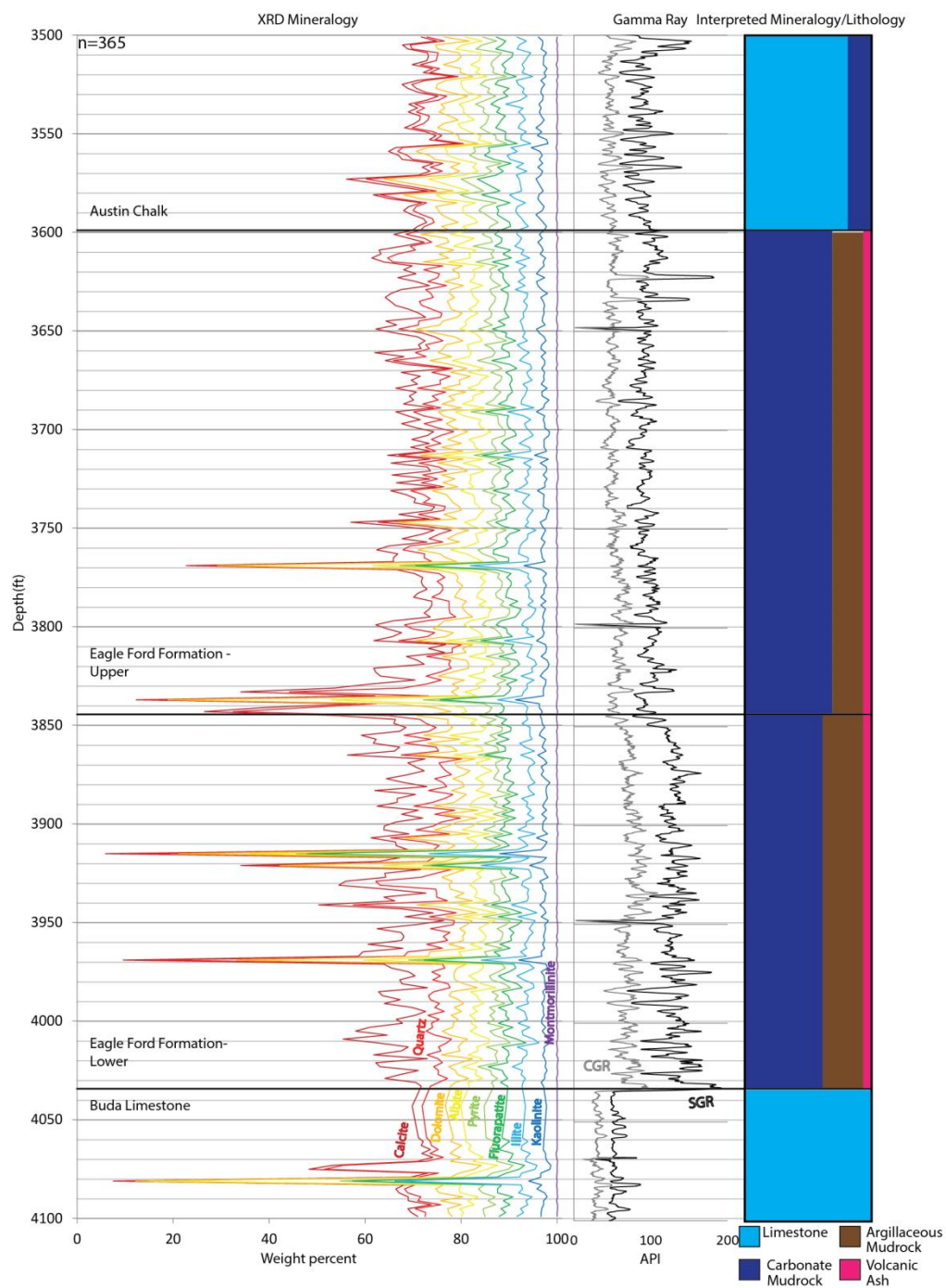


Figure 9: XRD for conventional core samples from Core-X. Nine minerals are presented in weight percent. CGR and SGR are provided in the center. Interpreted mineralogy/lithology is shown on the right.

Figure 10 displays elemental data against depth. Calcium, aluminum, potassium, silicon, titanium and zirconium content can be used to interpret mineralogy and provenance of sediments. Calcium content is associated with intrabasinal and biogenic carbonates (Rowe et al., 2008). Aluminum, potassium, and titanium are associated with detrital clays (Calvert and Pedersen, 1993). Silicon and zirconium are used as a proxy for detrital influx, either associated with clay or another grain variety. Silicon versus aluminum ratio highlights areas where silicon is enriched and not bound within a phyllosilicate mineral structure (Algeo and Tribovillard, 2009). Molybdenum has been included on the far right as a proxy for paleoceanographic conditions.

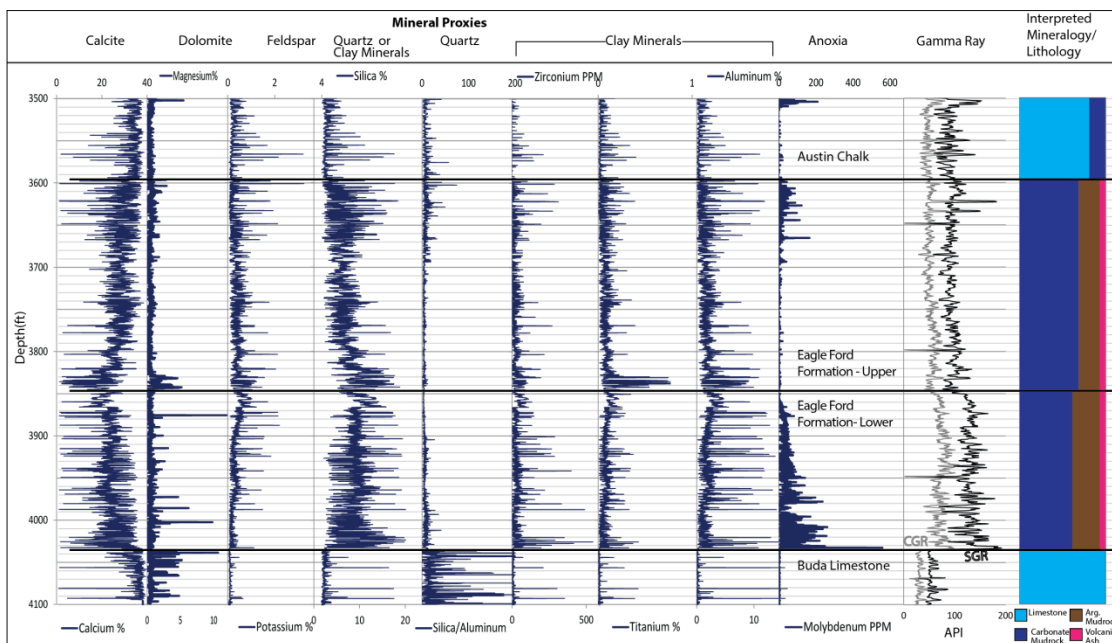


Figure 10: XRF data showing proxies for mineralogy for Core-X conventional core samples. Samples are plotted as either ppm or weight percent. Gamma ray response and interpreted mineralogy/lithology is included on the right.

Interpretation

XRD data (Fig. 9) confirm that the Eagle Ford Group is composed dominantly of calcite with lesser contributions from an assortment of quartz, dolomite, feldspar, or clay.

Buda Limestone

The Buda Limestone contains the highest quantity of consistent dolomite throughout the section (Fig. 9). Increased clay mineral content within the Buda Limestone occurs along pressure solution seams. Elemental data collected from the Buda Limestone demonstrate a system with high calcium content and punctuated siliciclastic influence (Fig. 10). Calcium in a marine setting is interpreted to be intrabasinal. Punctuated, mirrored increases in aluminum, potassium, silicon, zirconium, and titanium define detrital clay minerals. Each detrital clay mineral deposit correlates with a cluster of horsetail solution seams (Appendix A); it can be concluded that pressure solution seams form along detrital clay mineral beds deposited within the Buda Limestone. Silicon/aluminum values are extremely high throughout the purer limestones within the Buda. This shows that silicon within the system is not associated with clay minerals and is related to quartz enrichment.

The thin clay mineral deposits within the calcium and calcite rich system (Fig. 9, 10) likely represent sequence boundaries and possible sea-level changes that caused a thin drape of clay minerals to be deposited.

Eagle Ford Group

The lower and upper Eagle Ford strata are generally similar, containing high quantities of calcite and variable amounts of quartz (silt) and dolomite (Fig. 9). Calcite is the dominant mineral throughout the system. These data show that carbonaceous mudrock is dominant in the Eagle Ford Group; all samples (other than volcanic ash or

those altered by diagenesis) are greater than 50% calcite. The carbonate mud can be divided by considering the lesser quantities of other minerals present in the system (Figs. 9, 10). Quartz is more abundant in the lower Eagle Ford strata than in the upper Eagle Ford strata (Fig. 9). Increased clay mineral and feldspar content occurs within volcanic ash deposits and in a thicker interval at the base of the upper Eagle Ford. Variations in calcite levels are related to stratigraphic position— higher calcite content intervals are correlative to peloidal crystalline mudrock (Fig. 31). The contact between the lower and upper Eagle Ford strata is marked by a major increase in dolomite abundance (Fig. 9).

The lower Eagle Ford exhibits greater influence by extrabasinal sedimentation than the underlying Buda Limestone or the overlying upper Eagle Ford. Calcium values are high because of intrabasinal carbonate sedimentation (Fig. 10). Major decreases in calcium content are matched by major increases in aluminum, potassium, zirconium, and titanium (Fig. 10). These increases represent detrital sedimentation in lower Eagle Ford strata. Silicon/aluminum values are low throughout the lower Eagle Ford strata indicating that silicon abundance is related to clay mineral content (Fig. 10). The basal 15 ft of the lower Eagle Ford strata are more densely enriched in elements that indicate terrestrial clay mineral sedimentation (Fig. 10). This indicates a more consistent terrestrial input at the initiation of Eagle Ford Group deposition.

The contact between the lower and upper Eagle Ford strata as defined in this study using gamma ray, mineralogic, fauna, and facies data has several interesting characteristics. Calcium values in the lower Eagle Ford strata gradually decrease approaching the contact from the lower Eagle Ford to the upper Eagle Ford, and slowly increase again shortly after the initial deposition of the upper Eagle Ford strata (Fig. 10). Aluminum, potassium, silicon, and titanium are greatly increased in the basal upper Eagle Ford strata (Fig. 10). This enrichment in terrigenous detrital elements correlates with the

massive argillaceous claystone lithofacies (Fig. 23) indicating that the massive argillaceous claystone signifies detrital influx at the base of the upper Eagle Ford strata. This deposit is very different from the surrounding carbonate mud and should be considered a marker of the base of the upper Eagle Ford member. The contact between the lower-upper Eagle Ford strata is defined by a gradual decrease in calcium content and molybdenum values and a sharp increase in titanium, aluminum, potassium, and silicon values (Fig. 10). These elemental proxies define intrabasinal carbonate sedimentation in lower Eagle Ford strata and a change to brief detrital, terrigenous (titanium-rich) sedimentation in the basal upper Eagle Ford strata. This is in agreement with the major enrichment in kaolinite, illite, and montmorillinite in the basal upper Eagle Ford strata (Fig. 9).

The upper Eagle Ford strata contain high calcium content and punctuated intervals of increased aluminum, potassium, silicon, zirconium, and titanium content (Fig. 10). Calcium values respond inversely to elemental proxies for detrital terrigenous sedimentation (Fig. 10). This pattern is similar to that of the lower Eagle Ford strata suggesting normal intrabasinal carbonate sedimentation is mixed with moderate detrital terrigenous clay mineral influx. The uppermost upper Eagle Ford strata from 3,600-3,720 ft depict greater titanium enrichment as well as silicon/aluminum enrichment (Fig. 10). This zone is more heavily influenced by detrital sedimentation causing for a dilution of carbonate amount. The increase in silicon/aluminum indicates that not all silicon enrichment in this zone is related to clay mineral content (confirmed in Fig. 9); silicon enrichment may be related to increased volumes of detrital quartz silt (documented in thin section).

Austin Chalk

The Austin Chalk defined using mineralogic, gamma ray, lithofacies, and petrographic data different from the upper and lower Eagle Ford strata. Calcite has an even greater abundance in the Austin Chalk than in the carbonate-dominated underlying Eagle Ford Group. XRF data best display the elemental change between the Eagle Ford Group and Austin Chalk by the decreased frequency and quantity of clay mineral proxies (Fig. 10). Quartz content is the lowest in the Austin Chalk as compared to the underlying section (Fig. 9). Quartz and dolomite systematically increase correlative to lithofacies alternations to laminated argillaceous planktonic foraminifera wackestone (Fig. 19). The Austin Chalk has a very different elemental character than the underlying upper and lower Eagle Ford strata (Fig. 10). Calcium content is higher than the upper and lower Eagle Ford strata with fewer intervals of detrital clay influx (evidenced by aluminum, potassium, silicon, zirconium, and titanium increases; Calvert and Pedersen, 1993). Increased detrital clay zones correlate roughly with laminated argillaceous planktonic foraminifera wackestone (Fig. 10). Silicon/aluminum values show that not all present silicon is contained within clay material; increased silicon is from increased quartz or other non-clay minerals (Algeo and Tribovillard, 2009).

Winterbotham J.M. Jr. #1 Conventional Core

Figure 11 contains XRD weight percent data for the Winterbotham J.M. Jr. #1 core from Zavala County (Fig. 3). Calcite is the most abundant mineral by weight percent. XRD results show that the section is composed over 50% calcite, and is therefore limestone. Quartz, dolomite, albite, pyrite, and fluorapatite occur in varying amounts with a relatively constant background of clay minerals, showing that the section is not a clean limestone. Quartz enrichment occurs from either terrestrial quartz silt or biogenic quartz (radiolarians) – variety of quartz causing enrichment must be further investigated visually

for each depth with documented enrichment. Clay minerals and pyrite increases in volcanic ash beds because of original igneous composition and provenance. At 6,246 ft and 6,251 ft there is significant enrichment in quartz to 57% and 43%, respectively. This enrichment may be related to quartz – thin sections are inconclusive as to the exact variety of quartz causing the enrichment. In general, quartz decreases above 6,245 ft.

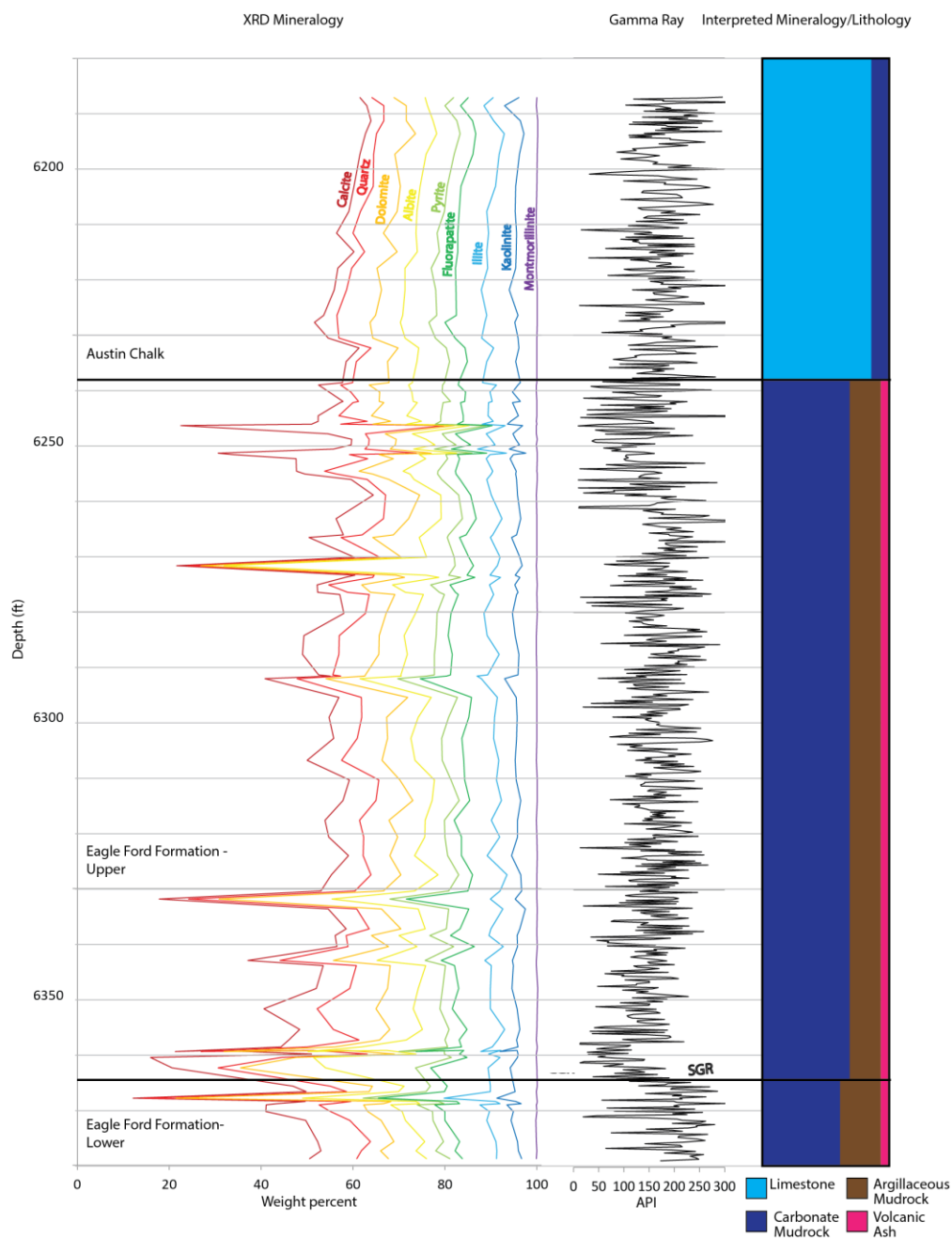


Figure 11: XRD for conventional core samples from Winterbotham J.M. Jr. #1 Nine minerals are presented in weight percent. SGR are provided in the center. The SGR curves have been created using XRF elemental data – not downhole instruments or handheld gamma-spectrometer. An interpreted mineralogy/lithology is provided on the right.

Figure 12 displays major elemental data for elements associated with detrital input. Aluminum, potassium, silicon, titanium, and zirconium are used to show detrital sediment provenance (Calvert and Pedersen, 1993; Algeo and Tribovillard, 2009). Calcium content represents intrabasinal carbonates (Rowe et al., 2008). Aluminum, potassium, and titanium demonstrate detrital phyllosilicate influx. Silicon versus aluminum ratio emphasizes areas of enriched silicon not attached to clay mineral structure (Algeo and Tribovillard, 2009).

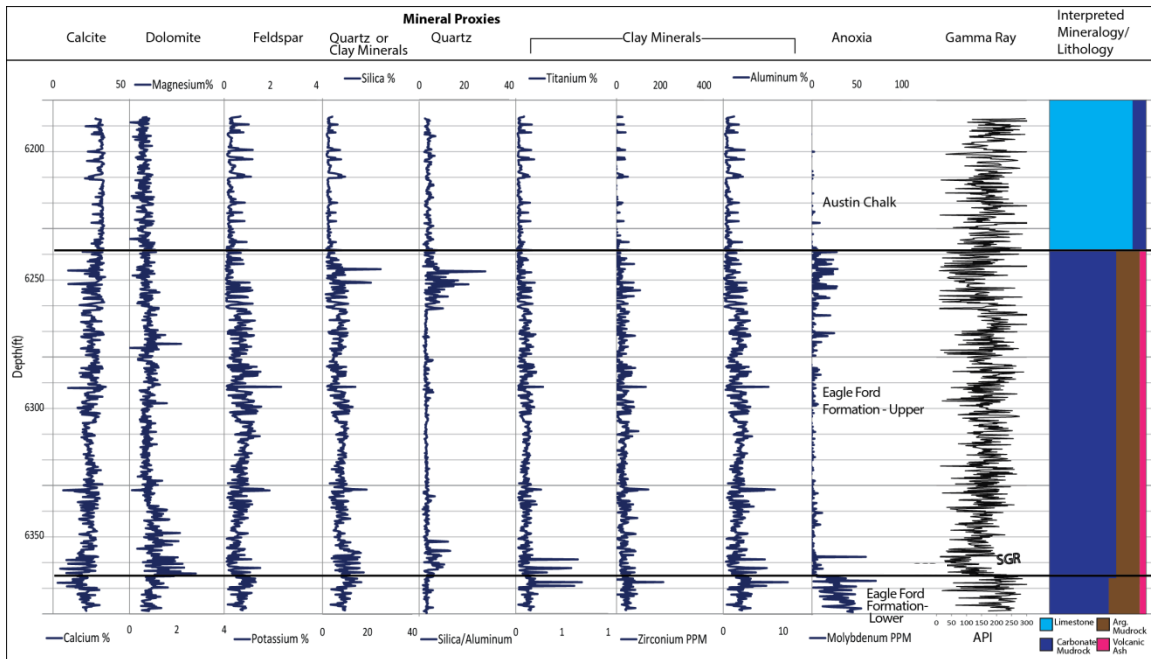


Figure 12: XRF data showing proxies for mineralogy for Winterbotham J.M. Jr. #1 conventional core samples. Data are plotted in either ppm or weight percent. SGR and interpreted mineralogy/lithology has been provided on the right.

Interpretation

Eagle Ford Group

XRD data with proposed divisions is provided in Figure 11. Mineralogy of the Eagle Ford Group is dominated by calcite with variable quantities of quartz, dolomite, feldspar, and clay. Calcite abundance increases through the section, with an average of 44.5% in the lower Eagle Ford strata, 49.5% in the upper Eagle Ford strata, and 58.8% in the Austin Chalk (Fig. 11). This increasing upward calcite content trend demonstrates that the lower Eagle Ford has more influence from terrigenous material; the section is not a limestone, rather a lime-dominated mudrock succession with varying levels of phyllosilicate influence. The upper Eagle Ford strata contains a sizeable quartz silt increase right before the boundary with the Austin Chalk (Fig. 11). The lower Eagle Ford strata contains more quartz with an average of 9.7% compared to the upper Eagle Ford strata containing 8.5% quartz and the Austin Chalk containing 3.0% quartz. Albite and dolomite decrease throughout the section. Quantity of clay minerals remains relatively consistent, with the most notable change in illite content diminishing up section – likely diluted from increased carbonate input.

The lower Eagle Ford strata is composed of dominantly carbonate as shown by high calcium percent (Fig. 12). Aluminum, potassium, silicon, and titanium at the top of the lower Eagle Ford strata show an increase in detrital clay minerals entering the system (Fig. 12). Silicon/aluminum values are very low; indicating the majority of silicon is contained within clay minerals. These data show that detrital phyllosilicate sedimentation has increased as is diluting the amount of carbonate within the system. This change may be tied to a change in sea level representing a transgressive systems tract and retrogradational parasequence set, similar to that described by Lock et al. (2010).

The transition from the lower to upper Eagle Ford is identifiable in several ways. Calcium percent gradually decreases upward towards the contact and then increases away from it, creating a slight divot appearance (Fig. 12). Decreased intrabasinal calcium accumulation is accounted for by increased terrigenous detrital sedimentation. A very distinct, titanium- and aluminum-rich chemofacies straddles the contact between lower and upper Eagle Ford strata at 6,362 ft (Fig. 12). This section may represent an aggradational parasequence set as described by Lock et al. (2010).

The rest of the upper Eagle Ford strata are dominated by calcium sedimentation with punctuated detrital influence. Detrital zones are identified by a slight decrease in calcium content and increases in aluminum, potassium, titanium, and zirconium content (Fig. 12). These zones are likely composed of terrigenous clay minerals. More magnified increases of detrital elements commonly represent discrete volcanic ash deposits (i.e., 6,332 ft and 6,292 ft; Fig. 12). These increased phyllosilicate zones can be matched to volcanic ash deposits in the core (see *Facies Successions*); the samples were collected directly from volcanic ash beds in the core to serve as calibration. While the XRD (Fig. 11) and XRF (Fig. 12) data show several thin intervals of phyllosilicate or aluminum, potassium, and titanium enrichment, the sample spacing of collected samples do not define every individual occurrence of volcanic ash. This is because of the size of the individual volcanic ash beds or laminations.

Austin Chalk

The Austin Chalk has a significantly different elemental signature as compared to the underlying Eagle Ford strata (Fig. 12). Calcium values are more consistently high (averaging 58.8% carbonate), demonstrating the increase in intrabasinal carbonate sedimentation and a major decrease in detrital clay mineral sedimentation and

accumulation. High carbonate production has diluted detrital sediment accumulation. This change in calcium signature related to carbonate sediment abundance is the defining feature for the separation of the upper Eagle Ford strata and the Austin Chalk (Fig. 12); the Austin Chalk contains, on average, 10% more carbonate than the upper Eagle Ford member.

PALEOCEANOGRAPHY

The following section provides data and interpretation regarding the paleoceanographic conditions present during deposition of the Boquillas Formation and Eagle Ford Group.

Paleoproductivity can be evaluated using copper, zinc, uranium, and nickel (Boling, 2014). These elements are essential for animal and plant life. Phosphorous may also be considered a proxy for paleoproductivity; however, it can mobilize under anoxic conditions (Van Cappellen and Ingall, 1994; Ingall and Jahnke, 1997). Molybdenum, vanadium, and uranium are redox sensitive trace metals used as indicators of anoxic conditions. Redox sensitive trace metals are mobile in an oxic system and are forced to precipitate in an oxygen depleted or anoxic system (Tribovillard et al., 2006). Additionally, when compared to TOC, these trace elements can be used to interpret basinal restriction (Algeo and Rowe, 2012). Manganese and iron are also redox sensitive elements; however, these elements behave inversely to molybdenum, vanadium, and uranium. Manganese and iron are generally mobile in an anoxic environment and precipitate in an oxic environment (Tribovillard et al., 2006). This rule can be untrue in reducing environments where iron is stored in pyrite or other sulfides and manganese is precipitated in carbonate (authigenic calcite, dolomite, etc.).

Hot Springs Outcrop

Figure 13 contains enrichment factors for redox sensitive elements with degree of enrichment on the x-axis and relative elevation on the y-axis. Molybdenum, zinc, vanadium, and uranium can become enriched in oxygen deficient environment, while manganese (abundant in deep ocean environments) can become enriched in sediments in oxygen-rich environments.

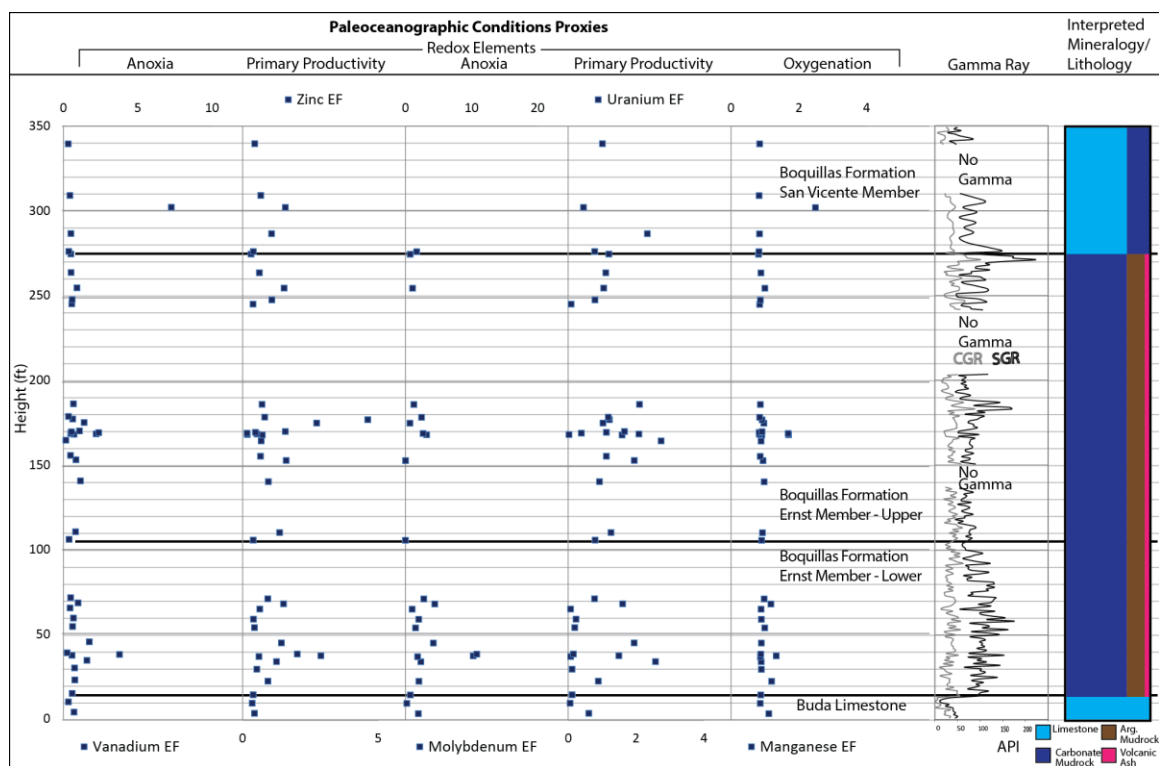


Figure 13: XRF data showing trace elements and proxies for paleoceanographic conditions for Hot Springs outcrop samples. Gamma ray response and interpreted mineralogy are included on the right.

Interpretation

Boquillas Formation

Redox sensitive elements (Fig. 13) show scattered patterns for the Ernst Member of the Boquillas Formation. The lower Ernst Member contains the highest enrichment (up

to 50 ppm, Fig. 13) of molybdenum documented throughout the entire section. Molybdenum enrichment indicates an oxygen-depleted or anoxic environment. Manganese values remain low, confirming lack of oxygenation (Tribovillard et al., 2006). Enrichment in uranium and zinc confirm moderate to high productivity occurring during deposition (Boling, 2014). Anoxia coincident with high productivity denotes water-column stratification –nutrients and oxygen are required to sustain life.

The upper Ernst Member has slight enrichment in molybdenum; however values never reach as high as those documented in the lower Ernst Member (Fig. 13). Slight enrichment of molybdenum is followed by enrichment in manganese, signaling a reintroduction of oxygen into the water-column (Tribovillard et al., 2006). The highest enrichment of zinc occurs directly after the manganese, mirroring the increased oxygenation and increased productivity levels (Fig. 13).

The lack of molybdenum in the San Vicente Member potentially indicates oxygenated bottom-waters at the sediment water interface (Fig. 13) – molybdenum remained in an aqueous state and did not precipitate in sediments (Algeo and Lyons, 2006; Algeo et al., 2007; Algeo et al., 2008). Presence of zinc demonstrates productivity; however levels remain low because the nutrient is recycled while oxygen is in the system. Oxygen-presence and nutrient recycling is supported by burrowing documented in the San Vicente Member (Fig. 35).

Core-X Conventional Core

Figure 14 displays the enrichment factors of redox sensitive elements plotted against depth. Enrichment factors highlight areas that are higher than that of the average background shale. Vanadium, uranium, molybdenum, and zinc increase in oxygen-depleted environments. Manganese increases in oxygen-rich environments.

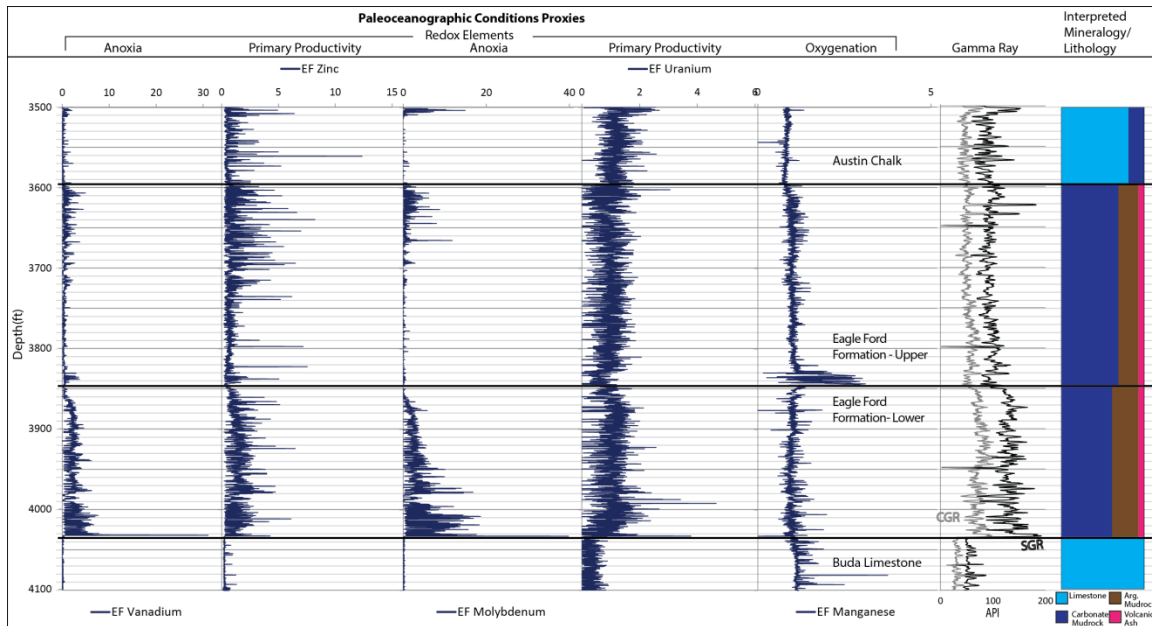


Figure 14: XRF data showing trace elements and proxies for paleoceanographic conditions for Core-X. Redox sensitive elements are plotted as enrichment factors to show increase of element in terms of elemental concentration in the rest of the section. Gamma ray response and interpreted mineralogy are included on the right.

Interpretation

Buda Formation

. Water chemistry (as well as sediments subsequent to burial) in the Buda Limestone is defined using redox sensitive elements (Fig. 14). Molybdenum, zinc, vanadium, and uranium maintain low values, indicating an oxygenated environment. Manganese is present, suggesting regularly oxygenated bottom-waters.

The abrupt change in elemental character in both major and trace elements highlights the abruptness of the unconformity between the Buda Limestone and Eagle Ford Group (Fig. 14; see Fig. 37 for photographic documentation of an unconformity between the Buda Limestone and the Eagle Ford Group). Several changes occur across

the contact: gamma ray API increases, molybdenum increases, calcium decreases. The change in character demonstrates the great difference in both sediment deposition type and water chemistry present during deposition of the Eagle Ford Group. The Buda Limestone shows oxygenated, homogenized carbonate sediments, while the Eagle Ford Group shows anoxic, heterogeneously laminated, mixed-mineralogy sediments.

Eagle Ford Group

Paleoceanographic data in the lower Eagle Ford (the unit deposited above the Buda Limestone) defines an anoxic environment with brief periods of oxygenation. Molybdenum and vanadium are extremely sensitive to lack of oxygen within the water-column, both have increased enrichment factor values in the base of the lower Eagle Ford strata (Fig. 14). Molybdenum values are extremely high, up to 559 ppm. Zinc and uranium nutrient enrichment indicate bottom-water anoxia; however, they suggest that productivity elsewhere in the water-column was moderate. Values of molybdenum gradually decrease – this trend could suggest lack of deep-water renewal wherein the amount of molybdenum in the water-column is never renewed. Enrichment in zinc throughout the section suggests productivity higher in the water-column, suggesting that water-column was density stratified.

Molybdenum values near the lower-upper Eagle Ford strata contact decreases towards the contact (Fig. 14). The contact between lower and upper Eagle Ford is defined by API value decreases, molybdenum decreases, and a change in facies. This can indicate a depletion of molybdenum in the water-column because of slow water renewal times or dilution of molybdenum from increased sedimentation. Manganese is greatly enriched in the basal upper Eagle Ford strata (Fig. 14) indicating oxygen introduction into bottom-waters. This shows oxygenation in the basal upper Eagle Ford strata.

Paleoceanic water chemistry in the upper Eagle Ford strata contains low values of molybdenum signaling an oxygenated depositional environment. Molybdenum and vanadium are enriched from 3,600-3,720 ft from values in the lower portion of the upper Eagle Ford strata (Fig. 14). Enrichment of redox sensitive elements in this section is far lower than the values displayed by the lower Eagle Ford strata. Manganese is also enriched in this section suggesting that bottom-waters were alternating between anoxic and oxic. Oxygen depletion in this zone may be linked to increased productivity (as identified by zinc enrichment).

Austin Chalk

Molybdenum and vanadium remain relatively low throughout the Austin Chalk indicating oxygenation of bottom-waters (Fig. 14). Enrichment of molybdenum within the Austin Chalk in this succession shows a period of anoxia. Enriched zinc and uranium show high productivity throughout the Austin Chalk.

Winterbotham J.M. Jr. #1 Conventional Core

Figure 15 displays redox sensitive trace elements for the Winterbotham J.M. Jr. #1. Molybdenum, zinc, vanadium, and uranium can become enriched in oxygen-depleted or anoxic environment. Manganese reacts inversely, becoming enriched in oxygenated environments.

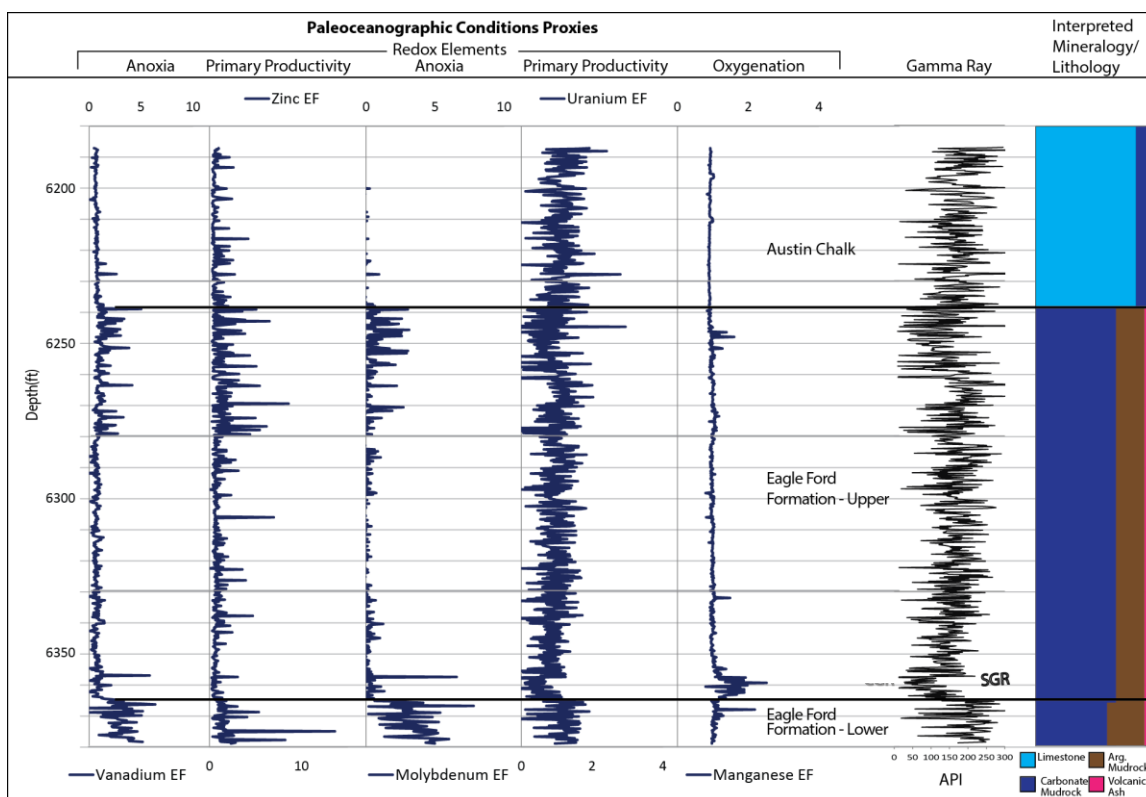


Figure 15: XRF data showing trace elements and proxies for paleoceanographic conditions for Winterbotham J.M. Jr. #1. Redox sensitive elements are plotted as enrichment factors to show increase of element in terms of elemental concentration in the rest of the section. Gamma ray response and interpreted mineralogy are included on the right.

Interpretation

Oceanographic conditions during deposition of the lower Eagle Ford strata were anoxic as shown by high molybdenum, up to 71ppm (Fig. 15). Vanadium and uranium enrichment factor values in the lower Eagle Ford strata are in agreement with enriched molybdenum values, defining an anoxic environment.

Molybdenum values across the boundary between lower and upper Eagle Ford significantly drop off while manganese becomes significantly enriched as compared to adjacent strata (Fig. 15). The variation in molybdenum and manganese shows a switch in

redox sensitive environments form anoxic in the lower Eagle Ford strata to oxic in the upper Eagle Ford strata. Molybdenum will precipitate out of solution when oxygen is absent in a system, whereas manganese will precipitate out of solution when oxygen is re-introduced into a previously oxygen deficient system (Algeo and Lyons, 2006; Algeo et al., 2007; Algeo et al., 2008). This change between redox sensitive trace metals has been used as the dominant factor in determining the contact between lower and upper Eagle Ford strata.

Molybdenum is used to identify three thinner intervals deposited during anoxic conditions within the upper portion of the upper Eagle Ford strata (Fig. 15). A zone from 6,284-6,298 ft and another from 6,271-6,279 ft show some moderate molybdenum enrichment indicating low-oxygen or anoxic conditions. Molybdenum values remain low, either indicating short lived periods of anoxia, or possible low molybdenum content in the water. The third thin anoxic, molybdenum-rich event at the top of the upper Eagle Ford strata occurs from 6,236-6,264ft. This interval exhibits a greater increase in molybdenum, as well as a major increase in silicon/aluminum relative to the two underlying thin molybdenum-rich intervals. This association infers that during this minor anoxic event there was a minor influx of quartz silt (Figs. 12, 15). Quartz silt is documented in this interval in thin section; however, increased skeletal debris (biogenic silica) might contribute to the elevated silicon content as well. This zone also correlates with a major increase in zinc, inferring increased surface productivity relative to the underlying upper Eagle Ford strata. Anoxia here may be the result of high productivity and the subsequent depletion of oxygen in the water-column.

Redox and trace elements in the Austin Chalk have a very different character as compared to signatures demonstrated throughout the underlying section. Redox sensitive

elements such as molybdenum and vanadium in this unit are low indicating normally oxygenated waters with moderate primary productivity (Fig. 15).

TOTAL ORGANIC CARBON

The following section displays graphs showing measured total organic carbon (TOC) within each individual section. Organic matter preservation allows for meaningful conclusions to be made regarding oceanographic conditions present during sediment accumulation as well as productivity levels. TOC is also important for potential industrial utilization of the Eagle Ford Group for economic hydrocarbon recovery. All carbon presented here and within is measured from the organic carbon fraction.

C/N atomic ratios for algae are between 4 and 10, while the ratio for land-plants is greater than 20 (Premuzic et al., 1982; Jasper and Gagosian, 1990; Meyers, 1994; Prahl et al., 1994). Greater values of C/N, potentially 40-60, demonstrate contributions from cellulosic land-plants to the organic matter content (Ertel and Hedges, 1985). C/N ratios lower than 4 may be the result of organic matter degradation. Nitrogen compounds break down producing ammonia that becomes contained in clay minerals while CO₂ is released during organic matter oxidation (Müller, 1977).

Hot Springs Outcrop

Figure 16 contains TOC, C/N atomic ratio, molybdenum ppm, and uranium ppm versus depth for the Buda Limestone and Boquillas Formation at the Hot Springs outcrop in Big Bend National Park. The C/N atomic ratio has an average value of 13.6 with a minimum value of 2.5 and a maximum value of 35.6. TOC has an average 0.3wt% with a maximum value of 1.6wt%. Molybdenum parts per million is included on the far right.

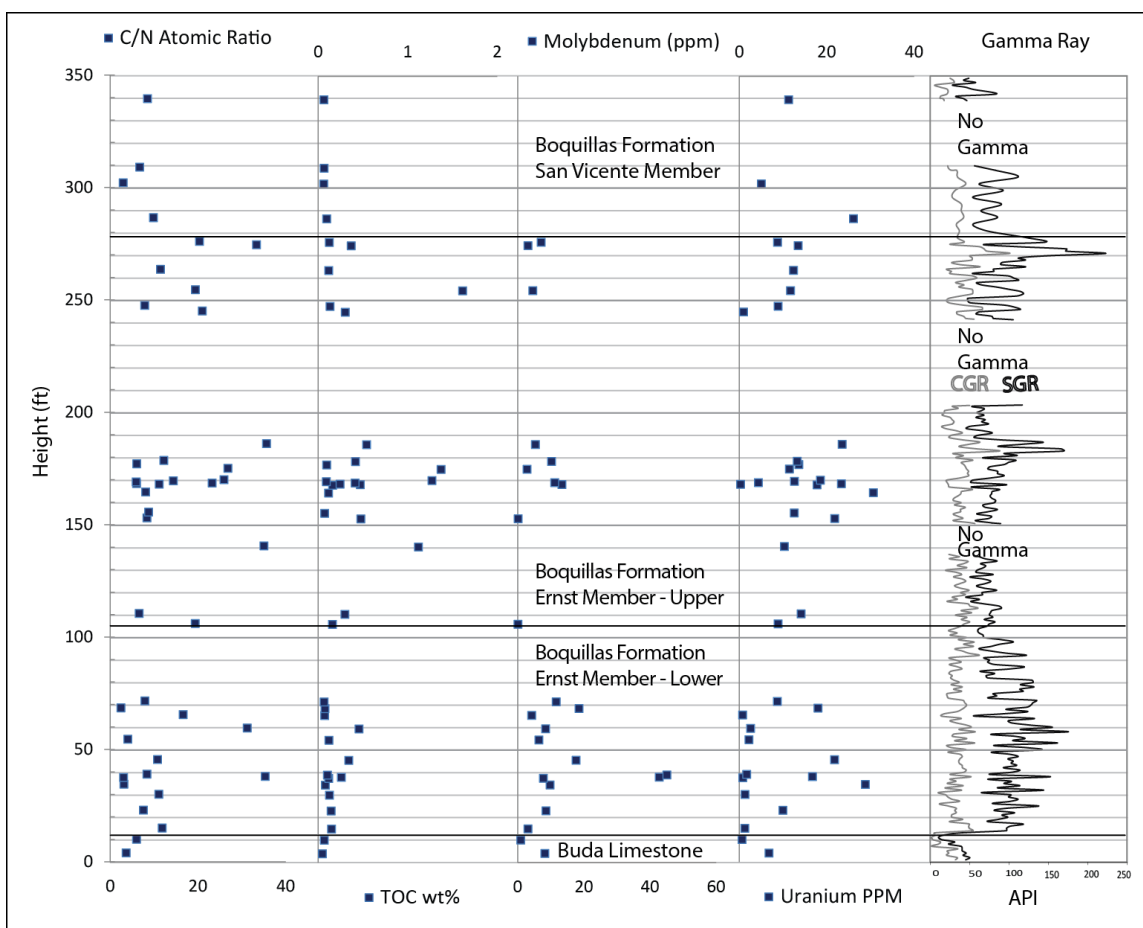


Figure 16: C/N atomic ratio, TOC, molybdenum ppm, uranium ppm, and gamma ray data for outcrop samples from the Hot Springs outcrop. Exposure to weathering can decrease the amount of preserved organic matter.

Interpretation

Buda Limestone

The Buda Limestone has an average C/N is 4.8 and indicates the dominant form of organic matter accumulating is from algae (Fig. 16). Average TOC is extremely low in the Buda Limestone.

Boquillas Formation

C/N values in the lower Ernst Member have an average of 11.8, just outside of the accepted range for marine algae (Fig. 16). While there may have been some influence from airborne terrestrial organic matter, this value is most likely because of some degradation of marine-organic matter while settling through an oxygenated water-column. TOC values are low, likely related to weathering and poor preservation at the surface. Gamma ray (CGR and SGR) values increase greatly from the Buda Limestone into the Boquillas Formation. This increase is because of increased organic matter, as well as increase in argillaceous material.

The upper Ernst Member has a C/N value of 16.7 (Fig. 16). Additionally, the C/N value is outside of the accepted ratio for sole algal organic matter. Mixing of vascular land-plant matter with intrabasinal algal material has increased the C/N ratio towards the accepted value for land-plants. Average TOC for the upper Ernst Member is 0.46wt% (Fig. 16). Preservation of organic matter is better in the upper Ernst Member than in the lower Ernst Member.

The San Vicente Member of the Boquillas Formation contains an average C/N ratio of 7.05 (Fig. 16). The average C/N value of 7.05 falls within the accepted ratio for algae. TOC preservation is lowest within the measured section, with an average of 0.07wt%.

All data show that the succession at the Hot Springs outcrops within Big Bend National Park is dominated by marine-organic matter with low values of TOC. Comparatively, the Ernst Member is influenced more by terrestrial, vascular plant input than the Buda Limestone or San Vicente Member of the Boquillas Formation. The lower Ernst Member demonstrates more marine and algal organic matter accumulation when compared to the upper Ernst Member, which contains slightly more terrestrial plant material. Greater influence from terrestrial organic matter was likely in the form of

airborne material. Increased molybdenum in the Ernst Member defines an anoxic environment that allowed for slightly better preservation of organic matter reflected by higher TOC weight percent. The San Vicente Member and the Buda Limestone are similar and predominantly contain marine-organic matter.

Core-X Conventional Core

Figure 17 contains $\delta^{13}\text{C}$, C/N atomic ratio, and TOC versus depth for the Core-X core. The atomic ratio of C/N has an average value of 28.1, with a minimum value of 0.69 and a maximum value of 60.4. The average value of TOC in the core is 1.97 wt%. The lowest TOC documented is 0.103 wt% and the highest TOC documented is 6.5 wt%.

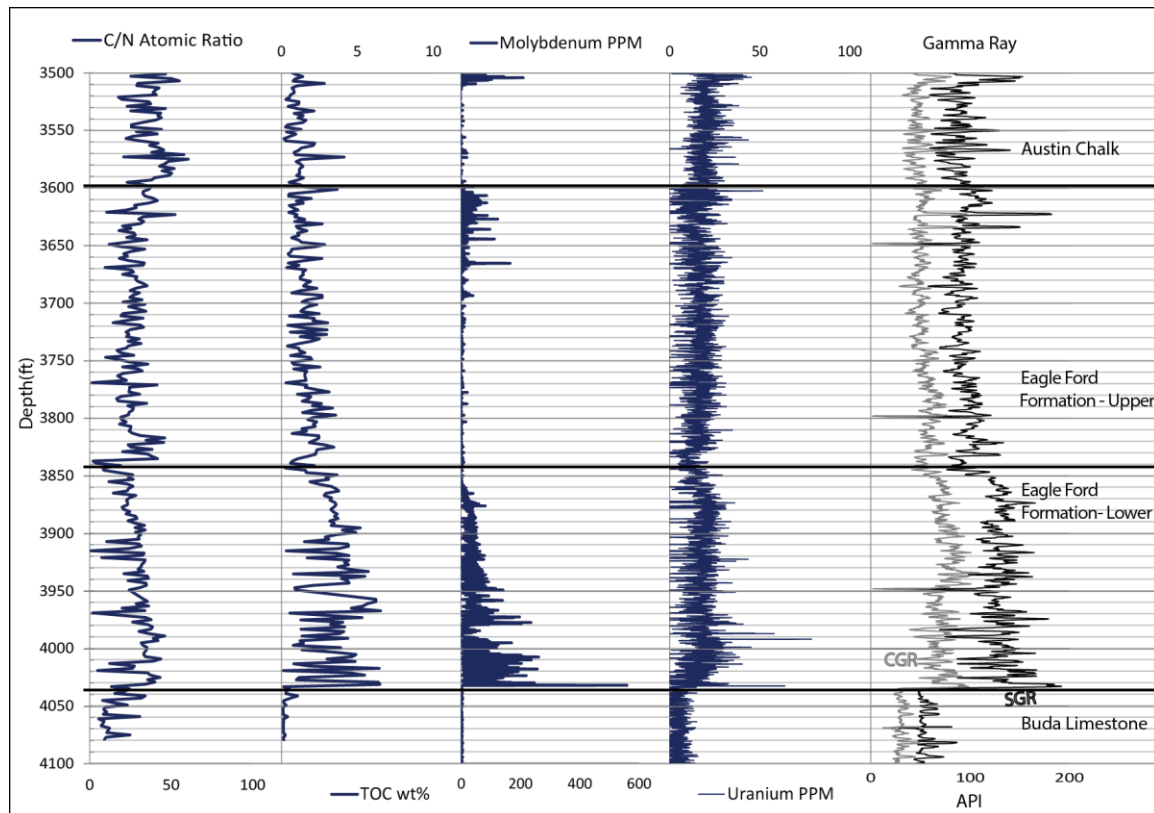


Figure 17: C/N atomic ratio, TOC, molybdenum ppm, uranium ppm, and gamma ray for Core-X conventional core samples.

Interpretation

The Buda Limestone contains dominantly marine-organic matter. A majority of marine carbon has been normally degraded, causing for an increased ratio in C/N values. An average C/N ratio of 15.2 suggests algae are prominent with very little influence from terrestrial material (Fig. 17). TOC weight percent in the Buda Limestone are less than 1% and are the lowest within the Core-X core. Because the Buda Limestone accumulated during oxic conditions, it is determined that organic matter was not preserved. Both CGR and SGR for the Buda are low because of low quantities of clay mineral content in a dominantly calcite section.

The lower Eagle Ford strata has an average C/N ratio of 28.3, suggesting greater terrestrial organic matter influence than in the Buda Limestone (Fig. 17). While terrestrial organic matter may have been more prevalent in the lower Eagle Ford strata, marine-organic matter is still dominant. The increased C/N ratio may simply reflect increased marine-organic matter degradation during particle settling. C/N values range from 0.69 to 46.1; the minimum value indicates degradation of deposited organic matter and the maximum value represents land-plant matter (Fig. 17). TOC weight percent on average in the lower Eagle Ford strata is the highest within the core, up to 6.5 wt%. Molybdenum enrichment in the lower Eagle Ford strata signals anoxic bottom-waters; lack of oxygen allows for organic matter preservation and thusly higher TOC values. Both CGR and SGR values greatly increase from the Buda Limestone and into the Eagle Ford. The increase in API supports the major increase in argillaceous material and increased preserved organic matter because of the impact that clay minerals have on water flow and circulation of water in sediments.

C/N values in the upper Eagle Ford strata have an average of 26.2 and a range from 1.49 to 52.3 (Fig. 17). This set of values describes a similar system to the lower

Eagle Ford strata – algal material is the dominant organic matter type with some mild influence from a terrestrial organic matter source. The low C/N value of 1.49 suggests algal matter degradation (Fig. 17). TOC averages 1.52% showing moderate preservation of organic matter (Fig. 17). The increase in terrigenous, argillaceous material is mirrored within the high gamma ray values. Spectral gamma ray values increase through zones of increased molybdenum, confirming increased uranium and TOC preservation during anoxic conditions.

The Austin Chalk shows C/N values with an average of 38.09 and a range from 17.5 to 60.4 (Fig. 17). Nitrogen is commonly a limiting factor within marine systems; degradation of settling algal organic matter can cause for an increased C/N ratio, even though dominant organic matter type is marine. TOC values in the Austin Chalk average 1.10%, but can be as much as 4.13% (Fig. 17). TOC preservation is greater within the thin intervals of laminated argillaceous planktonic foraminifera wackestone (Figs. 17, 20). Periods of oxygenation within the water-column have allowed for degradation of organic matter, causing increased C/N values and lower preserved TOC (Fig. 17). Argillaceous, mineral seams allow for preservation of trapped organic matter. CGR and SGR decrease from the Eagle Ford into the Austin Chalk, this is because of the decrease in TOC and argillaceous minerals.

Winterbotham J.M. Jr. #1 Conventional Core

Figure 18 contains C/N atomic ratio, TOC weight percent, molybdenum ppm, and uranium versus depth for the Winterbotham J.M Jr. #1. The C/N ratio has an average value of 27.9 and a minimum value of 0.613 and a maximum values 71.5. Total organic carbon within the Winterbotham J.M. Jr. #1 has an average of 2.01wt%, with a minimum 0.15wt% and a maximum 6.57wt%.

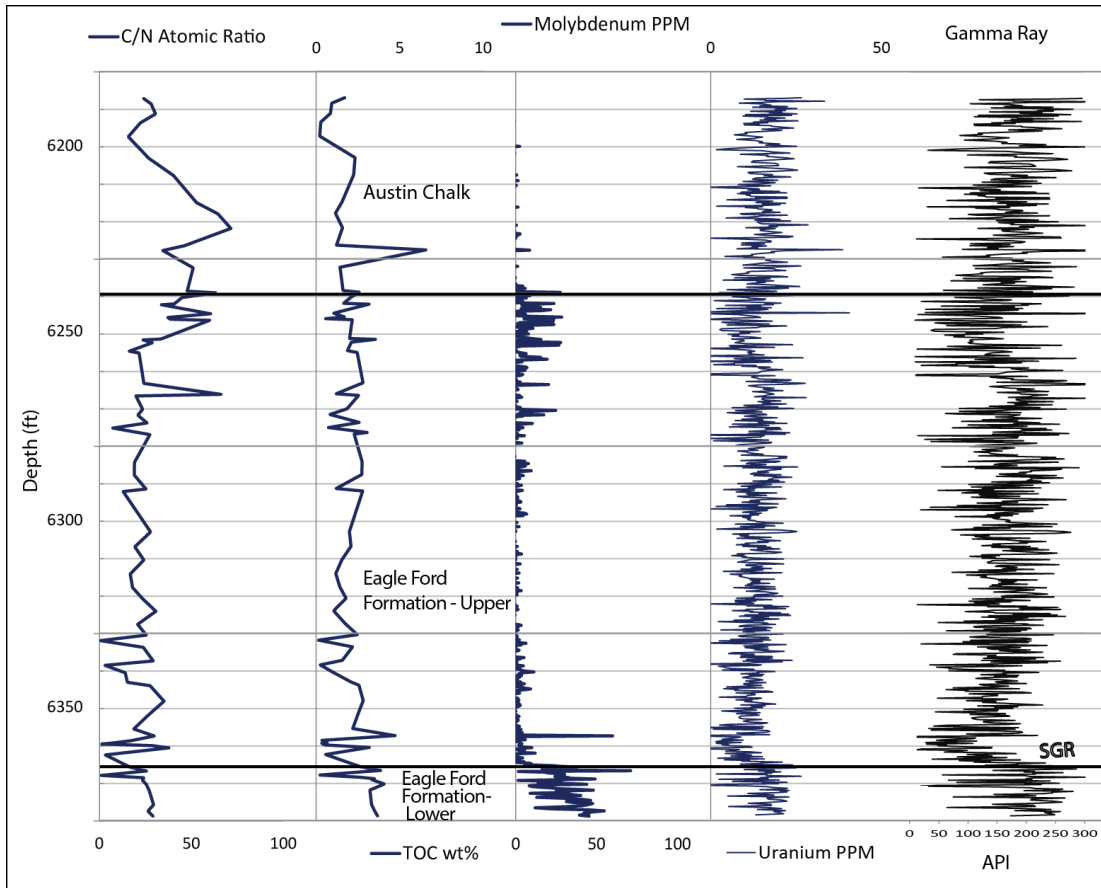


Figure 18: C/N atomic ratio, TOC, molybdenum ppm, uranium ppm, and gamma ray for Winterbotham J.M. Jr. #1 conventional core samples. Gamma ray values have been computed using XRF data.

Interpretation

C/N values within lower Eagle Ford strata are the lowest amongst all stratigraphic divisions within the section with an average ratio of 22.9 (Fig. 18). The C/N confirms mixed provenance of organic matter, with a dominant contribution from marine-organic matter. TOC values are highest on average within the lower Eagle Ford strata. TOC preservation potential is enhanced because of anoxic conditions present during deposition

(Figs. 15, 18). SGR values within the lower Eagle Ford strata are high, showing the dominance of argillaceous material and uranium abundance.

The C/N atomic ratio in the upper Eagle Ford strata is 28.8, indicating dominance of marine-organic matter with some minor influence from land plant matter (Fig. 18). The C/N value may also be higher than expected because of degradation of original algal organic matter as it settled through an oxygenated water-column. TOC preservation within the upper Eagle Ford strata is lower than that of the lower Eagle Ford strata. This is related to oxygenation of bottom-water and sediments allowing for degradation of accumulated organic matter. Lower organic matter values for the upper Eagle Ford strata may additionally be impacted by lower rates of accumulation.

The C/N atomic ratio in the Austin Chalk has an average of 39.1 (Fig. 18). The extremely high C/N atomic ratio indicates degradation while settling of primary marine-organic matter within an oxygenated environment. TOC values are lowest in the Austin Chalk, averaging 1.7%. Oxygenation and bioturbation of sediments allows for degradation of original organic matter.

LITHOFACIES

Ten lithofacies, two pseudolithofacies, and one diagenetic lithofacies have been identified and described from both core and outcrop. Each described lithofacies has an accompanying photo plate. Table 6 lists each lithofacies abbreviation, name and gives a short summary of each defined lithofacies. Fissility as mentioned below refers to the outward character of a rock and the ability to easily split along bedding planes (Ingram, 1963). XRD and XRF data have shown a calcite-dominated system; the majority of ‘muds’ discussed herein are calcareous, but may demonstrate variable levels of argillaceous or siliciclastic material. Eagle Ford Group lithofacies generally contain

similar mineralogic composition, but may show changes in sedimentary features/structures or fauna. An average mineralogic composition based only on carbonate, quartz, and clay mineral content is provided for each lithofacies (not included for unsampled pseudolithofacies or diagenetic lithofacies). Lithofacies described herein are named using either Dunham (1962) or Folk (1980) classification styles.

Lithofacies Name	Occurrence	Formation	Weathering Character	Dominant Allochems	Sedimentary Structures	Brief Summary	Mineralogy/TOC
Burrowed skeletal wackestone	Hot Springs, Core-X.	Buda Limestone	White-grey, massive and robust beds with a pitted appearance	Gastropods, planktonic foraminifera, benthic foraminifera, calcispheres	Pervasive burrowing has erased original sedimentary features	Calcite mud with sub-vertical burrows and clay solution seams	Calcite 71% Quartz 2% Phyllosilicate 11% TOC: 0.2%
Laminated argillaceous planktonic foraminifera wackestone	Hot Springs, Core-X, Winterbotham J.M. Jr. #1	Boquillas, Eagle Ford, Transitiona l Austin Chalk	Buff, fissile beds with thin cemented laminations	Planktonic foraminifera, <i>Inoceramus</i>	Winnowed starved ripples, grain laminations	Millimeter-scale sub-horizontal planktonic foraminifera laminations separated by centimeter-scale mud laminations.	Calcite 67% Quartz 9% Phyllosilicate 11% TOC: 2.8%
Laminated argillaceous <i>Inoceramid</i> wackestone	Hot Springs, Core-X, Winterbotham J.M. Jr. #1	Boquillas, Eagle Ford	Buff, fissile beds with thin cemented laminations	<i>Inoceramus</i> , planktonic foraminifera, radiolarians	Winnowed starved ripples, grain laminations	<i>Inoceramus</i> fragments and shell pavements create laminations in mud matrix	Calcite 66% Quartz 9% Phyllosilicate 11% TOC: 3.7%
Weakly laminated wackestone	Core-X, Winterbotham J.M. Jr. #1	Eagle Ford	N/A	Planktonic foraminifera, radiolarians	Faint, bedding parallel laminations	Centimeter-scale mud laminations with matrix-supported forams, no grain dominated laminations	Calcite 65% Quartz 9% Phyllosilicate 12% TOC: 3.0%
Massive argillaceous claystone	Core-X, Winterbotham J.M. Jr. #1	Eagle Ford	N/A	Planktonic foraminifera	Thin, plain beds, interbedded with laminated argillaceous planktonic foraminifera wackestone	Fissile, unbedded, blue, clay-rich mudrock	Calcite 28% Quartz 7% Phyllosilicate 15% TOC: 1.2%
Laminated calcisphere grainstone	Core-X	Eagle Ford	N/A	Calcispheres, radiolarians, planktonic foraminifera	Ripples with current migration	Wavy, nodular bedding. With alternating dark (mud) and off-white (calcisphere or skeletal) laminations	Calcite 68% Quartz 5% Phyllosilicate 12% TOC: 1.3%
Laminated skeletal grain-dominated packstone	Hot Springs, Winterbotham J.M. Jr. #1	Boquillas, Eagle Ford	Recessive, buff beds with visible grain laminations	Planktonic foraminifera, <i>Inoceramus</i> , echinoids	Small debris flow grain laminations	Frequent alternations between cm-scale grain-dominated laminations and mud, contains intraclasts	Calcite 56% Quartz 6% Phyllosilicate 16% TOC: 1.5%

Table 6 (cont.)

Lithofacies Name	Occurrence	Formation	Weathering Character	Dominant Allochems	Sedimentary Structures	Brief Summary	Mineralogy
Burrowed foraminifera wackestone	Hot Springs, Core-X, Winterbotham J.M. Jr. #1	Transitiona l Austin Chalk, Boquillas (San Vicente)	Generally recessive, but can be robust depending on level of cementation	Planktonic foraminifera	Petrographic solution seams, generally unlaminated	Grey-white, unbedded, burrowed limestone with cyclic alternations with laminated argillaceous planktonic foraminifera wackestone	Calcite 74% Quartz 9% Phyllosilicate 11% TOC: 1.2%
Laminated skeletal packstone-grainstone	Hot Springs	Boquillas (Ernst)	Robust, thin bedded with orange and purple leisengang banding	Radiolarians, calcispheres, planktonic foraminifera, <i>Inoceramus</i>	Soft sediment deformation, laminations-scale folding, dewatering structures	Grain supported allochem laminations interbedded with mud laminations, contains thin ammonite bed	Calcite 52% Quartz 7% Phyllosilicate 17% TOC: 0.1%
Volcanic ash	Hot Springs, Core-X, Winterbotham J.M. Jr. #1	Boquillas, Eagle Ford	Yellow, orange, or red fissile and recessive	None	None	Yellow ash deposits contain phyllosilicate, feldspar, and quartz phenocrysts, often pyritized	Calcite 5% Quartz 4% Phyllosilicate 52%
Massive limestone	Hot Springs	Boquillas	Buff robust, non-recessive beds	N/A	N/A	Undifferentiated robust outcrop beds; no thin section for lithofacies specification	Unsampled
Recessive argillaceous mudrock	Hot Springs	Boquillas	Recessive, friable, buff	N/A	N/A	Fissile, poorly preserved marls in outcrop; no thin section for lithofacies specification	Unsampled
Peloidal crystalline mudrock	Hot Springs, Core-X, Winterbotham J. M. Jr. #1	Boquillas, Eagle Ford	Robust, non-recessive	Radiolarians, planktonic foraminifera	Rare preserved starved ripple laminations	Diagenetic lithofacies. Pervasive matrix calcitization with sub-hedral, granular calcite and calcitized radiolarians	Unsampled

Table 6: Summary of lithofacies. The table contains lithofacies name, in which locations it occurs, what formations it occurs in, the weathering character if applicable, dominant fauna per lithofacies, sedimentary structures, and a brief summary of the lithofacies. Mineralogy and TOC values included for each facies represent an average of values.

Burrowed Skeletal Wackestone

The burrowed skeletal wackestone facies is found within the Buda Limestone and is observed with Core-X in the Maverick Basin and in outcrop at the Hot Springs locality in Big Bend National Park.

The burrowed skeletal wackestone is a white-grey burrowed limestone with abundant fauna (Figs. 19A, 19B). Average mineralogy is 71% carbonate, 2% quartz, and 11% clay minerals. Fauna are matrix-supported and consist of calcispheres, oyster fragments, nektonic echinoid fragments (saccocomids), and some planktonic foraminifera (Fig. 19C). Bedding and primary depositional fabric has been destroyed by burrowing. Individual burrows can rarely be identified, among which rare *Planolites* or subhorizontal burrows can be observed. Authigenic pyrite and equant calcite spar have replaced select grains and burrows.

Argillaceous horsetail solution seams are extremely common throughout burrowed skeletal wackestone (Fig. 19B). Solution seams are a dark grey and wispy; seams generally concentrate through a short interval and subsequently feather outwards. Seams are commonly accompanied by euhedral, authigenic dolomite precipitation (Fig. 19D). Stylolites with teeth are also present but are less abundant. Authigenic mineral precipitation is common along solution seam and stylolite pathways, dominated by rimmed, euhedral dolomite and small pyrite framboids.

Mineralogy discussed above, shows that this facies (which composes the Buda Limestone), is a calcite dominated facies. This facies contains 35-39% calcium and up to 75% carbonate. The dark grey, wispy seams (Fig. 19B) are dominated by terrigenous, argillaceous clay minerals. Redox sensitive trace elements show that the burrowed skeletal wackestone is deposited during oxygenated conditions.

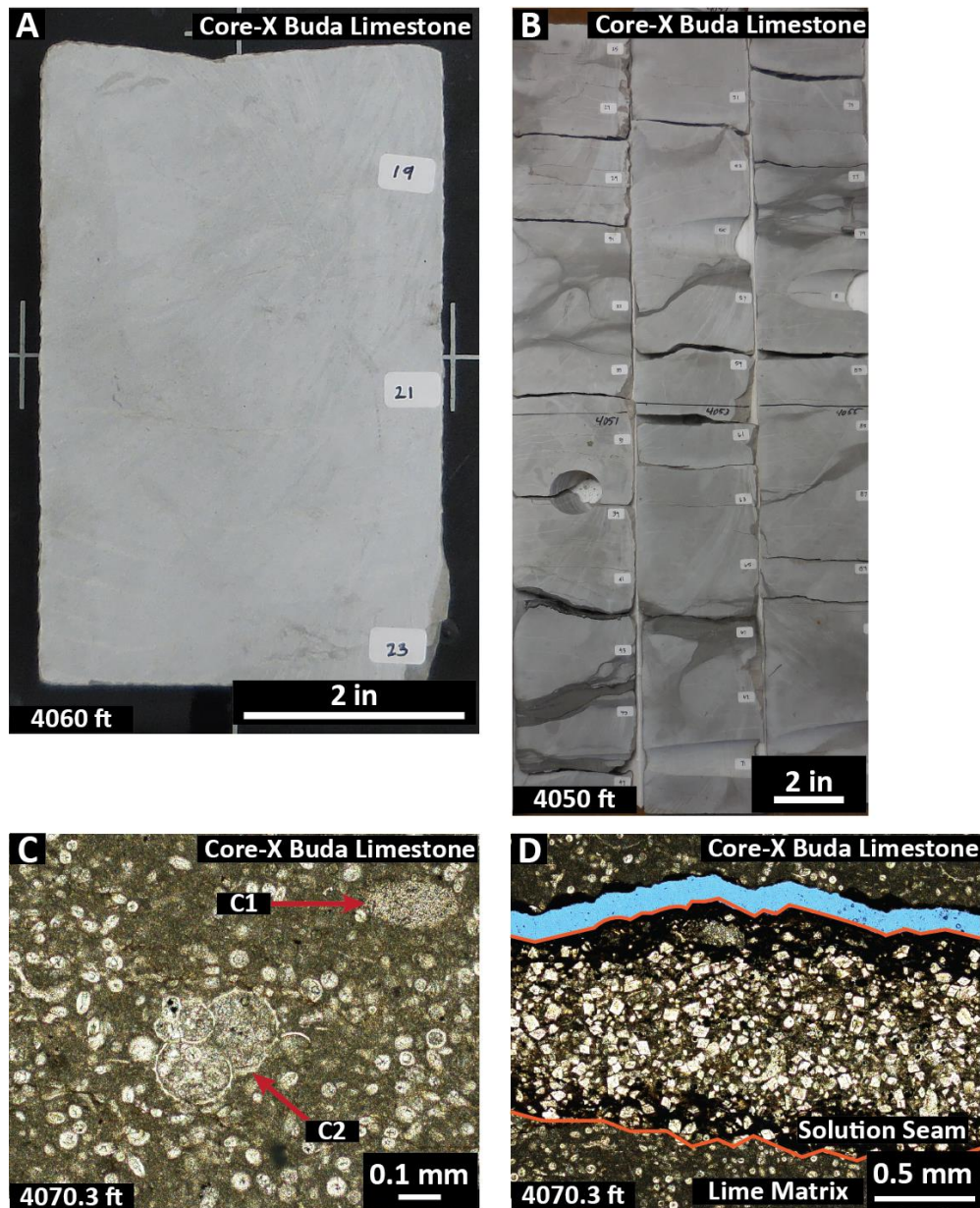


Figure 19: Burrowed skeletal wackestone: A) Burrowed skeletal wackestone in core slab in Buda Limestone. B) Horsetail stylolites are dark grey in burrowed skeletal wackestones in Buda Limestone. C) Photomicrograph of burrowed skeletal wackestone with abundant calcispheres, echinoid fragment (C1), and planktonic foraminifera (C2) in Buda Limestone. D) Stylolite with dolomitization along seam in Buda Limestone.

Laminated argillaceous planktonic foraminifera wackestone

This lithofacies is most common in the lower Eagle Ford strata. It appears at the base of the upper Eagle Ford strata. Additionally, thin argillaceous intervals in the transitional Austin Chalk are classified as the laminated argillaceous planktonic foraminifera wackestone. This facies is observed in both outcrop and core at the Hot Springs and within Core-X and Winterbotham J.M. Jr. #1.

The laminated argillaceous planktonic foraminifera wackestone facies is composed of a muddy, peloidal matrix with winnowed and reworked planktonic foraminifera lags (Fig. 20A). The mud in this facies is carbonaceous (65% calcite on average) with a distinctive argillaceous signature (average 12%) as noted in the lithofacies name. Lags are either small accumulations of planktonic foraminifera or have been reworked into small, winnowed ripples. Millimeter-scale grain laminations are subparallel to bedding and are both continuous and discontinuous (Fig. 20B). Fauna are concentrated within laminations and lags, however, planktonic foraminifera appear sometimes within the pelagic, peloidal matrix. Fauna are dominantly planktonic foraminifera, with rare inoceramid fragments and fish bones.

Small soft-sediment folds and slumps occur within laminated argillaceous planktonic foraminifera wackestone. Coherent laminations are folded plastically and are overturned. Slumps show no sign of brittle breakage or individual clasts. Fauna within folded beds are similar to the surrounding in-situ population.

The laminated argillaceous planktonic foraminifera wackestone facies is commonly interbedded with the laminated argillaceous inoceramid wackestone, as well as volcanic ash and the diagenetic facies peloidal crystalline mudrock.

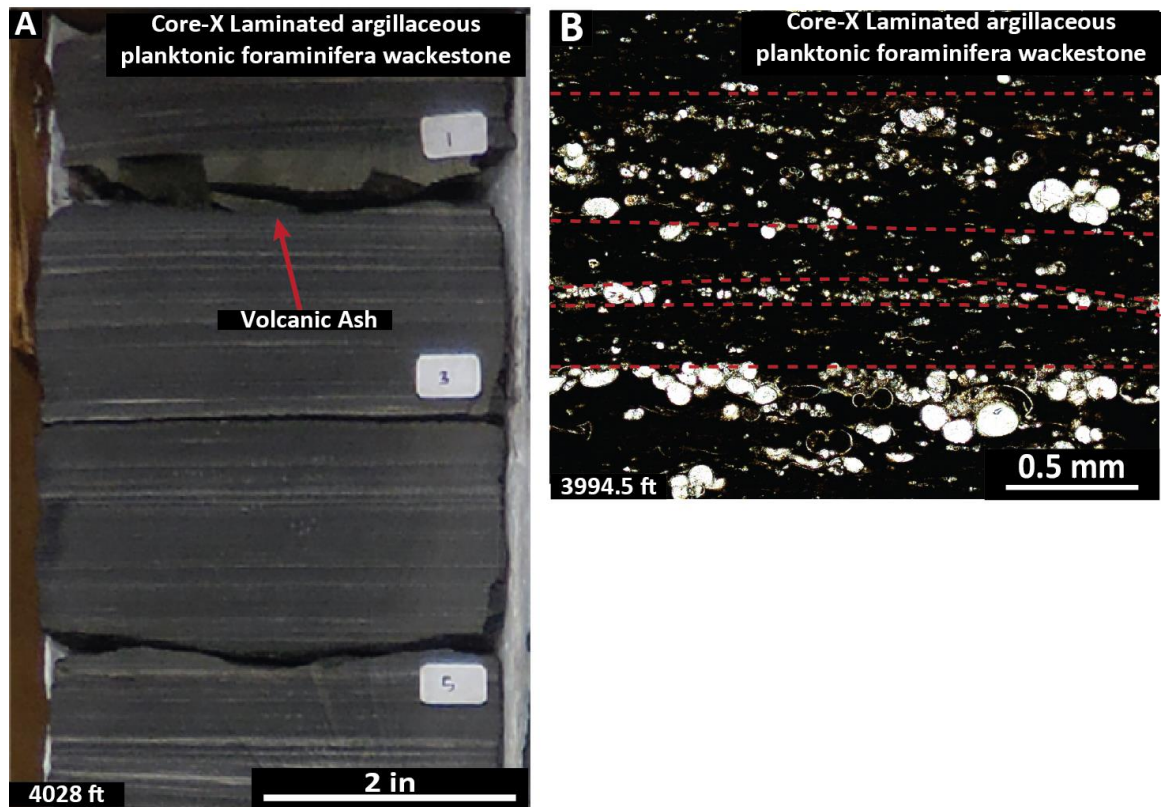


Figure 20: Laminated argillaceous planktonic foraminifera wackestone: A) Core slab Laminated argillaceous planktonic foraminifera wackestone with interval of diagenetic calcite and volcanic ash in lower Eagle Ford strata. B) Photomicrograph with planktonic foraminifera laminations (outline by dashed red lines) in lower Eagle Ford strata.

Laminated argillaceous inoceramid wackestone

This facies occurs most commonly in the lower Eagle Ford strata and sometimes in the upper Eagle Ford strata. It is observed within both cores (Core-X and Winterbotham J.M. Jr. #1) located within the Maverick Basin. This facies is rich in clay minerals in the matrix and calcite in the matrix, cement, and skeletal debris. This facies is documented in molybdenum-rich environments.

Laminated argillaceous inoceramid wackestone is composed primarily of peloidal, argillaceous mud matrix with inoceramid shells and shell fragments parallel to

bedding (Fig. 21A). The average mineralogy is composed of 66% carbonate, 9% quartz, and 11% clay minerals. Broken inoceramid columnals accumulate as small lag deposits or create a shell hash (Fig. 21B). Inoceramid filaments are abundant within pelagic, peloidal layers (Fig. 21C). Up to 1-inch thick shell pavements of inoceramid and oysters develop parallel to bedding. Equant calcite spar forms as a cement within interparticle pores within the shell pavement. Crushed ammonites are present but are extremely rare. Planktonic foraminifera (and rare agglutinated foraminifera) are present within pelagic, peloidal muds (carbonate) but are not reworked into lags or laminations (Fig. 21D).

Thin grain accumulations occur along bedding surfaces (Figs. 21A, 21B). Grain accumulations are composed of inoceramid columnals and shell fragments, as well as phosphatic fish bones. Debris-flow accumulations have a basal scour into underlying peloidal carbonate mud and generally fine upward. Laminations are millimeter scale and grains show evidence of reworking.

Cone-in-cone cement is present within laminated argillaceous inoceramid wackestone (Fig. 21E). The calcite cement occurs subhorizontal or parallel to bedding, ranging in thickness from 1-10mm. Calcite cones form perpendicular to bedding.

The laminated argillaceous inoceramid wackestone facies occurs interbedded with laminated argillaceous planktonic foraminifera wackestone and contains thin intervals of volcanic ash and diagenetic peloidal crystalline mudrock. Radiolarians are common in some intervals of diagenetic calcite. Radiolarians within the laminated argillaceous inoceramid wackestone intervals were first pyritized then calcitized.

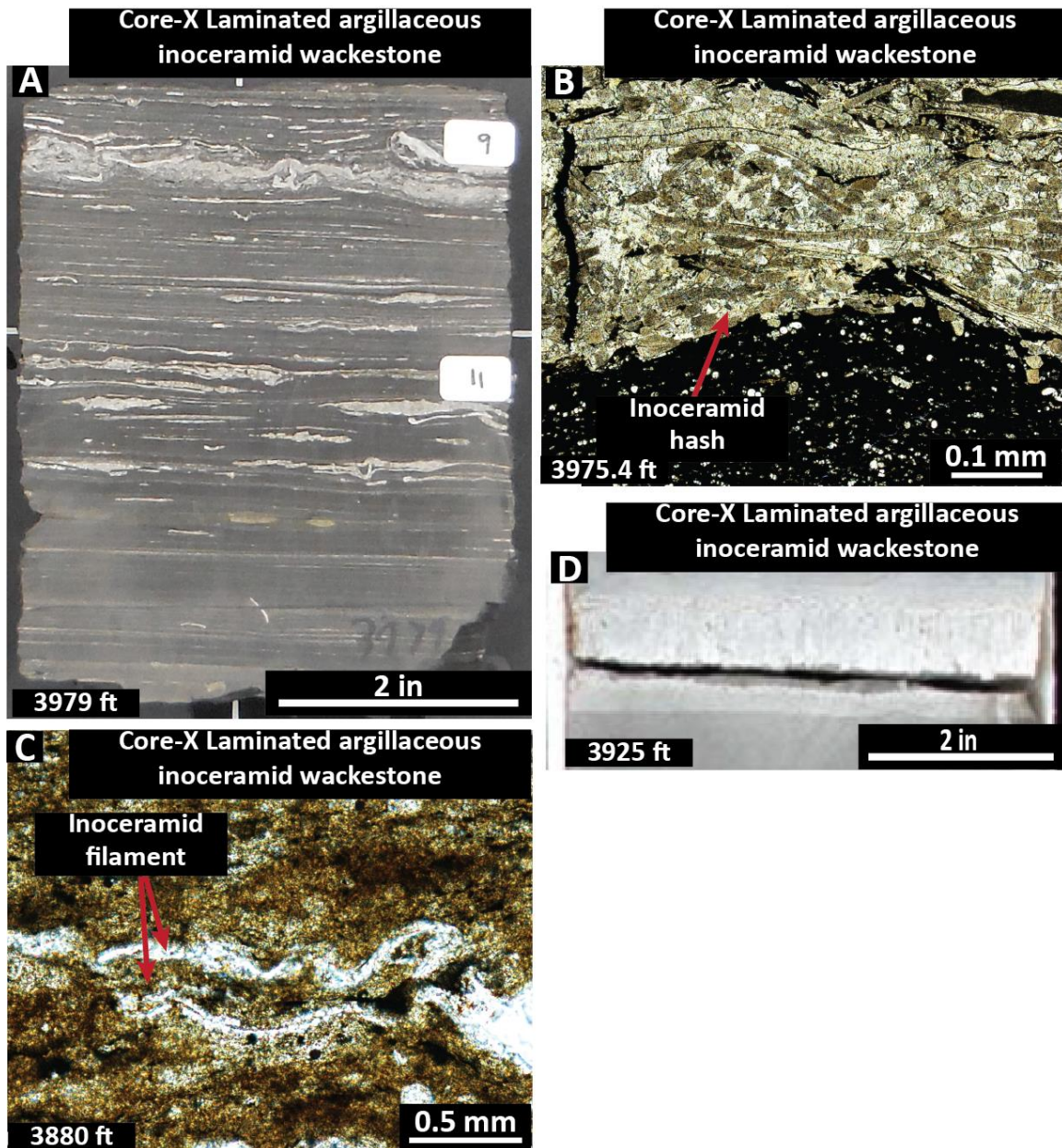


Figure 21: Laminated argillaceous inoceramid wackestone: A) Core slab showing dominant inoceramid along bedding planes in lower Eagle Ford strata. B) Accumulation of inoceramid prisms in lower Eagle Ford strata. C) inoceramid filament in lower Eagle Ford strata. D) Cone-in-cone cement in lower Eagle Ford strata.

Weakly laminated wackestone

This facies is found in the upper, lower Eagle Ford strata, and within the middle and lower portions of the upper Eagle Ford strata. This facies is observed within core (Core-X and Winterbotham J.M. Jr. #1) located within the Maverick Basin. Mineralogy shows that this facies is composed of both argillaceous and calcareous matrix.

Weakly laminated wackestone is a peloidal mudrock with few to no developed grain laminations or grain accumulations (Fig. 22A) and commonly contains argillaceous mud. The average mineralogy is 65% carbonate, 9% quartz, and 12% clay minerals. Horizontal, parallel laminations 1-2cm apart are visible, but are created by a darkened argillaceous mud seam rather than grains as in other defined facies (Fig. 22B). Planktonic foraminifera are common, but are extremely small and difficult to photograph (Fig. 22C). Foraminifera are matrix-supported and do not accumulate in lag deposits or show signs of reworking. The matrix is composed of argillaceous clay with small, silt grains, and peloids (Fig. 22D). Authigenic pyrite framboids are common within the matrix. Larger fossils are rare.

The weakly laminated wackestone facies does not occur commonly interbedded with any other facies. Volcanic ash beds are rarely interbedded within this facies. Diagenetic facies (peloidal crystalline mudrock) do not occur interbedded within this facies.

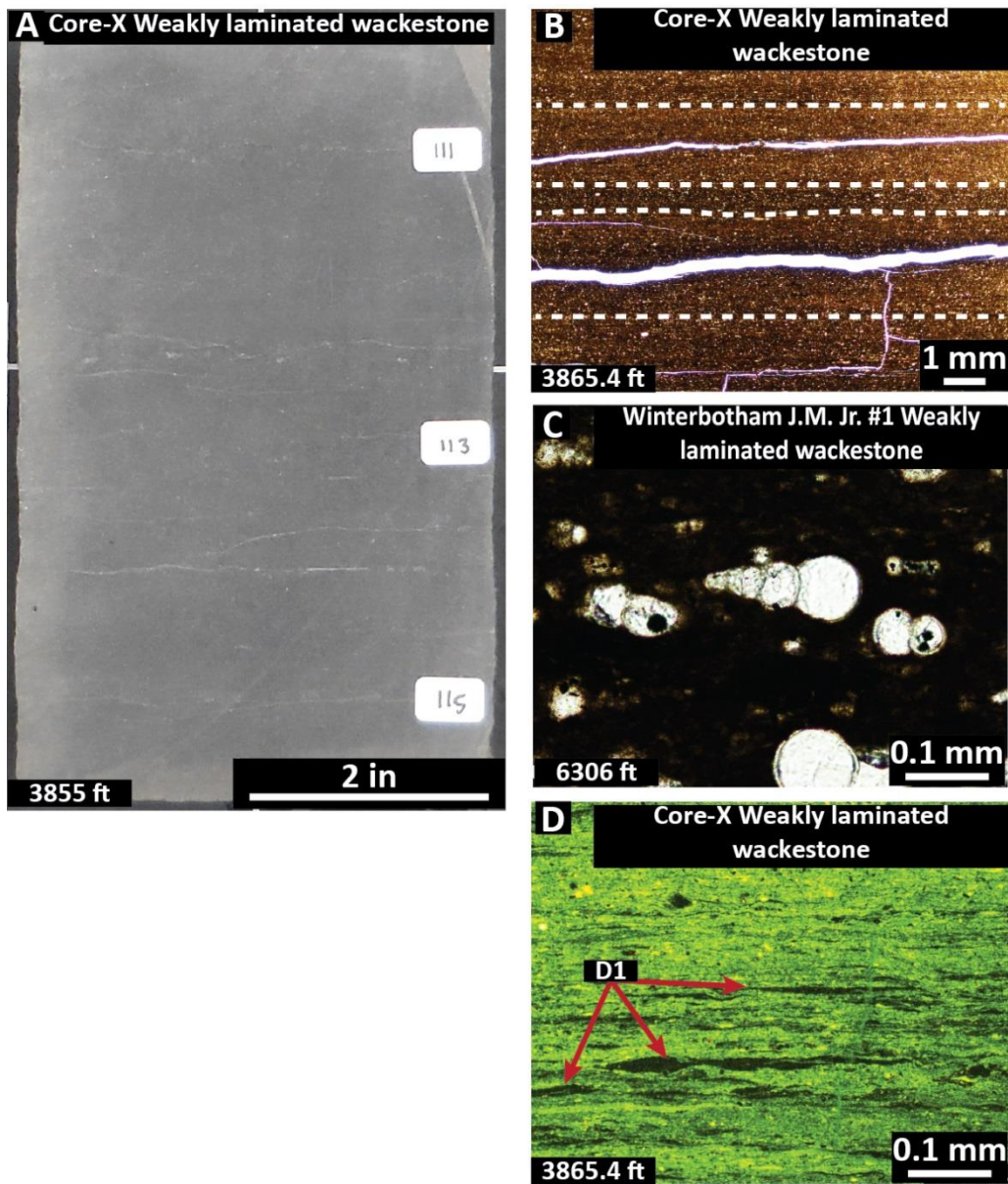


Figure 22: Weakly laminated wackestone: A) Weakly laminated wackestone core slab in lower Eagle Ford strata. B) Photomicrograph of horizontal mud laminations outlined in white in lower Eagle Ford strata. C) Photomicrograph of *Heterohelix* sp. foraminifera in lower Eagle Ford strata. D) UV + yellow filter photomicrograph of weakly laminated wackestone with clay matrix and peloids (D1) in lower Eagle Ford strata.

Massive argillaceous claystone

The massive argillaceous claystone occurs in the lowermost, upper Eagle Ford strata, at the contact with the lower Eagle Ford strata. This facies is observed within the Core-X and Winterbotham J.M Jr. #1 conventional cores. This lithofacies coincides with the zone of titanium enrichment that serves as the dividing marker between upper and lower Eagle Ford (Figs. 10, 12).

Massive argillaceous claystone has few to no depositional structures or sedimentary features (Fig. 23A). The average mineralogy is 28% carbonate, 7% quartz, and 15% clay minerals – this facies also contains up to 45% dolomite. This dolomite is diagenetic. The rocks are friable in core slab. Massive argillaceous claystone grades and interfingers into the overlying planktonic foraminifera laminated facies until it eventually disappears. Light microscopy demonstrates a yellow, aphanitic, clay-rich matrix that is extinct when viewed in cross-polarized light (Fig. 23B). Fauna are almost exclusively contained within thin, peloid-rich laminations with matrix-supported radiolarians or planktonic foraminifera (Fig. 23C). Planktonic foraminifera are rarely found within massive argillaceous claystone; however, those that are have undergone pervasive recrystallization (Fig. 23D). Small, silt grains contained within the dominant yellow clay matrix suggest a potential detrital origin.

Deposits of massive argillaceous claystone are thickest in the first bed (Fig. 23A); beds gradationally thin upward and begin to interfinger with laminated argillaceous planktonic foraminifera wackestone as that facies becomes the primary depositional facies (Fig. 23A). Volcanic ash deposits and peloidal crystalline mudrock occur adjacent to massive argillaceous claystone (Fig. 23).

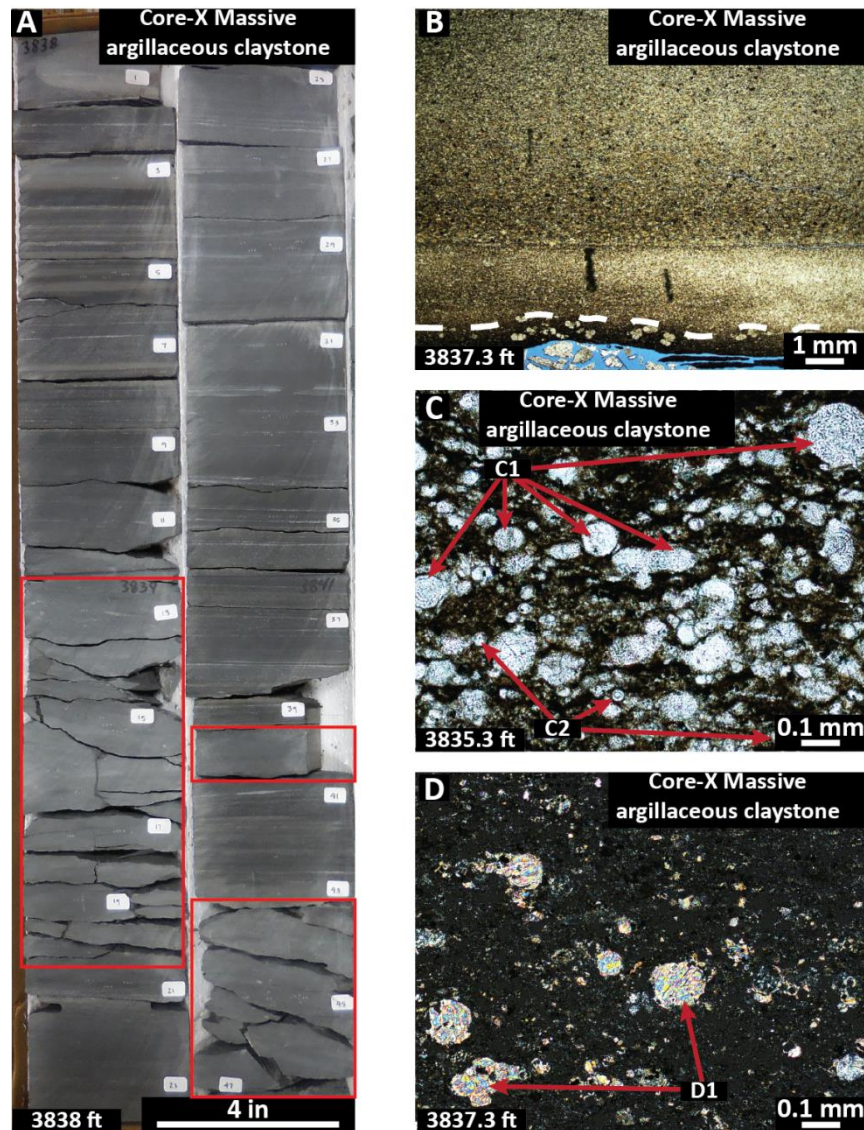


Figure 23: Massive argillaceous claystone: A) Core slab shows massive argillaceous claystone (red boxes) interfingering with laminated argillaceous planktonic foraminifera wackestones in upper Eagle Ford strata. B) Photomicrograph of argillaceous mud lamination with planktonic foraminifera below massive argillaceous claystone in upper Eagle Ford strata. C) Photomicrograph of abundant, calcified radiolarians (C1) and calcispheres (C2) within mud matrix in upper Eagle Ford strata. D) Photomicrograph in XPL of recrystallized planktonic foraminifera within extinct, argillaceous matrix in upper Eagle Ford strata.

Laminated calcisphere grainstone

The laminated calcisphere grainstone facies is found within the upper Eagle Ford in the Core-X conventional core from Maverick Basin. Volcanic ash beds and diagenetic peloidal crystalline mudrock are commonly found adjacent to the laminated calcisphere grainstone facies. This facies may be correlative to Motif 4B (defined as Nodular Cycles by Forkner, 2013).

Well-developed ripples composed of fauna dominate the laminated calcisphere grainstone; ripples interlaminated with possibly argillaceous mud have produced extensive differential compaction giving the laminated calcisphere grainstone a wavy, nodular appearance (Fig. 24A). Average mineralogy is 68% carbonate, 5% quartz, and 12% clay minerals. Compaction around nodules has caused cracking and syn-compactional fracturing of underlying and overlying beds. Reworked and accumulated fauna are a bright white compared to the much darker, muddy laminations (Fig. 24B). Developed ripples have a sharp basal contact and scour of the underlying laminations.

Soft-sediment deformation and folding are common within the laminated calcisphere grainstone (Fig. 24C). Deposits are characterized by basal accumulations of subangular, pebble-sized, lithified intraclasts composed of calcisphere and calcite cement. Small-scale, lamination-sized flows are also present. Such debris-flows have an increase in fish bones and inoceramid fragments. Soft-sediment deformation is present in mud laminations as well as small flame structures in allochem-dominated grain laminations. Slumping is characterized by plastically folded and overturned, semi-coherent beds. Laminations in folded beds show some signs of contortion, but remain relatively intact.

Grain accumulations (ripples and laminations) displaying the least compaction are composed dominantly of calcisphere accumulations (Fig. 24D). inoceramid prisms and echinoid fragments are also common to abundant within calcisphere laminations.

Compaction is most extensive in areas lacking calcispheres. Planktonic foraminifera are rarely present in calcisphere accumulations; however, foraminifera are common within peloidal layers (Fig. 24E). Muddier layers sometimes contain foraminifera lags.

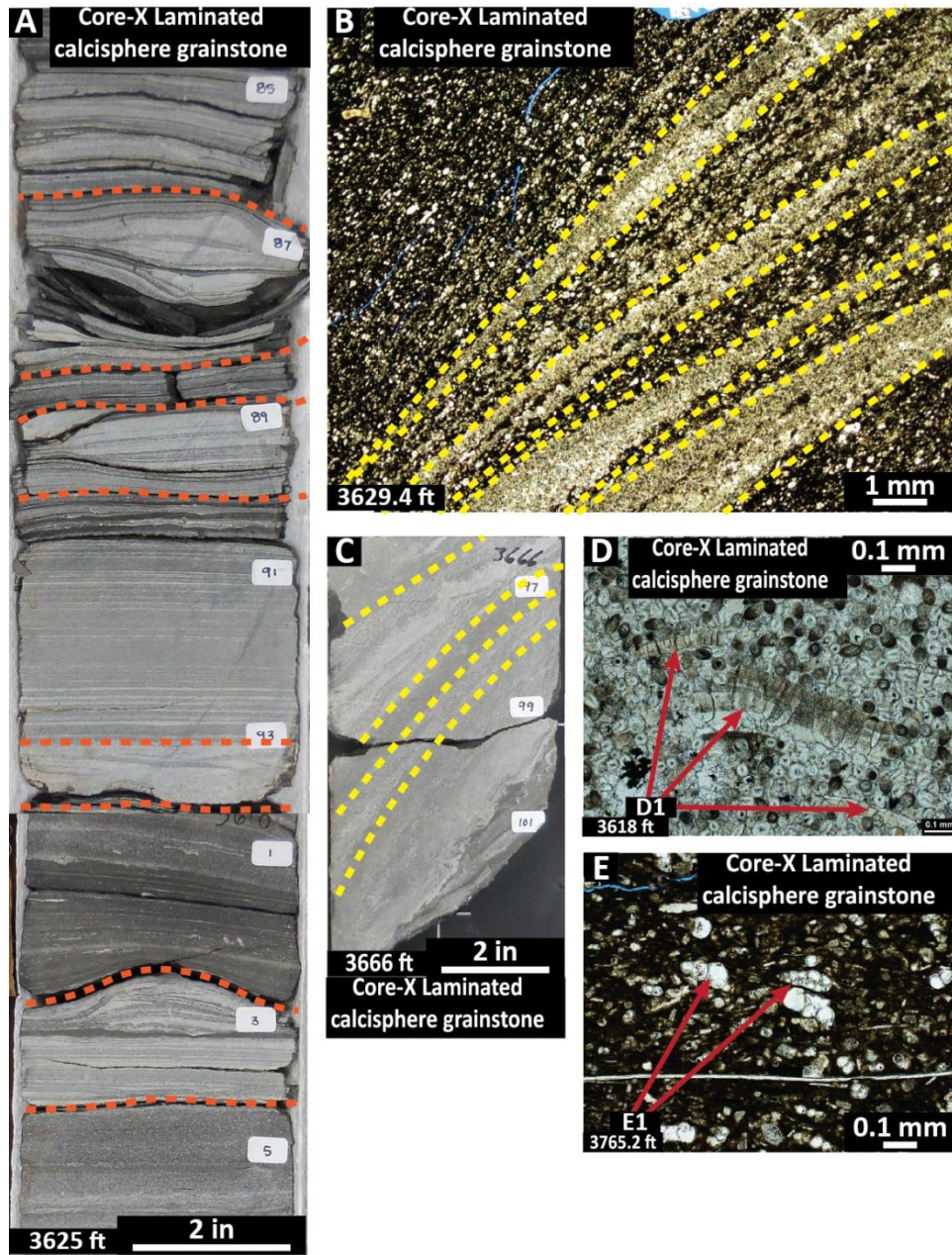


Figure 24: Laminated calcisphere grainstone: A) Core slab with calcisphere bed forms outlined in orange in upper Eagle Ford strata. B) Photomicrograph of inclined calcisphere lamina (yellow) with differential compaction in upper Eagle Ford strata. C) Photomicrograph of semi-coherent ductile fold, bedding outlined in yellow in upper Eagle Ford strata. D) Photomicrograph of inoceramid (D1) in calcisphere grain lamination in upper Eagle Ford strata. E) Heterohellicidae planktonic foraminifera (E1) within possibly argillaceous muddy lamination in upper Eagle Ford strata.

Laminated skeletal grain-dominated packstone

The laminated skeletal grain-dominated packstone facies is observed in both Hot Springs outcrop samples from Brewster County and Winterbotham J.M. Jr. #1 core samples from Zavala County. This facies is found within the upper Eagle Ford strata (core) and within the Boquillas Formation (mostly San Vicente and rare occurrence in the Ernst Member) in outcrop.

Laminated skeletal grain-dominated packstone is a pale to dark grey carbonate mudstone dominated by grain-dominated allochem laminations (Fig. 25A). Average mineralogy is 56% carbonate, 8% quartz, and 17% clay minerals. Because this facies is only documented in outcrop, average mineralogic values may not be correlative to values of the same facies documented in the subsurface. Laminations are up to 1 cm thick and commonly have an erosive base and contain allochem lags and ripples (Fig. 25B). Fauna within laminations are dominantly planktonic foraminifera; accompanied by calcispheres, oysters, fish bones, phosphates, echinoids, inoceramid fragments, and angular quartz silt (Figs. 25C, 25D). Grains are winnowed and show evidence of transport and re-working. Some laminations are truncated because of burrowing. *Planolites* are present but infrequent.

Soft-sediment deformation is common in carbonate mud-laminated skeletal planktonic foraminifera grain-dominated packstone. Flame structures, water escape structures, and differential compaction are present on the laminations scale (Fig. 25A). Large-scale deformation, folding, and mass-transport deposits are also present. Semi-lithified beds are ductily folded and remain semicoherent. Mass-transport deposits commonly have basal intraclasts of brittle, angular laminated mudstone. Lithified intraclasts are composed of planktonic foraminifera and calcisphere accumulations (Fig. 25E).

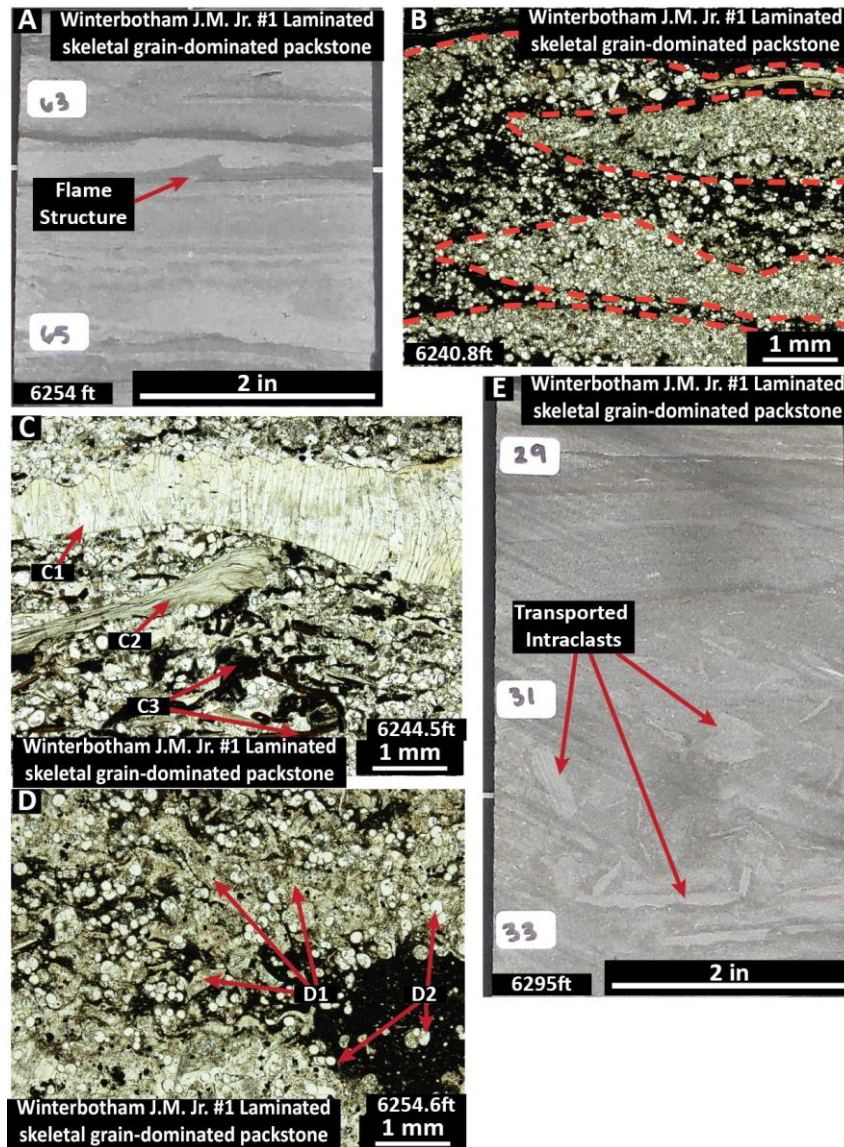


Figure 25: Laminated skeletal grain-dominated packstone: A) Core slab with flame structure in carbonate mud lamination in upper Eagle Ford strata. B) Photomicrograph of grain laminations outlined in red in upper Eagle Ford strata. C) inoceramid (C1), oyster (C2), and fish bones (C3) in grain lamination in upper Eagle Ford strata. D) Saccocomid echinoid fragments (D1) have a fuzzy, angular appearance compared to white, globular planktonic foraminifera (D2) in upper Eagle Ford strata. E) Core slab with angular intraclasts in in upper Eagle Ford strata.

Burrowed foraminifera wackestone

The burrowed foraminifera wackestone facies is found within both outcrop and core. Outcrop samples from the Hot Springs locality at Big Bend National Park are from the San Vicente Member of the Boquillas Formation. Core samples of borrowed foraminifera wackestone are found within Core-X and Winterbotham J.M. Jr. #1 from the Maverick Basin. This facies (with argillaceous alternations) constitutes the transitional Austin Chalk and Austin Chalk.

The burrowed foraminifera wackestone facies interfingers with laminated mudstone intervals (these mudstone intervals are grouped as laminated argillaceous planktonic foraminifera wackestone) (Fig. 26A). The average mineralogy is 74% carbonate, 9% quartz, and 11% clay minerals. Bioturbation within more calcic, limestone layers has erased any primary bedding structures, fauna are unsorted and matrix supported. Burrows are approximately 1 cm wide and several centimeters long (Fig. 26B). They may be vertical, subvertical, or subhorizontal and cut perpendicular to bedding. The faunal assemblage consists of a variety of planktonic foraminifera, echinoid fragments, and rare to uncommon calcispheres or inoceramid fragments (Figs. 26C, 26D). Laminated mudstone intervals appear similar to and are concluded to be the same as laminated argillaceous planktonic foraminifera wackestone (Fig. 20). Laminations are parallel to bedding and composed of small allochem lags and starved ripples. Contacts between the burrowed intervals and laminated mudrock intervals are either sharp or gradational.

Authigenic dolomite is common within this facies as documented in thin section and supported by XRD data. Some burrowed limestone layers are pervasively dolomitized, destroying any primary depositional fabric (Fig. 26E). Individual peloids are

commonly not dolomitized. Relic fauna are rare. Volcanic ash is present within burrowed foraminifera wackestone.

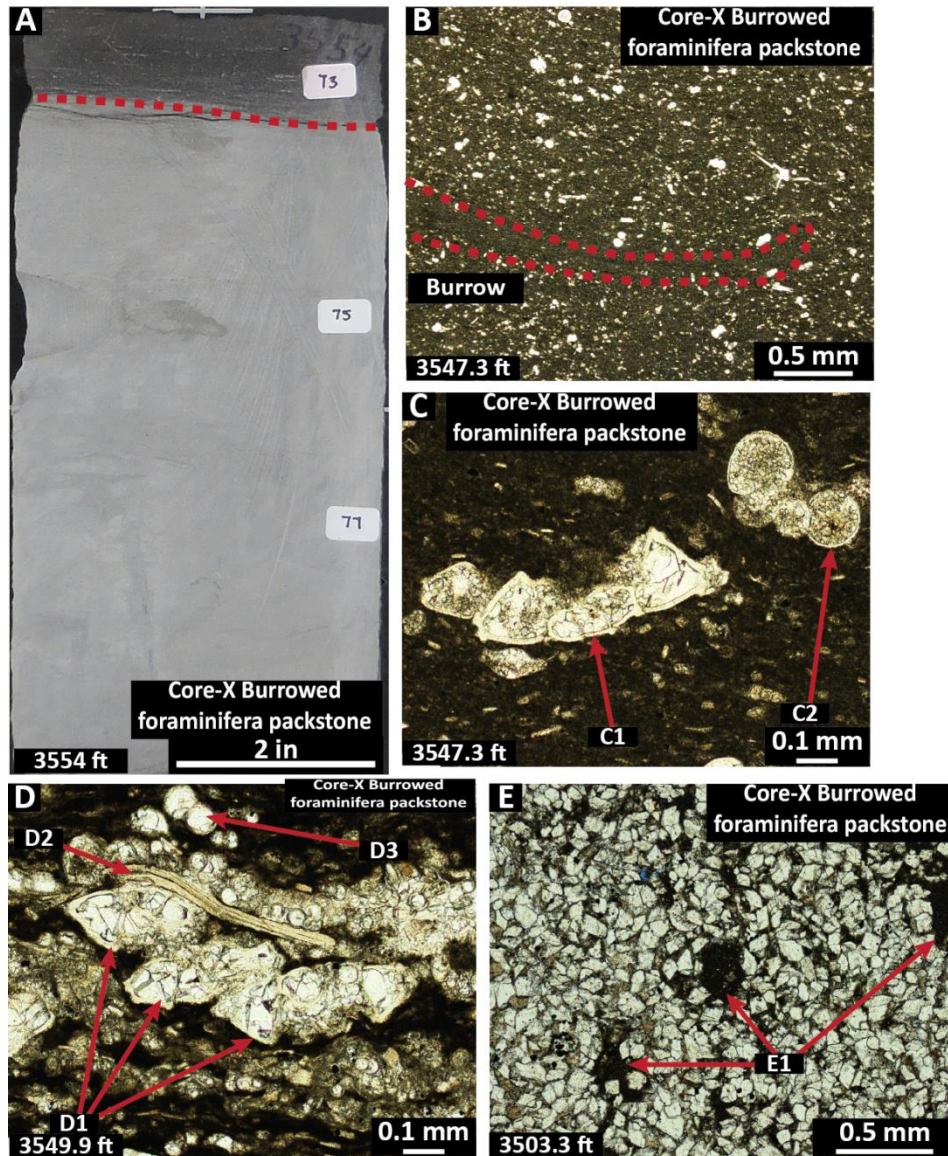


Figure 26: Burrowed foraminifera wackestone: A) Core slab with red line dividing burrowed zone and laminated zone in Austin Chalk. B) Burrow in unlaminated interval in Austin Chalk. C) Keeled (C1 *Marginotruncana* (poss.) sp.) and globular (C2 *Whiteinella* (poss.) sp.) planktonic foraminifera in burrowed interval in Austin Chalk. D) Imbricated keeled planktonic foraminifera *Marginotruncana* (poss.) sp. (D1), oyster fragment (D2), and globular foraminifera (D3) in grain lamination in Austin Chalk. E) Abundant dolomitization and unaltered peloids (E1) in Austin Chalk.

Laminated skeletal packstone-grainstone

This facies is found in outcrop at the Hot Springs locality. It is documented within the lowest Ernst Member of the Boquillas Formation above the contact with the Buda Limestone. It is accompanied by thin beds of peloidal crystalline mudrock (Fig. 27A).

The laminated skeletal packstone-grainstone facies consists of discrete grain-supported, allochem laminations and mud laminations (Fig. 27A). The average mineralogy consists of 52% carbonate, 7% quartz, and 17% clay minerals. The average mineralogy for this lithofacies will likely differ from similar facies documented in the subsurface because all samples for this facies have been exposed to surface conditions. This facies is exclusively documented in outcrop. Mud laminations are richer in argillaceous material but still have a dominant calcite signature. Beds are centimeter scale and are never thicker than fifteen centimeters. Alternating laminations are discrete. Grain laminations are interbedded and do not contain mud-size particles or matrix within primary pore space (Fig. 27B). Fauna within grain laminations are dominantly planktonic foraminifera mixed with inoceramid prisms and fish bones (Fig. 27C). Mud laminations contain radiolarians (Fig. 27D). Laminations are generally planar and continuous.

Soft-sediment deformation on lamination to bed-scale is abundant within laminated skeletal packstone-grainstone (Fig. 27E). Laminations have been deformed but remain coherent. Grain laminations are reworked into ripples and show scour along bed forms.

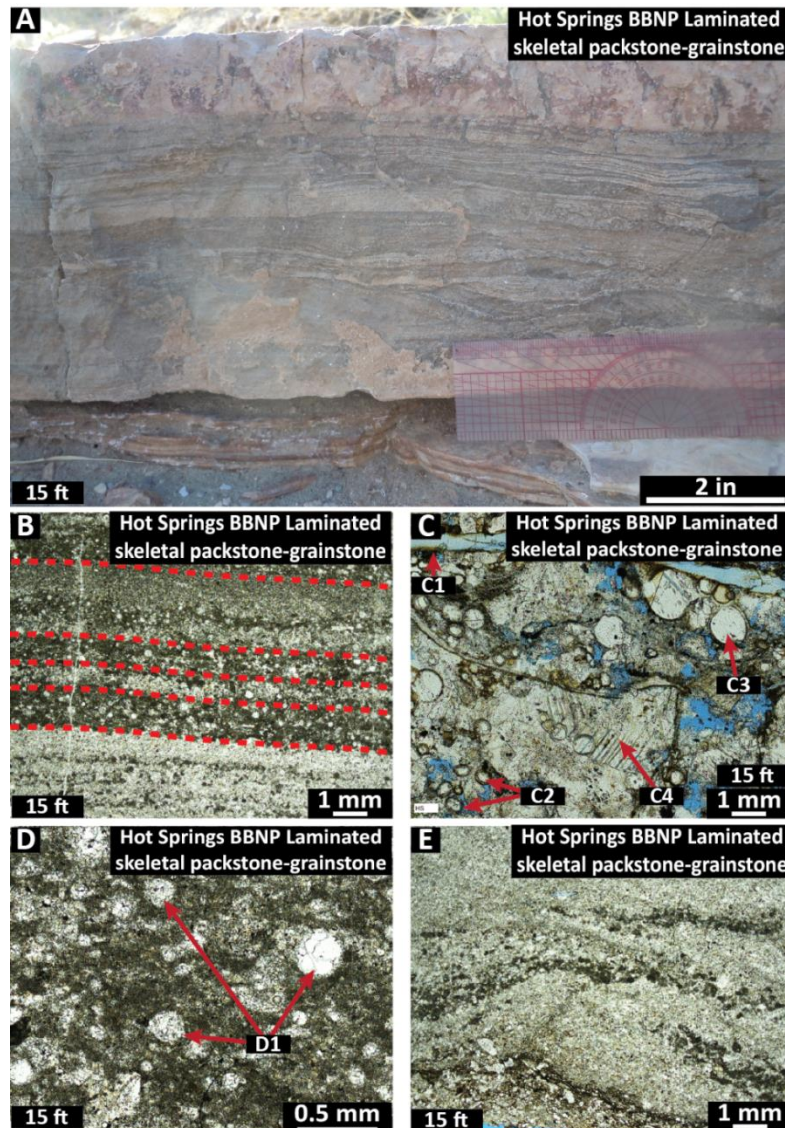


Figure 27: Laminated skeletal packstone-grainstone: A) Outcrop photo of laminated skeletal packstone-grainstone with white grain laminations and brown carbonate mud laminations in lower Boquillas strata. B) Photomicrograph of laminated skeletal packstone-grainstone in lower Boquillas strata. C) Photomicrograph of grain lamination with relic fish bones (C1), calcispheres (C2), globular planktonic foraminifera (C3), and an echinoderm with calcite overgrowth (C4) in lower Boquillas strata. D) Photomicrograph of carbonate mud lamination with matrix-supported radiolarians (D1) in lower Boquillas strata. E) Photomicrograph of deformed grain and mud laminations from water escape in lower Boquillas strata.

Volcanic ash

Volcanic ash deposits are found in both outcrop and core. Outcrop samples from the Hot Springs outcrop section are recessive and fissile, and are identifiable by weathering character and distinct yellow, orange, or red colors. Volcanic ash at the Hot Springs outcrop section is dominantly found within the Ernst Member of the Boquillas Formation. Volcanic ash is observed in both Core-X and Winterbotham J.M. Jr. #1 cores. Yellowish ashes are friable and are associated with secondary pyrite. Beds are observed throughout the Eagle Ford Group.

Volcanic ash (Fig. 28A) deposits occur as discrete beds or mixed with surrounding marine lithofacies. The average mineralogy is 5% carbonate, 4% quartz, and 52% clay. Clay mineral composition is dominated by illite with lesser amounts of montmorillinite and kaolinite. This is different from Pierce (2014); however, samples used in said study were from outcrop deposits and may not be correlative to subsurface mineralogy because of instability of minerals under surface weathering conditions. Discrete ash deposits range in thickness from submillimeter to 25 centimeters. Volcanic ash most commonly forms discrete beds with a sharp basal contact and are friable (Fig. 28A). Phenocrysts at the base of volcanic ashes are generally unsorted and unoriented (Fig. 28B); grains within the ash become aligned parallel to bedding throughout the deposit. Phenocrysts within the ash beds vary in abundance. Light microscopy reveals that phenocrysts of anhedral flakes of a clay mineral are the most common grain variety, closely followed by angular beta quartz (Figs. 28C, 28D). Zircon and apatite can sometimes be identified in thin-section. The ash matrix is aphanitic and composed of dominantly clay minerals (Fig. 28B). Unaltered clay mineral matrix goes to extinction in cross-polarized light. Diagenesis of some ash beds has produced irregular, patchy calcite within the clay matrix (Fig. 28D).

Volcanic ash is mixed within the matrix of mudrock samples. Small grains of beta quartz stand out as heterogeneities within the dark brown matrix. Examination with ultraviolet light and a yellow filter allows for the ash matrix to be distinguished from individual peloids (Fig. 28E). Ash-rich matrix (as well as discrete beds) fluoresces bright yellow-green when viewed under ultraviolet light.

Because of the thicknesses and frequency of ash beds, deposits have been recorded stratigraphically in two ways. Beds thicker than 2 mm were documented as individual deposits within the stratigraphic log (Figs. 35, 36, 38). Thin ash beds less than 2 mm in thickness were not documented individually on the stratigraphic log because of the scale of documentation on the log. All volcanic ash beds (both greater and less than 2 mm) were counted by depth and recorded graphically in the form of a histogram for subsurface sections (Figs. 36, 38). The histogram displays individual ash bed occurrence against depth to graphically display the frequency of ash beds and the relative distribution of volcanic ash throughout the cored intervals.

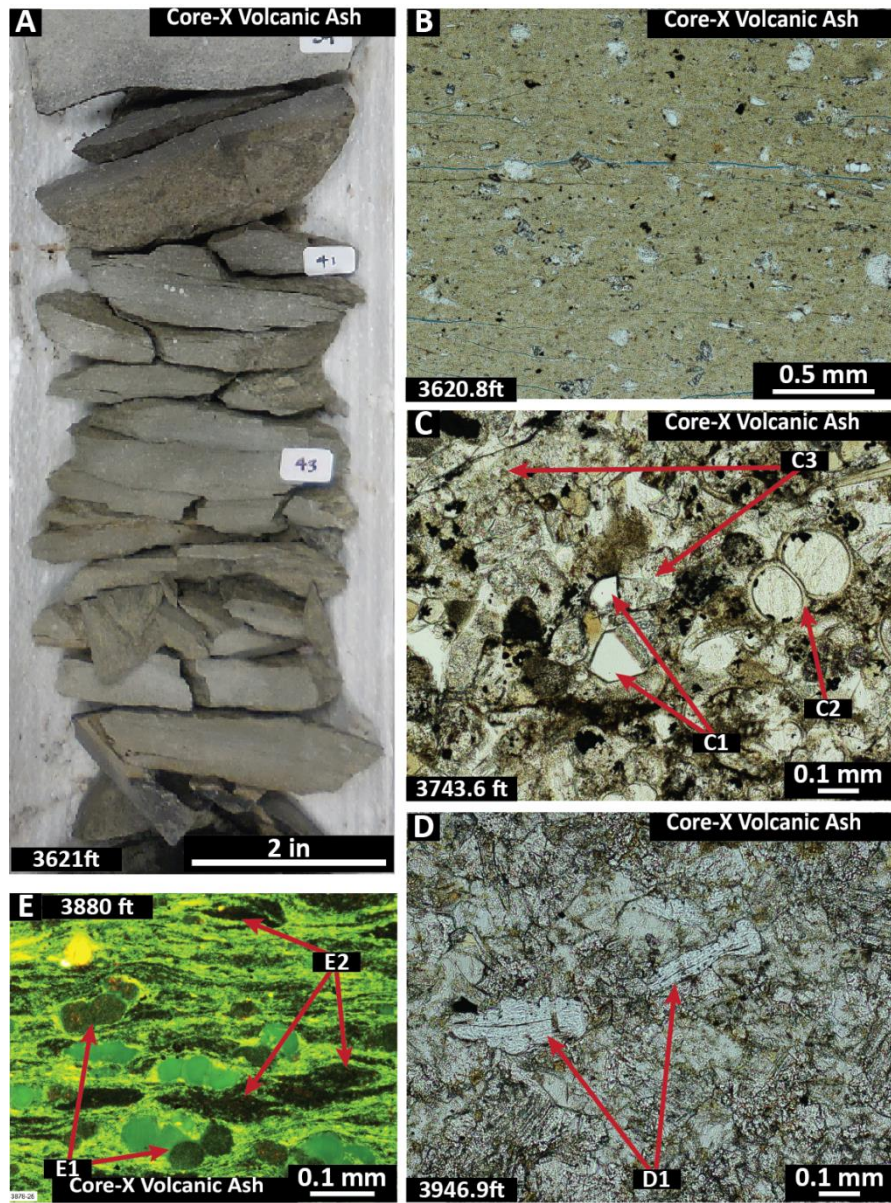


Figure 28: Volcanic ash: A) Outcrop slab of volcanic ash is grey-yellow and fissile in Eagle Ford strata. B) Photomicrograph has pale yellow clay matrix with various phenocrysts in Eagle Ford strata. C) Photomicrograph with beta quartz (C1), globular planktonic foraminifera (C2), and inoceramid prisms (C3) in ash in Eagle Ford strata. D) Phyllosilicate grain within calcitized ash matrix in Eagle Ford strata. E) UV + yellow filter photomicrograph of globular planktonic foraminifera (E1) and peloids (E2) in fluorescing ash matrix in Eagle Ford strata.

Massive limestone

Heterogeneity of indurated outcrop beds observed in thin-section has shown that while beds may have a similar outcrop profile, matrix and faunal assemblage differ on a fine scale that cannot be explicitly defined using weathering characteristics. This pseudolithofacies exclusively pertains to outcrop beds that were not sampled for thin-sections.

Massive limestone is defined as nonrecessive, calcite dominant beds observed in Big Bend National Park (Fig. 29A). Massive limestone is well cemented and withstands erosion. Beds vary in thickness (foot scale) and geometry. Indurated beds are planar, tabular, or discontinuous. Discontinuous indurated beds occur along the same bedding plane as irregular, lensoid deposits (Fig. 29B). There are sometimes grain laminations contained within indurated beds, but such laminations are contained within the base of bed.

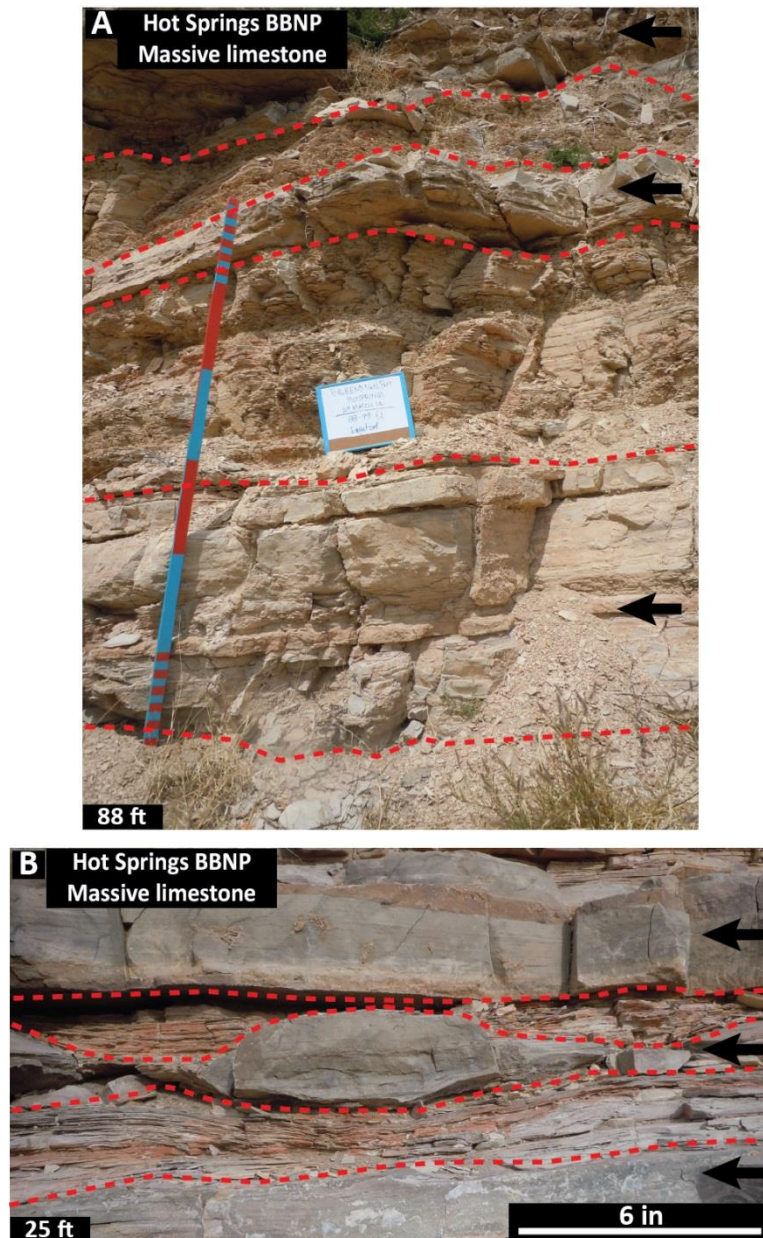


Figure 29: Massive limestone pseudolithofacies: Black arrows show massive limestone beds. A) Outcrop photo in the upper Ernst Member of plane-bedded indurated limestone outlined in red, color alternations on staff equal 1 ft. B) Outcrop photo in the lower Ernst Member of planar and lenticular laminated limestone interbedded with recessive argillaceous mudrock.

Recessive argillaceous mudrock

This pseudolithofacies represents unsampled, recessive outcrop beds in Big Bend National Park. Heterogeneity observed in sampled intervals (thin-section analyses) reveals that unsampled beds (those not observed in thin-section) cannot be grouped into specific lithofacies by outcrop appearance and relative weathering.

Recessive argillaceous mudrock is defined as any poorly cemented section at the Hot Springs locality in Big Bend National Park (Fig. 30A). Recessive beds are fissile and break into small chips along bedding planes, suggesting moderate clay mineral content. Considering high carbonate content in other lithofacies, it is likely that the recessive argillaceous mudrock pseudolithofacies are composed of carbonate-dominated mud with moderate amounts of argillaceous material. Deposits are soft and easily eroded. Deposits may be considered laminated because of fissile parting of the recessive units along bedding planes.

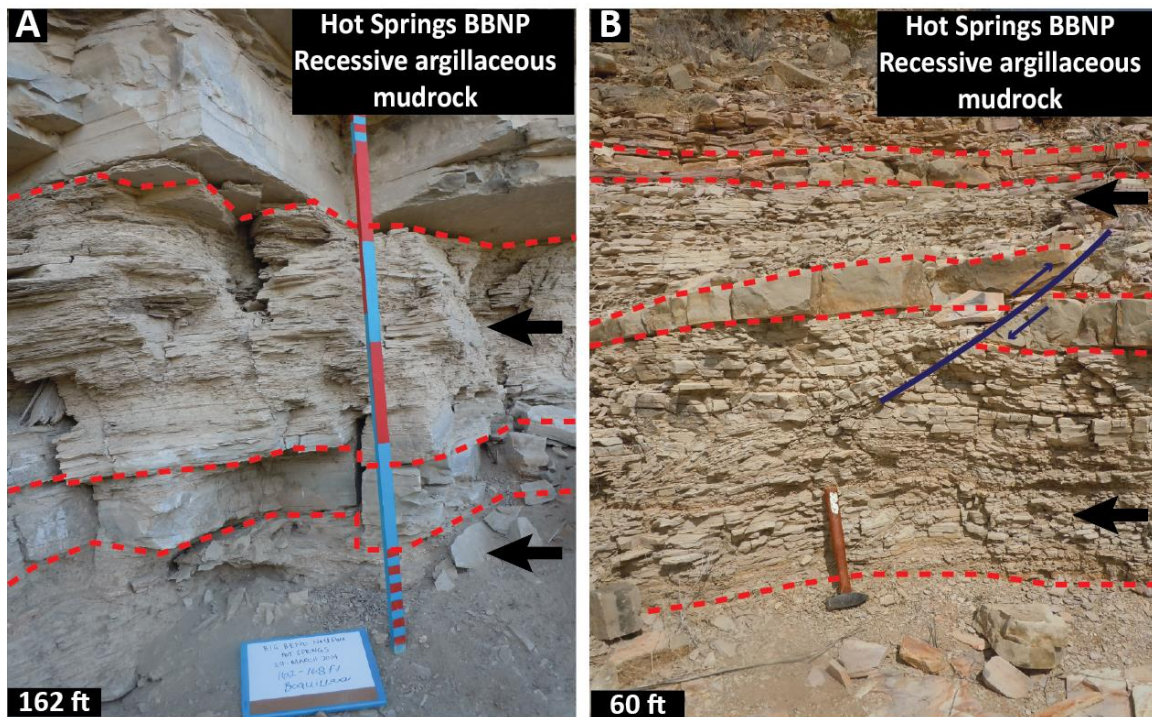


Figure 30: Recessive argillaceous mudrock pseudolithofacies: Black arrow highlights recessive argillaceous mudrock beds. A) Outcrop photo of alternating recessive marl and massive limestone in upper Boquillas Member, staff equals 6ft. B) Outcrop photo of recessive argillaceous mudrock with small thrust fault in lower Boquillas Member.

Peloidal crystalline mudrock

Peloidal crystalline mudrock is a robust, completely crystalline diagenetic facies documented in both outcrop and core (Figs. 31, 32). This facies is documented throughout the Eagle Ford and Boquillas Formation, with highest abundances lower in the sections (lower Eagle Ford and Ernst Member strata). The thick bedded peloidal crystalline mudrock facies observed in outcrop show evidence that the primary depositional fabrics have been erased by pervasive subhedral calcite spar. Beds may have different appearances in outcrop and weathering expression (Figs. 31A, 31B), but can be identified as similar in thin-section. Fauna are rare to common, and are dominated by radiolarians (Fig. 31C). Planktonic foraminifera are present but are not common (Fig.

31D). Peloids present within peloidal crystalline mudrock are not recrystallized (Fig. 31C). Original mud matrix in this facies was likely carbonaceous.

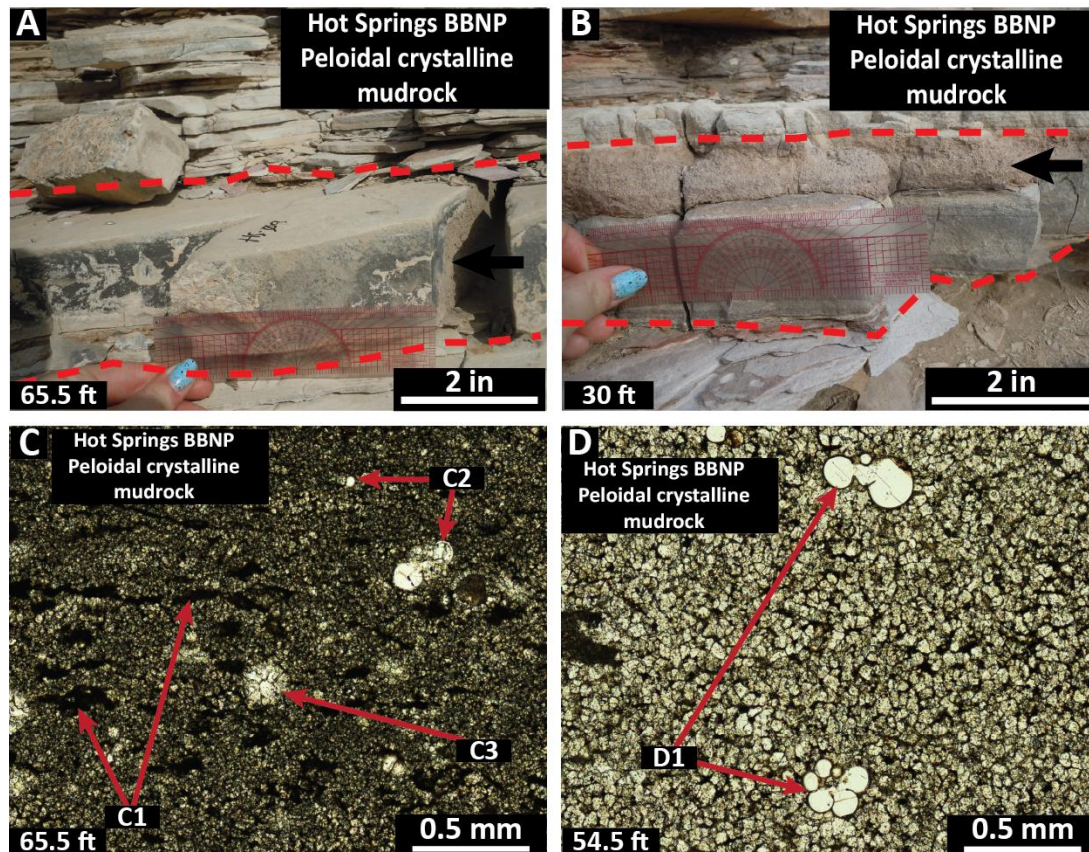


Figure 31: Peloidal crystalline mudrock: A and B) Peloidal crystalline mudrock in lower Boquillas strata as it appears in discrete beds at outcrop. Beds can have different outward appearance but look comparable when observed in thin-section. C) Small interlocking calcite crystals within the matrix with recrystallized radiolarians, planktonic foraminifera, and unaltered peloids in lower Boquillas strata. D) Hedbergellid planktonic foraminifera within secondary calcite crystals in lower Boquillas strata.

Peloidal crystalline mudrock observed in core is present within several different defined lithofacies including laminated argillaceous planktonic foraminifera mudrock, laminated argillaceous inoceramid wackestone, weakly laminated wackestone, massive

argillaceous claystone, laminated calcisphere grainstone, burrowed foraminifera wackestone, and laminated skeletal packstone-grainstone (Fig. 32A). In core slab, peloidal crystalline mudrock is a fuzzy, light grey color and overprints primary sedimentary laminations. Peloidal crystalline mudrock is defined by authigenic calcite growth within argillaceous matrix (Fig. 32B) and commonly contains subvertical ductile deformation or folded fractures cemented with equant calcite spar. Relic laminations can be seen in some cases but are faint. Peloidal crystalline mudrock beds generally have a sharp basal contact that parallels bedding. Authigenic calcite growth that creates the peloidal crystalline mudrock facies shows crystallization within the matrix and commonly avoids peloids (Fig. 32C). Calcite crystals are not euhedral and create a patchy, interlocking network within the matrix. Peloidal crystalline mudrock intervals commonly contain abundant, calcitized radiolarians (Fig. 32B). In some samples, radiolarians were first pyritized and later calcitized (defined by crosscutting relationships; Fig. 32C). Sometimes planktonic foraminifera are found within diagenetic calcite intervals, but are rare.

Timing of the diagenetic calcite is relatively early within the compactional history of the system. Laminations overprinted by diagenetic limestone are thicker and far less compacted as compared to laminations outside of a diagenetic calcite zone.

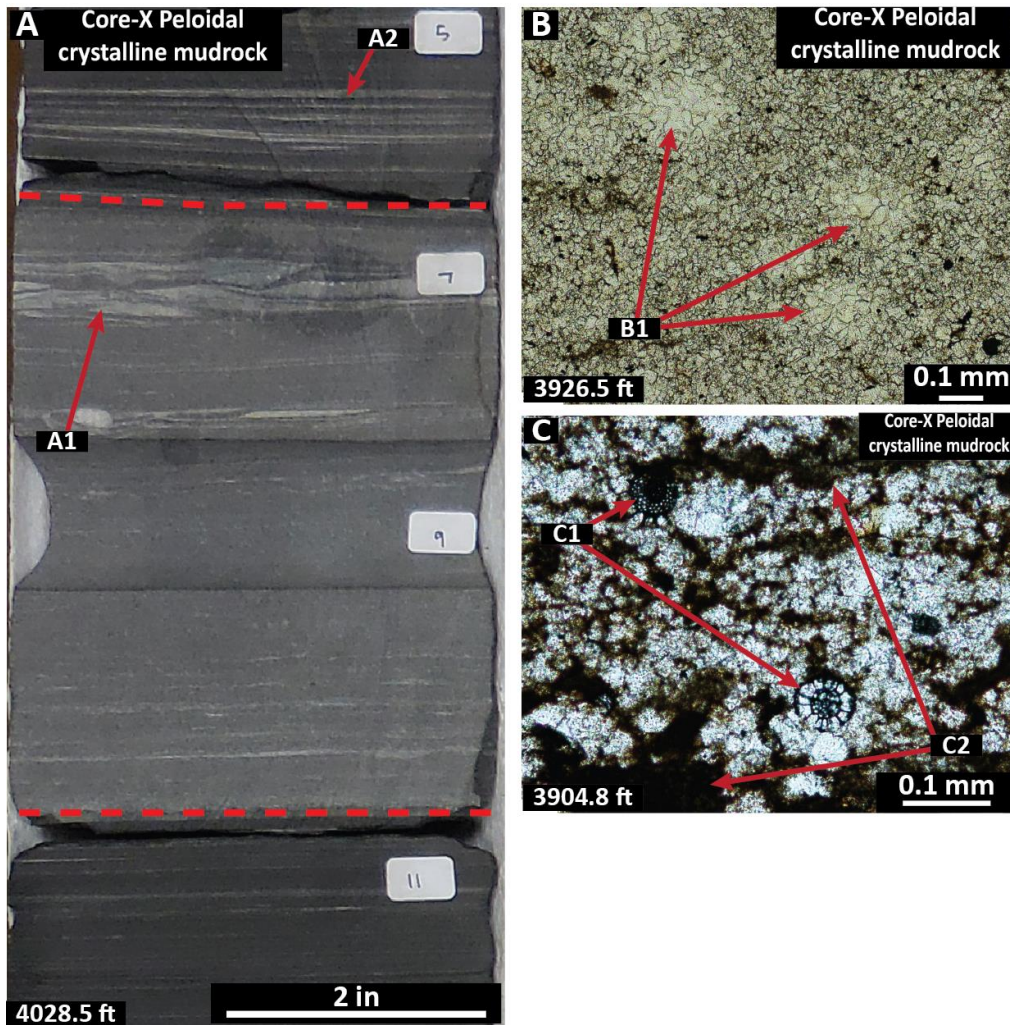


Figure 32: Peloidal crystalline mudrock in core: A) Core slab in lower Eagle Ford strata of diagenetic calcite has sharp base and gradational top. Laminations in peloidal crystalline mudrock (A1) are less compacted than compacted lamina (A2). B) Pervasive crystallization of matrix and radiolarians (B1) in lower Eagle Ford strata. C) Pyritized radiolarians (C1) and peloids (C2) within diagenetic calcite crystals in lower Eagle Ford strata.

FACIES SUCCESSIONS

Facies successions have been logged and compiled for each individual location (see Fig. 3). Lithostratigraphies included in this section integrate visual and

chemostratigraphic data with gamma ray data from borehole and handheld devices. Two-dimensional (2D) facies profiles have been created showing the succession as logged per core or outcrop section, with proposed stratigraphic divisions. Expanded outcrop and core stratigraphies can be viewed in Appendix A. Figure 33 contains a legend to lithofacies colors and symbols that are presented in the following section.

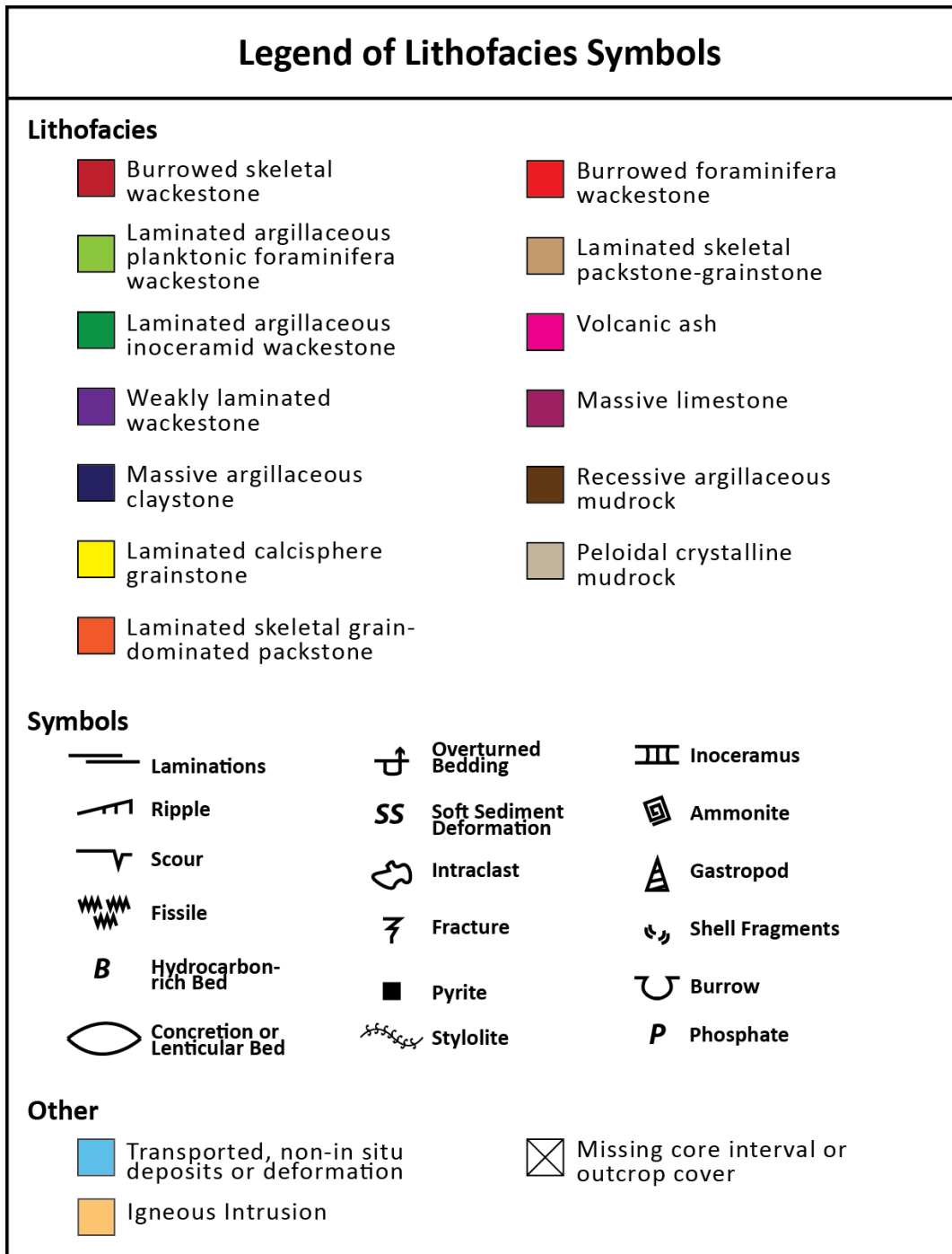


Figure 33: Legend for stratigraphic sections included within this chapter and within the appendix.

Hot Springs Outcrop

Figure 34 contains outcrop photos that pertain to elements discussed in the drafted lithostratigraphy. Figure 35 contains handheld gamma-spectrometer and facies profiles for the Hot Springs locality in Big Bend National Park (Figs. 3, 6). The measured section is dominated by alternating recessive and robust beds with interbedded volcanic ash deposits. The gamma ray data displays high-frequency fluctuations in amplitude because of high-frequency alternations between clay-mineral-rich mudrocks (high gamma) and calcite-dominated limestone (lower gamma).

The mapped section at the Hot Springs locality within Big Bend National Park begins with the uppermost Buda Limestone as it outcrops along the Rio Grande north river bank. The following Boquillas Formation was mapped following the river and moving upward in the section along dip.

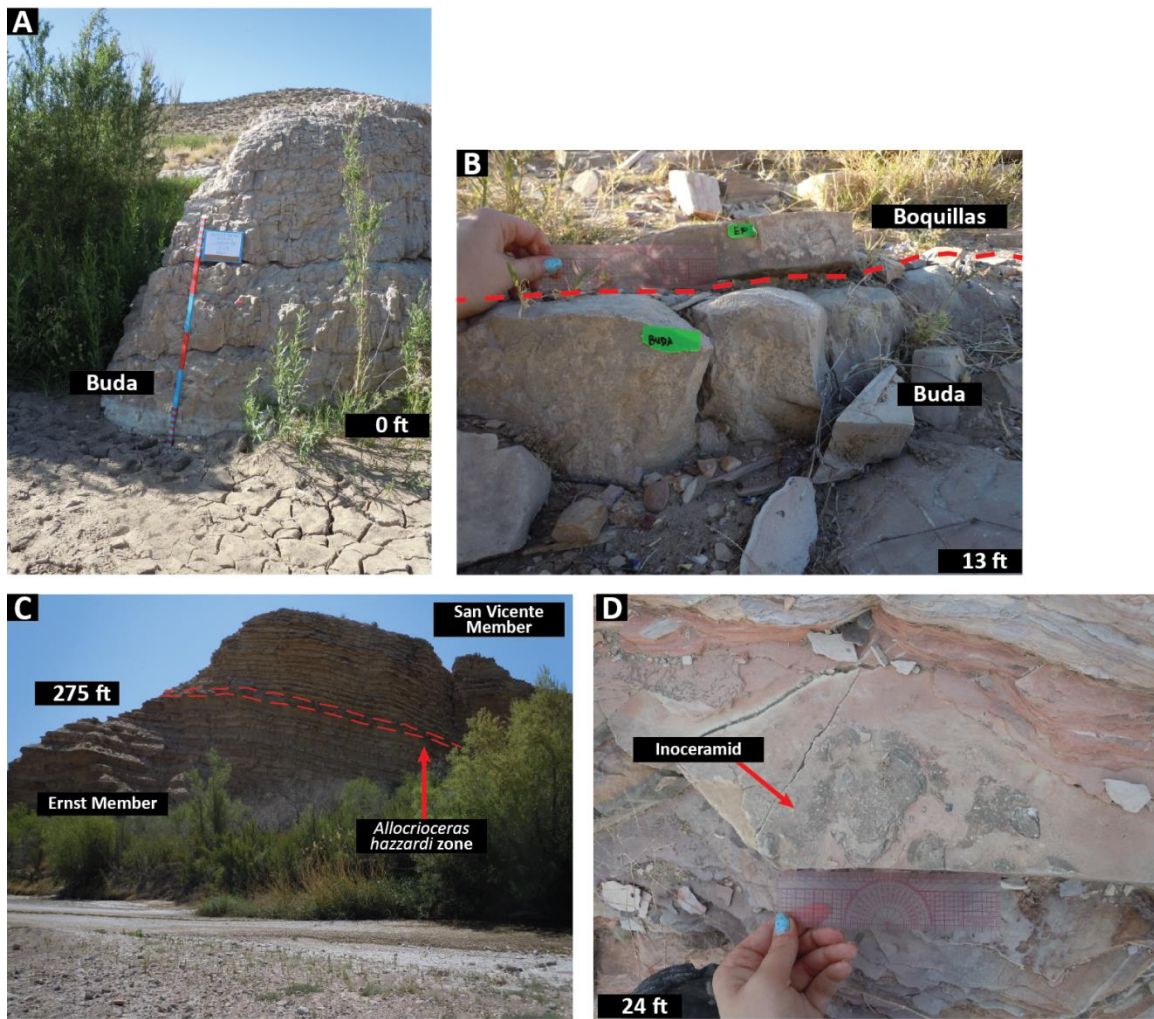


Figure 34: Outcrop photos from the Hot Springs locality in Big Bend National Park. A) Base of measured section with the Buda Limestone (burrowed skeletal wackestone, 0 ft) outcropping in the Rio Grande river bed. B) Boquillas Formation as it appears in outcrop (13 ft). Contact between the Buda (lower bed, burrowed skeletal wackestone) and Ernst Member of the Boquillas Formation (upper bed, laminated skeletal packstone-grainstone). C) Contact between the Ernst and San Vicente Members of the Boquillas Formation (275 ft) marked by the *Allocrioceras hazzardi* zone outlined in red (note cyclicity of massive limestone and recessive argillaceous mudrock). D) Large in situ inoceramid in the Ernst Member of the Boquillas Formation on the bedding plane of laminated skeletal packstone-grainstone (24 ft).

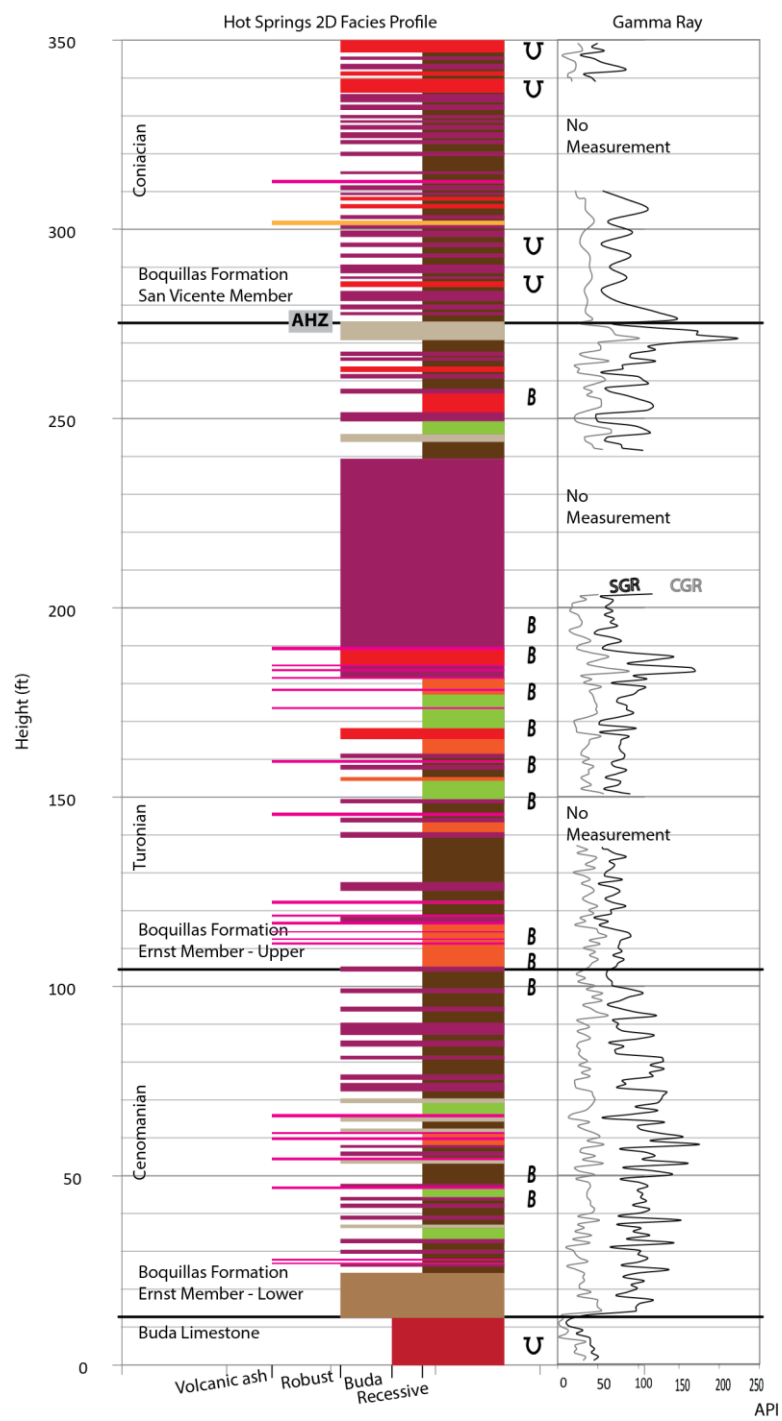


Figure 35: Hot Springs outcrops, Big Bend National Park lithostratigraphy. Color blocks refer to facies defined in Fig. 33.

The basal 13 feet is the Buda Limestone (Fig. 34A). At 13 feet, the Buda Limestone unconformably underlies the Ernst Member of the Boquillas Formation. The top of the Buda Limestone is composed of one lithofacies, burrowed skeletal wackestone. The basal Ernst Member is composed of thin-bedded, laminated skeletal packstone-grainstone. The contact between the two units is abrupt. This observation agrees with the gamma ray data; the change from the Buda Limestone to the Ernst Member of the Boquillas Formation is marked by an abrupt increase in gamma ray response (Fig. 35). This abrupt shift is confirmed in outcrop by the abrupt contact and facies change from the Buda Limestone to the Boquillas Formation (Fig. 34B). This change is also documented by the shift in outcrop profile from Buda (Fig. 34A) to Boquillas (Fig. 34C). The Buda Limestone is a mottled, relatively massive limestone while the Boquillas is flaggy, well-bedded, and regularly alternates between massive limestone and recessive argillaceous mudrock.

A prominent inoceramid pavement is located at 27 ft (Fig. 35) from the base of the section (Fig. 34D). Inoceramid are in-situ, intact and range from several millimeters thick and up to thirty centimeters in diameter. The deposit is planar and continuous across the exposed inoceramid pavement.

An interval from 75-110 ft (Fig. 35) represents a section of relatively few ash deposits as compared to the lower Ernst Member. The gamma ray gradually decreases through this interval.

At 168 ft (Fig. 35), the first petrographic observation of burrowed foraminifera wackestone is documented. This example of the facies at this depth is unbedded. This observation serves as the lower-most observation of the burrowed foraminifera wackestone facies that is generally associated with Austin Chalk deposition within the Maverick Basin.

The interval from 220-240 ft (Fig. 35) coincides with an area where the outcrop was inaccessible for a comprehensive description or collection of gamma ray data. The undefined section is dominated by a relatively uniform section of massive limestone.

The *Allocrioceras hazzardi* zone as defined by Cooper and Cooper (2014) correlates to 271-276 ft (Fig. 35). This boundary is composed of 4 lenticular peloidal crystalline mudrock beds in a recessive argillaceous mudrock (Fig. 34C) – these lenticular bodies correlate to the iron-stained beds discussed by Cooper (2014). This 5 ft-thick marker zone represents the contact between the Ernst and San Vicente Members of the Boquillas Formation, as well as the stage boundary between the Turonian and Coniacian. Gamma ray values in the AHZ are far higher than beds below or above.

At 302 ft (Fig. 35), a planar igneous intrusion is documented parallel to bedding. The intrusion does not appear to greatly deform or alter surrounding sedimentary beds. No contact metamorphism is documented. The igneous intrusion may, however, display quenched margins.

Interpretation

Buda Limestone

The Buda Limestone is composed of burrowed skeletal wackestone. Petrographic analysis shows that burrowing is pervasive and all original sedimentary fabric and depositional structures have been obscured. Low gamma ray API values indicate the lack of clay minerals within the matrix of the Buda Limestone. Fauna present (gastropods, echinoids, planktonic foraminifera) indicate a habitable, normal marine, drowned shelfal environment. Stacking in the Buda Limestone shows massive-bedded limestone units (burrowed skeletal wackestone) with thin parting layers between beds. Parting layers are recessive and cannot be sampled, and are likely composed of clay minerals and represent a possible flooding surface.

The contact between the Buda Limestone and the Boquillas Formation is abrupt (Figs. 34B, 35). Lithofacies on both sides of the contact have different sedimentary structures, fauna, composition, and gamma ray values. Because of the substantial heterogeneity between the two formations, this contact is interpreted as an unconformity.

Boquillas Formation

The Ernst Member of the Boquillas Formation is composed of cyclic beds consisting of indurated (calcite) and recessive (argillaceous) mudrocks (Fig. 34C). Several facies appear within the Ernst Member: laminated skeletal packstone-grainstone, laminated argillaceous planktonic foraminifera wackestone, mud-laminated skeletal planktonic foraminifera grain-dominated packstone, burrowed foraminifera wackestone, and peloidal crystalline mudrock. The recessive argillaceous mudrock beds are thicker (several feet) than the indurated massive limestone beds (approximately one foot). The massive limestone beds show preferential diagenesis (recognized in thin section as peloidal crystalline mudrock). These beds may represent cemented primary depositional fabrics such as ripples or dunes. Changes in pseudolithofacies may indicate cementation of primary sedimentary fabrics rather than sequence tops.

Laminated skeletal packstone-grainstone crops out within the lowest Ernst Member (Fig. 35) – exhibiting cyclic laminations varying between winnowed grain laminations and carbonate-dominated with some argillaceous material within mud laminations. Soft-sediment deformation (dewatering structures or flame structures) on a lamination-scale infers rapid deposition of sediments that exceeded the rate of lithification, compaction, and dewatering (Fig. 27). This succession is thin-bedded and does not follow the same indurated-recessive lithofacies motif observed in the rest of the

Ernst Member. Laminated skeletal packstone-grainstone stops abruptly after the appearance of the inoceramid pavement (Fig. 34D).

Laminated argillaceous planktonic foraminifera wackestone is recessive in outcrop and contains thin grain laminations when observed in thin-section (Fig. 21). Fauna in this facies show evidence of reworking into thin, starved ripples. Lack of burrowing in sediments suggests that sediments were not habitable. Grain quantity is far lower than matrix within this lithofacies, implying either low grain accumulation rates or high peloid and detrital matrix accumulation rates.

Laminated skeletal grain-dominated packstone contains a more diverse preserved fauna and higher quantity of fauna present. This lithofacies is most likely composed of discrete gravity-flows and high energy reworking events because of complete winnowing of clay-size material in grain layers. The appearance of this lithofacies coincides with a gradational decrease in gamma ray values and an increase in faunal abundance and variety (Figs. 25, 35). This documented decrease in gamma ray API confirms winnowing of clay minerals within this facies and section.

Burrowed foraminifera wackestone documented in the upper Ernst Member signifies the transitional change to a more habitable depositional environment (Figs. 26, 35) from the increase in burrowing. Laminated skeletal packstone-grainstone, laminated argillaceous planktonic foraminifera wackestone, and mud-laminated skeletal planktonic grain-dominated packstone are either not burrowed, or contain rare, short-lived, lamination scale burrowing episodes. Burrowed calcisphere packstone is burrowed and contains few preserved primary sedimentary structures. Lack of burrowing in underlying sediments suggests that sufficient oxygen or nutrients may not have been present, whereas pervasive burrowing in the burrowed foraminifera wackestone shows that both oxygen and nutrients were available to sustain a habitable environment.

Peloidal crystalline mudrock documented in the Ernst Member is concluded to be a result of pervasive diagenesis of the original rock matrix (Fig. 31). While this facies has been interpreted as an *Inoceramite* (inoceramid fragment-dominated rock, Sanders, 1988), relic laminations and 180°, 3-way interlocking calcite crystals imply that the fabric is diagenetic (Fig. 31).

The dominant facies documented within the Ernst Member are well bedded and well laminated. Fauna are commonly reworked into thin, starved ripples and are undisturbed by burrowing. Above 150ft (Fig. 35), burrowing appears within the Ernst Member showing a gradational change into the San Vicente Member above.

The contact between Turonian and Coniacian age strata defined by the appearance of the AHZ zone (Figs. 34C, 35) is coincident with an abrupt spike in gamma ray API values. Gamma ray values in the Coniacian-age, San Vicente Member have a lower base line than the underlying Ernst Member. This contact is defined biostratigraphically by the appearance of the *Allocrioceras hazzardi* by Cooper (2014). The ratio of indurated massive limestone and recessive argillaceous mudrock changes into the Coniacian section. The ratio essentially switches from that observed in the underlying Ernst Member: massive limestone and burrowed calcisphere packstone has units several feet thick, and thinner recessive argillaceous mudrock beds (approximately 4:1 ratio). This change to dominant massive limestone beds, as well as the presence of burrowed calcisphere packstone, suggests that the Coniacian represents a time of better nutrient and oxygen availability in an environment capable of supporting life.

The San Vicente Member is composed of thick to massive-bedded cycles of indurated and recessive limestone (massive limestone) and marl beds (recessive argillaceous mudrock; Fig. 35). The lithofacies present within the San Vicente Member is

burrowed calcisphere packstone. Burrowing is generally pervasive, implying an environment with habitable bottom-water sediments.

The Cenomanian-Coniacian section (Fig. 4) documented at the Hot Springs outcrop section demonstrates a variable depositional environment. The Buda Limestone represents a time where sediments were oxygenated and habitable based on burrowing and fauna documented in petrographic analyses completed for this study. The Ernst Member is deposited unconformably onto the Buda Limestone. Deposition in the lower ~140 ft of the Ernst Member is dominated by reworked grain accumulations and peloids as shown laminated argillaceous planktonic foraminifera wackestone and recessive argillaceous mudrock. Pristine preservation of laminations, primary sedimentary structures, and lack of burrows imply that sediments were not oxygenated but anaerobic or dysaerobic. Above 150 ft in the Ernst Member of the Boquillas Formation, burrowing is present, showing increased habitability and oxygenation at the sea floor. A gradational transition from the Turonian to Coniacian strata at the contact between the Ernst and San Vicente Members (Cooper, 2014) demonstrates the interplay of habitable (burrowed) and uninhabitable sediments. Sediments in the Coniacian are burrowed and contained enough oxygen to sustain life. Alternations between indurated and recessive facies within the succession likely represent the impact of detrital argillaceous sedimentation and dilution by carbonate sedimentation. The change from well-laminated sediments in the Ernst Member to burrowed sediments in the San Vicente Member is linked to a change in oxygen and nutrient availability, and possible circulation or upwelling patterns (rather than a sea level change).

Core-X Conventional Core

Figure 36 shows gamma ray data, lithofacies stratigraphy, and a histogram of volcanic ash abundance for Core-X. Volcanic ash is abundant within the Core-X core, containing 328 individual beds. Ashes thicker than 2 millimeters have been documented within the stratigraphic section. Volcanic ash deposits thinner than 2 millimeters have been documented within the ash abundance histogram (Fig. 36). Gamma ray data shows high-frequency variability because of lamination scale heterogeneity and has four different motifs: 1) 4,100-4,032 ft, 2) 4,032-3,845 ft, 3) 3,845-3,599 ft, 4) 3,599-3,498 ft. The Buda Limestone CGR and SGR trends show a low baseline with small, infrequent peaks. The lower Eagle Ford gamma ray data exhibits an abrupt shift to a new, increased baseline with very large jumps in API value. Gamma ray data (CGR and SGR) show a gradual decrease in API values at the contact between the upper Eagle Ford strata. The upper Eagle Ford strata exhibit a lower API baseline reading than the underlying lower Eagle Ford strata. CGR and SGR readings show high-frequency alternations in increase and decreased API with lower amplitude variability than displayed by the lower Eagle Ford strata. The Austin Chalk exhibits a baseline that is slightly lower than the underlying Eagle Ford Group. Increased amplitude in gamma ray signal correlates with thin clay-mineral-rich deposits of laminated argillaceous planktonic foraminifera wackestone.

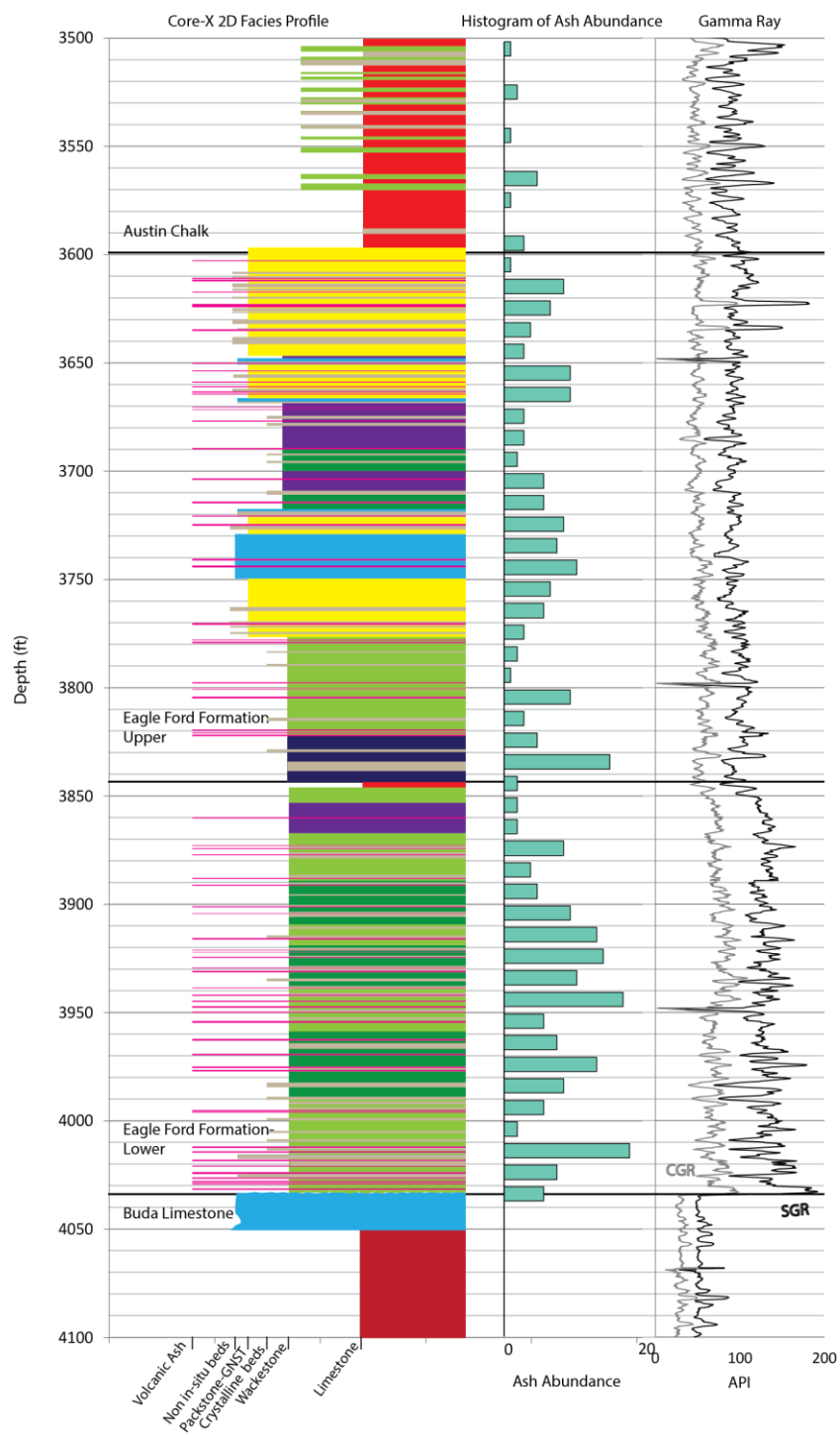


Figure 36: Core-X lithostratigraphy. A key to lithologies can be found in Fig. 33. Ash abundance histogram (center) represents number of ashes present per 10 ft bin. Gamma (right) is from downhole logs.

The Buda Limestone from 4,032.5-4,100 ft (Fig. 36) is burrowed and contains wispy, horsetail solution seams. Argillaceous solution seams correspond with increased gamma ray API (both CGR and SGR). Gamma ray values remain relatively low in the Buda Limestone, with an average reading of 54.46 API. There are no volcanic ash deposits within the Buda Limestone.

The upper 17.5 ft of the Buda Limestone, from 4,032.5-4,050 ft (Fig. 36), is composed of a prominent debris-flow. The debris-flow is composed of disrupted beds, as well as pebble- to cobble-sized soft-mud intraclasts. Table 7 details the debris-flow at the top of the Buda Limestone.

Thickness	Description
4,032.5- 4,033.5 feet	Massive grey-white limestone. Pebble-sized clasts and <i>Planolites</i> . Contact with overlying Eagle Ford is unconformable and stylolitized.
4,033.5- 4,038 feet	Breccia zone. Pebble- to cobble-sized, subround to subangular matrix supported limestone intraclasts. Compactional horsetail pressure solution seams form within matrix between clasts.
4,038- 4,044 feet	Matrix color is mottled brown and white. Brown matrix is more crystalline with common, subvertical calcite-spar filled pygmatic fractures. Rare burrow or clasts.
4,044- 4,048 feet	Dark grey-brown lime mudstone with pervasive to common horsetail solution seams. Argillaceous seams are densely clustered. Sharp-peak or seismogram stylolites are rare.
4,048- 4,050 feet	Clasts have irregular outer contacts have experienced some burrowing. Ductile lime mud matrix shows soft-sediment deformation and differential compaction.

Table 7: Description of debris-flow at the top of the Buda Limestone. The Buda Limestone is composed of burrowed skeletal wackestone; the debris flow described above is composed of brecciated clasts of the same facies.

The contact between the Buda Limestone and Eagle Ford Group (Fig. 37) occurs at 4,032.5ft. The contact is abrupt, jagged, and stylolitized with small, angular clasts of Buda Limestone in the basal Eagle Ford Group. Sediment fabrics shift from burrowed strata in the Buda Limestone to laminated and unburrowed strata in the Eagle Ford Group. The total gamma ray data shows abrupt increase defining the shift from Buda

Limestone (54 API) to Eagle Ford Group (191 API; Fig. 36). The transition from the Buda Limestone to the Eagle Ford Group also marks a change in discrete volcanic ash bed preservation; ash beds are abundant in the Eagle Ford Group, whereas they do not appear in the Buda Formation contained within this core (Fig. 36). While volcanic ash is not documented in the Buda Limestone, the lack of documented deposits does not necessarily mean volcanism did not occur during deposition, simply that discrete beds were not preserved (either from lack of accumulation, lack of volcanism, increased dilution, or homogenization of sediments from burrowing).

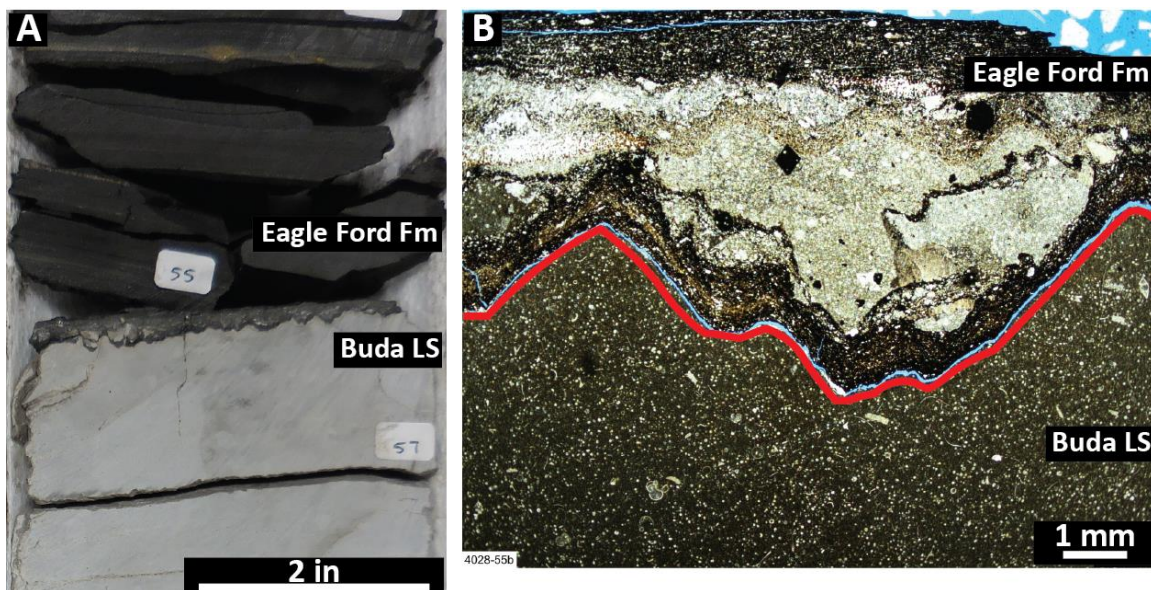


Figure 37: Contact between Buda Limestone and Eagle Ford Group at 4,032.5 ft. A) Core slab showing the stark color contrast between the Buda Limestone (burrowed skeletal wackestone) and Eagle Ford Group (laminated argillaceous planktonic foraminifera wackestone). B) Photomicrograph showing Buda Limestone lithoclasts within the Eagle Ford Group. The contact is outlined in red.

The interval from 3,973-3,979 ft (Fig. 36) contains the highest abundance of in-situ inoceramid shells within a shell pavement and transported inoceramid prisms.

Oysters also appear attached to the top of some in-situ inoceramid shells. Within the lower Eagle Ford there is an increase in clay mineral abundance captured in gamma ray API – CGR values gradually increase above 3,950 ft (Fig. 36).

The contact between lower and upper Eagle Ford occurs at 3,842.5 ft (Fig. 36). The contact is represented by a change in gamma ray response and coincides with the appearance of burrowed foraminifera wackestone. Gamma ray values decrease (Fig. 36) from the lower into the upper Eagle Ford, mirroring the decrease in clay mineral abundance in the upper Eagle Ford member. The interval of burrowed foraminifera wackestone from 3,842.5-3,844.5ft (Fig. 36) marks the lowest documented occurrence of fabric destructive burrowing within the Eagle Ford Group. Volcanic ash abundance below the burrowed foraminifera wackestone is much lower compared to the rest of the Eagle Ford Group (Fig. 36). The massive argillaceous claystone facies overlies the burrowed foraminifera wackestone. This is the single occurrence of this lithofacies in Core-X (Fig. 36). This lithofacies shift marks a change from burrowed to unburrowed rocks.

At a depth of 3,773 ft (Fig. 36) there is a pronounced change in fauna and sedimentary features. Grain laminations above this depth (shallower) are more abundant than mud laminations (carbonaceous or argillaceous), which have been the dominant lamination variety throughout the underlying Eagle Ford section. This change in lamination is documented in the facies changes from laminated argillaceous planktonic foraminifera wackestone (Fig. 20) and laminated argillaceous inoceramid wackestone (Fig. 21) to laminated calcisphere grainstone (Fig. 24). This is supported by the dominant facies shift from laminated argillaceous planktonic foraminifera wackestone and laminated argillaceous inoceramid wackestone to laminated calcisphere grainstone. Total gamma ray data in this section of the upper Eagle Ford (Fig. 36) show variation in

frequency, but have low-magnitude amplitude changes in API values – showing relatively consistent uranium, potassium, and thorium values and therefore consistent clay mineral content. Volcanic ash beds start to increase in abundance (Fig. 36).

An interval from 3,727-3,748 ft (Fig. 36) contains non-in-situ, transported beds that have experienced soft-sediment deformation. This interval contains pebble-size intraclasts as well as common, bed-scale folding of the laminated calcisphere grainstone facies (Fig. 24). The sediments were semi-coherent at the time of deformation; beds contain intact laminations that have been ductily deformed. Volcanic ash layers (Fig. 28) documented within this interval are bedded and contained within the folded and deformed units.

At 3,631 ft (Fig. 36), occurs the thickest volcanic ash deposit within the Eagle Ford Group in Core-X. The eight inch thick deposit is grey-yellow, friable, and parts easily along bedding planes. The deposit contains phenocrysts of beta quartz and phyllosilicate grains, as well as authigenic pyrite (Fig. 28). SGR and CGR data across the ash bed show increase values related to increase clay mineral volume increase.

At a depth of 3,599 ft (Fig. 36) marks the contact between the Eagle Ford Group and the overlying Austin Chalk. The gamma ray response shows a decrease in API values (Fig. 36). Lithofacies styles shift above 3,599 ft (Fig. 36) (shallower) to pervasive burrowing that has obliterated any primary depositional fabric. Lithofacies below 3,599 ft such as laminated argillaceous planktonic foraminifera wackestone (Fig. 20), laminated argillaceous inoceramid wackestone (Fig. 21), and laminated calcisphere grainstone (Fig. 24) are well laminated and contain well-preserved sedimentary features. Burrowed foraminifera wackestone (Fig. 26) above 3,599 ft (Fig. 36) contains fewer primary sedimentary features and fewer volcanic ash (Fig. 28) deposits.

Interpretation

Buda Limestone

The Buda Limestone is composed of burrowed skeletal wackestone (Fig. 19). Burrowing, abundant calcispheres and skeletal fragments, and lack of bedding features lead to the conclusion the depositional setting was that of an open-marine carbonate shelf. While pressure solution seams occur as a product of compaction, the density and thickness of solution seams in the Buda Limestone infer that there may be a lithologic change across these zones. It is proposed that stylolite seams represent phyllosilicate-rich sediment deposition within the Buda Limestone. These phyllosilicate deposition events may represent a storm deposit or a flooding surface. Pressure solution seams show preferential nucleation of authigenic minerals (Fig. 19). API values in the Buda are the lowest within the Core-X succession (Fig. 36); this is related to low redox sensitive uranium and low quantities of clay minerals.

The upper Buda Limestone is capped with a prominent mass-transport deposit composed of eroded intraclasts (Fig. 36, Table 7). Intraclasts are similar to the burrowed skeletal wackestone but containing fewer fauna. Intraclasts are subrounded to subangular with distinct, rounded edges. These observations suggest that clasts may have been semi-lithified, or soft rather than brittle during the high-energy mass-transport deposit.

The contact between the Buda Limestone and Eagle Ford Group represents a prominent unconformity (Fig. 36, 37) because of the change in facies type, mineralogy, oxygen-level, stylolitization, abruptness of the change, and bioturbation. Lithofacies shift from bioturbated (burrowed skeletal wackestone; Fig. 19) in the Buda Limestone to laminated carbonate-dominated mudstones such as laminated argillaceous planktonic foraminifera wackestone (Fig. 20), laminated argillaceous inoceramid wackestone (Fig. 21), massive argillaceous claystone (Fig. 23), and laminated calcisphere grainstone (Fig.

24) in the Eagle Ford Group. These facies changes show the change from a habitable, oxygen-rich environment to an oxygen-poor environment because sediments were not habitable (Fig. 14). The abrupt increase in gamma ray values agrees with the abrupt increase in clay mineral volume and uranium volume (Fig. 36).

Eagle Ford Group

The lower Eagle Ford strata are dominated by alternating laminated argillaceous planktonic foraminifera wackestone and laminated argillaceous inoceramid wackestone (Figs. 20, 21, 36). While the dominant fauna in these facies differ between planktonic foraminifera and inoceramids, sedimentary structures, mineralogy, and grain abundance remain similar. Laminations are composed of lags and winnowed ripples composed of fauna, indicating that there were active bottom-current reworking fauna. Alternation between grain laminations and argillaceous mud laminations suggests cyclic processes in deposition or change in current speed that allowed or disallowed the deposition of mud-size particles (Schieber et al., 2013). Lack of burrowing suggests that sediments were uninhabitable. Appearance of in-situ, intact, bedding parallel inoceramid shells (no evidence of transport) indicates varying levels of low-oxygen above the sediment because inoceramid bivalves have adapted specifically in morphology and anatomy to survive in oxygen-depleted or “chemically deleterious” environments (Kaufmann, 1988; Kauffman and Harries, 1992; MacLeod and Hoppe, 1992; Harries et al., 1996). Some laminations contain broken inoceramid fragments, suggesting shells have also been transported or re-worked; this also confirms that the surrounding environment was oxygen-depleted. This is confirmed by molybdenum enrichment throughout the interval (Fig. 10). Alternations between these two lithofacies are likely related to water chemistry and ability for inoceramid bivalves to live on the sea floor in the surrounding environment. Nutrients

and oxygen, while not in high quantities, were more available during deposition of the laminated argillaceous inoceramid wackestone (Fig. 21) than during the deposition of laminated argillaceous planktonic foraminifera wackestone (Fig. 20). API values throughout the lower Eagle Ford section display the greatest difference between CGR and SGR (Fig. 36) – this observation is supported by the increased quantities of volcanic ash and clay minerals in the lower Eagle Ford strata (Fig. 9, 10).

Weakly laminated wackestone in the upper portion of the lower Eagle Ford strata has parallel laminations and lacks grain accumulations or ripples (Figs. 22, 36). Deposition in this lithofacies is similar to that of the laminated argillaceous planktonic foraminifera wackestone (Fig. 20) and laminated argillaceous inoceramid wackestone (Fig. 21). Bottom-currents can help procure planar laminations (Schieber and Southard, 2009). Observed decrease in grain content is most likely related to an increase in mud-size material rather than a decrease in grain contribution (Figs. 20, 21).

A total 168 individual ash beds were documented in the lower Eagle Ford strata (Fig. 36). Volcanic ash in the lower Eagle Ford strata creates an approximate bell curve with the greatest number of preserved ashes in the middle of the lower Eagle Ford strata. Volcanic ash gradually increases from the Buda Limestone-Eagle Ford Group contact and decreases towards the lower-upper Eagle Ford strata contact. Volcanic ash (Fig. 28) is commonly adjacent to peloidal crystalline mudrock (Fig. 31) and abundant radiolarians. While there may be a relationship between these features (peloidal crystalline mudrock Fig. 31, volcanic ash Fig. 28, radiolarian abundance), evidence from this study is not conclusive as to how they are interrelated.

The contact between the lower and upper Eagle Ford strata has several defining features. Gamma ray values in the lower Eagle Ford strata gradually decrease to a new baseline representing the upper Eagle Ford strata (Fig. 36). Decrease in gamma ray

values is supported by decrease in clay mineral volume (Fig. 9, 10) and mirrors a decrease in TOC weight percent (Fig. 17). Lithofacies dominant in the upper Eagle Ford strata such as laminated calcisphere grainstone (Fig. 24) have greater grain abundance and less clay-rich matrix, explaining the decrease in gamma ray values. Approximately 1.5 ft of burrowed foraminifera wackestone (Fig. 26) appears at the contact between lower and upper Eagle Ford strata (Fig. 26, 36). This lithofacies represents a substantially different depositional environment than had been present in the underlying lower Eagle Ford strata. Sediments are burrowed, indicating habitable and oxygenated sediments and water-column (Fig. 17). This substantial change may be linked to water depth; however, no evidence explicitly shows this. This change may be related to water chemistry and circulation. Volcanic ash abundance decreases towards the contact and increases away from the contact.

The upper Eagle Ford strata are composed of four main lithofacies: massive argillaceous claystone (Fig. 23), laminated argillaceous planktonic foraminifera wackestone (Fig. 20), weakly laminated wackestone (Fig. 22), and laminated calcisphere grainstone (Figs. 24, 36). The massive argillaceous claystone occurs as a lithofacies that grades into laminated argillaceous planktonic foraminifera wackestone. Beds and laminations are planar, suggesting that bottom-currents and sediment deposition is similar between these lithofacies. The massive argillaceous claystone deposits may represent a change in deposition or regional climate impacting sedimentation within the basin for a brief period. The grain-dominated laminations within laminated argillaceous planktonic foraminifera wackestone are winnowed of mud-size material and reworked into starved ripples. Ash abundance in the upper Eagle Ford demonstrates a different character than that of the lower Eagle Ford (Fig. 36). Ashes are still very common within the upper Eagle Ford but are more dispersed (more evenly distributed) than the bell-curve pattern

of ash abundance in the lower Eagle Ford. This may be related to more consistent volcanism during deposition.

Laminated calcisphere grainstone is the most distinctive lithofacies of the upper Eagle Ford strata (Fig. 36). Calcisphere laminations are reworked into ripples (Fig. 24). Compaction of ripples and bars has produced substantial differential compaction around each feature, creating the nodular and wavy appearance preserved in core (Fig. 24). Soft-sediment deformation, flame structures, and water escape structures demonstrate sediments were deformed after sediment accumulation and deposition (Fig. 24). Well-developed ripples indicate the presence of bottom-current influence on grain accumulations (Fig. 24). Pristine preservation of primary sedimentary structures implies that sediments were not habitable and were not pervasively bioturbated. Brief appearance of millimeter-size, lamination-scale burrows imply that ‘doomed pioneer’ fauna may have attempted to colonize the area but were unable.

The shift between laminated argillaceous planktonic foraminifera wackestone (Fig. 20), weakly laminated wackestone (Fig. 22), and laminated calcisphere grainstone (Fig. 24) represents a shift in sediment supply and depositional processes (Fig. 36). Winnowing of starved ripples in laminated argillaceous planktonic foraminifera wackestone (Fig. 20), planar beds in weakly laminated wackestone (Fig. 22), and well-developed ripples in laminated calcisphere grainstone (Fig. 24) is strong evidence that bottom-current were an important and active feature of deposition in the upper Eagle Ford strata. It is proposed that the change in preserved structures (ripple variety) is largely related to the quantity of fauna versus the quantity of mud (clay matrix, peloids, peloidal material, carbonate or siliciclastic or argillaceous). Matrix clay minerals and peloids are the dominant deposited sediment within weakly laminated wackestone (Fig. 22); grains are diluted by matrix material. In laminated calcisphere grainstone, high

quantity of fauna dilutes the amount of matrix material (Fig. 24). Additionally, the variety of fauna present is a function of changing water habitability.

The upper Eagle Ford strata have several bed- to lamination-scale episodes of soft-sediment deformation, folding, and transported material (Fig. 36). These styles of deposits are interpreted as mass-transport slumps of intrabasinal material from a slightly more proximal location. Plastic deformation of semi-coherent beds can be used to interpret that slumping occurred in ductile sediments (Fig. 24). Many grain-dominated laminations composed of mixed fauna could be interpreted as individual gravity-flow deposits, wherein nonlithified grains have been transported from other locations within the basin.

Volcanic ash (Fig. 28) in the upper Eagle Ford strata is less consistently abundant than in the lower Eagle Ford strata (Fig. 36). A total of 147 individual volcanic ash beds are observed in the upper Eagle Ford strata. The thickest volcanic ash deposit is located at the top of the upper Eagle Ford strata (Fig. 36). This 17 cm ash should be considered a marker indicating the nearness of the contact between upper Eagle Ford strata and the Austin Chalk.

The contact between the upper Eagle Ford the Austin Chalk can be identified several ways. Gamma ray values gradationally decrease to a new baseline within the Austin Chalk (Fig. 36) indicating a decrease in clay mineral volume (Figs. 9, 10). Preserved, discrete volcanic ash beds significantly decrease into the Austin Chalk (Fig. 36). Lithofacies and associated depositional environment change from well-laminated and well-preserved sedimentary features to fabric destructive bioturbation.

The Austin Chalk is composed of burrowed foraminifera wackestone with thin layers of laminated argillaceous planktonic foraminifera wackestone (Figs. 20, 26, 36). Bioturbation in burrowed foraminifera wackestone (Fig. 26) is pervasive; the bioturbation

destroys any primary sedimentary features. This lithofacies indicates that the depositional environment was habitable and able to support life within the sediment and water-column (Fig. 17). Cyclic interbeds of laminated argillaceous planktonic foraminifera wackestone represents periods wherein sediments were not habitable (Fig. 36). The thin intervals of laminated argillaceous planktonic foraminifera wackestone (Fig. 36) shows a period of gradational transition from the underlying Eagle Ford Group to the Austin Chalk above.

Winterbotham J.M. Jr. #1 Conventional Core

Figure 38 illustrates the gamma ray, lithofacies, and volcanic ash stratigraphy for the Winterbotham J.M. Jr. #1 core from Zavala County, Texas (Fig. 3). Gamma ray data documented in a photo of the original 1971 drilling document does not have calibrated numerical data to accompany the curve; thusly, CGR and SGR have been calculated using XRF data. The high-frequency alternations of the gamma curves is most likely related to small-scale lamination heterogeneity from calcite-dominated to clay-mineral-dominated laminations within the core. The core contains 152 appearances of volcanic ash. The majority of volcanic ash within this core is mixed with matrix sediments (discrete beds are less common). Computed gamma ray from XRF data is more accurate in the SGR curve.

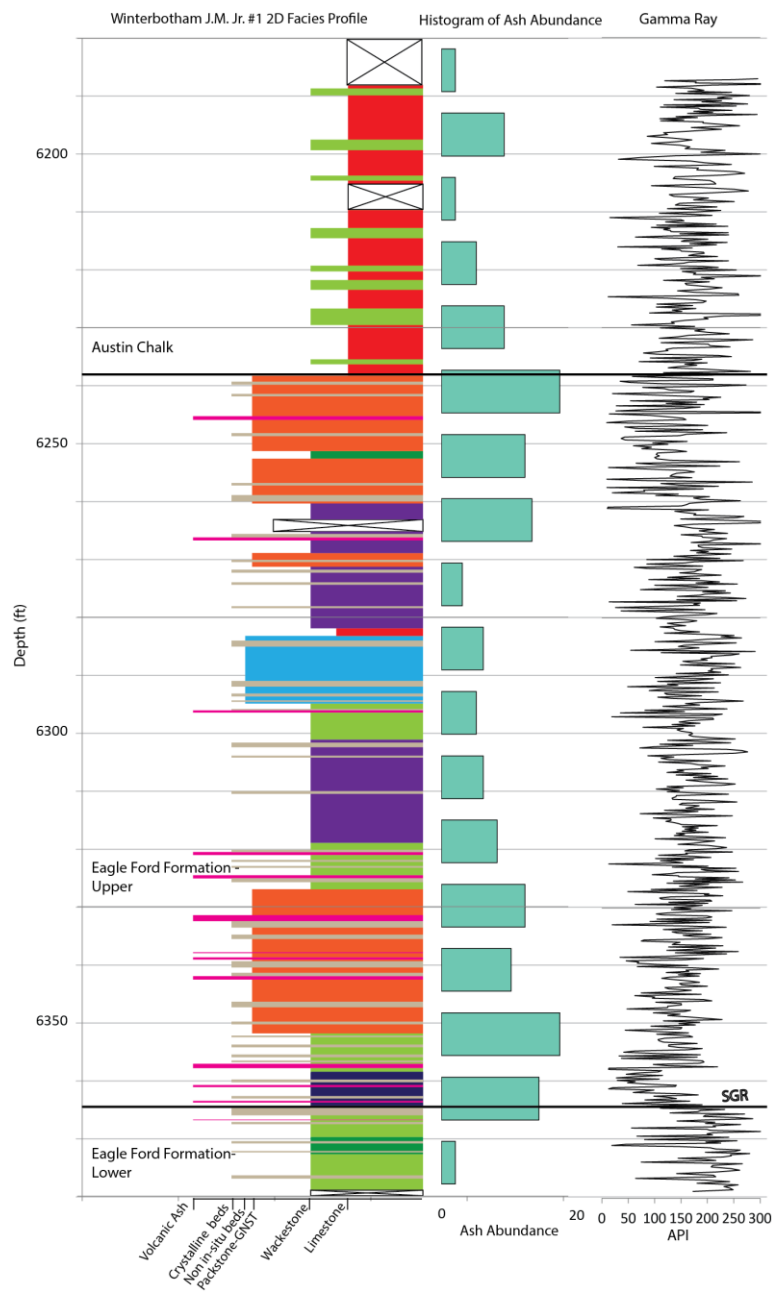


Figure 38: Winterbotham J.M. Jr. #1 lithostratigraphy. Ash abundance is displayed as a histogram showing ash beds per nine foot interval. Gamma ray values have been computed using XRF data. Key is contained in Fig. 33.

The lowest documented occurrence of burrowing within the Eagle Ford Group is documented at a depth of 6,339 ft (Fig. 38). Burrows are up to 1 cm in diameter and disrupt and truncate original sedimentary laminations.

The thickest volcanic ash layer in the Winterbotham J.M. Jr. #1 core is documented at a depth of 6,332 ft (Fig. 38). The 10 cm thick volcanic ash is composed of a clay-rich, yellow groundmass with various phenocrysts including beta quartz, phyllosilicate flakes, plagioclase feldspar, as well as authigenic pyrite (Fig. 39). The gamma ray log at 6,332 ft (Fig. 38) shows an increase in API related to increased potassium content and increased clay mineral volume within the ash.

The interval from 6,295-6,285 ft (Fig. 38) highlights a section of transported intraclasts and beds. This unit contains angular, pebble- to cobble-sized lithoclasts of cemented, calcisphere and planktonic foraminifera laminations and contains laminated skeletal grain-dominated packstone lithofacies (Figs. 25, 38). Above the intraclast deposit, beds are folded and contorted. Laminations remain coherent and are plastically deformed without brittle breakage. Volcanic ash beds (Fig. 28) are contained within the folded and contorted beds. The section from 6,260-6,238 ft (Fig. 38) delineates a section of laminated skeletal grain-dominated packstone (Fig. 25) containing by both large-scale and small-scale soft-sediment deformation. Bed-scale folds remain coherent with identifiable laminations. Deformation is ductile. Lamination-scale deformation of laminated skeletal grain-dominated packstone is documented by uneven scour of siliceous, argillaceous, or carbonate mud laminations, differential compaction, and flame structures (Fig. 25).

A change in dominant lithofacies from laminated argillaceous planktonic foraminifera wackestone (Fig. 20) to burrowed foraminifera wackestone (Fig. 26) occurs at a depth of 6,238 ft (Fig. 38). This change documents a change in habitability of

sediments as documented in shift from no bioturbation to pervasive bioturbation. The gamma ray log at this point shows a small increase in API 6,245 ft (Fig. 38) followed by a gradational decrease to a new, lower baseline.

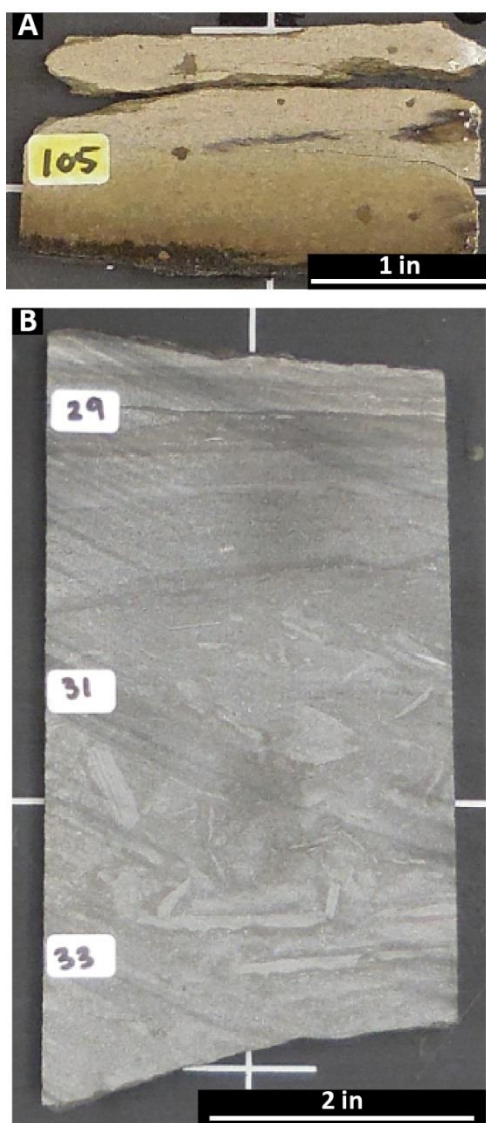


Figure 39: Winterbotham J.M. Jr. #1 photographs and photomicrographs. A) Thickest volcanic ash bed in the core at 6,332 ft I the upper Eagle Ford strata. The small dark patches are authigenic pyrite. B) Brittle lithified intraclasts in a debris-flow deposit in the upper Eagle Ford Group at 6,293 ft (overlain by laminated skeletal grain-dominated packstone).

Interpretation

Eagle Ford Group

Fourteen feet of the lower Eagle Ford strata are preserved in the Winterbotham J.M. Jr. #1 (Fig. 38). The division between lower and upper Eagle Ford in the Winterbotham J.M. Jr. #1 core was defined by a decrease in API values (Fig. 38), a decrease in redox sensitive elements (Fig. 15), and increase in manganese (Fig. 15), and the appearance of the titanium-rich massive argillaceous claystone (Fig. 23). This section contains laminated argillaceous planktonic foraminifera wackestone (Fig. 20), laminated argillaceous inoceramid wackestone (Fig. 21), volcanic ash (Fig. 28), and peloidal crystalline mudrock (Fig. 31). Laminated argillaceous planktonic foraminifera wackestone contains winnowed starved ripples (Fig. 20). Winnowing and reworking of allochem-rich laminations support the influence of bottom-current processes within the section. Inoceramid shells located within bedding planes express an environment that is oxygen-poor (Kaufmann, 1988; Kauffman and Harries, 1992; MacLeod and Hoppe, 1992; Harries et al., 1996). Lack of bioturbation indicates poor living conditions within the sediment supported by increased molybdenum (Fig. 15). Volcanic ash abundance within the lower Eagle Ford strata is low in comparison to the ash content observed in the upper Eagle Ford (Fig. 38). Because the lower Eagle Ford section in this core is incomplete, a relationship between ash abundance in the lower and upper Eagle Ford strata cannot be derived. The decrease in ash in the upper portion of the lower Eagle Ford documented in the Winterbotham J.M. Jr. #1 parallel the trend documented in the upper, lower Eagle Ford in Core-X. Less volcanic ash documented in the lower Eagle Ford strata as compared to the upper Eagle Ford strata in the Winterbotham J.M. Jr. #1 cannot be related to increased volcanism in the upper Eagle Ford strata. The transition between the lower and upper Eagle Ford is signaled by a gradual decrease in SGR values

representing the decrease in clay mineral volume from the lower to upper Eagle Ford strata. SGR gamma ray values show high variability in readings because of high cyclicity and changing of laminations (Fig. 38).

The upper Eagle Ford strata is more diverse than the lower Eagle Ford strata (Fig. 38) and contains laminated argillaceous planktonic foraminifera wackestone (Fig. 20), laminated argillaceous inoceramid wackestone (Fig. 21), laminated skeletal grain-dominated packstone (Fig. 25), weakly laminated wackestone (Fig. 22), massive argillaceous claystone (Fig. 23), volcanic ash (Fig. 28), and peloidal crystalline mudrock (Fig. 31). Laminated argillaceous planktonic foraminifera wackestone contains winnowed allochem laminations indicating the presence of an active bottom-current. Parallel-laminated mudrock may have been deposited under similar bottom-current conditions; however, peloidal and matrix material accumulation rates or input would have been high enough to prohibit the accumulation and reworking of grains on a bedding plane. Burrowing within the upper Eagle Ford strata is present within the laminated skeletal grain-dominated packstone (Figs. 25, 38). Burrowing is generally contained within a single lamination (~5 mm); indicating sediment was not completely habitable. The laminated skeletal grain-dominated packstone contains allochem supported laminations that are poorly sorted and contain a broad assortment of fauna (saccocomid fragments, planktonic foraminifera, fish bones). Soft-sediment deformation in the vicinity of these laminations and poor sorting of grains leads to the interpretation that laminations are the result of gravity-flows or small mass-wasting deposits. Larger, soft-sediment deformation is also present within the section interpreted as slumping (Fig. 39). The succession of well-laminated, matrix sediments with no burrowing and restricted fauna (planktonic foraminifera and inoceramids) changes to grain-supported laminations and a larger variety of fauna (planktonic foraminifera, echinoids, calcispheres) documents the gradual

change to a more nutrient-rich, habitable environment in the upper Eagle Ford. This may be related to increased circulation introducing more nutrients into the system.

Austin Chalk

The Austin Chalk in the Winterbotham J.M. Jr. #1 is composed of burrowed foraminifera wackestone (Fig. 26) with thin intervals of laminated argillaceous planktonic foraminifera wackestone (Fig. 20). This section contains less volcanic ash than the underlying section. Pervasive burrowing has erased original sedimentary features and suggests oxygenation of sediments (Fig. 15). Thin intervals of planktonic foraminifera wackestone show reworked foraminifera laminations and starved ripples indicating deposition under the influence of bottom-currents.

Peloidal crystalline mudrock (Fig. 31) within the lower and upper Eagle Ford strata (Fig. 38) is concluded to be the result of diagenesis. Calcite crystals pervasively precipitate within the clay matrix and do not affect peloids. Peloidal crystalline mudrock appearance is generally coincident with abundant radiolarians.

Fauna and Biostratigraphy

Seven faunal divisions have been described: three different groups of planktonic foraminifera, radiolarians, calcispheres, inoceramid, and inoceramid filaments. The biostratigraphy has been created by assigning relative abundance values based on abundance of each individual groups of biologic fauna collected using petrographic description. The majority of faunal identifications were done under the guidance of Dr. Richard Denne.

FAUNAL DESCRIPTIONS

The following section contains a brief evaluation of each different faunal group used for biostratigraphic analyses. Each faunal group has been selected because of occurrence within the section and potential relationship to environmental conditions. The following defined faunal taxa do not represent the total diversity of fossils found within the Buda Limestone, Boquillas Formation, Eagle Ford Group, or Austin Chalk, but are the most significant for this study.

Planktonic Foraminifera

Planktonic foraminifera have been divided into three classes based on depth of living environment. Major changes occur within test morphology and geometry with increasing depth as planktonic foraminifera adapt to exploit oxygen at deeper water depths. Three main divisions were defined using classifications described by Boudagher-Fadel (2013) and Denne et al. (2014) (Fig. 41). The first family, Hedbergellidae, contains *Hedbergella* and *Whiteinella*. The tests of these planktonic foraminifera are trochospiral, with rounded and/or globular chambers. These genera dwell in the shallow, surface zone and are eutrophic (Boudagher-Fadel, 2013). The second family, Heterohelcidae, contains the genus *Heterohelix*. These planktonic foraminifera lived in deeper surface to intermediate water depths and are mesotrophic (Boudagher-Fadel, 2013). A morphological change occurs in *Heterohelix* genus from the Cenomanian to Turonian. In the Cenomanian, some tests are narrow and chambers are small (*Heterohelix moremani*), whereas some tests in the Turonian are larger more obtuse tests with globular chambers (*Heterohelix globulosa*; Boudagher-Fadel, 2013). The third division, keeled planktonic foraminifera, contains *Rotalipora cushmani*, *Rotalipora greenhornensis*, *Rotalipora* sp., and *Globotruncana*. The last group contains any evolutionarily complex planktonic foraminifera that dwell in deep neritic waters (Boudagher-Fadel, 2013). This taxon of

foraminifera is commonly oligotrophic (Boudagher-Fadel, 2013). *Rotalipora cushmani* is specifically important because it is the marker species for the end of the Cenomanian stage (Boudagher-Fadel, 2013).

For the purposes of this study, depth of habitation of planktonic foraminifera will be discussed in terms of habitation zone and relative nutrient availability. Planktonic foraminifera will be characterized by eutrophic, mesotrophic, or oligotrophic.

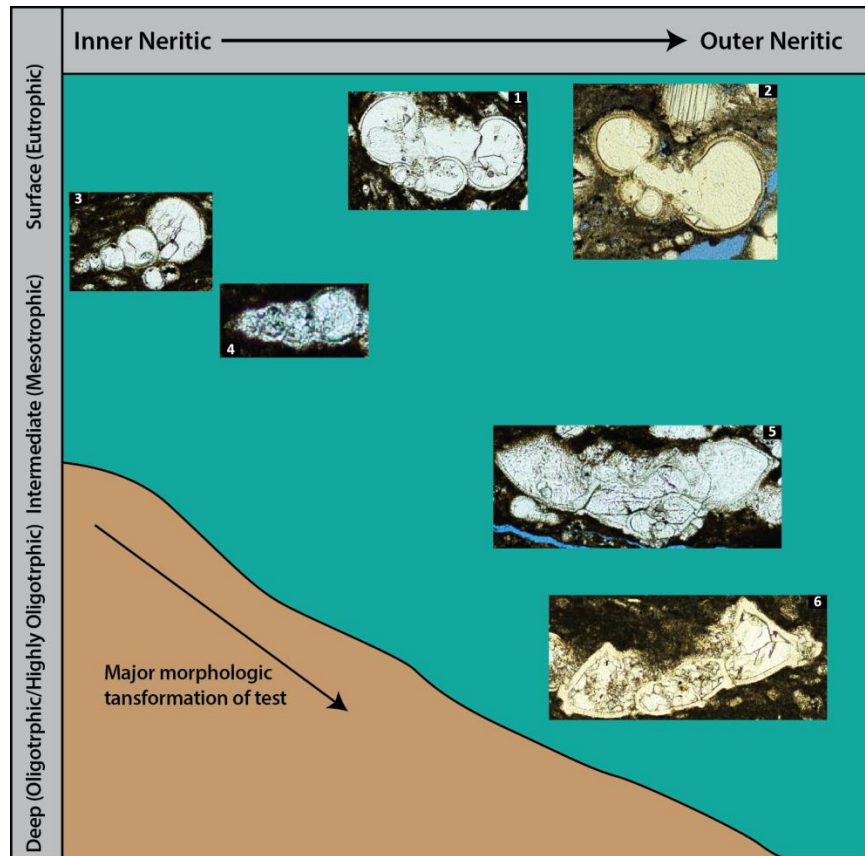


Figure 40: Generalized distribution of Cretaceous planktonic foraminifera within the water-column. This image is a visual model and should not be read to scale. Modified from Boudagher-Fadel (2013) and Denne et al. (2014). Hedbergellidae represents surface-dwelling planktonic foraminifera and are eutrophic (1: *Hedbergella* sp. in Core-X lower Eagle Ford strata in laminated argillaceous planktonic foraminifera wackestone at 4,008 ft and 2: *Whiteinella* in Hot Springs upper Ernst Member strata in laminated skeletal grain-dominated packstone at 168 ft). Heterohelicidae represents intermediate water-depth planktonic foraminifera and generally exist in eutrophic to mesotrophic water conditions (3: *Heterohelix* sp. in Core-X in lower Eagle Ford strata laminated argillaceous planktonic foraminifera wackestone at 3,955 ft and 4: *Heterohelix* sp. in Core-X upper Eagle Ford strata at 3,720 ft). Keeled planktonic foraminifera represent deep-dwelling planktonic foraminifera that can live in more specialized conditions (5: *Rotalipora cushmani* in Core-X lower Eagle Ford strata in laminated argillaceous planktonic foraminifera wackestone at 3,851 ft and 6 *Globotruncana* sp. in the Core-x Austin Chalk strata in burrowed foraminifera wackestone at 3,550 ft).

CLASS FORAMINIFERA Lee, 1990

ORDER GLOBIGERINIDA Lankaster, 1885

Superfamily GLOBIGERINOIDEA Carpenter, Parker and Jones, 1862

This superfamily contains members with a trochospiral test. Chambers appear rounded to angular. The keel is peripheral or occurs as an imperforate band with a double keel. The primary aperture may be either covered by tegilla or umbilical with portici. If covered by tegilla, it may have accessory apertures. The surface of the chamber wall may be muricate, spinose, with perforation cones, without perforation cones, or smooth. The wall can be either macro- or microperforate. Aperture may be intra-extraumbilical, umbilical, or interiomarginal. Intra-extraumbilical apertures may be bordered by a lip.

Family Hedbergellidae Loeblich and Tappan, 1961

The family Hedbergellidae test is trochospiral and macroperforate. Irregular rugosities may be formed through fusing of the muricate and muricae on the first whorls. Imperforate, irregular ridges may form on early chambers of the last whorl because of coalescing of perforation cones. The umbilicus has small unfused portici. The aperture is intra-extraumbilical. The family exists from Cretaceous (Late Aptian) to Paleocene.

- *Hedbergella* Brönniman and Brown 1958 (Type species: *Anomalina lorneiana* d'Orbigny variation *trocoidea* Gandolfi, 1942). Cretaceous (Late Albian) to Paleocene (Danian) with four to four and one half chambers per whorl. Short portici cover the umbilicus.
- *Whiteinella* Pessagno, 1967 (Type species: *Whiteinella archaeocretacea* Pessagno, 1967). Cretaceous (Middle Cenomanian to Early Campanian) age with relict apertures and a weak keel on periphery

of late chambers and does not extend to dorsal features. The aperture has no tegillum and broad, long portici, as well as a broad umbilicus. The test is generally similarly muricate and biconvex.

Family Rotaliporidae Sigal, 1958

The family Rotaliporidae test has a single keel and is macroperforate and trochospiral. Long portici cover the central umbilicus and may sometimes fuse together to form additional apertures. The main aperture has a prominent apertural lip and is intraextraumbilical. The family exists from Cretaceous Late Aptian to Cenomanian.

- *Rotalipora* Brotzen 1942 (Type species: *Rotalipora turonica* Brotzen, 1942). Cretaceous Middle Cenomanian to Late Cenomanian with angular chambers and a single keel. Sutures are elevated on umbilical and spiral sides. Extensions from the chambers can form sutural, supplementary apertures.

Family Globotruncanellidae Maslakova, 1964

The family Globotruncanellidae test has compressed chambers that is either plano- or concavo-convex and is trochospiral. Tegilla or portici cover the umbilicus and the test has intra-extraumbilical apertures. Chamber walls have well-developed muricae and are macroperforate. The family exists from Cretaceous Late Albian to Maastrichtian.

- *Dicarinella* Porhault 1970 (Type species: *Globotruncana indica* Jacob and Sastry, 1950). Cretaceous Turonian to Santonian with a compressed test with closely placed keels on the periphery. Short portici are associated with an open umbilicus. Sutures can be either compressed (umbilical) or raised (spiral).

Family Globotruncanidae Brotzen, 1942

The family Globotruncanidae test is trochospiral and macroperforate, and has irregularly arranged rugosities formed by muricae fusing on the first whorls. Unfused portici or tegillum occur with the widely open umbilicus. The test may have a peripheral keel or two keels with an angular truncated peripheral margin. The family exists from Cretaceous Turonian to Maastrichtian.

- *Globotruncana* Cushman 1927 (Type species: *Pulvinulina* Cushman, 1927). Cretaceous Late Coniacian to Maastrichtian with a biconvex test with circular to lobate outline and crescentic to globular chambers. It is double keeled with a possible intermediate imperforate band; the keels may be reduced to a single keel towards the final chamber. The primary aperture is covered by a tegillum and is intraumbilical.
- *Marginotruncana* Hofker, 1956 (Type species: *Rosalina marginata* Reuss 1845). Cretaceous-aged (Middle Turonian to Santonian) plano- to biconvex test with keeled spiral sutures and umbilical, as well as an intra-extraumbilical primary aperture with portici. An imperforate band (part of the periphery) is located between the two keels.

ORDER HETEROHELICIDAE FURSENKO, 1958

Superfamily HETEROHELICOIDEA Cushman, 1927

This superfamily contains members with a biserial or triserial test (early stages may be uniserial). The apertures may have either a high to low arch in the final stage. Apertures may also be terminal within the uniserial stage. Test walls can be muricate or smooth, and are composed of radial calcite. Cretaceous (Aptian) to present day.

Family Heterohelicidae Cushman, 1927

The family Heterohelicidae test is biserial, triserial, or multiserial in later stages. Early stages are commonly uniserial. Chamber walls of the test can be either macroperforate or microperforate. The aperture is asymmetrical. Asymmetry occurs along the equatorial axis. The family exists from Cretaceous (Late Albian) to Eocene (Priabonian).

- *Heterohelix* Ehrenberg, 1843 (Type species: *Textilaria Americana* Ehrenberg, 1843). Cretaceous (Late Albian to Maastrichtian). Test is biserial with possible multiserial terminal stage and no planispiral coil. The chambers are subglobular and microperforate. A simple aperture is symmetrical with a lip.
- *Pseudotextularia* Rzehak, 1891 (Type species: *Cuneoolina elegans* Rzehak, 1843). Cretaceous (Coniacian to Maastrichtian). The macroperforate test is initially planispiral, and is later biserial. Chambers greatly increase in thickness. A lip borders broad apertures.
- *Pseudoguembelina* Brönniman and Brown, 1953 (Type species: *Guembelina excolata* Cushman, 1926). Cretaceous (Coniacian to Maastrichtian). A portici or plate separates opposed chambers of the macroperforate, biserial test. When viewed in the axial plane, chambers are thinner than when observed in the equatorial plane. Secondary apertures may occur in later chambers.

Radiolarians

Radiolarians are a siliceous microfossil within the superorder Polycystina (Scholle, 2003). The radiolarians discussed herein are not sorted into family, genus, or species because of their poor state of preservation. Radiolarians are marine plankton and

are found at varied depths within the water-column (Scholle, 2003). Occurrence of radiolarians within deposits indicates pelagic sedimentation (Scholle, 2003). Because of the original skeletal composition of opaline silica and the highly porous skeletal structure, radiolarian tests are commonly heavily recrystallized. Samples within this study show both pyritization of original siliceous material, and calcite replacement and growth within the originally open, porous structure.

Calcispheres

Calcispheres are considered a microproblematica; however, have more recently been defined as an algal cyst (Flügel, 2010). Calcispheres are observed in thin-section as small calcite globular or spherical microfossils, generally less than 100 microns. The calcitic wall of the test is much thicker than those calcitic test walls observed in planktonic foraminifera and are multi-layered (Flügel, 2010). Calcispheres are also far smaller than foraminifera observed within the sample set presented herein. Calcispheres found within wackestones are indicative of open marine environments, and are considered to be resultant from deep shelf, slope, and basinal setting deposition (Flügel, 2010).

Inoceramids and Filaments

Inoceramids are an evolved, specialized variety of bivalve within Class Pelecypoda (Scholle, 2003). Inoceramid genera and species are not interpreted within this study and are documented within the same ‘inoceramid’ classification. Inoceramid bivalves have adapted specifically to live in oxygen-depleted or “chemically deleterious” environments (Kaufmann, 1988; Kauffman and Harries, 1992; MacLeod and Hoppe, 1992; Harries et al., 1996). Inoceramids can be identified in thin-section by the columnar

structure within the shell wall composed of monocrystalline, porous calcite hexagonal prisms (Fig. 21).

Inoceramid filaments are defined as the planktonic larval stage of the adult inoceramid bivalve (Negra et al., 2011). Filaments can be identified in thin-section as very thin, generally bedding parallel, wisps of calcite (Fig. 21; Denne, 2014).

BIOSTRATIGRAPHY

The following sections show graphically the biostratigraphy for each individual locality. Each defined faunal group is documented in where it appears, as well as in general abundance. Biostratigraphic markers and interpretations were made following the work and advice of Dr. Richard A. Denne (Denne et al., 2014).

Hot Springs Outcrop

Figure 41 shows biostratigraphy for the Hot Springs outcrop section and Figure 42 shows examples of described fauna. Planktonic foraminifera are the most represented organisms. Radiolarians, calcispheres, and inoceramids are also abundant.

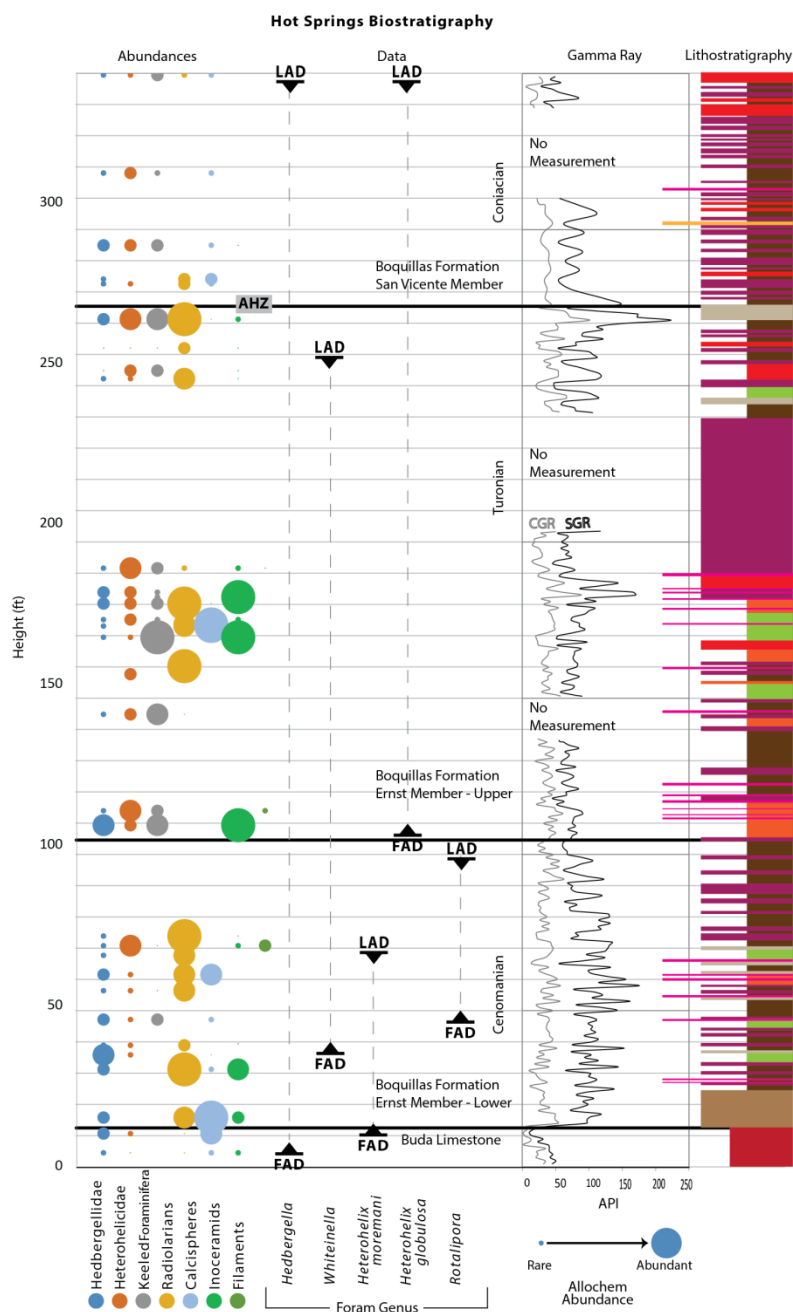


Figure 41: Hot Springs outcrop section biostratigraphy. Bubble size denotes general abundance, smaller bubbles correlate to rare or lesser abundance, larger bubbles correlate to commonly abundant to dominant. FAD = first appearance datum; LAD – last appearance datum.

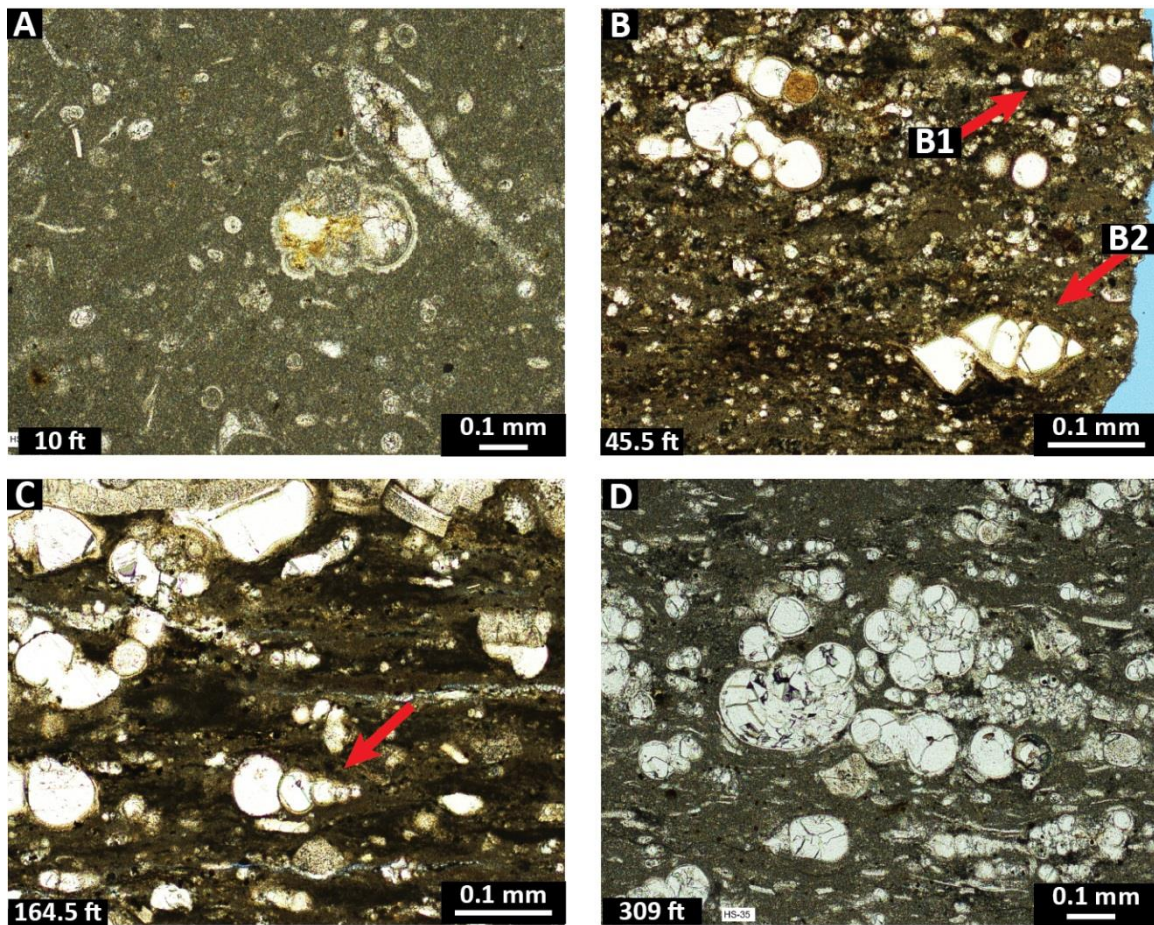


Figure 42: Photo plate of Hot Springs outcrop section biostratigraphy microfossils. A) Buda Limestone (burrowed skeletal wackestone) with large hedbergellid planktonic foraminifera and small calcispheres. B) Lower Ernst Member (laminated argillaceous planktonic foraminifera wackestone) with small *Heterohelix* sp. (B1) and possible *R. greenhornensis* (B2). C) *Heterohelix globulosa* in the upper Ernst Member (laminated skeletal grain-dominated packstone). (D) Undifferentiated hedbergellid and heterohelicid foraminifera in the San Vicente Member (burrowed foraminifera wackestone).

In the Buda Limestone from 0-13 ft, the present types of organisms are quite different from the overlying Boquillas Formation (Fig. 41). The Buda Limestone is dominated by calcispheres and Hedbergellidae; no keeled planktonic foraminifera are

observed within the Buda Limestone (Fig. 41). Tests are randomly oriented because of intense burrowing of the sediments.

The first keeled planktonic foraminifera are observed at 45.5 ft in the Boquillas section (Fig. 41). *Rotalipora greenhornensis* was identified along with other undifferentiated, keeled planktonic foraminifera (rotaliporid).

At 68.5 ft, there is an abundance of inoceramid filaments (Figs. 41, 42). Lags of thin calcareous shells of the inoceramid filaments drape sediments. Filaments appear in one other documented location within the section as observed from the collected sample set.

The first Heterohelcidae with globular chambers (*Heterohelix globulosa*) are observed at 106 ft (Figs. 41, 42). All observed Heterohelcidae observed prior are narrow and have small chambers (*Heterohelix moremani*; Fig. 41).

Fauna begins to diversify at 168 ft (Fig. 41). Burrowing has scattered preserved skeletal fragments so that they do not appear to accumulate solely along bedding planes in the form of grain laminations. Keeled planktonic foraminifera (possibly *Marginotruncana* sp.) are abundant in addition to radiolarians, calcispheres, and inoceramid (Fig. 41).

Above the *Allocrioceras hazzardi* zone (AHZ) at 276 ft, the quantity of any observed fauna greatly decreases (Fig. 41). Faunal abundance within San Vicente Member samples are far lower than faunal abundances observed in the Ernst Member or in the Buda Limestone.

Interpretation

The assemblage of preserved fauna (especially the appearance of planktonic foraminifera types and presence of inoceramids) in the Ernst Member of the Boquillas

Formation demonstrates a depositional environment with continually productive surface-waters and rare to sometimes oxygenated bottom-waters.

The enrichment of filaments (inoceramid larvae; Fig. 41) is interpreted as the filament event documented elsewhere in the global oceans during the Cenomanian (Negra et al., 2011; Denne et al., 2014). This event is documented to have occurred prior to the OAE2 and the Cenomanian-Turonian boundary (Negra et al., 2011; Denne et al., 2014).

The first *Heterohelix globulosa* are documented at 106 ft (Figs. 41, 42). The appearance of the Turonian-style Heterohelcidae test first appears within the mud-laminated skeletal planktonic foraminifera grain-dominated packstone. Because of gaps in sampling, the closest lower sample containing Heterohelcidae is at 71.5 ft; Heterohelcidae within this sample are narrow with small test chambers (*Heterohelix moremani*, Fig. 41). The change in Heterohelcidae test morphology is used to propose that the Cenomanian-Turonian transition occurs between 71.5-106 ft.

Handheld gamma-spectrometer data demonstrates a gradational decrease in gamma ray readings beginning at 100 ft (Figs. 41, 42). This gamma ray response, in correlation with the FAD of *Heterohelix globulosa* is used to propose that the Cenomanian-Turonian boundary occurs near 100 ft in the measured section (Fig. 41) and defined the boundary between lower and upper Ernst Member. Poor sampling resolution and outcrop weathering disallows for a more precise proposal of the C-T boundary.

Core-X Conventional Core

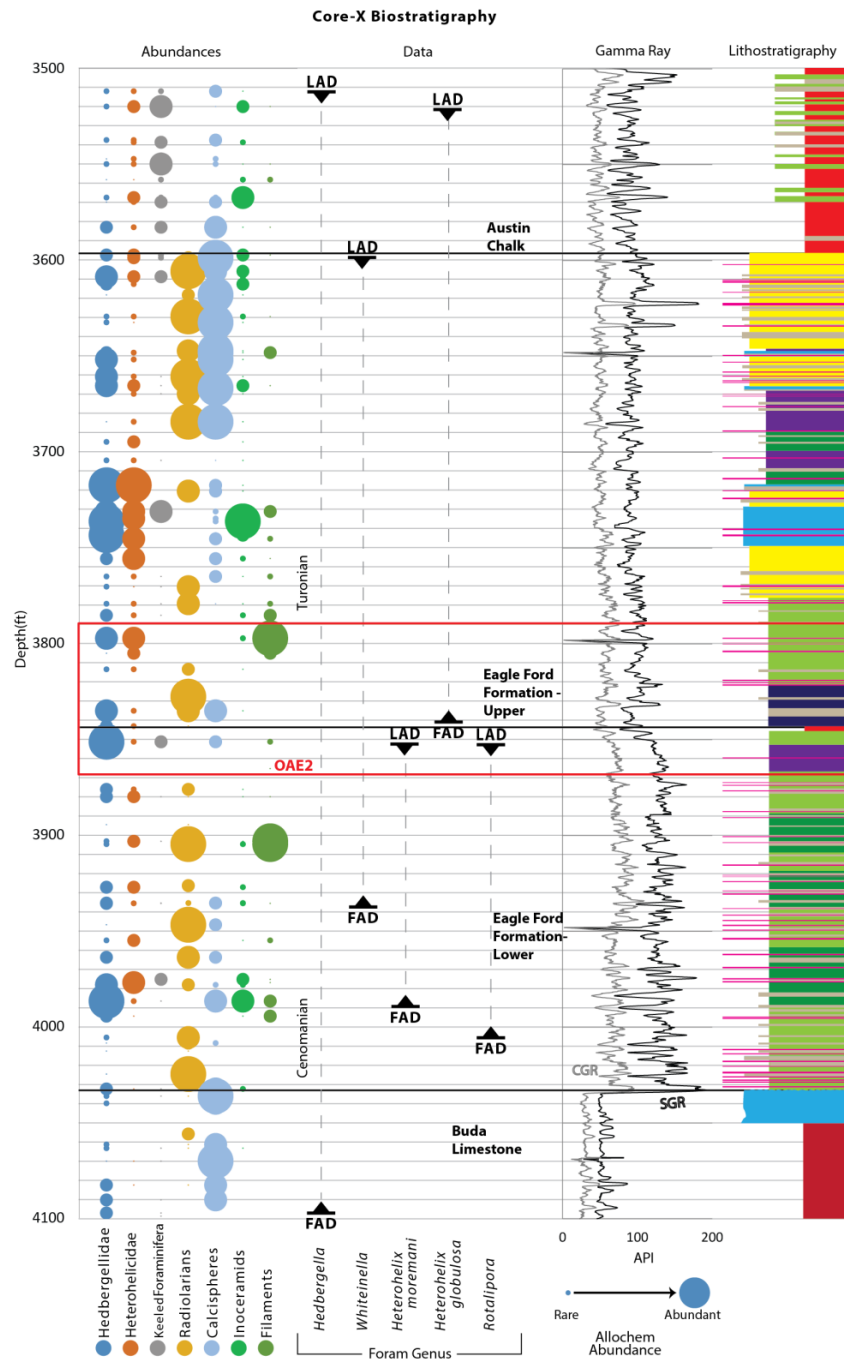


Figure 43: Core-X biostratigraphy. Bubble size denotes general abundance, smaller bubbles correlate to rare or lesser abundance, larger bubbles correlate to common or extremely abundant. FAD = first appearance datum, LAD = last appearance datum. The red box shows the position of the OAE2.

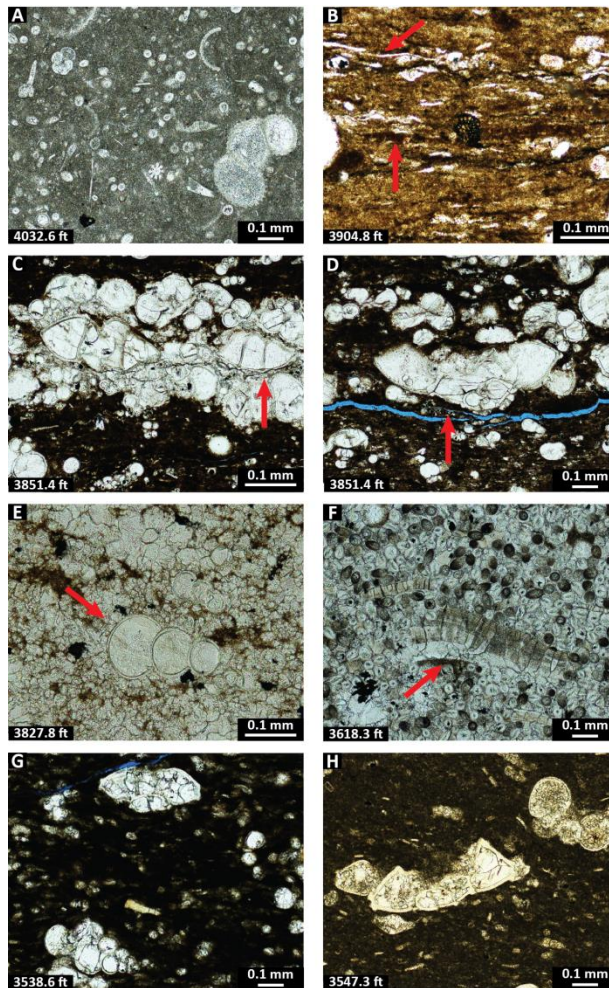


Figure 44: Photo plate of Core-X biostratigraphy microfossils. A) Planktonic foraminifera (hedbergellids) and calcispheres in Buda Limestone (burrowed skeletal wackestone). B) Two red arrows show inoceramid filaments in lower Eagle Ford. C) *Rotalipora* (poss.) *greenhornensis* in the lower Eagle Ford (laminated argillaceous planktonic foraminifera wackestone). D) *Rotalipora cushmani* in the lower Eagle Ford (laminated argillaceous planktonic foraminifera wackestone). E) *Heterohelix globulosa* (red arrow) in upper Eagle Ford (laminated argillaceous planktonic foraminifera wackestone). F) Inoceramid fragment (red arrow) in calcispheres in the upper Eagle Ford (laminated calcisphere grainstone). G) *Heterohelix globulosa* (bottom left) and unidentified keeled planktonic foraminifera (possibly a globotruncanid, top middle) in burrowed foraminifera wackestone in the Austin Chalk. H) Unidentified keeled planktonic foraminifera (left, globotruncanid) and hedbergellid foraminifera (right) in Austin Chalk (burrowed foraminifera wackestone).

Burrowed skeletal wackestone in the Buda Limestone from 4,032.5-4,100 ft contains a very different faunal assemblage as compared to the overlying Eagle Ford Group (Fig. 43). The Buda Limestone is dominated by calcispheres and Hedbergellidae (Fig. 44). No Heterohelicidae or keeled planktonic foraminifera were found in this interval.

The greatest enrichment of inoceramid filaments (Fig. 44) occurs from 3,909-3,905 ft (Fig. 43). Filaments and radiolarians comprise the dominant assemblage in this interval, while all varieties of foraminifera are rare or absent. Heterohelicidae are narrow with very little test size increase between chambers, and have been identified as *Heterohelix moremani*.

Depth 3,851.4 ft contains a diverse assemblage of keeled planktonic foraminifera, as well as Hedbergellidae, Heterohelicidae, calcispheres, and inoceramid filaments. *Rotalipora greenhornensis* and *Rotalipora cushmani* are both identified in the thin-section (Figs. 43, 44). The first documentation of *Heterohelix globulosa* is observed at 3,827 ft.

The interval from 3,600-3,700 ft contains different faunal abundances when compared to other portions of the Eagle Ford Group (Fig. 43). Radiolarians and calcispheres are the dominant fossil type, with fewer amounts of planktonic foraminifera (Fig. 43). Unidentified keeled planktonic foraminifera through the interval are rare to absent.

Above 3,583 ft, the faunal assemblage and abundance changes compared to underlying Eagle Ford Group deposits (Fig. 43). In this section, all documented faunal abundances decrease, while variety of fauna and diversity remain high. Radiolarians do not appear above 3,583ft (Fig. 43). Keeled planktonic foraminifera (globotruncanids) in

this section are the most commonly observed fauna and the most abundant – this trend is not observed anywhere else within the core.

Interpretation

The Buda Limestone is dominantly composed of coccoliths and assorted fauna (Kerans and Loucks, 2013). Two main fauna can be identified in thin-section (Fig. 44): Hedbergellidae planktonic foraminifera and calcispheres. Both fauna indicate high levels of productivity at the surface. Absence of Heterohelicidae and keeled planktonic foraminifera imply that water conditions were not preferable for intermediate and bottom-water dwelling planktonic foraminifera (Figs. 40, 44). Pervasive burrowing throughout the Buda Limestone supports well-oxygenated bottom sediment.

The lower Eagle Ford strata contain relatively persistent Hedbergellidae and Heterohelicidae (Fig. 43). Appearances of both indicate that surface-waters and intermediate water depths had moderate levels of productivity; water in these intervals was oxygenated. Heterohelicidae present are narrow with small test chambers (*Heterohelix moremani*). Sporadic appearances of keeled planktonic foraminifera and inoceramid bivalves indicate that deepwaters were periodically suboxic (oxygen levels rose above what would be defined as anoxic). Inoceramid filament enrichment (Figs. 43, 44) at 3,905-3,909 ft is interpreted as the inoceramid filament event that occurs prior to the OAE2 (Negra et al., 2011; Denne et al., 2014). A brief period of deep-water oxygenation is documented at 3,851 ft by a diverse assemblage of deep dwelling, oligotrophic (BouDagher-Fadel, 2013; Denne, 2014), matrix-supported keeled planktonic foraminifera (Fig. 44). Within this lamination, both marker foraminifera *Rotalipora greenhornensis* and *Rotalipora cushmani* have been identified signaling the upper Cenomanian.

Documentation of *Heterohelix globulosa* observed at 3,827 ft helps to define the boundary between Cenomanian and Turonian and between the upper and lower Eagle Ford strata (Figs. 43, 44). This stage transition is coincident with the documented OAE2 (see *Isotope Data*, Fig. 49)

The upper Eagle Ford strata contain Hedbergellidae, Heterohelicidae, calcispheres, inoceramid, and inoceramid filaments (Fig. 43). Hedbergellidae and Heterohelicidae occur in greater abundance within the upper Eagle Ford strata than in the lower Eagle Ford strata, suggesting that intermediate and surface-waters may have been better oxygenated (Figs. 14, 43). Keeled planktonic foraminifera are rare and commonly coincide with the appearance of inoceramid bivalves, indicating rare deep-water dysoxia. A substantial fauna shift occurs at the top of the upper Eagle Ford strata (Fig. 43). Abundance of planktonic foraminifera decrease substantially; radiolarians and calcispheres become the dominant preserved fauna. Both radiolarians and calcispheres suggest open marine deposition on slope or shelf environment (Berkyova, and Munnecke, 2010; Flügel, 2004).

Both Hedbergellidae and Heterohelicidae are common (Fig. 43) throughout the upper and lower Eagle Ford strata suggesting generally consistent surface level productivity and common intermediate water-depth productivity. Rare appearances of keeled planktonic foraminifera indicate sporadic occurrences of increased levels of oxygen at depth. These trends suggest a stratified water-column.

The Austin Chalk (defined lithologically) contains the lowest general abundances of fauna (Fig. 43). Hedbergellidae and Heterohelicidae are present but rare, and keeled planktonic foraminifera (possibly globotruncanids) become the more common variety of planktonic foraminifera (Fig. 44). This shift in dominant planktonic foraminifera variety

(Fig. 43) indicates a more consistently oxygenated deep-water environment, or potentially better circulation and renewal of oxygen to deepwaters.

Winterbotham J.M. Jr. #1 Conventional Core

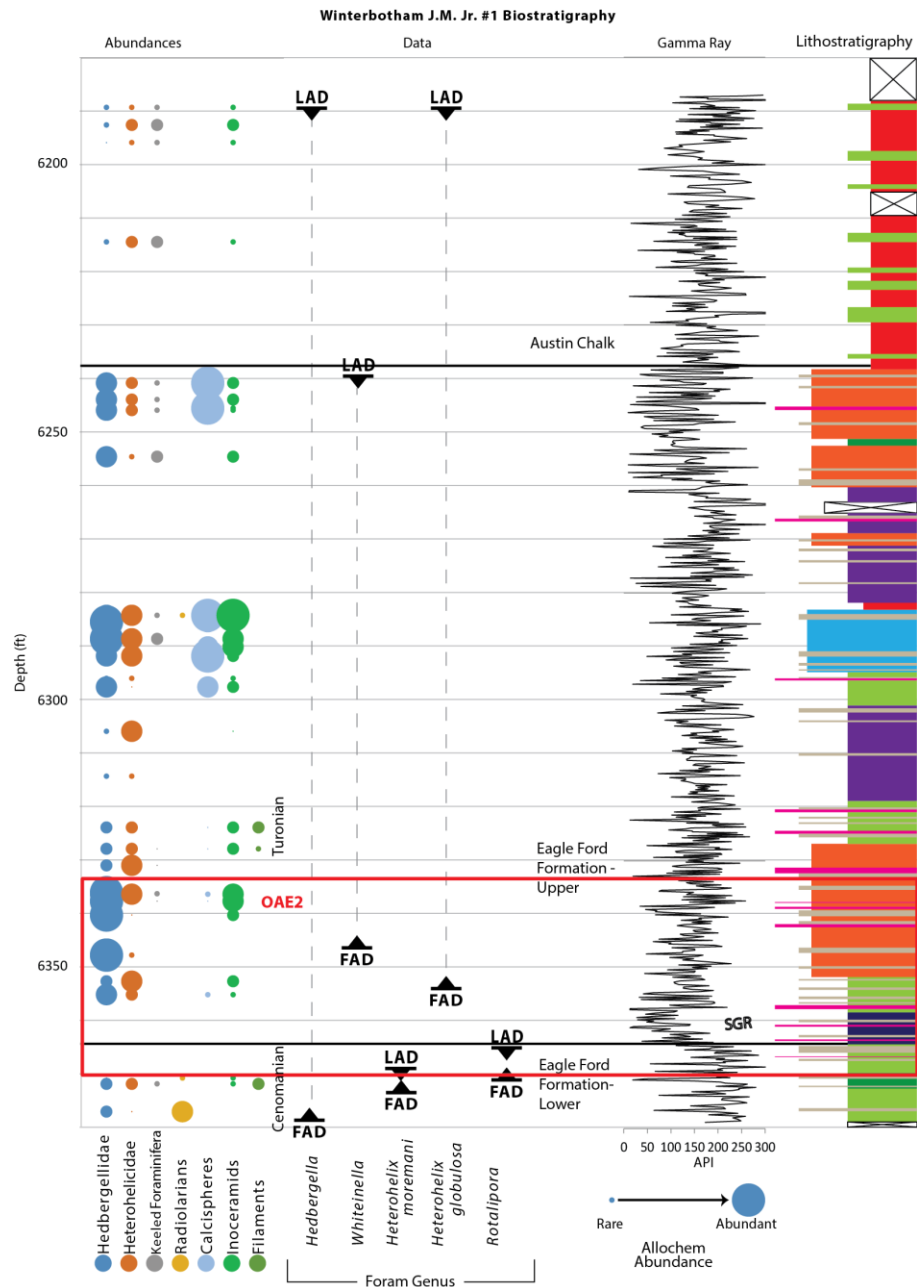


Figure 45: Winterbotham J.M. Jr. #1 core biostratigraphy. Bubble size denotes general abundance, smaller bubbles correlate to rare or lesser abundance, larger bubbles correlate to common or extremely abundant. FAD = first appearance datum, LAD = last appearance datum. The red box shows the position of the OAE2.

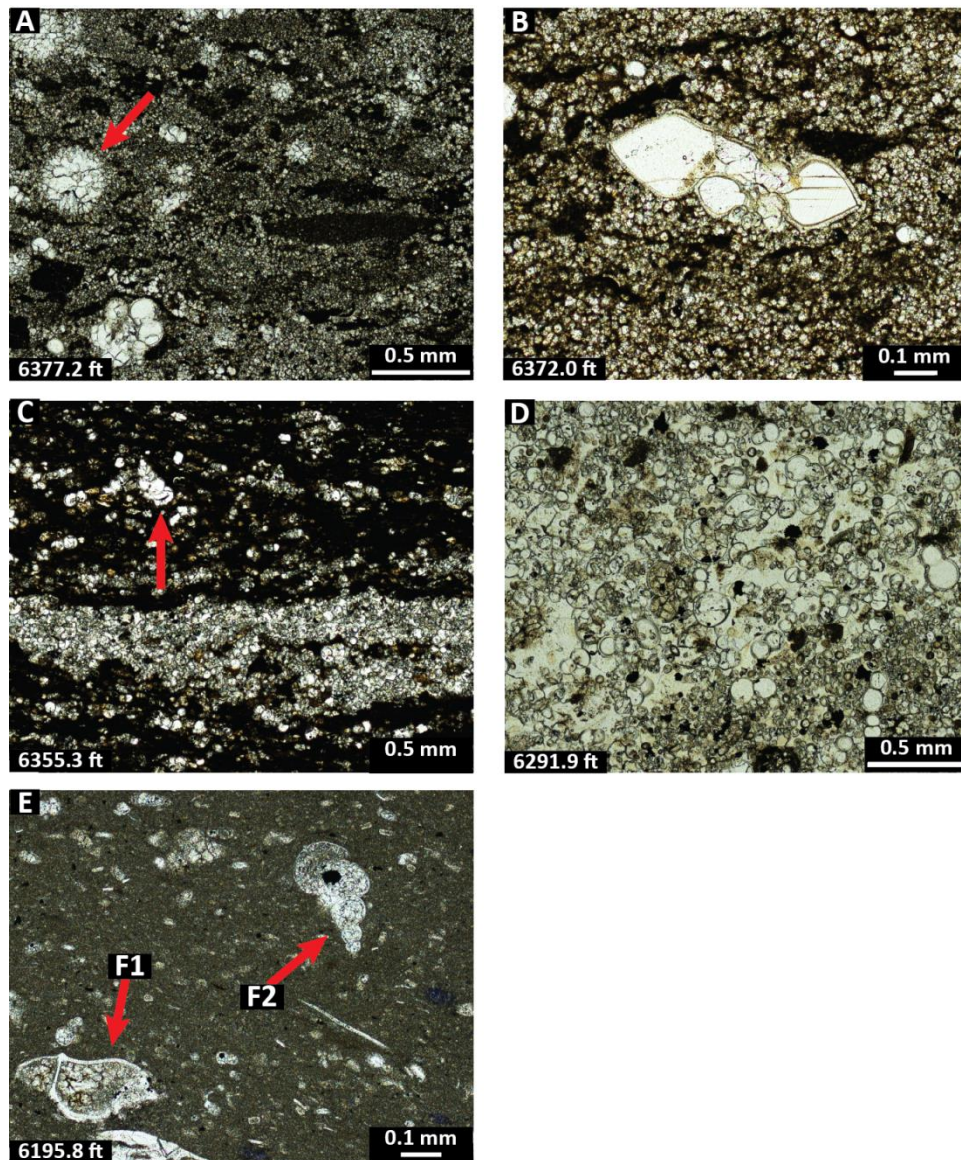


Figure 46: Photo plate of Winterbotham J.M. Jr. #1 core biostratigraphy microfossils. A) Calcite recrystallization within the remnant of a radiolarian in the lower Eagle Ford (laminated argillaceous planktonic foraminifera wackestone). B) Possible *Rotalipora* sp. in the lower Eagle Ford. C) *Heterohelix globulosa* ? (red arrow) in the upper Eagle Ford (laminated argillaceous planktonic foraminifera wackestone). D) Calcite-cemented, undifferentiated *Hebergella* sp. and calcispheres in the upper Eagle Ford (in mass transport unit similar to laminated skeletal grain-dominated packstone). E) Unidentified keeled planktonic foraminifera (E1) and *Heterohelix globulosa* ? (E2) in the Austin Chalk (burrowed foraminifera wackestone).

The sole substantial documentation of common radiolarians occurs at 6,377 ft (Fig. 46A). Heterohelicidae, keeled planktonic foraminifera, calcispheres, inoceramid, and filaments are absent from this individual core sample.

At 6,372 ft, the core contains moderate abundances of several different faunal groups (Fig. 45). Heterohelicidae tests are narrow with small chambers. Filaments are common draping lamination surfaces. Keeled planktonic foraminifera are documented but cannot be identified to acute certainty.

Heterohelicidae documented at 6,355 ft are globular and obtuse and interpreted as Turonian-age, *Heterohelix globulosa* (Figs. 45, 46).

The deformed and transported unit from 6,286-6,295 ft contains very abundant calcispheres (Figs. 45, 46). This is the first documented appearance of abundant calcispheres within the Winterbotham J.M. Jr. #1 core; calcispheres as a dominant bioclast does not agree with deposited beds immediately above or below.

Faunal abundance decreases sharply above 6,238ft (Fig. 45). Undifferentiated keeled planktonic foraminifera are more commonly observed through the upper portion of the core.

Interpretation

Biostratigraphy with proposed stratigraphic divisions is presented in Figure 45. The lower and upper Eagle Ford strata contain several different fauna (Fig. 45). Hedbergellidae planktonic foraminifera are the most common and most abundant taxon observed in this section. This shows that primary productivity was present and active within surface and shallow waters. Abundant calcispheres also support high surface level productivity (Fig. 45). Calcispheres within slumped beds show that more proximal sediments where slumps originated also have high primary productivity at the surface

(Fig. 46). Heterohelcidae are also common, suggesting some oxygen was available (not anoxic). At a depth of 6,372 ft (Figs. 45, 46) the last *Heterohelix moremani* is documented. At a depth of 6,355 ft (Figs. 45, 46), the lowest Turonian *Heterohelix globulosa* are documented. The observance of *Heterohelix globulosa* at 6,355 ft allows for the placement of the Cenomanian-Turonian boundary between 6,355-6,372 ft. The C-T transition zone as defined here, in addition to change in molybdenum concentration (Figs. 12, 15), has been used to define the boundary between lower and upper Eagle Ford strata. Rare appearances of keeled planktonic foraminifera show that deeper water depths were only rarely subjected to increases of oxygen concentrations. Periodic inoceramid documentation infer that oxygen levels were low near the sediment-water interface. The majority of inoceramid fragments documented are broken because of transport and do not represent their in-situ conditions; unbroken, bedding-parallel shells may have been in situ. Radiolarians are present within peloidal crystalline mudrock.

The Austin Chalk contains Hedbergellidae, Heterohelcidae, undifferentiated keeled planktonic foraminifera (possibly globotruncanids), and inoceramids (Fig. 45). Abundances of each fauna are low compared to the underlying Eagle Ford strata, possibly because of sediment homogenization related to burrowing. The presence of oligotrophic planktonic foraminifera (rotaliporids and globotruncanids) indicates nutrient availability or nutrient levels were low or restricted, as well as potential low levels of oxygen in deepwater. This is in agreement with documented inoceramids within the section (Fig. 45). The presence of inoceramids indicate oxygen levels were low at the sediment-water interface.

Isotope Data

Measurements of $\delta^{13}\text{C}$ can be helpful in determination of organic matter provenance, as well as identifying the OAE2. By definition, the OAE2 is defined by a positive excursion of $\delta^{13}\text{C}$ (Schlanger, et al., 1976). $\delta^{15}\text{N}$ has been omitted from this sample set because nitrogen values were too low within these samples to produce a reliable $\delta^{15}\text{N}$ data set. All carbon discussed is from the organic carbon fraction, not inorganic carbon.

Land-plants use atmospheric CO_2 to produce organic matter with $\delta^{13}\text{C}$ values near -27‰ whereas marine algae use dissolved bicarbonate to produce organic matter with $\delta^{13}\text{C}$ values between -20‰ to -22‰ . (O'Leary, 1988; von Breymann et al., 1991; Meyers, 1994; Meyers, 1997). The atomic ratio of C/N for vascular land-plants is 20 or greater, whereas the atomic C/N ratio for algae is between 4 and 10 (Premuzic et al., 1982; Jasper and Gagosian, 1990; Meyers, 1994; Prahl et al., 1994).

HOT SPRINGS OUTCROP

The average $\delta^{13}\text{C}$ value is -27.83‰ . The most positive excursion of $\delta^{13}\text{C}$ occurs at 65.5ft with a value of -21.91 . These data are plotted against depth in Figure 47.

Figure 48 contains two cross plots. Graph A shows $\delta^{13}\text{C}$ versus C/N. Graph B contains TOC weight percent plotted against molybdenum parts per million. Correlation is poor; the slope of a trend line plotted through the data is 1.27.

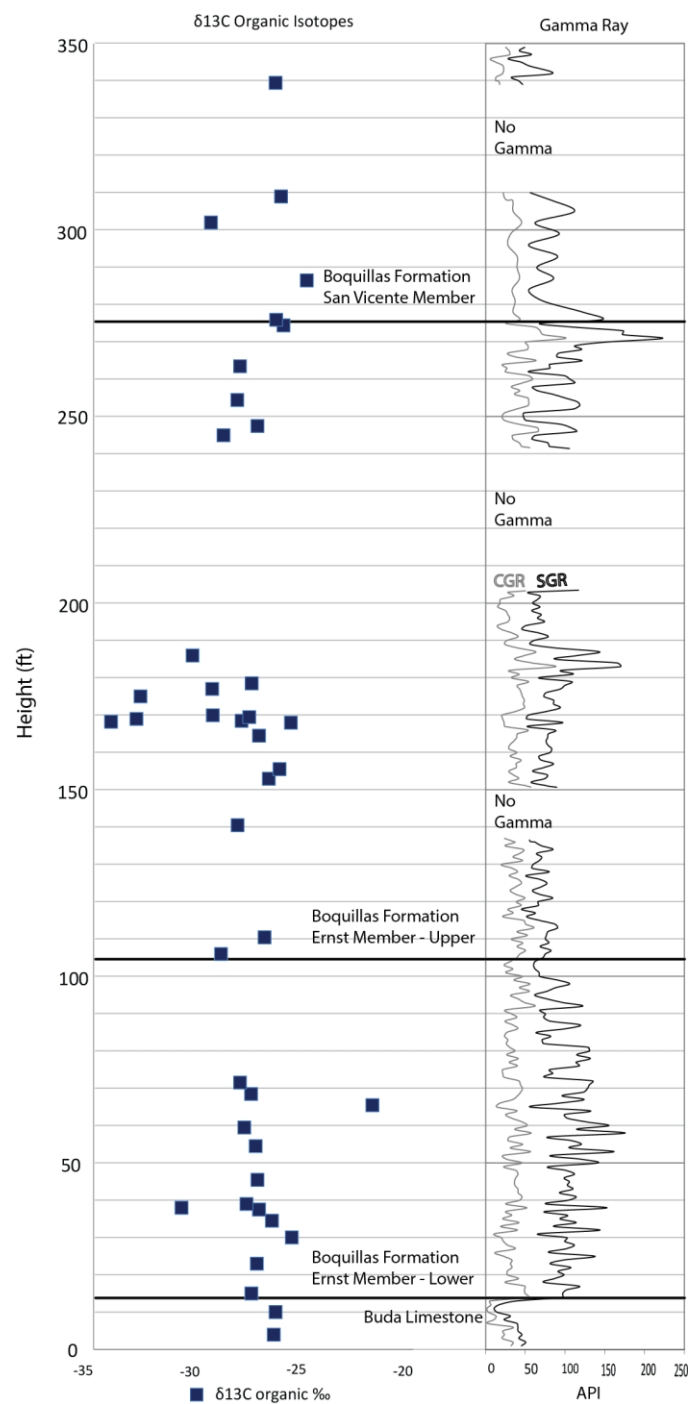


Figure 47: Hot Springs outcrops isotope stratigraphy. Data points are plotted individually without a trend line because of poor data resolution. Gamma ray is included for correlation.

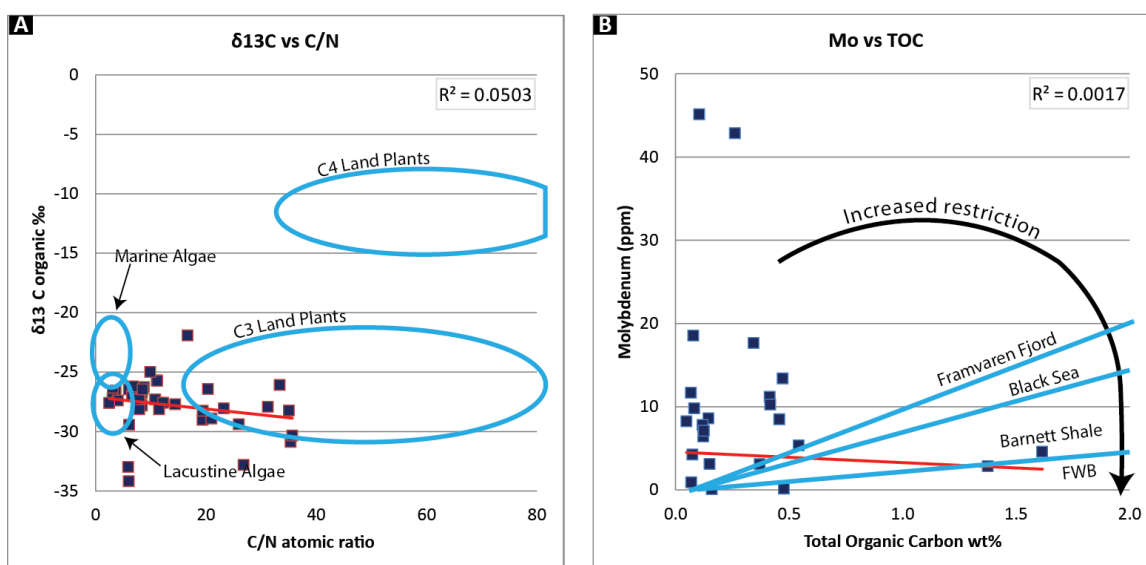


Figure 48: Hot Springs outcrops organic carbon crossplots. A) Annotations after Meyers (1997) help delineate organic matter variety. B) Annotations after Algeo and Lyons (2006) and Rowe et al. (2008) showing basin restriction.

Interpretation

The Buda Limestone has an average $\delta^{13}\text{C}$ of -26.5 ‰ (Fig. 47). This value is more positive than the accepted value for pure terrestrial organic matter, indicating that marine algal organic matter is present. Marine and algal matter dominance in the Buda Limestone is in agreement with fauna and facies discussed in previous chapters.

The lower Ernst Member of the Boquillas Formation has an average $\delta^{13}\text{C}$ of -27.2 ‰ (Fig. 47). Two data points demonstrate a positive excursion from the average $\delta^{13}\text{C}$ baseline, one at 30 ft with a value of -25.7 ‰ and one at 65.5 ft with a value of -21.9 ‰. The first excursion at 30 ft may be interpreted as the OAE2; however, with poor data resolution this footage is not confirmed as the OAE2. The second excursion at 65.5 ft is in the accepted range for marine-organic matter; however, because this excursion is not acknowledged in adjacent data, this excursion cannot be interpreted as the OAE2.

The upper Ernst Member has an average $\delta^{13}\text{C}$ of -28.5 ‰ (Fig. 47). The $\delta^{13}\text{C}$ value is nearest that of terrestrial land-plants; however, this value is largely because of degradation of organic material during settling. Comparing lithofacies and fauna, it can be concluded that the organic carbon accumulated within the system is from marine organisms.

The San Vicente Member of the Boquillas Formation has an average $\delta^{13}\text{C}$ of -26.8 ‰ (Fig. 47). The $\delta^{13}\text{C}$ is the most positive value within the section, signaling more input of marine-organic matter.

The slope of the C vs. N trend line (Fig. 48) is outside of the traditional Redfield Ratio slope for accepted C/N slope (Redfield et al., 1934; Hecky et al., 1993). The accepted Redfield Ratio for marine phytoplankton is between 3-8 defined by the C:N:P, 106:16:1 ratio. While the slope may be skewed because of terrestrial plant organic matter influence and organic matter degradation, outcrop weathering may have also greatly impacted the accuracy of the ratio. Extremely low quantities of Mo ppm and TOC % (Fig. 48) cause the slope and y-intercept to not correlate with basins reported on by Algeo and Rowe (2006) or Rowe et al. (2008).

Figure 48 includes annotated cross plots for the Hot Springs outcrop samples. The red line in both graphics shows the trend line for each cross plot's dataset. Low sample quantity and sample weathering has caused poor correlativity of measured data. Data show that organic matter at the Hot Springs outcrops is composed of algae (Fig. 48). Data plotted in Figure 48 show a negative slope displaying poor correlation of the data set. Because TOC is greatly decreased because of surface weathering, these data cannot be used to confidently draw a conclusion regarding degree of basinal restriction.

CORE-X CONVENTIONAL CORE

The average value of $\delta^{13}\text{C}$ in the core is -26.76 ‰ (Fig. 49). Two positive excursions of $\delta^{13}\text{C}$ are outlined within the red boxes. Excursions have a magnitude of between 2 and 5 points.

Figure 50 contains two cross plots. The graph on the left shows $\delta^{13}\text{C}$ versus C/N. The crossplot on the right compares molybdenum parts per million to weight percent total organic carbon. A trend line of the data has a slope of 0.27.

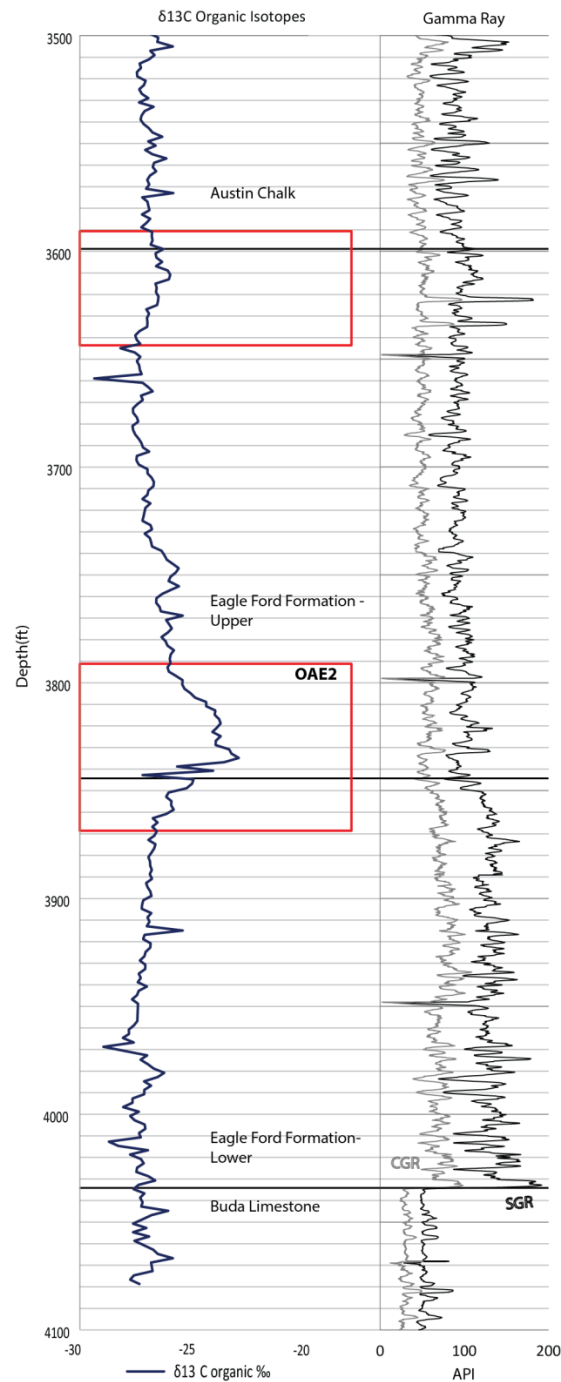


Figure 49: Core-X conventional core isotope stratigraphy. Two red boxes outline areas of positive excursions of $\delta^{13}\text{C}$. The OAE2 encompasses the lower positive isotope excursion. Gamma ray is included for correlation.

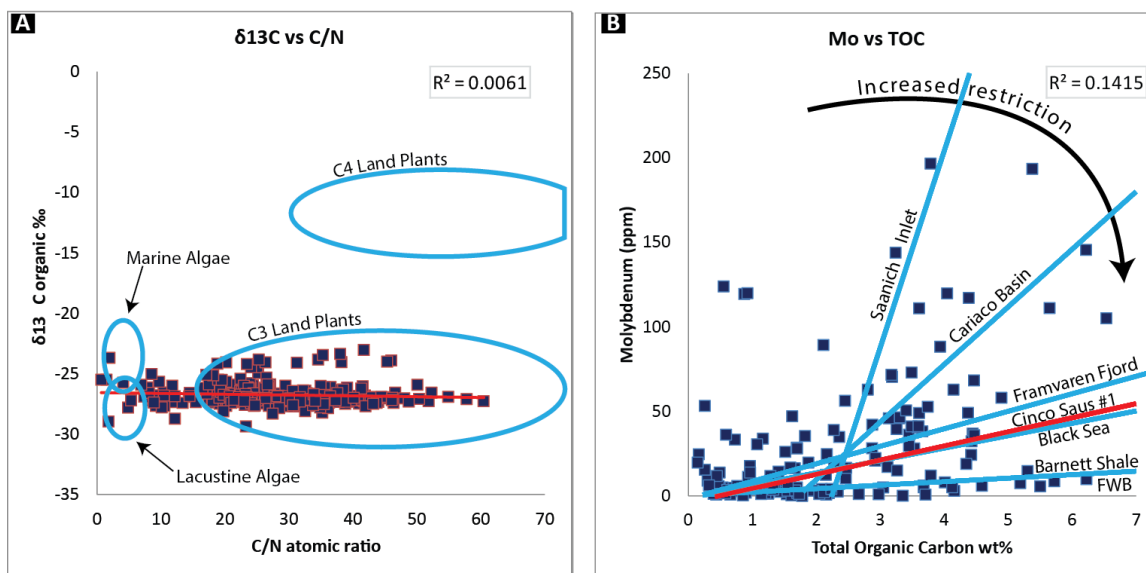


Figure 50: Core-X conventional core organic carbon crossplots. A) Annotations after Meyers (1997) help to delineate organic matter variety. B) Annotations after Algeo and Lyons (2006) and Rowe et al. (2008) show basin restriction.

Interpretation

The Buda Limestone has an average $\delta^{13}\text{C}$ of -27.2 ‰ and a range of -27.8 ‰ to -25.9 ‰ (Fig. 49). The average $\delta^{13}\text{C}$ values are acceptable for marine carbon organic material. Values may be skewed because of degradation of organic material during settling.

The lower Eagle Ford strata an average $\delta^{13}\text{C}$ of -27.1 ‰ and a range of -28.9 ‰ to -25.0 ‰ (Fig. 49). These values suggest relatively normal marine carbon cycling with some possible input of terrestrial and dominant algal matter being preserved.

A red box traces the contact between the lower and upper Eagle Ford strata in the $\delta^{13}\text{C}$ curve (Fig. 49). This highlighted area from 3,795-3,851 ft contains a positive excursion of $\delta^{13}\text{C}$ to the most positive value of -23.04 ‰. This represents a 4 ‰ positive excursion. This zone is interpreted as the OAE2 using the initial definition defined by Schlanger and Jenkyns (1976). The positive excursion contains three peaks and two

troughs, consistent with OAE2 descriptions from around the world (Pearce et al., 2009; Jarvis et al., 2011). More positive values of $\delta^{13}\text{C}$ are meant to reflect increased preservation of marine-organic matter. Considering molybdenum and manganese values within the same interval (Figs. 10, 14), it can be concluded that at least one period of the OAE2 was oxygenated. Oxygenation during an anoxic event is counter intuitive; however, elemental data and bioturbated lithofacies coincident with the event confirm sediment and bottom-water oxygenation. C/N values increase during the third (youngest) peak of the OAE2 suggesting that more terrestrial organic matter was also being buried (Fig. 50). Positive $\delta^{13}\text{C}$ suggests a strong marine algal signal. Preserved TOC decreases into the OAE2, slightly increasing during the third (youngest) peak.

The upper Eagle Ford strata has an average $\delta^{13}\text{C}$ is -26.8 ‰ with a range from -29.4 ‰ to -23.04 ‰ (Fig. 49). The extremely positive maximum $\delta^{13}\text{C}$ value represents the third stage (last and broadest peak) of the OAE2. The more negative minimum of -29.4 ‰ and an average of -26.4 ‰ show burial of algal organic matter.

The second red box, outlining the area from 3,590-3,646 ft (Fig. 49), contains a second, smaller positive $\delta^{13}\text{C}$ excursion. This section has a net excursion of 2.15 ‰ away from the baseline. This interval correlates with an increase redox sensitive trace metals molybdenum and vanadium. This section appears to represent a secondary anoxic event at the top of the upper Eagle Ford strata.

The Austin Chalk has an average $\delta^{13}\text{C}$ of -26.9 with a range from -25.9 to -27.5 (Fig. 49). These values suggest influence from land-plant and marine algal preservation.

Figure 50 contains annotated cross plots. Figure 50A is used to determine the variety of organic matter presented in the Core-X core. The trend shows that organic matter may be mixed in provenance. Figure 50B shows Core-X core data plotted against other known restricted and low-oxygen basins (Algeo and Lyons, 2006; Rowe et al.,

2008). The Core-X trend line plots nearly parallel to that of the Black Sea. The Black Sea has experienced extreme hydrographic restriction and very slow deep-water renewal time between 500-4000 years (Algeo and Lyons, 2006). Data show that the depositional environment of the lower Eagle Ford strata in Core-X within the Maverick Basin was extremely restricted with very slow deep-water renewal times.

WINTERBOTHAM J.M. JR. #1 CONVENTIONAL CORE

Figure 51 shows $\delta^{13}\text{C}$ data for the Winterbotham J.M. Jr. #1 conventional core. The average value of $\delta^{13}\text{C}$ within the core is -25.51 ‰ . $\delta^{13}\text{C}$ vs. depth displays a positive $\delta^{13}\text{C}$ excursion of 2-4 points within the red outlined box.

Figure 52 contains two cross plots. The cross plot of the left shows $\delta^{13}\text{C}$ versus C/N. The cross plot on the right shows molybdenum parts per million plotted against TOC weight percent. A trend line through the data has a slope of 6.66.

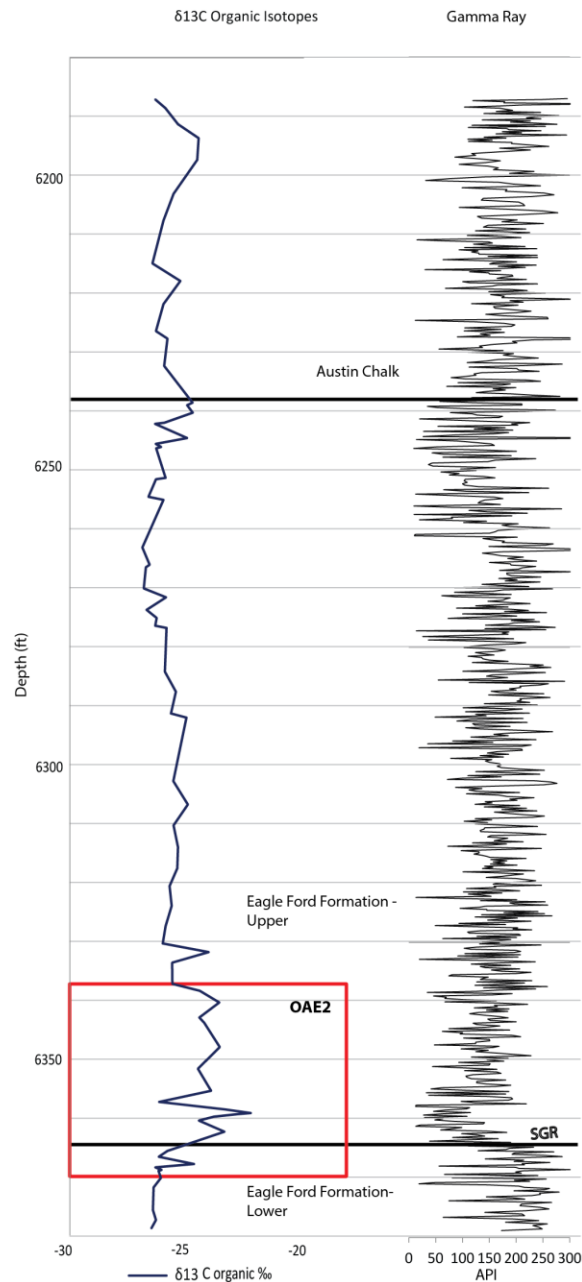


Figure 51: Winterbotham J.M. Jr. #1 conventional core isotope stratigraphy. The red box outlines a zone of positive excursions of $\delta^{13}\text{C}$. The OAE2 occurs during the boxed positive isotope excursion. Gamma ray is included for correlation.

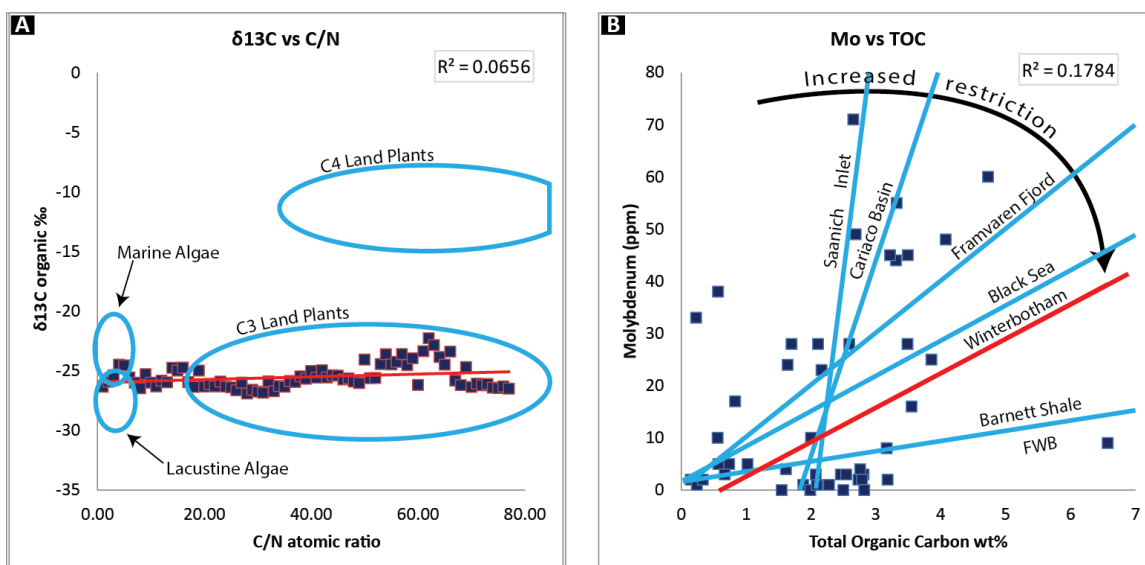


Figure 52: Winterbotham J.M. Jr. #1 conventional core organic carbon crossplots. A) Annotations after Meyers (1997) help to delineate organic matter variety. B) Annotations after Algeo and Lyons (2006) and Rowe et al. (2008) show basin restriction.

Interpretation

The lower Eagle Ford strata contain the most negative values of $\delta^{13}\text{C}$, with an average of -26.1‰ (Fig. 51). These values are associated with carbon that was preserved that was dominantly from marine algal carbon with minor contributions from land plant material.

A red box outlines an interval from 6,338-6,368 ft (Fig. 51). This 30 ft interval contains a three peak, two trough pattern that defines the overall positive $\delta^{13}\text{C}$ excursion. The excursion is between 2-3 ‰ from the underlying baseline average. This isotopic shift is interpreted as the OAE2 based on the Schlanger (1987) definition. The first of the three peaks occurs within the Cenomanian stage lower Eagle Ford strata. The following two peaks occur within the Turonian stage upper Eagle Ford strata (stage boundaries have been defined previously within Biostratigraphy). The positive excursion of $\delta^{13}\text{C}$ implies increased burial of marine or algal organic matter (Schlanger, 1987). Dissimilar

to the original definition of an OAE, the event that occurs within the Winterbotham J.M. Jr. #1 appears to be oxygenated. Oxygenation during the OAE2 in this study is defined by manganese enrichment, molybdenum depletion, and $\delta^{13}\text{C}$ troughs. The onset of the second (middle) $\delta^{13}\text{C}$ peak is coincident with the detrital element enrichment (Fig. 12). C/N atomic ratio averages 18.2 during the excursion, indicating increased algal organic matter influence as compared to adjacent rocks (Fig. 51).

After the OAE2 positive $\delta^{13}\text{C}$ excursion, values of $\delta^{13}\text{C}$ return back to a more negative baseline, with an average of -25.8 (Fig. 51). This value is consistent with normal marine-organic matter.

The Austin Chalk is influenced the most by algal organic matter. $\delta^{13}\text{C}$ has an average of -25.7, which is an accepted value for a marine-dominated system (Fig. 51). This is in agreement with observed fauna.

Figure 52 contains annotated cross plots for the Winterbotham J.M. Jr. #1. $\delta^{13}\text{C}$ plotted against C/N atomic ratio (Fig. 52A) demonstrates that the majority of organic matter within the system originated from C3 land-plants, with lesser marine algal organic matter influence (Meyers, 1997). A trend line plotted through molybdenum versus TOC demonstrates basinal restriction using methods developed by Algeo and Lyons (2006) and Rowe et al. (2008). A trend line of the data collected in this study shows that the depositional environment present during Eagle Ford Group deposition was highly restricted – plotting between the Black Sea and Barnett Shale.

CARBON ISOTOPE REGIONAL COMPARISON

Investigation of the OAE2 has been ongoing since its identification (Schlanger et al., 1987). The OAE2 by definition is the ‘Cenomanian-Turonian stage boundary anoxic

event' (Schlanger et al., 1987); however, the event has been documented to occur during an approximately 500 kyr period (Sageman et al., 2006; Voigt et al., 2008). The OAE2 as defined by a positive $\delta^{13}\text{C}$ excursion (Schlanger and Jenkyns, 1976) and is documented in this study to contain three main excursion $\delta^{13}\text{C}$ peaks (Figs. 49, 51). The localities herein present the C-T boundary occurring (as identified biostratigraphically) within the OAE2. This study has also documented burrowing (Figs. 26, 36, 38) and planktonic foraminifera (Figs. 43, 44, 45, 46) that present oxygenation during the OAE2 (Figs. 49, 51). This finding differs from the classic understanding of an anoxic event (Schlanger and Jenkyns, 1976) as being 'anoxic' and having specific deposition/lithologic style (extremely condensed, OM-rich resulting from such conditions).

Figure 53 displays $\delta^{13}\text{C}$ data as recorded in this study compared with the $\delta^{13}\text{C}$ data presented by Phelps (2011) and Donovan et al. (2012). The carbon isotope data provided in Phelps (2011) displays a similar positive excursion as that defined by this study (Figs. 49, 51, 53). The Wilson County data set (east of Maverick and Zavala Counties) uses 5-8 ft sample spacing, whereas this study uses a 2 ft sample spacing (Table 1). Larger sample spacing effectively decreases resolution of the data and may cause for a 'smoothing' of the main OAE2 excursion. While Phelps (2011) does not recognize the three individual peaks documented in the positive $\delta^{13}\text{C}$ excursion as shown in this study (Figs. 49, 51, 53), the duration of the OAE2 event and position in relation to the C-T boundary is very similar: the OAE2 begins in the late Cenomanian and the maximum positive $\delta^{13}\text{C}$ excursion occurs at the C-T boundary. The Terrell County isotope data (located west of Maverick and Zavala Counties) shown in Donovan et al. (2012) defines the OAE2 as younger than the C-T boundary using carbon isotope data and nannofossils. The OAE2 described by Donovan et al. (2012) is younger than that defined by this study (Figs. 49, 51, 53). Additionally, while the OAE2 in Terrell County (Fig. 53; Donovan et al., 2012)

shows two peaks during the $\delta^{13}\text{C}$ excursion, a third older, positive $\delta^{13}\text{C}$ excursion is not included in the interpreted OAE2. Including this older, positive $\delta^{13}\text{C}$ excursion into the defined OAE2 would create a $\delta^{13}\text{C}$ curve profile more similar to those presented within this study. Lowery et al. (2014) uses a similar Terrell County (Lozier Canyon) data set and defines the OAE2 to be a more extensive event as compared to what Donovan et al. (2012) proposes. Lowery et al. (2014) contains the first, older positive excursion that occurs at the C-T boundary (Fig. 53). Considering the defined position of the OAE2 in Terrell County, it is suggested that the OAE2 may have started earlier in Maverick, Zavala, and Wilson Counties. This observation suggests that the OAE2 may have begun earlier in the Cenomanian in the east and central portions of the Texas paleoshelf, and did not impact areas of West Texas until the early Turonian.

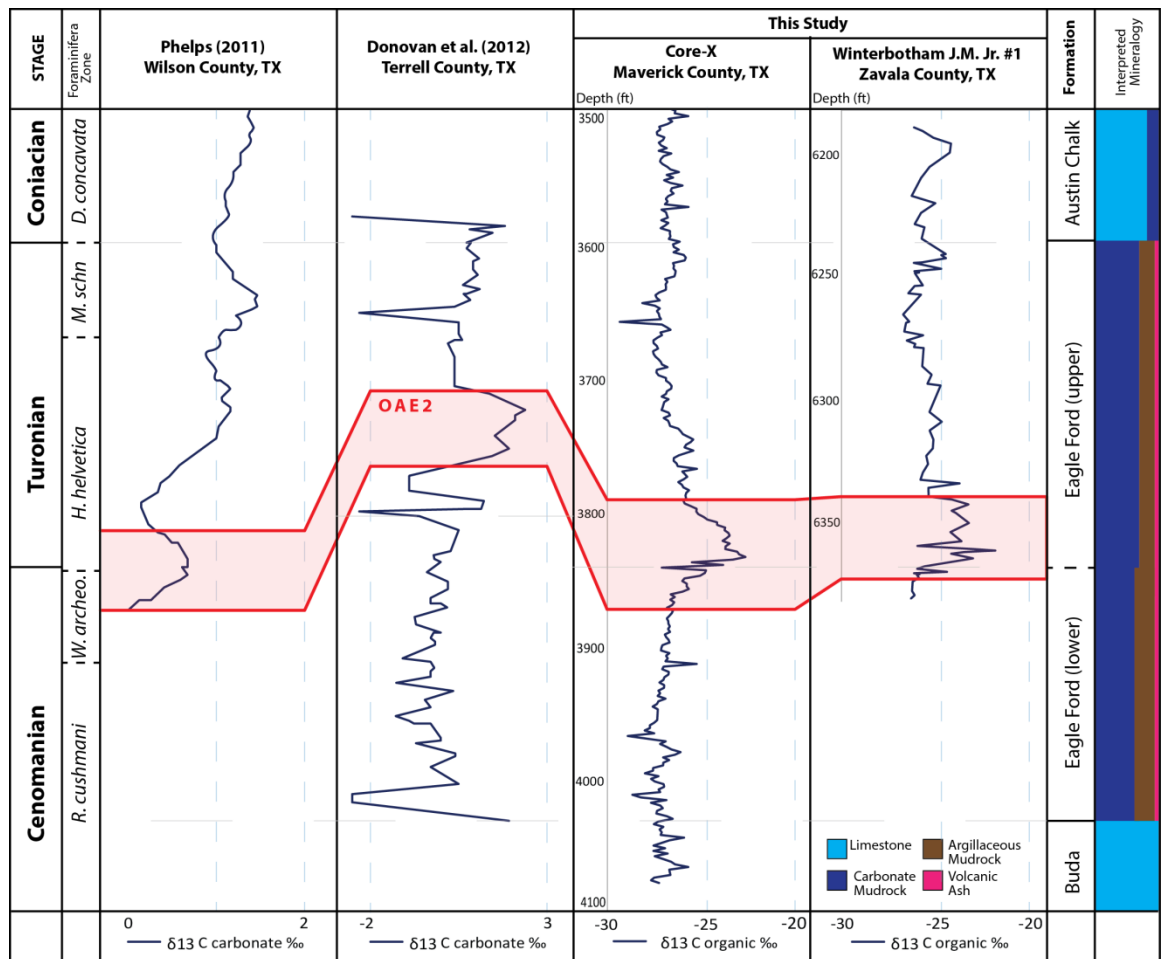


Figure 53: Comparison of $\delta^{13}\text{C}$ Data. Carbon isotope data is provided from Phelps (2011) and Donovan (2012) for comparison of the interpreted OAE2 shown in this study.

INTEGRATION OF MULTIDISCIPLINARY DATA SETS

Lithofacies, biostratigraphy, chemostratigraphy, and stratal architecture are integrated to create a comprehensive data set used to best define environmental and depositional conditions during accumulation of the Boquillas Formation and Eagle Ford Group.

Hot Springs Outcrop

The Hot Springs outcrop section within Big Bend National Park demonstrates a dynamic environment (Fig. 54). The Buda Limestone represents a burrowed, open-marine, shelfal limestone with little influence from detrital sediment deposition or terrestrial organic matter. $\delta^{13}\text{C}$ and C/N indicate that organic matter is dominantly algal. A major unconformity separates the Buda Limestone and the Boquillas Formation (Fig. 54).

The Cenomanian-age lower Ernst Member was deposited under anoxic conditions indicated by molybdenum enrichment (Fig. 54). Keeled planktonic foraminifera are rare, indicating deepwater was rarely oxygenated (Fig. 41). Burrowing is non-existent to rare and sedimentary features are well-preserved (Fig. 54). Preserved ripples and winnowed laminations indicate that deposition was influenced by bottom-currents (Figs. 20, 54). Organic matter was better preserved within the lower Ernst Member (as compared to underlying and overlying strata) because of anoxic conditions at the time of sediment and organic matter accumulation (Figs. 13, 16). Organic matter consists of a mix between algae and land-plants; however, algae are the more dominant organic matter variety (Figs. 16, 47, 48). High productivity near the ocean surface is indicated by organic-matter accumulation and the persistent appearance of Hedbergellidae.

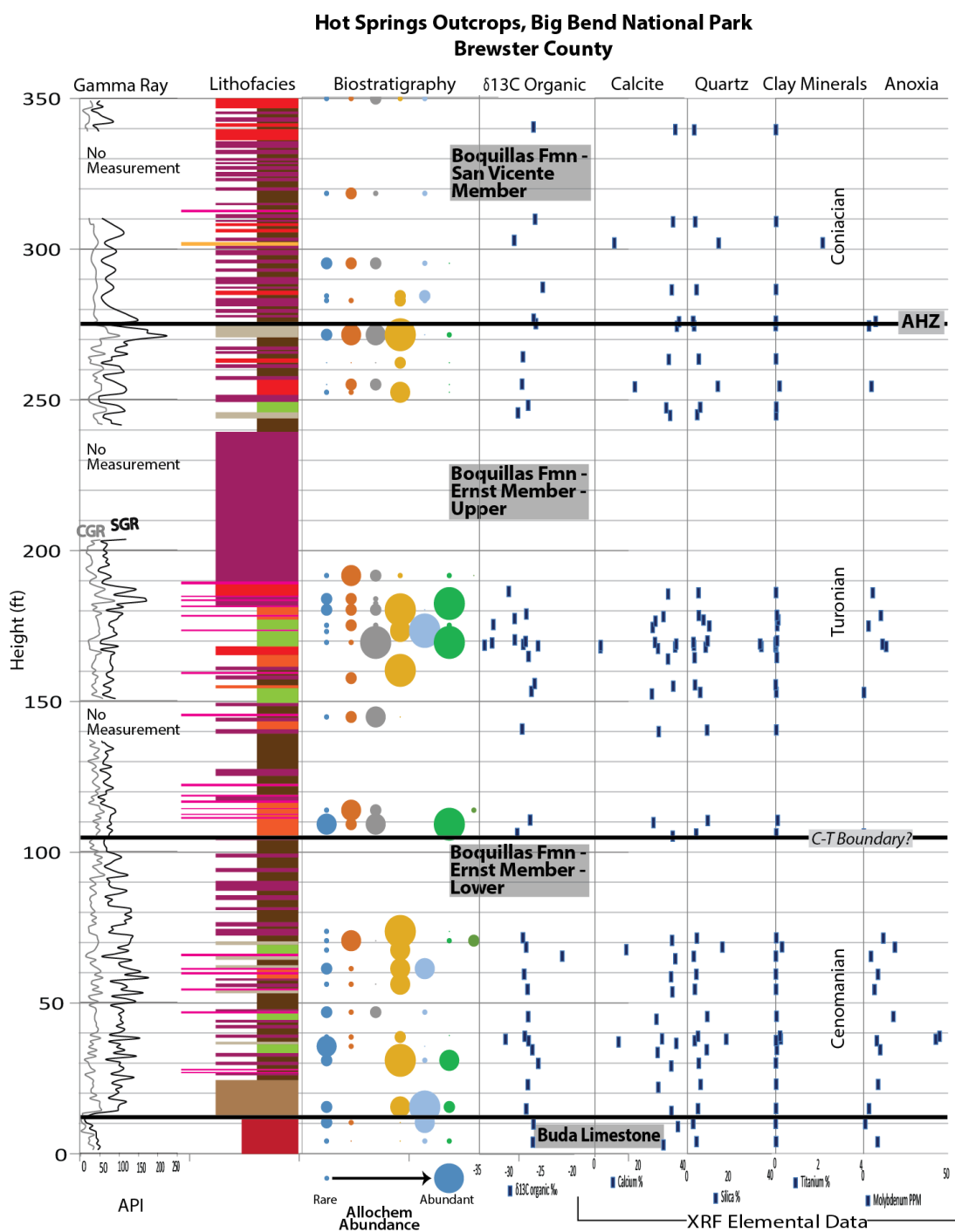


Figure 54: Hot Springs outcrop composite stratigraphy. Graphic integrates data from individual data sets to show correlation. Color keys for lithofacies and biostratigraphy are included in Fig. 35 and Fig. 41.

The upper Ernst Member represents deposition during the Turonian stage as identified by the appearance of *Heterohelix globulosa* planktonic foraminifera (Figs. 41, 42, 54). The morphological change from narrow tests (*Heterohelix moremani*) to globular tests (*Heterohelix globulosa*) indicates the transition into the Turonian section (Fig. 54). The upper Ernst Member has more commonly oxygenated deepwater as indicated by the presence of keeled planktonic foraminifera; however, the depositional setting was commonly anoxic at the sediment-water interface demonstrated by lack of burrowing and molybdenum enrichment (Figs. 8, 13, 41, 42, 54). Anoxia allowed for preservation of TOC (Figs. 13, 16). $\delta^{13}\text{C}$ and C/N show that terrestrial plant organic matter increased in the upper Ernst Member when compared to the lower Ernst Member (Figs. 16, 47, 48). The contact with the overlying San Vicente Member is gradational – burrowed, shelfal limestone alternates with laminated lithofacies until the burrowed limestone is the dominant lithofacies (Fig. 54).

The contact between the Ernst Member and the San Vicente Member is indicated by the AHZ zone and represents the Turonian-Coniacian stage boundary (Fig. 54). Deposition in the Coniacian is represented by healthy, shelfal limestone with little to no influence by terrestrial plant organic matter (Figs. 16, 41, 42). Marine algae are the dominant organic matter type (Fig. 16, 47). TOC is poorly preserved because of an oxygenated water-column (Fig. 16, 47, 48).

Core-X Conventional Core

The Eagle Ford Group (as represented by the Core-X) was deposited in a dynamic environment under the influence of bottom-waters and variable ocean-water oxygenation. The documented succession contains the OAE2 and the C-T boundary, shown both chemically and biologically. Figure 55 contains a composite section of important and defining curves for the Core-X.

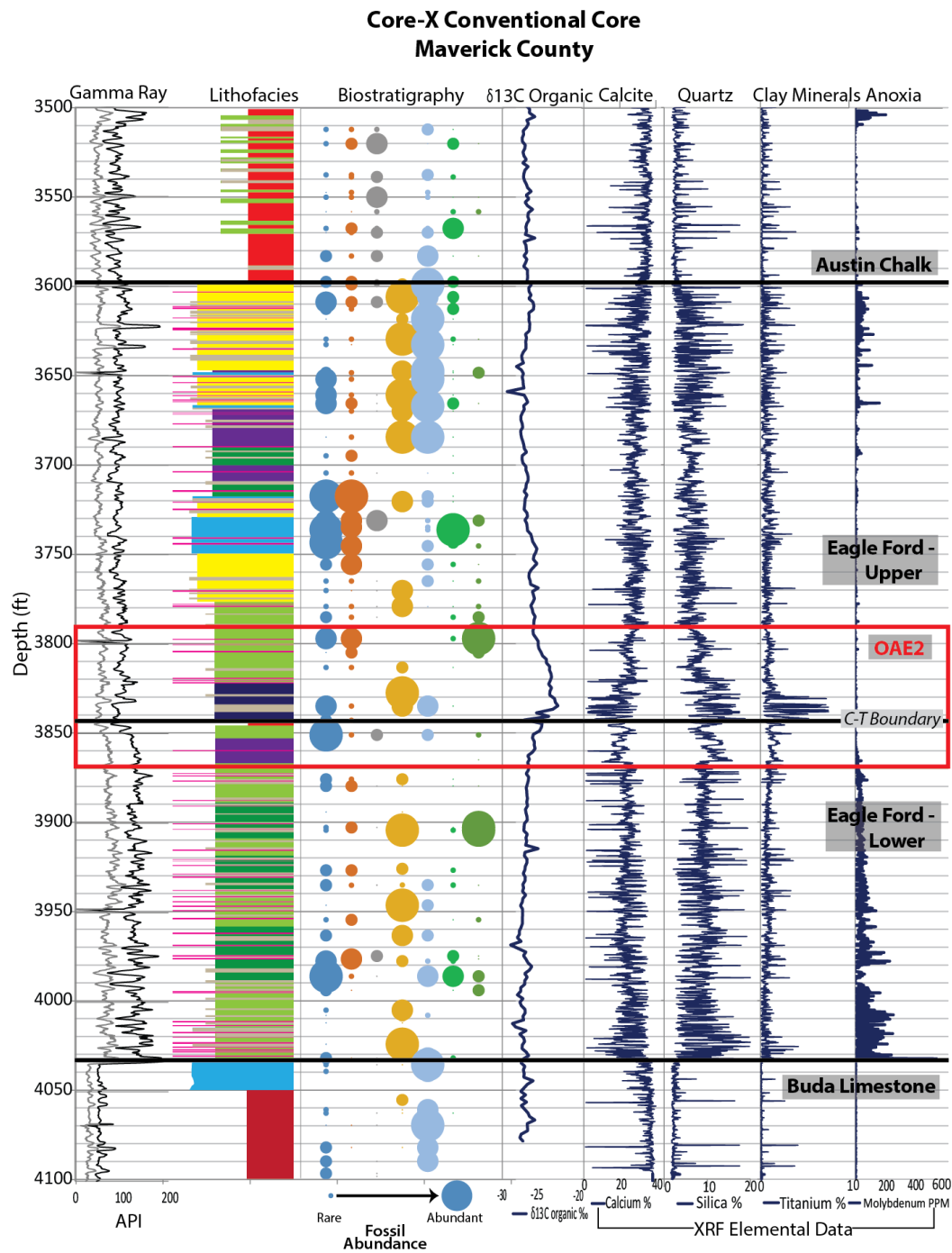


Figure 55: Core-X composite stratigraphy. Graphic integrates data from individual data sets to show correlation. Color keys for lithofacies and biostratigraphy are included in Fig. 36 and Fig. 43.

The Buda Limestone underlying the Eagle Ford Group represents a normal, open-marine shelfal limestone dominated by intrabasinal carbonate sedimentation (Fig. 55). Detrital clay sedimentation occurs as discrete beds that have been pervasively undergone pressure solution and were partially dolomitized (Figs. 9, 10). Lack of sedimentary features, with the exception of burrowing, documents homogenization of sediments as a result of bioturbation (Fig. 19).

The contact between the Buda Limestone and Eagle Ford Group represents a major unconformity (Fig. 37). Striking changes are documented in gamma ray data, lithofacies, volcanic ash abundance, and elemental composition (Figs. 9, 10, 14, 17, 55). The depositional environment shifts from that of a normal, open-marine, carbonate platform to an anoxic, stratified shelf (Fig. 55).

Cenomanian stage deposition in the lower Eagle Ford strata occurs under dominantly anoxic bottom-water conditions (Fig. 55). Major basinal restriction of the deepwater mass caused slow deep-water renewal times (Fig. 50). The water-column remained density stratified throughout Cenomanian time (Figs. 14, 43, 44). A gradational decrease observed in molybdenum values nearing the upper Eagle Ford strata is related to depletion of molybdenum within the stagnant water-column, not the introduction of oxygenated bottom-waters (Fig. 14). Intermediate and surface depth waters remained oxygenated and able to support primary producers as documented redox sensitive elements (Fig. 14), as well as the appearance of Hedbergellidae and Heterohelicidae planktonic foraminifera tests (Figs. 43, 44). Heterogeneity is preserved in lithofacies laminations and in elemental alternations (Figs. 9, 10, 14, 36); lack of burrowing allows for original lamination-scale heterogeneity to be preserved. TOC is preserved best in the lower Eagle Ford strata related to the perpetuation of anoxic bottom-water conditions (Figs. 14, 17). Carbon and nitrogen data show that the dominant preserved TOC is marine

with some possible influence from land plants, possibly transported through the air/dust (Figs. 10, 49, 50). Deeper water oxygenation occurs in the top of the lower Eagle Ford strata observed by the appearance of keeled planktonic foraminifera such as *Rotalipora cushmani* (Figs. 43, 44).

The Cenomanian-Turonian stage boundary, as well as the OAE2, occurs at the contact between the lower-upper Eagle Ford strata (Fig. 55). The OAE2 is a 56 ft interval defined by a positive $\delta^{13}\text{C}$ excursion of 4 ‰ (Figs. 49, 55). The excursion is composed of three peaks and two troughs, and demonstrates an increased preservation of marine carbon (Figs. 49, 55). The excursion documented within the Core-X is an oxygenated (at least partially) event documented by a 1.5 ft interval of pervasive bioturbation and oxic chemofacies dominated by manganese enrichment (Figs. 10, 14, 26). Water-column mixing introduces oxygen and renews trace metals shown by manganese enrichment within the OAE2 at the base of the upper Eagle Ford strata (Figs. 10, 14, 26). The C-T boundary is identified using Cenomanian and Turonian marker planktonic foraminifera. *Rotalipora cushmani* is identified at the top of the lower Eagle Ford strata (Figs. 43, 44). Heterohelicide morphology can be traced across the boundary (Figs. 43, 44) – tests in the Cenomanian are acute (*Heterohelix moremani*), tests in the Turonian are globular (*Heterohelix globulosa*).

The upper Eagle Ford strata display an immense degree of depositional heterogeneity both in lithofacies, chemofacies, and ocean chemistry (Fig. 55). The base of the upper Eagle Ford strata is defined by the influx of a detrital, manganese and titanium-rich chemofacies (Figs. 9, 10, 14). This distinct elemental character correlates with massive argillaceous claystone deposits (Figs. 10, 23, 36). The majority of the upper Eagle Ford strata is well-laminated and contains well-preserved ripples in the upper laminated calcisphere grainstone (Fig. 24, 36). Well-developed ripples infer the presence

of periodic, if not constant, bottom-current interaction at the sediment-water interface (Fig. 36). Burrowing occurs at the lamination-scale (~5 mm), exhibiting brief periods of habitability at the sea floor (Fig. 36). Planktonic foraminifera and calcispheres suggest that surface level primary productivity was moderate to high during deposition (Figs. 14, 36). Sporadic appearances of keeled planktonic foraminifera infer deep-water oxygenation and enough nutrient availability to support oligotrophic habitation (Figs. 43, 44). Elemental abundances within the upper Eagle Ford strata demonstrate an immense amount of heterogeneity (Figs. 10, 14). While described lithofacies are dominantly marine, chemofacies show that 10-15% of sediment (Table 6) is derived from extrabasinal, terrigenous sedimentation in the form of clay minerals and quartz (Figs. 10, 14). Primary productivity is high, reflected in nutrient enrichment (Fig. 14). A secondary anoxic event is present in the uppermost upper Eagle Ford strata confirmed by lack of burrowing or deep-water fauna, molybdenum enrichment, and a positive $\delta^{13}\text{C}$ (Figs. 10, 14, 36, 43, 49).

The Austin Chalk represents the gradational transition from the anoxic, laminated lower and upper Eagle Ford strata to a normal, open-marine carbonate platform present during Austin Chalk deposition (Fig. 55). Burrowing within the sediment has erased the majority of sediment heterogeneity (Figs. 26, 36). Increased molybdenum values at the top of Core-X in the Austin Chalk document a third period of low oxygen (Figs. 10, 14). Presence of keeled planktonic foraminifera throughout the Austin Chalk confirms deposition within an oxygenated deepwater mass (oligotrophic habitability) with brief periods of anoxia, likely driven by high-primary productivity shallower in the water-column (Figs. 10, 14, 43, 44).

Winterbotham J.M. Jr. #1 Conventional Core

The Winterbotham J.M. Jr. #1 was deposited in an environment under the influence of bottom-currents and variable ocean chemistry. The core has been divided into three distinct depositional systems defined using chemofacies and biostratigraphy. The C-T boundary and OAE2 are both present and definable within the system. Figure 56 compares different data sets used for interpretation.

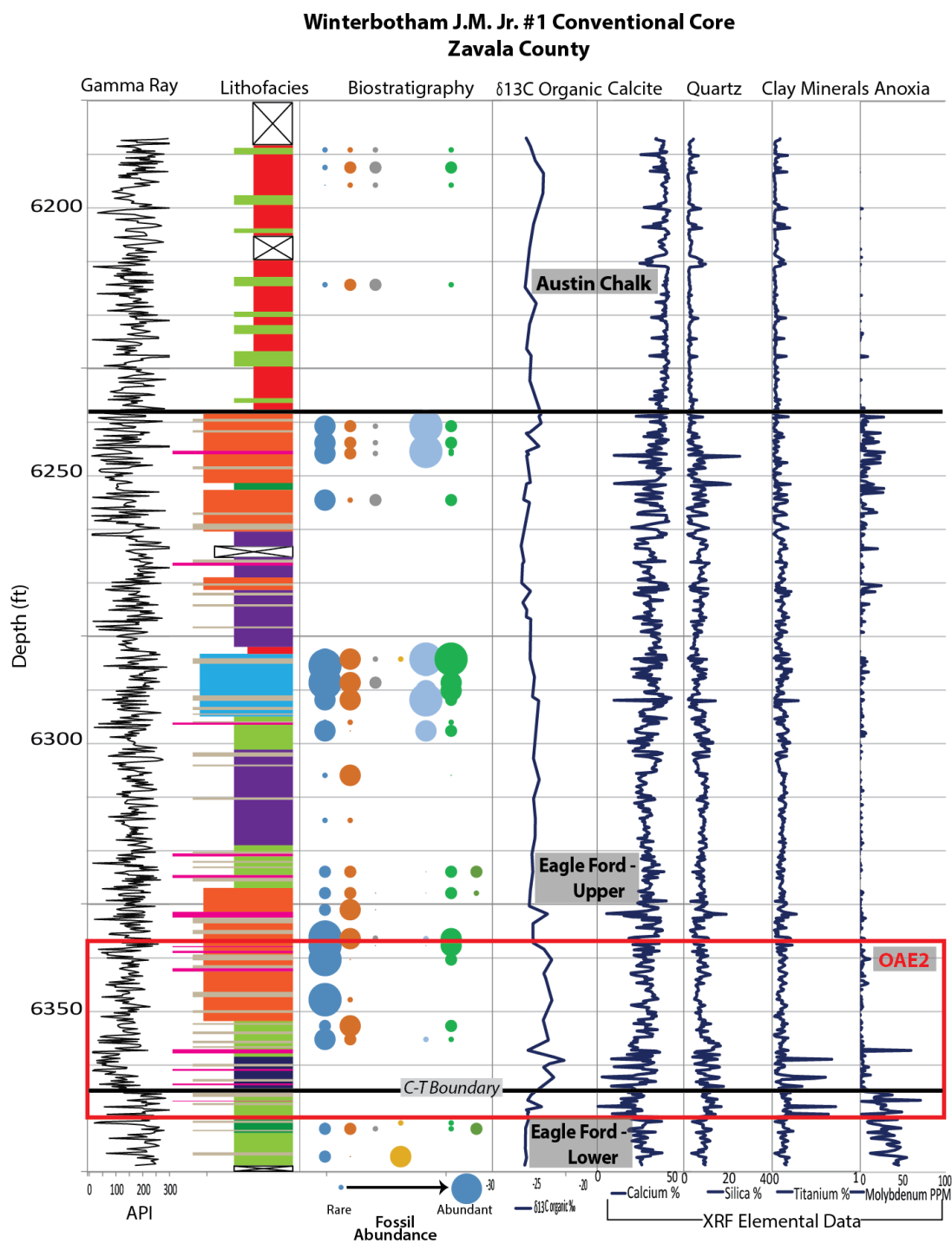


Figure 56: Winterbotham J.M. Jr. #1 composite stratigraphy. Graphic integrates data from individual data sets to show correlation. Color keys for lithofacies and biostratigraphy are included in Fig. 38 and Fig. 45.

The lower Eagle Ford strata in the Winterbotham J.M. Jr. #1 represent deposition in a restricted basinal environment under anoxic conditions (Fig. 56). Winnowed, starved ripples demonstrate bottom-current influence through the reworking of deposited fauna (Figs. 20, 21). Heterohelicidae within the lower Eagle Ford strata exhibit test morphologies indicative of Cenomanian planktonic foraminifera *Heterohelix moremani* (Figs. 45, 46). Presence of Hedbergellidae and Heterohelicidae planktonic foraminifera in tandem with high-nutrient levels express an environment with high productivity at intermediate and surface level water depths (Figs. 45, 46, 56). Oxygenation at intermediate depths and anoxia at deeper depths (lack of burrowing and increased molybdenum) infers a density stratified body of water present during Cenomanian deposition of the lower Eagle Ford strata (Figs. 12, 15, 45, 46).

The contact between lower and upper Eagle Ford strata marks a major change in depositional environment, as well as the C-T boundary and onset of the OAE2 (Fig. 56). The OAE2 within the Winterbotham J.M. Jr. #1 is a partially oxygenated event defined by a positive excursion of $\delta^{13}\text{C}$ (Figs. 15, 51). The OAE2 consists of three peaks, the lowermost beginning within the lower Eagle Ford strata during dominantly anoxic conditions (Figs. 15, 51). The upper two $\delta^{13}\text{C}$ excursions occur within the upper Eagle Ford strata and occur during a major oxygenation event as defined by increased manganese and decreased molybdenum (Figs. 12, 15, 51). Heterohelicidae tests observed in the lowest upper Eagle Ford strata exhibit test morphologies indicative of Turonian species (*Heterohelix globulosa*); thusly, marking the lowest Turonian in the Winterbotham J.M. Jr. #1 (Figs. 45, 46). The base of the upper Eagle Ford strata is defined by a titanium-rich detrital influx indicating a major change in sediment provenance (Fig. 12).

The upper Eagle Ford strata exhibit Turonian-stage deposition dominated by punctuated detrital influence, an increase in land-plant organic matter, and slope instability (Figs. 12, 15, 45, 46, 56). Lack of major or pervasive bioturbation within the upper Eagle Ford strata has allowed for preservation of heterogeneity in lithofacies and chemofacies (Fig. 56). Elemental abundances demonstrate that the detrital terrigenous influx commonly impacted the system and primary productivity remained high (Fig. 12). Slumping, folding, gravity-flows, and intraclasts demonstrate instability at a more proximal location during upper Eagle Ford strata deposition (Fig. 38). High primary productivity defined by nutrient-rich chemofacies and abundance of Hedbergellidae and Heterohelicidae is interpreted as the catalyst for low oxygenation, shown by increased molybdenum ppm (Figs. 12, 15) documented at the top of the upper Eagle Ford strata. Periods of low-oxygen and nutrient levels in deeper water (oligotrophic zone, sediment-water interface, or within the sediment) demonstrate periodic stratification of the water mass (Figs. 12, 15, 45, 46).

The Austin Chalk represents a transitional depositional environment from variably anoxic in the lower and upper Eagle Ford strata to that of an open-marine, carbonate platform present during Austin Chalk deposition (Fig. 56). Fauna are less abundant within the Austin Chalk; however, keeled planktonic foraminifera are more common, indicating a mixed and oxygenated body of water compared to the density stratified water-column present during underlying Eagle Ford deposition (Figs. 45, 46). Elemental abundances record sediment homogenization dominated by oxic, intrabasinal carbonates (Figs. 12, 15).

REGIONAL STRATIGRAPHY AND CORRELATION

Correlation between individual data sets is difficult because of the distance between each data set, and issues correlating outcrop and subsurface data. The following is an attempt to discuss the correlations between data sets, as well as short-comings in the data presented within this study. The following figure (Fig. 57) graphically represents correlation between the three data sets discussed herein.

A regional comparison of the data presented and discussed within this study shows that time-line correlation and formation correlation can be traced between locality data sets. The thickness and coverage of each section is variable, causing problems for reliable correlations. The Hot Springs outcrops and Core-X section both contain a full section from the Buda Limestone through the San Vicente Member and Austin Chalk. This section encompasses Cenomanian-Coniacian-age strata. The section presented within Core-X is thicker than that presented at the outcrops in Brewster County. The Zavala County data set does not represent a full 'Eagle Ford' section; the Buda Limestone and a portion of the lower Eagle Ford are missing. Comparing general thickness of the sections demonstrates a thickening of the section, and subsequent deposition, within the Maverick Basin in Maverick County.

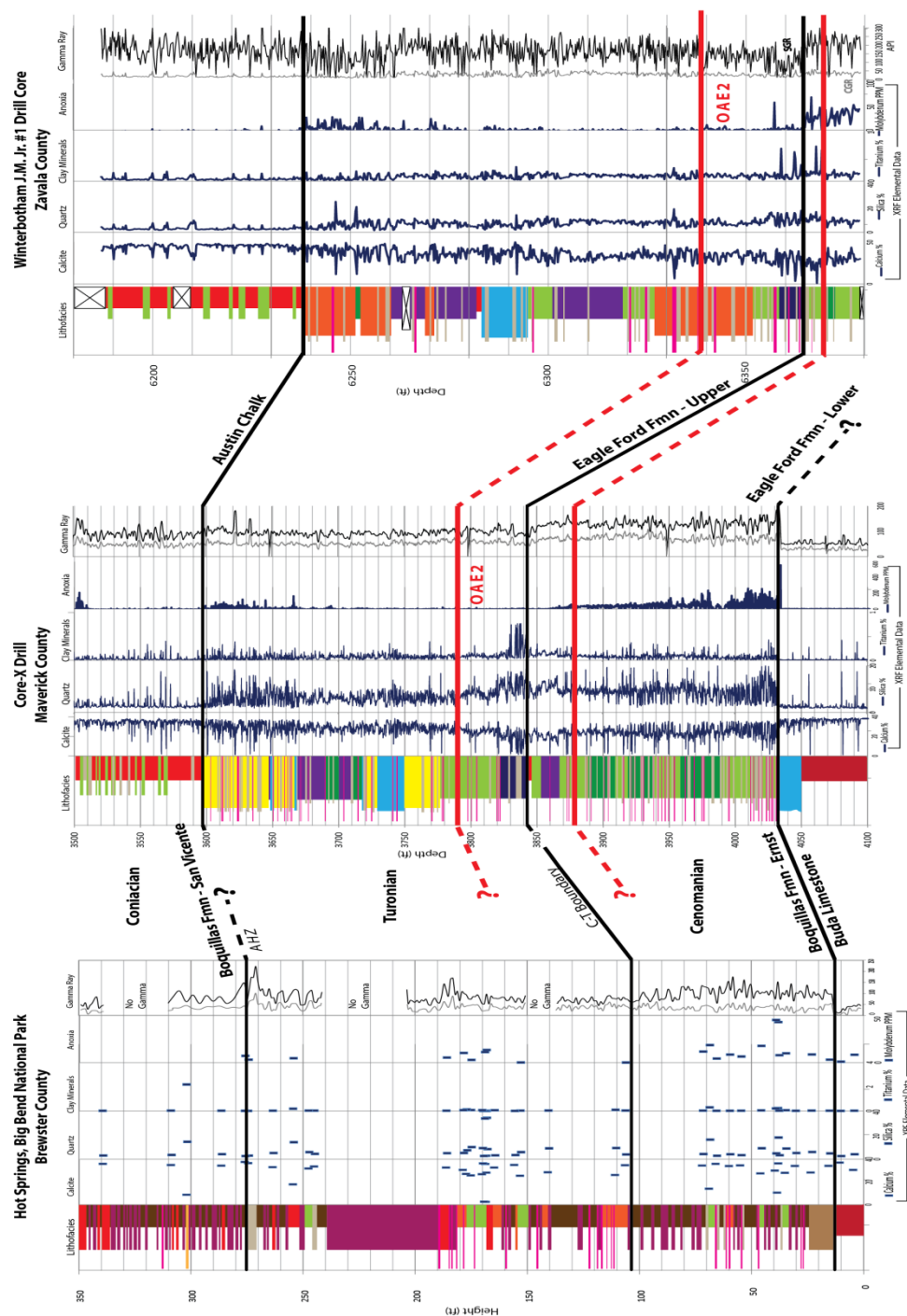


Figure 57: Regional cross section comparing all three data sets. CGR, SGR, calcium, silica, titanium, molybdenum (ppm), and $\delta^{13}C$ have been included for comparison. Cross section is not to scale and represents suggested correlations.

Outcrop versus Subsurface Data

Correlativity of outcrop to subsurface data is difficult because of outcrop weathering, degradation of original elemental signatures, and poor sampling resolution. Lithofacies defined petrographically demonstrate similarities in sedimentary features and faunal assemblages (Figs. 54, 55, 56). Laminated lithofacies in the lower Eagle Ford strata and lower Ernst Member show lack of burrowing within the original sediment and reworking of fauna by bottom-currents (Figs. 21, 22). Faunal assemblage similarities in planktonic foraminifera and inoceramids found within outcrop and subsurface deposits agree that deposition occurred during oxygen-deficient to anoxic water conditions with high productivity within surface-waters (Figs. 54, 55, 56). Molybdenum enrichment documented in outcrop and core confirms that the lower Ernst and Eagle Ford strata are deposited under anoxic conditions (Figs. 54, 55, 56). Simultaneous high surface-water productivity and anoxic bottom-waters suggests a stratified water-column (Figs. 54, 55, 56). While maximum basin restriction occurred within the lower Eagle Ford strata within both cores, degradation of organic matter at the outcrop has inhibited for a concrete interpretation to be made regarding restriction of the lower Ernst Member (Figs. 47, 49, 51). This unit is concluded to be an analog to subsurface lower Eagle Ford depositional environments.

The upper Eagle Ford strata and upper Ernst Member show agreement in changing sedimentary processes and fauna (Figs. 54, 55, 56). Both units contain increased detrital sediment, as well as gravity-flows, folded and deformed beds, and slumps (Figs. 8, 10, 12, 54, 55, 56). Keeled planktonic foraminifera become more common indicating better oxygenation of deepwaters (Figs. 41, 43, 45). Burrowing increases through the section, but is rarely pervasive (Figs. 54, 55, 56). Burrows are

contained to discrete laminations (Fig. 24, 25, 27). Molybdenum values indicate periodic anoxia during deposition of upper Ernst and Eagle Ford strata (Figs. 13, 14, 15). While there are several similarities regarding generalizations, exact lithofacies and chemical signatures do not correlate between outcrop and core using the data presented in this study (Fig. 57). This is because of differences in sampling scales, degradation of outcrop chemical and elemental signatures, and discrepancy of visual characteristics based on weathering have sufficiently obscured relatable data to inhibit accurate conclusions.

While the Austin Chalk and San Vicente Members are not chrono-synchronous, a major deviation can be seen in variety of sedimentation occurring in the units above the Ernst and lower/upper Eagle Ford strata (Fig. 57). While both units are pervasively bioturbated, there is a contrast in organic matter provenance. Isotopic data for the San Vicente Member depicts a strongly marine, algal-dominated environment with minimal land-plant organic matter contribution (Figs. 48, 50, 52). The Austin Chalk, while also demonstrating a marine-organic matter dominated environment, contains more (if only a small amount) land-plant matter contribution (Figs. 48, 50, 52).

From the data collected in this study, it can be concluded that outcrop and core sections from different intervals on the South Texas Shelf can be correlated on a broad, general scale (Fig. 57). The lower Eagle Ford Group or Ernst Member is laminated, shows influence of bottom-currents, has similar lithofacies, and was deposited during water-mass stratification and deep-water anoxia (Fig. 57). The upper Eagle Ford Ernst Members contain a more diverse faunal assemblage, substantial increase in grain abundance, periodic mass-wasting episodes on both multiple scales and increased oxygenation (Fig. 57). Because of immense, small-scale heterogeneity, these units cannot be correlated on a bed or lithofacies scale between wells. Additionally, poor resolution

and degradation of organic matter at the surface has caused for incompatible data sets between outcrop and subsurface.

Comparison between Core-X and Winterbotham J.M. Jr. #1 Cores

Both the Core-X and Winterbotham J.M. Jr. #1 cores contain three main stratigraphic divisions defining different depositional environments (Fig. 57). These two localities provide evidences of very similar depositional systems mineralogically, chemically, and lithologically (Figs. 55, 56). Core-X and the Winterbotham J.M. Jr. #1 also show similar character of the OAE2 defined isotopically and biostratigraphically (Fig. 53). The Winterbotham J.M. Jr. #1 is missing almost the entire lower Eagle Ford strata; however, the portion that is there can help to correlate the Zavala County section to Core-X in Maverick Basin using elemental, biostratigraphic, and isotopic data (Fig. 57).

The lower Eagle Ford represents Cenomanian-age sediments deposited in a dominantly anoxic setting under maximum basinal restriction (Figs. 14, 15, 50, 52). Deep-water renewal was extremely slow (Figs. 50, 52). The water-column was density stratified – oxygen-levels at intermediate and shallow-water depths were high enough to support biologic productivity (Figs. 43, 45). The presence of inoceramids demonstrates that the sediment-water interface sometimes contained minimal levels of oxygen (Figs. 43, 45). Bottom-currents influenced sediment accumulation by reworking fauna into starved ripples (Figs. 20, 21). Differences between organic matter results in the lower Eagle Ford of Core-X and Winterbotham J.M. Jr. #1 is may reflect increased degradation of marine-organic matter before settling. Nitrogen is the limiting component while carbon is abundant; as bacteria degrades settling marine-organic matter; it will deplete the sample of nitrogen, leaving a remaining amount of carbon (Harry Rowe, personal

communication). Because the majority of the lower Eagle Ford section is missing (not cored) from the Winterbotham J.M. Jr. #1, data may be skewed to represent the uppermost lower Eagle Ford strata and may not be representative of the full stratigraphic section (Fig. 57). Dominant anoxic conditions during deposition caused high organic matter preservation, reflected by the highest TOC values within both cores (Figs. 17, 18).

The contact between the lower and upper Eagle Ford strata is defined by a major detrital influx of titanium-rich sediment (Figs. 10, 12). This detrital lithofacies (massive argillaceous claystone; Fig. 23) coincides with a zone of manganese enrichment (Figs. 10, 12). The distinct lithofacies is documented within both cores (Fig. 57). These two chemical signatures serve as the main defining attributes of the lower-upper Eagle Ford strata contact (Figs. 10, 12, 57). The contact can also be described by observing a gradual decrease in gamma ray values (decrease in clay minerals), a slight decrease and subsequent increase in calcium percent, a major decrease in molybdenum concentration, and bioturbation (Figs. 55, 56). Secondary dolomitization occurs at the lower-upper Eagle Ford strata contact within the Core-X; however, this trait does not appear within the Winterbotham J.M. Jr. #1 (Figs. 55, 56).

The C-T boundary as identified in Core-X and the Winterbotham J.M. Jr. #1 coincides with the contact between lower and upper Eagle Ford strata (Figs. 43, 45, 57). The transition from Cenomanian to Turonian is defined by the appearance of the Cenomanian-stage-biomarker keeled planktonic foraminifera *Rotalipora cushmani* and *Rotalipora greenhornensis* (Figs. 43, 45). The morphologic change of Heterohelcidae planktonic foraminifera tests from acute (Cenomanian-age *Heterohelix moremani*) to globular (Turonian-age *Heterohelix globulosa*) is used to identify the lowest Turonian (Figs. 43, 45).

The OAE2 occurs within both cores (Fig. 53). The positive $\delta^{13}\text{C}$ excursion creates three dominant peaks (Fig. 53). The positive excursion of $\delta^{13}\text{C}$ reflects enhanced algal organic matter preservation, reflected in decreased C/N atomic ratios (Figs. 17, 18, 49, 51). The first and lowest peak begins within the Cenomanian and lower Eagle Ford strata (Fig. 53). The latter two peaks are both larger (more positive and broader), and occur in the lowest Turonian in the upper Eagle Ford strata (Fig. 53). The second and third peaks represent the most positive excursion and coincide with deposition of the massive argillaceous claystone lithofacies, titanium enrichment, and manganese enrichment (Figs. 10, 12, 53, 57). Enrichment of manganese and initiation of burrowing indicates that periods of the OAE2 were in fact oxygenated (Figs. 26, 55).

The upper Eagle Ford strata display an immense degree of heterogeneity both within itself and between the two cores. Elemental abundances within both cores (Figs. 9, 10, 11, 12) show contrasting oxygenated and anoxic environments, while also demonstrating dominant intrabasinal carbonate sedimentation, dominant detrital clay mineral sedimentation, and nutrient-rich sediments resultant from high levels of primary productivity. Lack of intense bioturbation has allowed for pristine preservation of original laminations and sedimentary features, as well as original sediment and water chemistry heterogeneities (Fig. 57). When compared to the lower Eagle Ford strata, the upper Eagle Ford strata in both cores has a more diverse faunal assemblage, increased grain abundance, better developed primary sedimentary structures, increased detrital sedimentation, and increased slope instability/failure (Fig. 57).

While both cores contain ductile deformation of firm beds, soft-sediment deformation, and gravity-flows, lithofacies in the uppermost section of the upper Eagle Ford strata are dissimilar (Fig. 57). The upper Eagle Ford section in Core-X (Fig. 55) is dominated by calcisphere-rich ripples, whereas the Winterbotham J.M. Jr. #1 (Fig. 56)

contains laminations of a mixed skeletal assemblage (saccocomid fragments, inoceramid fragments, planktonic foraminifera, and fish bones). Detrital clay sedimentation in the upper Eagle Ford is present within the both Core-X and Winterbotham J.M. Jr. #1 (Fig. 10, 12). Detrital signals originate within the matrix of the measured samples, indicating an additional source of terrigenous influence not in the form of discrete ash beds (Figs. 10, 12). Discrete volcanic ash beds in the two cores display a yellow, clay-rich aphanitic groundmass with varying quantities and varieties of phenocrysts (Fig. 28). Beta quartz and plagioclase feldspar phenocrysts are present in moderate to high quantities within discrete volcanic ash deposits within the Winterbotham J.M. Jr. #1, but are rare to absent within the #1 Core-X (Fig. 28).

Water conditions varied during Eagle Ford deposition (Figs. 14, 15). While the lower, upper Eagle Ford strata contain elements evidencing an oxygen-rich, habitable environment, the uppermost, upper Eagle Ford strata demonstrate periodic anoxia (Figs. 14, 15). While three individual anoxic events can be identified in the Winterbotham J.M. Jr. #1 at the top of the upper Eagle Ford strata, one broad event is observed in the Core-X (Figs. 53, 57). Because of location and paleogeographic difference in depositional location, it is proposed that the three smaller events described within the Winterbotham J.M. Jr. #1 are equivalent to the single, larger event within the Core-X (Fig. 53). The upper Eagle Ford strata anoxic event is defined by a positive excursion of $\delta^{13}\text{C}$, enrichment of molybdenum, enrichment of vanadium, and increased silicon/aluminum values (Figs. 10, 12, 14, 15, 53). Faunal assemblages preserved within this anoxic event define extremely high productivity from shallow to intermediate water depths (Figs. 43, 45). Lack of keeled planktonic foraminifera demonstrates an uninhabitable deeper (outer neritic) water mass (Figs. 43, 45). Elemental abundances alternate between anoxic and nutrient-rich confirming high surface level productivity (Figs. 14, 15). It is proposed that

high primary productivity created an oxygen-minimum zone and subsequently stratified the water-column (Figs. 14, 15). While abundant radiolarians within the Core-X could explain the increase in silicon/aluminum values, no radiolarians are documented in the upper Eagle Ford strata anoxic event in the Winterbotham J.M. Jr. #1 (Figs. 10, 12, 43). Terrigenous or volcanic quartz silt may have played a role in the increased silicon values; however, data are inconclusive as to the origin of silicon enrichment during the upper Eagle Ford strata anoxic event.

The Austin Chalk in both cores represents the gradational change in depositional environment from Eagle Ford-style deposition to that of a carbonate platform represented by the Austin Chalk Group (Fig. 57). Lithofacies variety decreases, as do elemental abundances. Intense bioturbation in certain intervals homogenized sediment (Fig. 55, 56, 57). Bottom-currents were still active, definable by ripples contained within thin, laminated sections (Figs. 21, 22). A minor anoxic event is documented in the Austin Chalk of the Core-X that is not documented within the Winterbotham J.M. Jr. #1 (Figs. 55, 56). Because neither core contains a complete section of the Austin Chalk, results are inconclusive as to whether this event was local to the Core-X or had regional representation (Figs. 55, 56). The faunal assemblage within the Austin Chalk depicts a very different depositional environment than the underlying lower and upper Eagle Ford strata (Figs. 43, 45). Keeled planktonic foraminifera are more common in the Austin Chalk demonstrating better nutrient availability within the oligotrophic (deepwater) habitation zone (Figs. 43, 45). This distinction demonstrates oxygenation of the deepwater mass and a potential change in water mass stratification and decrease of basinal restriction (Figs. 50, 52). Organic matter preserved within the Austin Chalk indicates marine-plant matter influx and preservation (Figs. 50, 52).

CONCLUSIONS

Analyses from this study show a range of depositional environments influenced by bottom-currents, detrital sedimentation, high primary productivity, and variable levels of oceanic oxygenation (or the lack thereof).

The Buda Limestone represents high-productivity and high-levels of available nutrients on a healthy carbonate platform. This is shown in the increased nutrients preserved in the sediment, low molybdenum values, and pervasive bioturbation. The contact between the Buda Limestone and overlying Eagle Ford Group represents a major unconformity. This contact represents a substantial shift in deposition style (from shelf to drowned shelf) and faunal habitability (high-nutrient levels and oxygenated sediments to low-nutrient levels and anoxic to euxinic sediments).

The lower Eagle Ford represents maximum basinal restriction and slow bottom-water renewal rates. High concentration of molybdenum confirms anoxia. Nutrient-rich elements and the appearance of Hedbergellidae and Heterohelicidae confirm a stratified water mass with oxygenated surface and intermediate waters and anoxic deepwaters.

The contact between the lower and upper Eagle Ford strata is coincident with the Cenomanian-Turonian Boundary and occurs during the three-stage, positive $\delta^{13}\text{C}$ excursion defining the OAE2. The first stage of the OAE2 occurred within the Cenomanian-age lower Eagle Ford strata. The second stage of the OAE2 occurs simultaneously with the base of the Turonian-age upper Eagle Ford strata defined by the influx of a titanium-rich detrital chemofacies and major manganese enrichment. The third and last stage of the OAE2 is both the most positive and most vertically expansive. Manganese enrichment and burrowing within the OAE2 section depict periodic oxygenation during the event. The C-T boundary is defined biostratigraphically by the

documentation of *Rotalipora cushmani*, *Rotalipora greenhornensis*, and morphologic changes in Heterohelcidae test geometries.

Following the OAE2, deposition within the upper Eagle Ford strata is, for a short time, oxygenated. Elemental abundance heterogeneity demonstrates a changing depositional environment. Excellent preservation of original laminations and ripples document the lack of intense bioturbation, poor sediment oxygenation, and influence of bottom-currents. Detrital sedimentation is decreased from that observed within the lower Eagle Ford strata, represented within both the matrix fraction of the deposited sediments as well as in less abundant discrete volcanic ash beds. Sediment slumping and plastic deformation of firm beds is common within the upper Eagle Ford strata, as well as burrowing. Surface level primary productivity was extremely high and was the catalyst for a second anoxic event that occurs at the top of the upper Eagle Ford strata. This event differs from the OAE2 in several ways. The second event is defined by a positive excursion of $\delta^{13}\text{C}$ (less positive than that of the OAE2), enrichment of molybdenum (less than that of the OAE2), and enrichment of silicon not bound within clay minerals (found in the upper Eagle Ford strata anoxic event).

The Austin Chalk represents the gradational shift between classic Eagle Ford deposition (anoxic, laminated) to that of the Austin Chalk Group (bioturbated, healthy carbonate). Renewed deep-water oxygenation is defined by the prevalence of keeled planktonic foraminifera, as well as potentially decreased basinal restriction. Elemental abundances depict homogenization of bioturbated sediments and detrital phyllosilicate dominance of thin, laminated sediments.

The studied successions are correlative on a broad scale. Similarities are documented in both ocean chemistry and depositional environment. Because of common, small-scale heterogeneity, individual lithofacies packages cannot be correlated at the bed-

scale. Correlation of Eagle Ford Group stratigraphic and prospects should be considered based on geochemistry and definition of the three defined stratigraphic intervals.

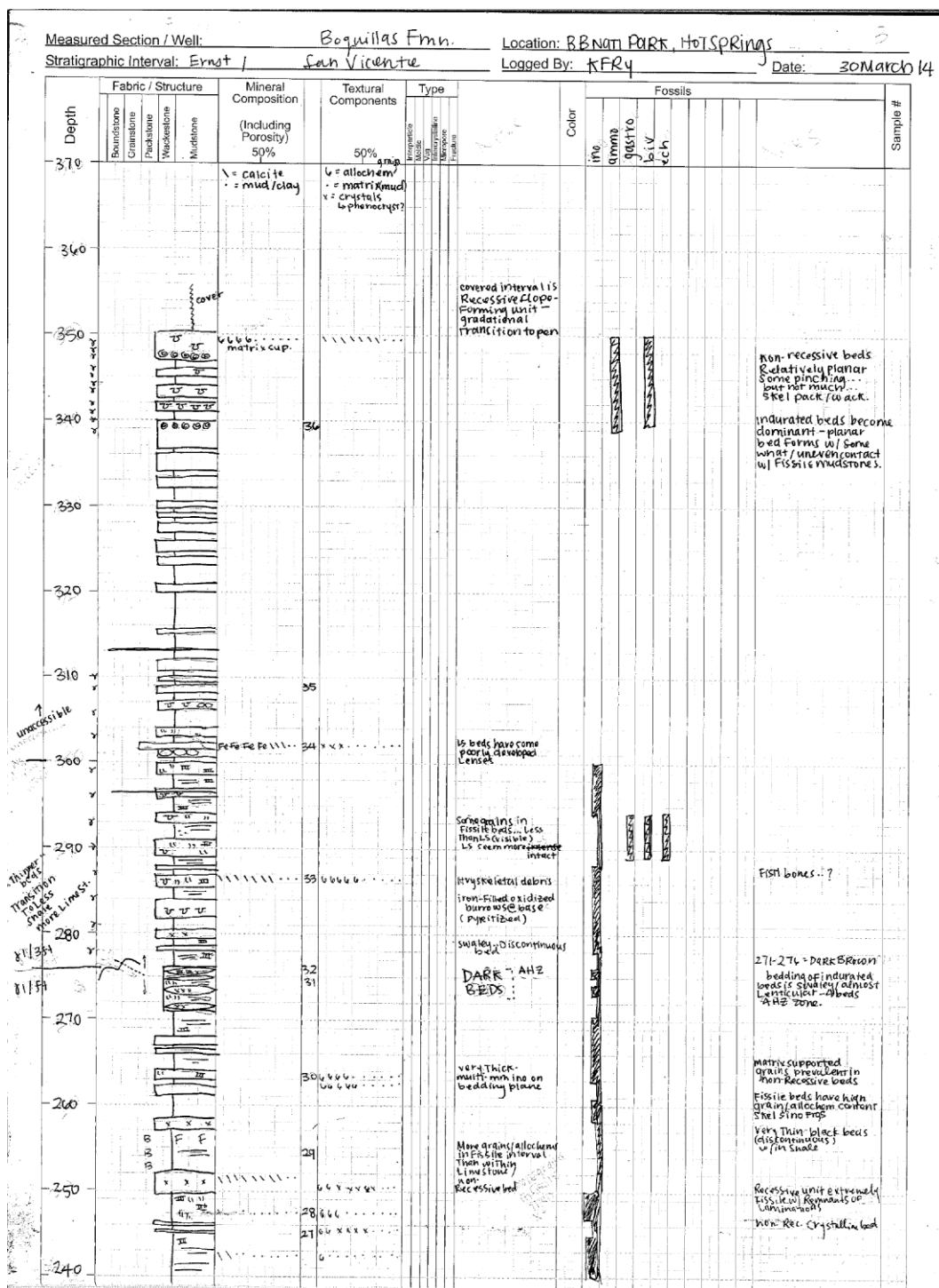
Characterization of lithofacies and chemofacies within the Eagle Ford Group help to better define and interpret the depositional system present on the Texas shelf during the Cenomanian-Turonian stages. High-resolution chemostratigraphy, isotope stratigraphy, and lithofacies analyses of the OAE2 and subsequent Late Cretaceous anoxic events provides insight into understanding the Eagle Ford and Boquillas depositional history.

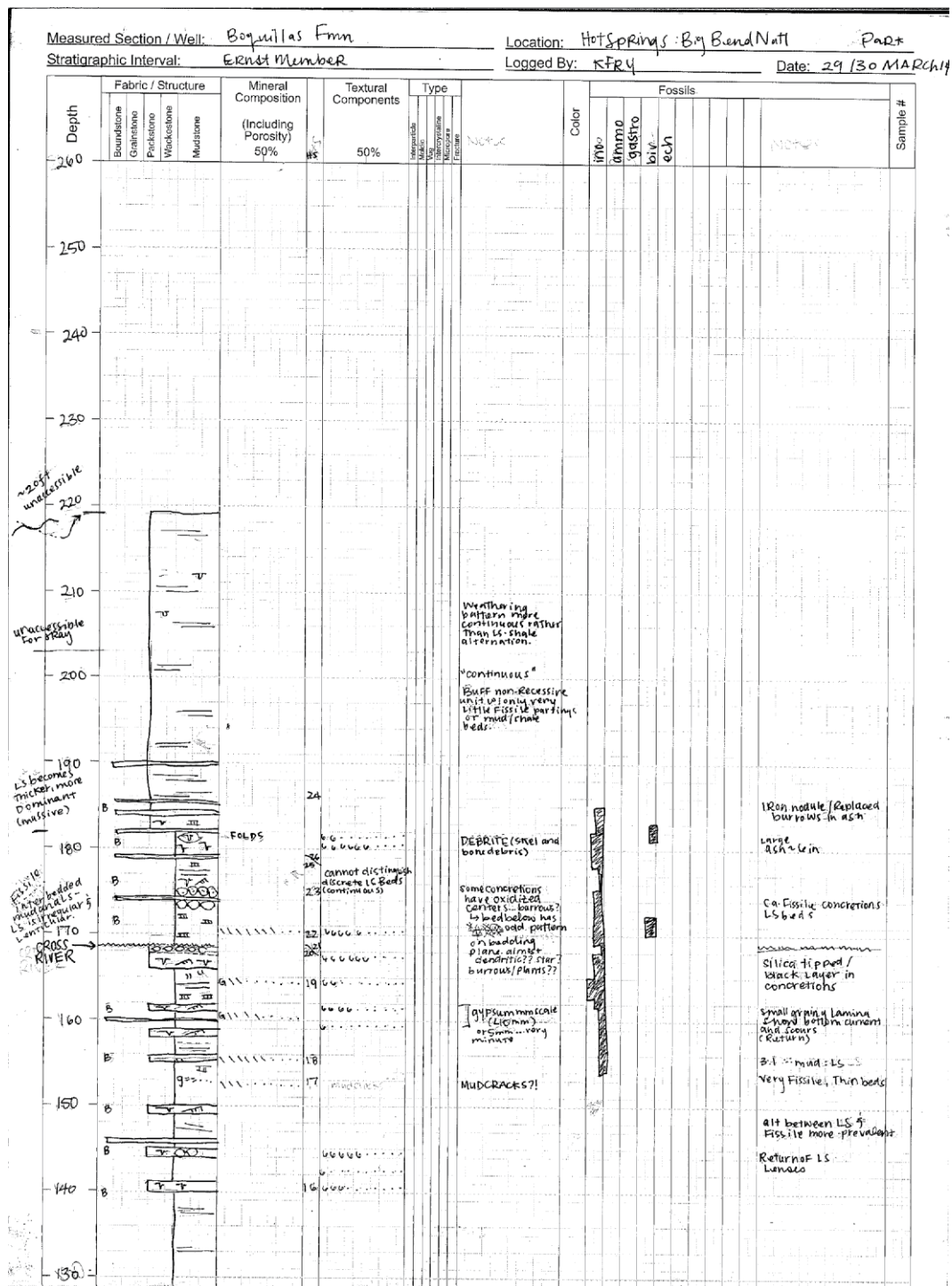
Appendices

Appendix A: Description of Core and Outcrop Sections

Appendix A contains original, hand-drafted stratigraphies and notes for each data set presented herein. Please refer to the symbol definitions presented in Figure 33. Width of each drafted lithofacies package is defined within the header of each drafting page.

HOT SPRINGS OUTCROP SECTION, BIG BEND NATIONAL PARK DESCRIPTION





Date: 29/29 March '14



Measured Section / Well:		Location:		Date:								
Stratigraphic Interval:		Logged By:										
Depth	Fabric / Structure	Mineral Composition (Including Porosity) 50%	Textural Components 50%	Type	Fossils						Sample #	
	Color				INVERTEBRATES	PROTOZOA	PHYTES	SPERMATOPHYTES	SEEDS	ANGIOSPERMS		GYMNOZPERMS
3490	TOP											
3500												
3510												
3520												
3530												
3540												
3550												
3560												
3570												

TOP

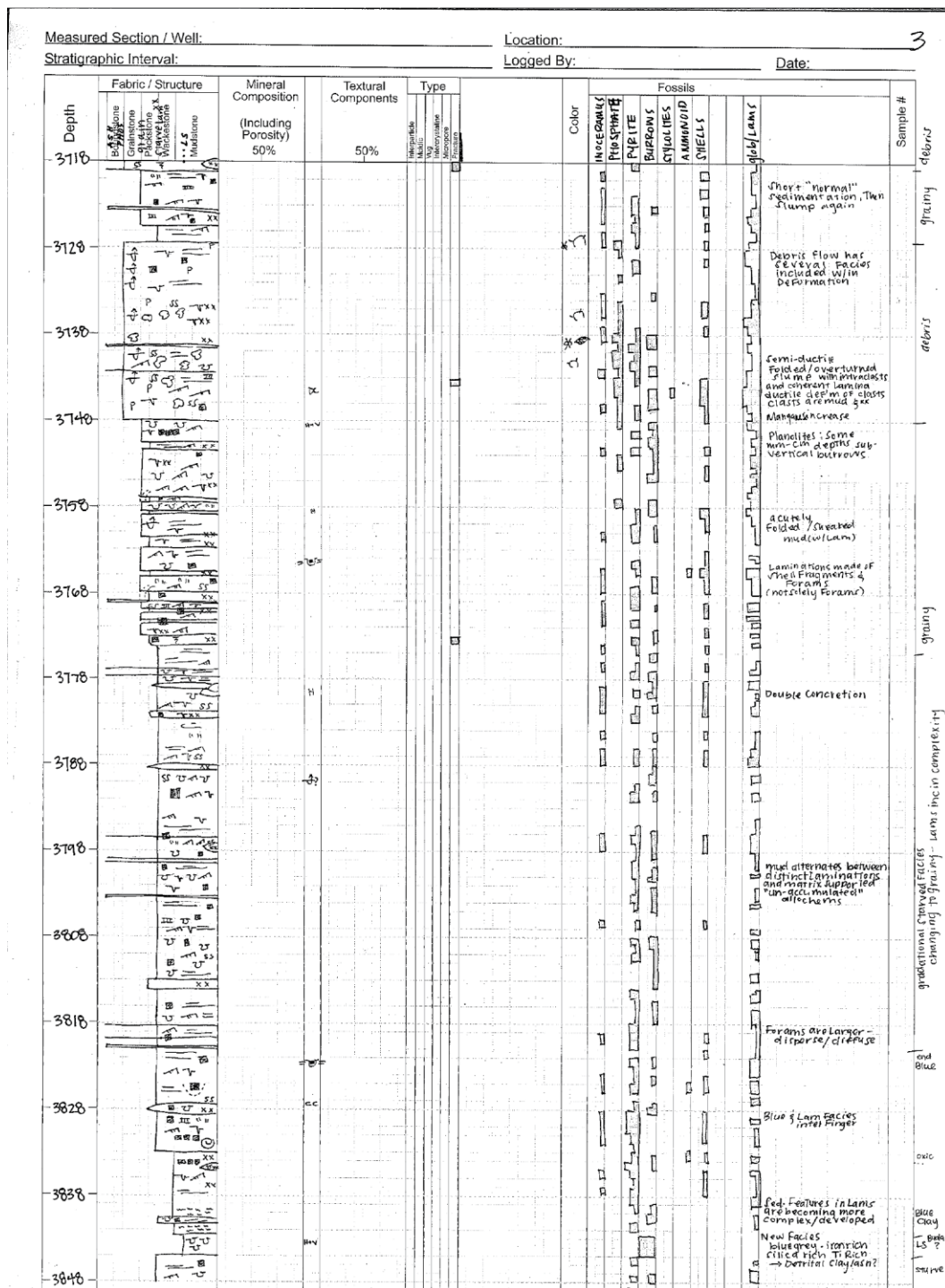
Burrows are less pervasive (deeper in?)

Blue smiting to come back

Remnant EF Lams
Visible but have been
converted finally to
concretions (hard lams)

↑ grey-ish
blue-ish

ALL
AUSP
CHAL



Measured Section / Well:

Location:

2

Stratigraphic Interval:

Logged By:

Date:

Depth	Fabric / Structure				Mineral Composition (Including Porosity) 50%	Textural Components 50%	Type		Color	Fossils						glob/Lams	Sample #
	Grainstone	Grainstone	Grainstone	Grainstone			Grainstone	Grainstone		INDETERMINATE	PHOSPHATE	PYRITE	BOREANUS	STYLOLITES	Ammonoid	Shells	
3840																	
3850																	
3860																	
3870																	
3880																	
3890																	
3900																	
3910																	
3920																	
3930																	
3940																	
3950																	
3960																	
3970																	
3980																	
3990																	
4000																	
4010																	
4020																	
4030																	
4040																	
4050																	
4060																	
4070																	
4080																	
4090																	
4100																	
4110																	
4120																	
4130																	
4140																	
4150																	
4160																	
4170																	
4180																	
4190																	
4200																	
4210																	
4220																	
4230																	
4240																	
4250																	
4260																	
4270																	
4280																	
4290																	
4300																	
4310																	
4320																	
4330																	
4340																	
4350																	
4360																	
4370																	
4380																	
4390																	
4400																	
4410																	
4420																	
4430																	
4440																	
4450																	
4460																	
4470																	
4480																	
4490																	
4500																	
4510																	
4520																	
4530																	
4540																	
4550																	
4560																	
4570																	
4580																	
4590																	
4600																	
4610																	
4620																	
4630																	
4640																	
4650																	
4660																	
4670																	
4680																	
4690																	
4700																	
4710																	
4720																	
4730																	
4740																	
4750																	
4760																	
4770																	
4780																	
4790																	
4800																	
4810																	
4820																	
4830																	
4840																	
4850																	
4860																	
4870																	
4880																	
4890																	
4900																	
4910																	
4920																	
4930																	
4940																	
4950																	
4960																	
4970																	
4980																	
4990																	
5000																	
5010																	
5020																	
5030																	
5040																	
5050																	
5060																	
5070																	
5080																	
5090																	
5100																	
5110																	
5120																	
5130																	
5140																	
5150																	
5160																	
5170																	
5180																	
5190																	
5200																	
5210																	
5220																	
5230																	
5240																	
5250												</					

Measured Section / Well: **Core-X**

Location: **MAVERICK COUNTY TX**

Stratigraphic Interval: **AL, RF, BUDA**

Logged By: **KPRY**

Date:

Depth	Fabric / Structure	Mineral Composition (Including Porosity) 50%	Textural Components 50%	Type	Color Soil Phase	Fossils	Sample #
3970	Blocky, massive, cherty						
3980	Blocky, massive, cherty						
3990	Blocky, massive, cherty						
4000	Blocky, massive, cherty						
4010	Blocky, massive, cherty						
4020	Blocky, massive, cherty						
4030	Blocky, massive, cherty						
4040	Blocky, massive, cherty						
4050	Blocky, massive, cherty						
4060	Blocky, massive, cherty						
4070	Blocky, massive, cherty						
4080	Blocky, massive, cherty						
4090	Blocky, massive, cherty						
4100	Blocky, massive, cherty						

WINTERBOTHAM J.M. JR. #1 CONVENTIONAL CORE DESCRIPTION

[illegible]

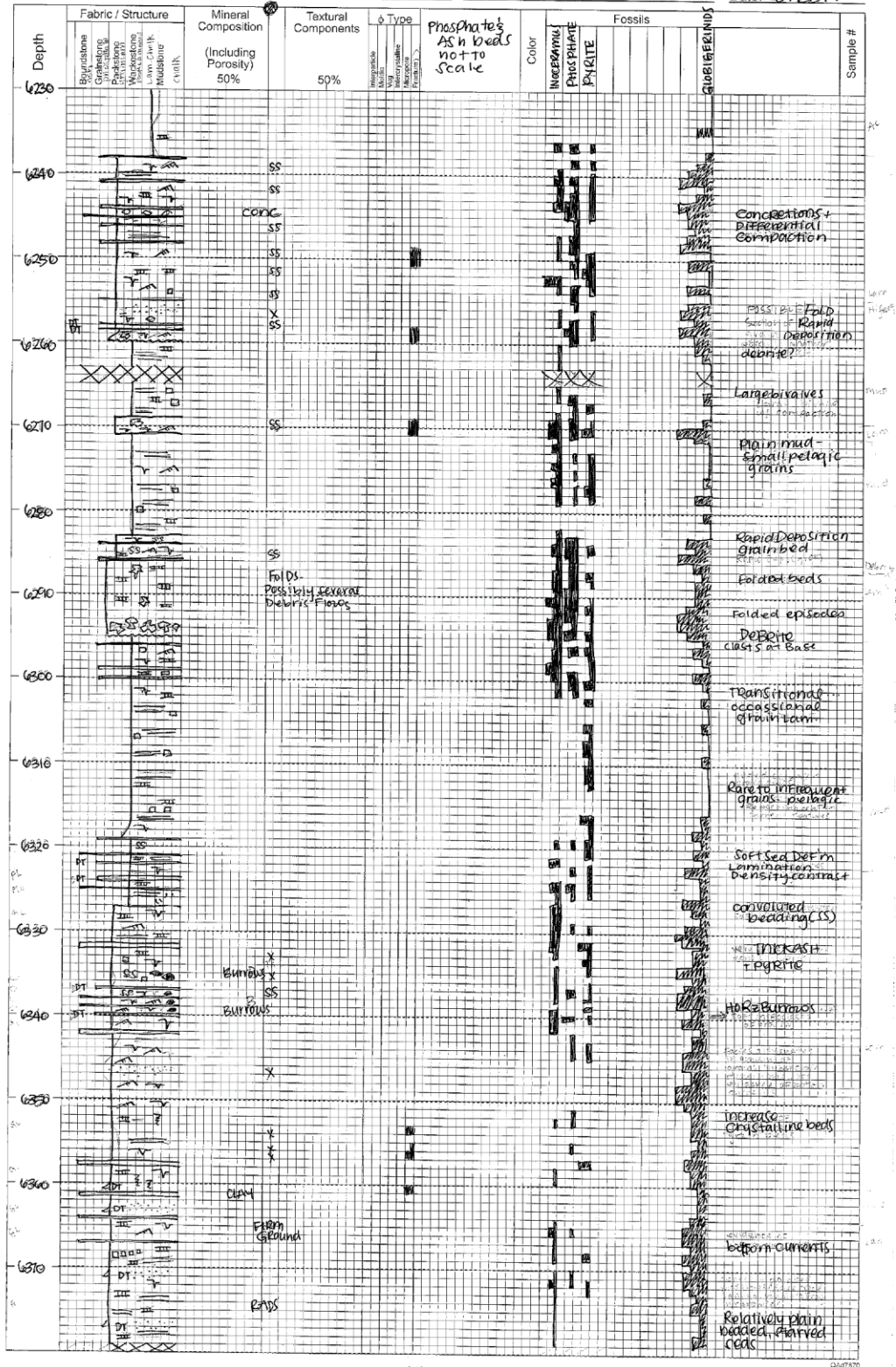
Measured Section / Well: WINTERBOTHAM

Location: ZAVALA COUNTY, TEXAS

Stratigraphic Interval: EAGLEFORD + AUSTIN CHALK

Logged By: KPEY

Date: 28 FEB 14



REFERENCES

- Adams, J. E., 1965, Stratigraphic-tectonic development of Delaware Basin: American Association of Petroleum Geologists Bulletin, v. 49, p. 2140-2148.
- Adkins, W. S., 1932, The Mesozoic systems in Texas, pt. 2 *in* The Geology of Texas: Texas University Bulletin, no. 3232, p. 239-518.
- Adkins, W. S., Lozo, F. E., 1951, Stratigraphy of the Woodbine and Eagle Ford, Waco area, Texas: Southern Methodist University, Fonder Science, v. 4, p. 105-161.
- Algeo, T. J., Heckel, P. H., Maynard, J. B., Blakey, R., Rowe, H., 2008, Modern and ancient epicratonic seas and the superestuarine circulation model of marine anoxia, *in* Paleontological and Geochemical Perspectives: Geological Association of Canada Special Publications, v. 48, p. 7-38.
- Algeo, T. J., Lyons, T. W., 2006, Mo-total organic carbon covariation in modern anoxic marine environments: implication for analysis of paleoredox and –hydrographic conditions: *Paleoceanography*, v. 21, pg. 23.
- Algeo, T. J., Lyons, W. L., Blakey, R. C., Over, D. J., 2007, Hydrographic conditions of the Devonian-Carboniferous North American Seaway inferred from sedimentary Mo-TOC relationships: *Paleogeography, Paleoclimatology, Paleoecology*, v. 256, p. 204-230.
- Algeo, T. J., Rowe, H., 2012, Paleoceanographic applications of trace-metal concentration data: *Chemical Geology*, v. 324-325, p. 6-18.
- Algeo, T. J., Tribouillard, N., 2009, Environmental analysis of paleoceanographic systems based on molybdenum-uranium co-variation: *Chemical Geology*, v. 268, p. 211-225.
- Arthur, M. A., Schlanger, S. O., Jenkyns, H. C., 1987, The Cenomanian/Turonian Oceanic Anoxic Event, II: Palaeoceanographic controls on organic matter production and preservation, *in* Marine Petroleum Source Rocks: Geological Society of London Special Publication, v. 26, p. 401–420.
- Barnes, V. E., 1977, Del Rio sheet of Texas Geologic Atlas, Robert Thomas Hill memorial edition: Texas Bureau of Economic Geology, Austin, scale 1:250,000.
- Blakey, R., 2013, Western North American Series: <http://www.cpgeosystems.com/paleomaps.html>.
- Boling, K. S., 2014, Controls on the Accumulation of organic matter in the Eagle Ford Group, Central Texas, USA: [Master's Thesis] Baylor University, Waco, Texas.

- Borg, S. G., DePaolo, D. J., 1994, Laurentia, Australia, and Antarctica as a Late Proterozoic supercontinent: constraints from isotopic mapping: *Geology*, v. 22, p. 307–310.
- Boudagher-Fadel, M. K., 2013, *Biostratigraphic and geological significance of planktonic foraminifera*, second edition: University College, London, UK.
- Brown, C. W., Pierce, R. L., 1963, Palynologic correlations in Cretaceous Eagle Ford Group, southeast Texas: *American Association for Petroleum Geologists Bulletin*, v. 46, no. 12, p. 2133-2147.
- Calvert, S., Pedersen, T., 1993, Geochemistry of recent oxic and anoxic marine sediments: implications for the geological record: *Marine Sediments, Burial, Pore Water Chemistry, Microbiology and Diagenesis*, v. 113, no. 1–2, p. 67–88.
- Coney, P. J., Reynolds, S. J., 1977, Cordilleran Benioff zones: *Nature*, v. 243, p. 403-406.
- Cooper, D. A., 2000, The *Allocrioceras hazzardi* zone (Turonian/Coniacian Boundary) in the Boquillas Formation of the Big Bend Region, Trans-Pecos, Texas: [Master's Thesis – unpublished] University of Louisiana at Lafayette.
- Cooper, R. W., Stevens, J. B., Cooper, D. A. R., Stevens, M. S., 2005, Proposed: Revise the contact between Ernst and San Vicente Members, Boquillas Formation, Big Bend National Park, Trans-Pecos, Texas: *Geological Society of America Abstracts with Programs*, v. 37, no. 3, p. 6.
- Cooper, D. A., Cooper, R. W., Stevens, J. B., Stevens, M. S., 2007, The Hot Springs Trail reference section (Cenomanian/Turonian/Coniacian Stages), Ernst Member, Boquillas Formation, Big Bend National Park, Texas: *Geological Society of America Abstracts with Programs*, v. 39, no. 6, p. 635.
- Cooper, R. W., 2011, *Geologic maps of Upper Cretaceous and Tertiary strata, Big Bend National Park, Texas*: Texas Bureau of Economic Geology, Miscellaneous map series, no. 0050.
- Cooper, R. W., Cooper, D. A., 2014, *Field guide to Late Cretaceous geology of the Big Bend region*: Houston Geological Society Field Guidebook.
- Cooper, R. W., 26 March 2014, Chronocorrelation of the Turonian-Coniacian Stage boundary in the Boquillas Formation, Big Bend region, Texas – *Allocrioceras hazzardi* zone, Houston Geological Society General Lunch, lecture conducted from Houston, Texas.
- Corbet, M. J., Watkins, D. K., 2013, Calcareous nanofossil paleoecology of the mid-Cretaceous Western Interior Seaway and evidence of oligotrophic surface waters during OAE2: *Palaeogeography, Palaeoclimatology, Palaeoecology*, doi: 10.1016/j.palaeo.2013.10.007.
- Cretaceous Period, 2014, In *Encyclopædia Britannica*. Retrieved from www.britannica.com/EBchecked/topic/142729/Cretaceous-Period.

- Culotta, R., Latham, T., Sydow, M., Oliver, J., Brown, L., and Kaufman, S., 1992, Deep structure of the Texas Gulf Passive Margin and its Ouachita-Precambrian basement: results of the COCORP San Marcos Arch survey: *The American Association of Petroleum Geologists Bulletin*, v. 76, p. 270-283.
- Dalziel, I. W. D., 1991, Pacific margins of Laurentia and East Antarctica–Australia as a conjugate rift pair: evidence and implications for an Eocambrian supercontinent: *Geology*, v. 19, p. 598–601.
- Dawson, W. C., 1997, Limestone microfacies and sequence stratigraphy: Eagle Ford group (Cenomanian-Turonian) North-Central Texas outcrops: *Gulf Coast Association of Geologic Societies Transactions*, v. 47.
- Dawson, W. C., 2000, Shale microfacies: Eagle Ford Group (Cenomanian-Turonian) North-Central Texas outcrops and subsurface equivalents: *Gulf Coast Association of Geologic Societies Transactions*, v. 50, p. 607-622.
- Dawson, W.C., Almon, W. R., 2010, Eagle Ford Shale variability: Sedimentologic influences on source and reservoir character in an unconventional reservoir unit: *Gulf Coast Association of Geological Societies Transactions*, v. 60, p. 181-190.
- Denne, R. A., Hinote, R. E., Breyer, J. A., Kosanke, T. H., Lees, J. A., Engelhardt-Moore, N., Spaw, J. M., Tur, N., 2014, The Cenomanian-Turonian Eagle Ford Group of south Texas: Insights on timing and paleoceanographic conditions from geochemistry and micropaleontologic analyses: *Palaeogeography, Palaeoclimatology, Palaeoecology*, <http://dx.doi.org/10.1016/j.palaeo.2014.05.029>.
- Donovan, A. D., Staerker, T. S., 2010, Sequence stratigraphy of the Eagle Ford (Boquillas) Formation in the subsurface of South Texas and outcrops of West Texas: *Gulf Coast Association of Geological Societies Transactions*, v. 60, p. 861-899.
- Donovan, A. D., Staerker, T. S., Pramudito, A., Li, W., Corbett, lowery, C. M., Romero, A. M., Gardner, R. D., 2012, The Eagle Ford outcrops of west Texas: A laboratory for understanding heterogeneities within unconventional mudstone reservoirs: *Gulf Coast Association of Geological Societies Journal*, v. 1, p. 162-185.
- Dravis, J. J., 1980, Sedimentology and diagenesis of the upper Cretaceous Austin Chalk Formation, South Texas and northern Mexico: Houston, Texas, Rice University.
- Driskill, B. Suurmeyer, N., Riling-Hall, S., Govert, A., Garbowicz, A., 2012, Reservoir description of the subsurface Eagle Ford Formation, Maverick Basin area, south Texas, USA: *Society of Petroleum Engineers*, no. 154528.
- Dunham, R. J., 1962, Classification of carbonate rocks according to their depositional texture, *in* Ham, W. E., (eds.), 1962, *Classification of carbonate rocks: a*

- symposium: American Association for Petroleum Geologists Memoir, no. 1, p. 108-121.
- Embry, A. F., Klován, J. E., 1971, A Late Devonian reef tract on Northeastern Banks Island, NWT: Canadian Petroleum Geology Bulletin, v. 19, p. 730-781.
- Ertel, J. R., Hedges, J. I., 1985, Sources of sedimentary humic substances: vascular plant debris: *Geochimica et Cosmochimica Acta*, v. 49, p. 2097-2107.
- Ewing, T., 2013, Eagle Ford – Colorado connection: Cenomanian to Coniacian in southwestern North America: AAPG Search and Discovery Article, no. 30288.
- Flügel, E., 2004, Microfacies of carbonate rocks: analysis, interpretation and application. Springer.
- Fairbanks, M. D., 2012, High resolution stratigraphy and facies architecture of the upper Cretaceous (Cenomanian-Turonian) Eagle Ford Group, central Texas: [Master's Thesis] University of Texas Austin, Austin, Texas.
- Folk, R. L., 1980, Petrology of sedimentary rocks: Austin, Texas, Hemphill Co., p. 182.
- Forkner, R., Minisini, D., Eldrett, J., Ozkan, A., Bergman, S., MacAulay, C., Lusk, M., 2013, Carbonate depositional motifs and cycle stacking patterns in the Eagle Ford Formation, Texas: American Association for Petroleum Geologists Search and Discovery Article, no. 50849.
- Freeman, V. L., 1961, Contact of the Boquillas flags and Austin chalk in Val Verde and Terrell Counties, Texas: American Association Petroleum Geologist Bulletin, v. 45, no. 1, p. 105-107.
- Freeman, V. L., 1968, Geology of the Comstock-Indian Wells area, Val Verde, Terrell, and Brewster Counties, Texas: Geological Survey Professional Paper, no. 594-K, p. 6-15.
- Galley, J. E., 1958, Oil and geology of the Permian Basin of west Texas and New Mexico, *in* Weeks, L. G. (eds.), Habitat of oil: Proceedings of symposium: American Association of Petroleum Geologists, Tulsa, OK, p. 395-446.
- Galloway, W. E., 2008, Depositional evolution of the Gulf of Mexico sedimentary basin, *in* Miall, A.D., (eds.), The sedimentary basins of the United States and Canada: New York, Elsevier, p. 610.
- Goldhammer, R. K., Johnson, C. A., 2001, Middle Jurassic-upper Cretaceous paleogeographic evolution and sequence-stratigraphic framework of the northwest Gulf of Mexico rim, *in* Bartolini, C., Buffler, R. T., Cantu-Chapa, A., (eds.) The western Gulf of Mexico Basin: Tectonics, sedimentary basins, and petroleum systems: American Association of Petroleum Geologists Memoir, v. 75, p. 45-81.

- Gray, J. E., Page, W. R., 2008, Geological, geochemical, and geophysical studies by the US Geological Survey in Big Bend National Park, Texas: United States Geological Survey Circular, no. 1327.
- Hackley, P. C., 2009, Preliminary vitrinite and bitumen reflectance, total organic carbon, and pyrolysis data for upper and lower Cretaceous strata, Maverick Basin, south Texas: United States Geological Survey Open File Report, no. 2009-1220.
- Harbor, R. L., 2011, Facies characterization and stratigraphic architecture of organic-rich mudrocks, upper Cretaceous Eagle Ford Formation, south Texas: [Master's Thesis] University of Texas Austin, Austin, Texas.
- Harries, P. J. and Kauffman, E. G., 1990, Patterns of survival and recovery following the Cenomanian-Turonian (Late Cretaceous) mass extinction in the Western Interior Basin, United States, *in* Kauffman, E. G. and Walliser, O. H. (eds.), Extinction events in Earth history: Berlin, Springer-Verlag, Lecture Notes in Earth History 30, p. 277-298.
- Harries, P. J., Kauffman, E. G., Crampton, J. S. (Redactors), Bengtson, P., Cech, S., Crame, J. A., Dhondt, A. V., Ernst, G., Hilbrecht, H., Lopez, Mortimore, G. R., Tröger, K.-A., Walaszyk, I. & Wood, C. J., 1996, Mitteilungen aus dem Geologisch: Paläontologischen Museum der Universität Hamburg, v. 77, p. 641-671.
- Hecky, R. E., Campbell, P., Hendzel, L. L., 1993, The stoichiometry of carbon, nitrogen, and phosphorous in particulate matter of lakes and oceans: Limnology Oceanography, v. 38, no. 4, p. 709-724.
- Hentz, T. F., Ruppel, S. C., 2011, Regional stratigraphic and rock characteristics of the Eagle Ford Shale in its play area: Maverick Basin to East Texas Basin: AAPG Search and Discovery Articles, no. 10325.
- Hill, R. T., 1887, The Texas section of the American Cretaceous: American Journal of Science, 3rd series, v. 34, p. 287-309.
- Hughes, E. N., 2011, Chemostratigraphy and paleoenvironment of the Smithwick Formation, Fort Worth Basin, San Saba County, Texas: [Master's Thesis] The University of Texas at Arlington, Arlington, Texas.
- Immenhauser, A., 2009, Estimating palaeo-water depth from the physical rock record: Earth Science Reviews, v. 96, p. 107-139.
- Ingall, E., Jahnke, R., 1997, Influence of water-column anoxia on the elemental fractionation of carbon and phosphorus during sediment diagenesis: Marine Geology, v. 139, no. 1, p. 219-229.
- Ingram, R. L., 1963, Fissility of mudrocks: Bulletin of the Geological Society of America, v. 64, p. 869-878.

- Jiang, M., 1989, Biostratigraphy and geochronology of the Eagle Ford shale, Austin chalk, and lower Taylor marl in Texas based on calcareous nannofossils: [PhD Dissertation] A & M University, College Station, Texas.
- Jarvis, I., Lignum, J. S., Gröcke, D. R., Jenkyns, H. C., Pearce, M. A., 2011, Black shale deposition, atmospheric CO₂ drawdown, and cooling during the Cenomanian-Turonian Oceanic Anoxic Event: *Paleoceanography*, v. 26, PA3201.
- Jasper, J. P.; Gagosian, R. B., 1990, Table 2 Contents and isotopic composition of carbon in sediments from DSDP Hole 96-619 *in* Supplement to: Jasper, J. P.; Gagosian, R. B., 1990, The sources and deposition of organic matter in the late Quaternary Pigmy Basin, Gulf of Mexico (Eds.): *Geochimica et Cosmochimica Acta*, v. 54, no. 4, p. 1117-1132.
- Jenkyns, H. C., 1980, Cretaceous anoxic events: from continents to oceans: *Journal of the Geological Society*, v. 137, p. 171-188.
- Jenkyns, H. C., 2010, Geochemistry of oceanic anoxic events: *Geochemistry, Geophysics, Geosystems*, v. 11, no. 3.
- Kauffman, E. G., 1988, The case of the missing community: Low-oxygen adapted Paleozoic and Mesozoic bivalves ("flat-clams") and bacterial symbioses in typical Phanerozoic oceans: *Geological Society of America, Abstracts with Programs*, v. 20, p. A48.
- Kauffman, E. G. and Harries, P. J., 1992, The ecology and life-habits of Cenomanian-Turonian Inoceramidae in North America: Workshop on Early Turonian Inoceramids (5-6 Oct, 1992, Hamburg) [Abstract].
- Kearns, T. J., 2011, Chemostratigraphy of the Eagle Ford Formation: [Master's thesis] University of Texas at Arlington, Arlington, Texas.
- Kerans, C. and Loucks, R., 2013, Reservoir characterization research laboratory research plans for 2013 outcrop and subsurface characterization of carbonate reservoirs for improved recovery of remaining hydrocarbons: *Bureau of Economic Geology*, p. 15.
- King, P. B., 1942, Permian of west Texas and southeastern New Mexico: *American Association of Petroleum Geologists Bulletin*, v. 26, p. 535-763.
- Liro, L. M., Dawson, W. C., Katz, B. J., Robison, V. D., 1994, Sequence stratigraphic elements and geochemical variability within a "condensed section": Eagle Ford Group, east-central Texas: *Gulf Coast Association of Geological Societies Transactions*, v. 44, p. 393-402.
- Liu, K., 2004, Seismic and sequence stratigraphy of upper Cretaceous strata, offshore Alabama and Mississippi area: *Gulf Coast Association of Geological Societies Transactions*, v. 54, p. 347-360.

- Lock, B. E., Peschier, L., 2006, Boquillas (Eagle Ford) upper slope sediments, West Texas: Outcrop analogs for potential shale reservoirs: Gulf Coast Association of Geological Societies Transactions, v. 56, p. 491-508.
- Lock, B. E., Bases, F. S., Glaser, R. A., 2007, The Cenomanian sequence stratigraphy of central to west Texas: Gulf Coast Association of Geological Societies Transactions, v. 57, p. 465-479.
- Lock, B. E., Peschier, L., Whitcomb, N., 2010, The Eagle Ford (Boquillas Formation) of Val Verde County, Texas – A window on the South Texas play: Gulf Coast Association of Geological Societies Transactions, v. 60, p. 419-434.
- Loucks, R., G., 1978, Pearsall Formation, lower Cretaceous, south Texas: depositional facies and carbonate diagenesis and their relationship to porosity: [PhD Dissertation], University of Texas at Austin, Austin, Texas.
- Lowery, C. M., Corbett, M. J., Leckie, R. M., Watkins, D., Romero, A. M., Pramudito, A., 2014, Foraminiferal and nannofossil paleoecology and paleoceanography of the Cenomanian-Turonian Eagle Ford Shale of southern Texas: *Palaeogeography, Palaeoclimatology, Palaeoecology*, <http://dx.doi.org/10.1016/j.palaeo.2014.07.025>.
- MacLeod, K. G. and Hoppe, K. A., 1992, Evidence that inoceramid bivalves were benthic and harbored chemosynthetic symbionts: *Geology*, v. 20, p. 117-120.
- Mancini, E. A., Puckett, T. M., 1995, upper Cretaceous sequence stratigraphy of the Mississippi-Alabama area: Gulf Coast Association of Geological Societies Transactions, v. 45, p. 377-384.
- Manning, C. D., Raghavan, P., Schutze, H., 2008, Introduction to information retrieval: Cambridge University Press, ch. 16-17.
- Martin, J. D., 2008, Using X Powder: A software package for Powder X-Ray diffraction analysis: www.xpowder.com D.L. GR 1001/04.ISBN 84-609-1497-6.
- Maxwell, R.A., and Dietrich, J. W., 1965, Geologic summary of the Big Bend region, IN *Geology of the Big Bend area, Texas, with road log and papers on natural history of the area*: West Texas Geological Society Special Publication, October, 1965, no. 65-51, p. 11-33.
- Maxwell, R.A., and Hazzard, R. T., 1967, Stratigraphy, *in* Maxwell, R.A., (Eds.) 1967, *Geology of Big Bend National Park, Brewster County, Texas*: University of Texas-Austin, Bureau of Economic Geology Publication, no. 6711, p. 23-156. [<http://www.lib.utexas.edu/books/landscapes/publications/txu-oclc-600183/txu-oclc-600183.pdf>]
- McCormick, C. L., Smith, C. I., Henry, C. D., 1996, Cretaceous stratigraphy *in* Henry, C. D., Muehlberger, W. R., *Geology of the Solitario dome, Trans-Pecos Texas: Paleozoic, Mesozoic, and Cenozoic sedimentation, tectonism, and magmatism*:

- The University of Texas at Austin, Bureau of Economic Geology Report of Investigations, no. 240, p. 30-46.
- McFarlan, E. M., Menes, L. S., 1991, lower Cretaceous, *in* Salvador, A., The geology of the Gulf Coast basin: Geological Society of America, Geology of North America, vol. J, p. 181-204.
- McGarity, H. A., 2013, Facies and stratigraphic framework of the Eagle Ford Shale in South Texas:[Master's Thesis] University of Houston, Houston, Texas.
- McNulty, C. L. Jr., 1964, Foraminifers from the Eagle Ford-Austin contact, North East Texas: Association Round Table, v. 48, no. 4, p. 537.
- Meyers, P. A., 1994, Preservation of elemental and isotopic source identification of sedimentary organic matter: Chemical Geology, v. 114, p. 289-302.
- Meyers, P. A., 1997, Organic geochemical proxies of paleoceanographic, paleolimnologic, and paleoclimatic processes: Organic Geochemistry, v. 27, no. 5/6, p. 201-250.
- Meyers, P. A., Sillman, J. E., 2004, 15. Organic matter in Pleistocene to Quaternary turbidites from sites 897, 898, 899, and 900, Iberia abyssal plain *in* Whitmarsh, R. B., Sawyer, D. S., Klaus, A., Masson, D. G. (Eds.), 1996, Proceedings of the Ocean Drilling Program, Scientific Results, v. 149, p: 305-313.
- Miller, R. W., 1990, The stratigraphy and depositional environment of the Boquillas Formation of southwest Texas: [Master's thesis] The University of Texas at Arlington, Arlington, Texas.
- Müller, P. J., 1977, C/N ratios in Pacific deep-sea sediments: Effect of inorganic ammonium and organic nitrogen compounds sorbed by clays: Geochimica et Cosmochimica Acta, v. 41, p. 765-776.
- Moores, E. M., 1991, Southwest U.S.–East Antarctic (SWEAT) connection: a hypothesis: Geology, v. 19, p. 425–428.
- Moran, L. M., 2012, High resolution geochemistry of the Cretaceous Eagle Ford Formation, Bee County, Texas: [Master's Thesis] University of Texas at Arlington: Arlington, Texas.
- Murray, G. E., 1961, Geology of the Atlantic and Gulf Coastal province of North America: Harper, New York, New York, p. 692.
- Negra, M. H., Zagarni, M. F., Hanini, A., Strasser, A., 2011, The filament event near the Cenomanian-Turonian boundary in Tunisia: filament origin and environmental signification: Societe Geologique de France, v. 182, no. 6, p. 507-519.
- O'Leary, M. H., 1988, Carbon isotopes in photosynthesis: BioScience, v. 38, no. 5, p. 328-336.

- Pearson, O. N., Rowan, E. L., Dubiel, R. F., and Miller, J. J., 2010, Mesozoic-Cenozoic structural evolution of East Texas - constraints and insights from interpretation of 126 regional 2D seismic lines and structural restoration: Gulf Coast Association of Geological Societies Transactions, v. 60, p. 571-582.
- Pessagno, E. A., 1967, upper Cretaceous planktonic foraminifera from the western Gulf Coastal Plain: *Paleontographica Americana*, v. 5, no. 37, p. 245-445.
- Pessagno, E. A., 1969, upper Cretaceous stratigraphy of the western Gulf Coast area of Mexico, Texas, and Arkansas: *Geological Society of America Memoir*, v. 111, p. 139.
- Phelps, R. M., 2011, Middle-Hauterivian to Lower-Campanian sequence stratigraphy and stable isotope geochemistry of the Comanche Platform, South Texas: [PhD Dissertation] University of Texas Austin, Austin, Texas.
- Pierce, J. D., 2014, U-Pb Geochronology of the Late Cretaceous Eagle Ford Shale, Texas; Defining chronostratigraphic boundaries and volcanic ash source: [Master's Thesis] University of Texas Austin, Austin, Texas.
- Pommer, M. E., 2014, Quantitative assessment of pore types and pore size distribution across thermal maturity, Eagle Ford formation, south Texas: [Master's Thesis] University of Texas Austin, Austin, Texas.
- Powell, J. D., 1965, Late Cretaceous platform-basin facies, Northern Mexico and adjacent Texas: *Bulletin of the American Association of Petroleum Geologists*, v. 49, no. 5, p. 511-525.
- Prahl, F. G., Ertel, J. R., Goni, M. A., Sparrow, M. A., Eversmeyer, B., 1994, Terrestrial organic carbon contributions to sediments on the Washington margin: *Geochimica et Cosmochimica Acta*, v. 58, p. 3035-3048.
- Premuzic E. T., Benkovitz C. M., Gaffney J. S., Walsh J. J., 1982, The nature and distribution of organic matter in the surface sediments of world oceans and seas: *Organic Geochemistry*, v. 4, p. 63-77.
- Raup, D. M., Sepkoski Jr., J. J., 1984, Periodicity of extinctions in the geologic past: *Proceedings of the National Academy of Sciences of the United States of America*, v. 81, no. 3, p. 801-805.
- Redfield, A. C., 1934, On the proportions of organic derivatives in sea water and their relation to the composition of plankton *in* James Johnstone Memorial Volume: University of Liverpool, UK, p. 176-192.
- Roemer, F., 1852, *Die Kreidebildungen von Texas und ihre organischen Einschlüsse*: Bonn (Germany), Adolph Marcus, p. 100.
- Rose, P. R., 1972, Edwards Group, surface and subsurface, Central Texas: Texas Bureau of Economic Geology Report of Investigations, Austin, v. 74, p. 198.

- Rose, P. R., 1986, Oil and gas occurrence in lower Cretaceous rocks, Maverick basin area, southwest Texas, *in* W. E. Stapp, ed., Contributions to the geology of south Texas, 1986: South Texas Geological Society, p. 408–421.
- Rowe, H. D., Loucks, R. G., Ruppel, S. C., Rimmer, S. M., 2008, Mississippian Barnett Formation, Fort Worth Basin,, Texas: Bulk geochemical inferences and Mo-TOC constraints on the severity of hydrographic restriction: *Chemical Geology*, no. 257, p. 16-25.
- Rowe, H., Hughes, N., 2010, Strategy for developing and calibrating shale and mudstone chemostratigraphies using hand-held x-ray fluorescence units: *American Association for Petroleum Geologists Search and Discovery Article*, no. 90104.
- Rowe, H. D., Hughes, N., Robinson, K., 2012, The quantification and application of handheld energy-dispersive x-ray fluorescence (ED-XRF) in mudrock chemostratigraphy and geochemistry: *Chemical Geology*, v. 324, p. 122-131.
- Sageman, B. B., Meyers, S. R., Arthur, M. A., 2006, Orbital time scale and new C-isotope record for Cenomanian-Turonian boundary stratotype: *Geology*, v. 34, p. 125–128.
- Salvador, A. and Muñeton, J. M. Q., 1989, Stratigraphic correlation chart Gulf of Mexico Basin, *in* Salvador, A., (eds.), The Gulf of Mexico Basin: Geological Society of America, The Geology of North America, v. J., plate 5.
- Schieber, J. and Southard, J. B., 2009, Bedload transport of mud by floccule ripples – Direct observation of ripple migration processes and their implications: *Geology*, v. 37, no. 6, p. 483-486.
- Schieber, J., Southard, J. B., Kissling, P., Rossman, B., Ginsburg, R., 2013, Experimental deposition of carbonate mud from moving suspensions: Importance of flocculation and implications for modern and ancient carbonate mud deposition: *Journal of Sedimentary Research*, v. 83, pg. 1025-1031.
- Schlanger, S. O., Jenkyns, H. C., 1976, Cretaceous oceanic anoxic events: causes and consequences: *Geologie en Mijnbouw*, v. 55, p. 179-184.
- Schlanger, S. O., Arthur, M. A., Jenkyns, H. C., Scholle, P. A., 1987, The Cenomanian-Turonian Oceanic Anoxic Event, I. Stratigraphy and distribution of organic-rich carbon beds and marine $\delta^{13}\text{C}$ excursion: *Geological Society of London Special Publication*, vol. 26, no. 1, p. 371-399.
- Scholle, P. A., Ulmer-Scholle, D. S., 2003, A Color Guide to the Petrography of carbonate Rocks: *American Association of Petroleum Geology Memoir* 77.
- Scott, R.W., 2010, Cretaceous stratigraphy, depositional systems, and reservoir facies of the northern Gulf of Mexico: *Gulf Coast Association of Geological Societies Transactions*, v. 60, p. 597-609.

- Sellards, E. H., Adkins, W. S., Plummer, F. B., 1933, The geology of Texas: University of Texas-Austin, University of Texas Bulletin, no. 3232, v. 1, p. 400-451.
- Shepard, T. M., Walper, J. L., 1982, Tectonic evolution of Trans-Pecos, Texas: Gulf Coast Association of Geological Societies Transactions, v. 32, p. 165-172.
- Sohl, N. F., Martinez R. E., Salmeron-Urena, P., Soto-Jaramillo, F., 1991, upper Cretaceous, *in* Salvador, A. eds., The Gulf of Mexico Basin, The Geology of North America: Geological Society of America, Boulder, CO, v. J, p. 205–244.
- Surles, M. A., 1987, Stratigraphy of the Eagle Ford Group (upper Cretaceous) and its source rock potential in the East Texas Basin: Baylor Geological Studies, no. 45.
- Tibco spotfire 4.0 user's manual, 2011, TIBCO Spotfire: TIBCO Spotfire Inc.
- Tiedemann, N. S., 2010, The sequence stratigraphy of the Comanchean-Gulfian interval, Big Bend National Park, west Texas: [Master's Thesis] Ball State University, Muncie, IN.
- Trevino, R. H., 1988, Facies and depositional environments of the Boquillas Formation, upper Cretaceous of southwest Texas: [Master's thesis] The University of Texas at Arlington, Arlington, TX.
- Tribovillard, N., Bout-Roumazelles, V., Algeo, T., Lyons, T. W., Sionneau, T., Montero-Serrano, J. C., Riboulleau, A., Baudin, F., 2008, Paleodepositional conditions in the Orca Basin as inferred from organic matter and trace metal contents: Marine Geology, v. 254, no. 1-2, p. 62–72.
- Turner, K. J., Berry, M. E., Page, W. R., Lehman, T. M., Bohannon, R. G., Scott, R. B., Miggins, D. P., Budahn, J. R., Cooper, R. W., Drenth, B. J., Anderson, E. D., Williams, V. S., 2011, Geologic map of Big Bend National Park, Texas: U.S. Geological Survey, Scientific Investigations Map 3142, scale 1:75,000, pamphlet 84.
- Udden, J. A., 1907, A Sketch of the Geology of the Chisos Country, Brewster County, Texas: University of Texas-Austin, Bulletin of the University of Texas, no. 93, p. 29-33.
- Urbanczyk, K. M., Rohr, D., White, J. C., 2001, Geologic history of west Texas *in* Mace, R. E., Mullican, W. F. III, Angle, E. S. (Eds.), 2001, Aquifers of west Texas: Texas Water Development Board Report, no. 356, ch. 2.
- Van Cappellen, P., Ingall, E. D., 1994, Benthic phosphorus regeneration, net primary production, and ocean anoxia: A model of the coupled marine biogeochemical cycles of carbon and phosphorus: Paleoceanography, v. 9, no. 5, p. 677–692.
- Verardo, D. J., Froelich, P. N., McIntyre, A., 1990, Determination of organic carbon and nitrogen in marine sediments using Carlo Erba NA-1500 analyzer: Deep-Sea Research, v. 37A, p. 157-165.

- Voigt, S., Erbacher, J., Mutterlose, J., Weiss, W., Westerhold, T., Wiese, F., Wilmsen, M., Wonik, T., 2008, The Cenomanian-Turonian of the Wunstorf section (North Germany): Global stratigraphic reference section and new orbital time scale for Oceanic Anoxic Event 2: *Newsletter Stratigraphy*, v. 43, p. 65–89.
- von Breymann, M. T., Berner, U., 1991, Isotopic characterization of secondary carbonates from Sulu and Celebes sea basalts: contrasting scenarios of basalt-seawater interaction *in* Silver, E. A., Rangin, C., von Breymann, M. T., *Proceedings of the Ocean Drilling Project, Scientific Results*, 124: College Station, TX (Ocean Drilling Program), p. 233–237.
- Walls, J. D., Diaz, E., Sinclair, S. W., 2011, Eagle Ford shale characterization by Digital Rock Physics (DRP): AAPG Southwest Sectional.
- Wilson, J. L., Ward, W. C., Finnerman, J., eds., 1984, A field guide to upper Jurassic and lower Cretaceous carbonate platform and basin systems, Monterrey-Salttillo area, northeast Mexico: Gulf Coast Section, Society of Economic Paleontologists and Mineralogists.
- Wilson, J. L., and Ward, W. C., 1993, Early Cretaceous carbonate platforms of northeastern and east-central Mexico, *in* Simo, J. S., Scott, R. W., Masse, J. P., eds., *Cretaceous carbonate platforms: American Association of Petroleum Geologists Memoir* 56, p. 35–50.
- Wilson, J. L., 1999, Controls on the wandering path of the Cupido Reef trend in northeastern Mexico *in* Bartolini, C., Wilson, J. L., Lawton, T. F., *Mesozoic sedimentary and tectonic history of north-central Mexico: Geologic Society of America Special Paper*, no. 340.
- Winker, C. D., Buffler, R. T., 1988, Paleogeographic evolution of early deep-water Gulf of Mexico and margins, Jurassic to Middle Cretaceous (Comanchean): *American Association of Petroleum Geologists Bulletin*, v. 72, p. 318–346.
- Wokasch, T., 2014, Elemental chemostratigraphy and depositional environment interpretation of the Eagle Ford Shale, south Texas: [Master's Thesis] Colorado School of Mines, Golden, Colorado.
- Wu, S., Vail, P. R., Cramez, C., 1990, Allochthonous salt, structure and stratigraphy of the north-eastern Gulf of Mexico. Part I: Stratigraphy: *Marine and Petroleum Geology*, v. 7, p. 318–333.
- Young, A., 1986, Cretaceous marine inundations of the San Marcos platform: *Cretaceous Research*, v. 7, p. 117–140.

VITA

Kathryn O'Rourke Fry grew up in Newhall, California and graduated from William S. Hart High School in spring 2008. In September 2008, she enrolled at the University of California at Santa Barbara where she studied both music and geology. While attending UCSB, Kathryn studied for one year at the University of Glasgow, Scotland. After returning to the states, she participated in geochemical research under the direction of Dr. Jim Boles. Kathryn completed a senior thesis focused on U-Pb dating of zircon and petrography of microdiorite intrusives from the Chambers Well dike swarm in the Whipple Mountains under the direction of Dr. Phil Gans. She received a Bachelor of Science in Geological Sciences in 2012. In the fall of 2012, Kathryn entered the Jackson School of Geosciences at the University of Texas at Austin. She anticipates graduating with a Master of Science in Geological Sciences in May, 2015.

Permanent e-mail: orourke.kathryn@gmail.com

This thesis was typed by Kathryn O'Rourke Fry.